Development of versatile Raman spectroscopy system for characterization of drug delivery devices and SERS applications

Slipets, Roman

Publication date:
2020

Document Version
Publisher's PDF, also known as Version of record

DTU Health Tech
Department of Health Technology

Development of versatile Raman spectroscopy system for characterization of drug delivery devices and SERS applications

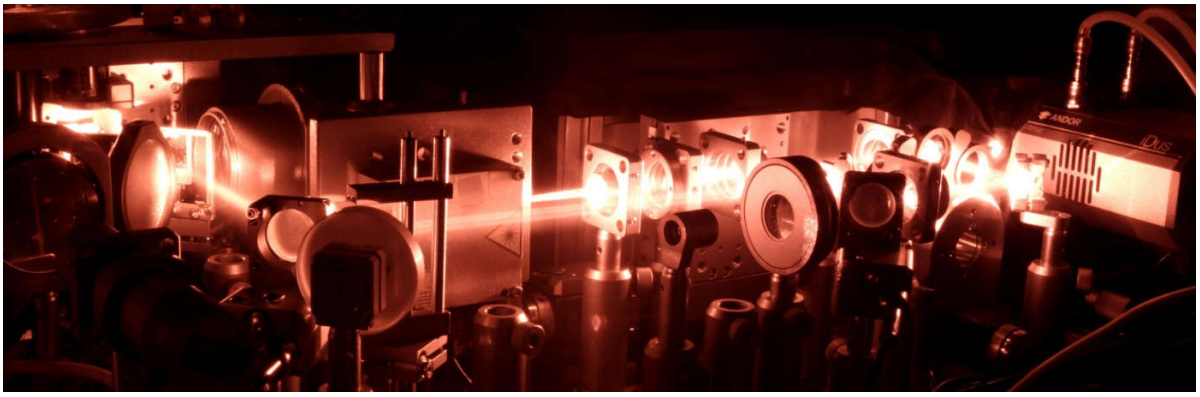

Roman Slipets
PhD Thesis

November 2020

Development of versatile Raman spectroscopy system for characterization of drug delivery devices and SERS applications

PhD thesis

Author: Roman Slipets

Supervisor: Anja Boisen
Co-supervisor: Tomas Rindzevicious

DTU Health Technology

Technical University of Denmark

2800 Kongens Lyngby
Denmark

November 2020

Danmarks Grundforskningsfond
Danish National Research Foundation

IDUN

VILLUM FONDEN

Preface

This PhD project is presented as a partial requirement for obtaining a doctoral degree from the Technical University of Denmark (DTU). The project was funded by the Danish National Research Foundation (DNRF122) and Villum Fonden (Grant No. 9301) and conducted as part of the Center for Intelligent Drug Delivery and Sensing Using Microcontainers and Nanomechanics (IDUN).

All research presented in this thesis was carried out at the Department Micro- and Nanotechnology (DTU Nanotech) from November 2017 to October 2020, which is called Department of Health Technology (DTU Health Tech) from 1st of January 2019. The PhD project was supervised by Professor Anja Boisen and Associate Professor Tomas Rindzevicius.

Acknowledgements

First of all, I would like to thank my principal supervisor Prof. Anja Boisen. She gave me the opportunity to join the team that stays on the front edge of modern technology and opened a view on a science-to-industry pathways. She is also being a helpful, inspiring, and responsible supervisor, has always supported my motivation in the diversified research directions.

In the same regard, I would like to express my gratitude to Associate Professor Tomas Rindzevicius. I highly appreciate for the scientific discussions and meetings we had and the substantial recommendations I received to employ in my research strategy. He provided great support to my work with useful suggestions and feedback.

Great thanks to Oleksii Ilchenko for being my research companion and for the support he has shown me in the beginning of my journey.

I am really grateful to the IDUN group, intelligent and creative people. I was inspired to work with all of you through these three years. I hope my input were no less and give growth to our group.

A special thanks goes to Professor En Te Hwu whose affable greetings and small talks brightened my scientific life and widened my personal interests.

Also, I am very appreciated to our administrative staff: Tine, Louise, Dorthe and Sanne; I would like to thank them all for their assistance.

I would like to thank my friends within and outside of the group. It was not so easy to start the project far away from home but with all the empathy I received from friends, staff and colleagues it made my life pleasant and fulfilled.

Abstract

Global industrialization and the following wide spread of products from chemical, cosmetic, and pharmaceutical industries into our life requires precise development and control of those substances. At the same time technological improvement and miniaturization of functional components like electronics, optical sensors and microcomputers open new opportunities for development of new analytical techniques, which can be applied in e.g. health monitoring and in quality control during manufacturing of pharmaceutical products.

This PhD thesis demonstrates a versatile Raman spectroscopic system, it's development stages and technical realizations of different modules for (i) drug characterization (microstructural chemical mapping, kinetic studies of transformation processes, crystal orientation determination), and (ii) low concentration drug detection in combination with external modules, like centrifugal microfluidics disc platform or heating/cooling microscopy stage.

The Raman system is designed as a modular platform, built with mostly elementary components with rich functionality. The system can be completely reconfigured, modified, or combined with specialized devices, with e.g. a view on a future miniaturization. The applications of the system have been focused on the development and evaluation of analytical methods for analysis of materials and devices developed within the IDUN center of excellence.

The high sensitivity and confocal possibilities of the system, as well as operation flexibility and integrated analytical tools made it possible for us to demonstrate volumetric mapping of microcontainers and multilayered tablets for oral drug delivery. The use of: (i) highly-optimized optics in the near-infrared range, (ii) fully-customizable scanning algorithm with exponential dependency of the frame exposition time and scanning order to not overheat the sample, and (iii) sample cooling stage with CO_2 purging allowed us to obtain a Raman signal from a depth of up to 200 μm. The signals were then used further chemical decomposition and 3-dimensional modeling of material distribution.

The long scanning time, which is typical for weak spontaneous Raman spectroscopy, was overcome by introducing laser line illumination of the sample together with design of an aberration-corrected spectrograph. This illumination mode provides 256 (with our type of CCD camera) simultaneous spectra measurements along the laser line on a sample, which allows us to significantly speed up the process of surface scanning, and improves the possibility of studying kinetic processes in a target material. The line scanning method was applied for a study of dehydration phase transformations of nitrofurantoin monohydrate and theophylline crystals. In comparison to bulk thermal methods of analysis, we demonstrated the possibility to spatially resolve the presence of different solid forms of a drug during thermal processes of dehydration and we could visualize the dynamics of single particles related to the presence of metastable intermediates.

A method for low concentration drug detection was established by combining a microfluidic platform and surface-enhanced Raman spectroscopy (SERS). Due to the huge Raman signal enhancement by SERS-active materials and the matrix complexity of real samples, a purification procedure was required to remove all interfered components. A centrifugal microfluidic disk, integrated with substrates for SERS based sensing, was utilized for separation, filtration and accurate exposure of an analyte media on the SERS substrates. A modified "wide line" illumination mode was used for fast and accurate

surface scanning, which allowed us to detect an order of magnitude lower molecule concentrations in two proof-of-concept applications, detecting melamine in raw milk and p-Coumaric acid production from E. coli bacteria culture.

Lastly, a multi-beam polarized laser illumination and multichannel analyzer unit made it possible to perform a fast crystal orientation determination. While the sample remains stagnant, it is possible to simultaneously collect Raman spectra with numerous combinations of the incident laser beam polarization and orientation of the analyzer at several on-axis and off-axis detecting directions. The orientation sample maps were obtained by fitting rotation angles to measured datasets. Crystal orientations of the surface elements could have an important effect on essential properties of drug products, like disintegration and dissolution behavior. A model tablet formulation with integration of carbamazepine dihydrate crystals was prepared in order to map crystallographic orientations on the surface for the first time by Raman-based imaging.

Resumé på dansk

Global industrialisering og den efterfølgende udbredelse af kemikalier, kosmetik og farmaceutiske midler i vores hverdag, kræver præcis fremstilling og kontrol af disse. Samtidig åbner teknologiske fremskridt, samt minituariseringen af komponenter, såsom elektronik, optiske sensorer og mikrocomputere, op for nye muligheder inden for udvikling af nye analytiske teknikker.

Denne PhD afhandling demonstrerer et alsidigt Raman spektroskopi system, dets udviklingsstadier og tekniske realisering af forskellige moduler for (i) medikament karakterisering (mikrostruktural kemisk kortlægning, kinetiske studier af transformationsprocessor, krystalorienterings bestemmelse), og (ii) detektering af lave medikament koncentrationer, i kombination med eksterne moduler, såsom centrifugale mikrofluide platforme.

Raman systemet er designet som en modulær platform, bygget fra de mest elementære komponenter med stor funktionalitet. Systemet kan komplet re-konfigureres, modificeres eller kombineres med specialiserede enheder, med henblik på en mulig kommende miniaturisering. Anvendelser af dette Raman system, er fokuseret omkring udviklingen og evalueringen af analytiske metoder, brugt på materialer og enheder i IDUN center of Excellence.

Den høje sensitivitet og de konfokale muligheder i systemet, samt operations-fleksibiliteten og integrerede analytiske værktøjer, har muliggjort volumetrisk kortlægning af mikrocontainere og flerlags kapsler til oral indtagelse af medikamenter. Brugen af: (i) særligt optimeret optik i det nær-infrarøde spektrum, (ii) en tilpasselig skannings algoritme med eksponentiel afhængighed mellem eksponeringstid og skanningsretning, for at undgå overophedning af prøven, og (iii) mikroskopi platform med nedkøling vha. CO_2, tillod os at måle Raman signaler fra en dybde på op til 200 µm. Signalerne blev derefter brugt til yderligere kemisk analyse og tredimensionel modellering af materialers fordeling.

Den lange skanningstid, som er typiske for spontan Raman spektroskopi, blev elemineret ved introduktion af såkaldt 'laser-linje illumination' af prøven, sammen med et design af en aberration-korregeret spektrograf. Dette illuminations-modus giver 256 (med vores type af CDD kamera) simultane spektre-målinger langs laser-linjen på prøven, hvilket gør det muligt at øge hastigheden af overflade skanningsprocessen betragteligt og dermed forbedre muligheden for at studere kinetiske processor i et ønskey materiale. Linje-skanningsmetoden blev brugt til studier af dehydrerings fase-tranformationer af nitrodurantoin monohydrat og theophylline krystaller. Sammenlignet med termiske målinger på større mængder af samme materialer, demonstrerede vi muligheden for at bestemme tilstedeværelsen af forskellige faste former af medikamenter i løbet af en termisk dehydreringsproces og vi kunne visualisere dynamikkerne i enkelte partikler, relateret til metastabile mellemprodukter.

En metode til detektering af lave medikament koncentrationer, blev udviklet i kombination med en mikrofluidisk platform og overflade-forstærket-Raman spektroskopi (SERS). Som konsekvens af den enorme forøgelse af Raman signalet pga. SERS-aktive materialer og på grund af prøvers (feks urin) kompleksitet, var der brug for et oprensningstrin for at ekskludere alle uønskede dele. En centrifugal

mikrofluidisk disk, med integrerede substarter til SERS baseret målinger, blev brugt til separation, filtration og præcis eksponering af en oprenset prøve på SERS substratet. En hurtig og præcis overflade skanning tillod os at detektere meget lavere molekylære koncentrationer i to proof-of-concept applikationer; Melamin i råmælk og p-Coumaric acid produktion fra en E. coli bakteriekultur.

Slutteligt, hurtig visualisering af krystalorientering blev gjort muligt ved hjælp af en multi-beam polariseret laser illumination og en multikanal-analyseenhed. Mens prøven holdes stillestående, er det muligt samtidigt, at indsamle Ramanspektre med utallige kombinationer af laser polariseringer og orienteringer af analyseenheden, for adskillige on-axis/off-axis spredningsretninger. Resultatet af orienteringsbestemmelserne fremkom ved tilpasnings af rotationsvinkler til de målte datasæt. Krystalorienteringen på en overflade kan have stor betydning for essentielle funktioner af medikamenter, såsom disintegration og opløselighed. En model-tablet formulering med integration af carbamazepine dehydrate krystaller blev brugt til at undersøge orienteringen på overfladen.

Contents

List of publications

Journal publications

1. **R. Slipets**, O. Ilchenko, C. Mazzoni, F. Tentor, L.H. Nielsen, and A. Boisen. "Volumetric Raman Chemical Imaging of Drug Delivery Systems." Journal of Raman Spectroscopy. 2020. https://doi.org/10.1002/jrs.5869.

2. O. Ilchenko, **R. Slipets**, T. Rindzevicius, O. Durucan, L. Morelli, M.S. Schmidt, K. Wu, and A. Boisen. "Wide Line Surface-Enhanced Raman Scattering Mapping." Advanced Materials Technologies. 2020. https://doi.org/10.1002/admt.201900999.

3. P.O. Okeyo, O. Ilchenko, **R. Slipets**, P.E. Larsen, A. Boisen, T. Rades, and J. Rantanen. "Imaging of Dehydration in Particulate Matter Using Raman Line-Focus Microscopy." Scientific Reports 9 (1). 2019. https://doi.org/10.1038/s41598-019-43959-0.

4. O. Ilchenko, Y. Pilgun, A. Kutsyk, F. Bachmann, **R. Slipets**, M. Todeschini, P.O. Okeyo, H.F. Poulsen, and A. Boisen. "Fast and Quantitative 2D and 3D Orientation Mapping Using Raman Microscopy." Nature Communications 10 (1). 2019. https://doi.org/10.1038/s41467-019-13504-8.

5. C. Mazzoni, F. Tentor, A. Antalaki, R.D. Jacobsen, J. Mortensen, **R. Slipets**, O. Ilchenko, S.S. Keller, L.H. Nielsen, and A. Boisen. "Where Is the Drug? Quantitative 3D Distribution Analyses of Confined Drug-Loaded Polymer Matrices." ACS Biomaterials Science and Engineering 5 (6). 2019. https://doi.org/10.1021/acsbiomaterials.9b00495.

Conference contributions

6. **R. Slipets**, O.Ilchenko P.O. Okeyo, T. Rades, J. Rantanen, A. Boisen "Volumetric structural mapping of API using polarized line-focus Raman microscopy" 26th International Conference on Raman Spectroscopy. 2018.

7. **R. Slipets**, O. Ilchenko, C. Mazzoni, F. Tentor, A. Boisen "Volumetric Raman mapping of microcontainers for oral drug delivery" 26th International Conference on Raman Spectroscopy. 2018.

8. P.O. Okeyo, P.E. Larsen, T. Rindzevicius, O. Ilchenko, **R. Slipets**, A. Boisen, T. Rades, J. Rantanen "Structural aspects of hydrates – insight into phase transformations using nanomechanical sensors" 11th annual meeting of the Pharmaceutical Solid State Research Cluster. 2017.

9. C. A. Antalaki, R.D. Jacobsen, J. Mortensen, F. Tentor, **R. Slipets**, O. Ilchenko, S. S. Keller, L.H. Nielsen, A. Boisen "Loading of poorly soluble drugs by supercritical CO_2 impregnation

into microcontainers for oral drug delivery" 11th World Meeting on Pharmaceutics, Biopharmaceutics and Pharmaceutical Technology. 2018.

10. C. Mazzoni, **R. Slipets**, O. Ilchenko, L. H. E. Thamdrup, L. H. Nielsen, A. Boisen "Stability of amorphous indomethacin loaded into microcontainers with different shapes and sizes" 2019 Controlled Release Society Annual Meeting & Exposition

11. P.O. Okeyo, O. Ilchenko, T. Rindzevicius, **R. Slipets**, P.E. Larsen, A. Boisen, T. Rades, J. Rantanen "Chemical mapping of hydrate-anhydrate transformations at a single particle level using a Raman line-focus method" Nordic POP 1st Annual Meeting. 2019.

List of Abbreviations

µC – Microcontroller
µTAS – Micro Total Analysis System
2D – Two Dimensional
3D – Three Dimensional
Ag – Silver
API – Active Pharmaceutical Ingredient
Au – Gold
AuNP – Gold-capped Nanopillar
CARS – Coherent Anti-Stokes Raman Spectroscopy
CCD – Charge-Coupled device
EBSD – Electron Backscatter Diffraction
GIS - Geographic Information System
LASER – Light Amplification by Stimulated Emission of Radiation
LF – Line-Focus
LoD – Lab-On-Disc
LSPR – Localized Surface Plasmon Resonance
MEMS - Microelectromechanical system
NA – Numerical Aperture
NIR – Near-infrared
NP – Nanopillar
ODF – Orientation Distribution Function
PRS – Polarization Raman spectroscopy
PRS – Polarized Raman Spectroscopy
PSF – Point Spread Function
RIE – Reactive Ion Etching
RMS - Root Mean Square
RPS – Revolutions Per Second
$scCO_2$ – Supercritical CO_2
SDK – Software Development Kit
SERS – Surface-Enhanced Raman Spectroscopy
Si – Silicon
SMB – Subminiature version B connector
SPI - Serial Peripheral Interface
SRS – Stimulated Raman Spectroscopy
VPH – Volume Phase Holographic
WAU - Wollaston Analyzer Unit
WL – Wide-Line
XRD – X-Ray diffraction

1 Introduction

The Raman effect was first discovered by two Indian scientists C. V. Raman and K. S. Krishnan in 1928. If a molecule is irradiated by a monochromatic light, most of the light is transmitted without a change, however, a small part of it is scattered [1–4]. The unshifted component of the scattered light is known as Rayleigh scattering, while the shifted component is referred to as Raman scattering. The Raman scattered light is very sensitive to the nature of chemical bonds in organic molecules as well as in inorganic crystal lattices. A typical Raman scattering spectrum is a distinct "spectral fingerprint" that can be used to identify a material.

In the past few decades, Raman spectroscopy has become a powerful tool for scientific and applied research due to the following advantages: non-invasiveness, contactless, no need for sample preparation, speed, the possibility of working with aqueous buffer solutions and combination with confocal, atomic force and electron microscopy [5–7]. The spectroscopic technique is widely used in a multitude of fields, e.g. chemistry, geology, ecology, material science, cosmetics, pharmacy, criminalistics, medicine [8–13].

Progressive instrumental evolution of charge-coupled devices (CCD), optical filters, tunable lasers, spectrographs, interferometers, microcontrollers made possible the development of novel Raman-based detection techniques and enabled miniaturization of traditionally bulky laboratory spectrometers. Nowadays, high-performance, handheld spectrometers are extremely user-friendly, and often capable to analyze samples via a non-contact analysis, e.g. through optically transparent containers, well plates [8]. Raman-based instruments are smaller, faster, mobile, and the "real word" sample analysis is available for not only scientific laboratories but also industry and first responders [14–16]. Raman spectroscopy analyzes techniques are recognized as reliable by pharmaceutical companies and regulatory authorities [17].

The analysis of various spectroscopic data is taking steps towards utilizing cloud computing and AI deep learning algorithms, which enables analysis of e.g. complex chemometric data using portable devices in field conditions, where just a mobile 3G-4G internet connection is required [18,19]. With a growing satellite internet infrastructure, it is expected that a high speed broadband internet connectivity will eventually be delivered even to remote regions on the planet [20].

The development of different Raman instrumentation techniques was also promoted by discovering phenomena associated with the Raman effect, such as Surface-Enhanced Raman Scattering (SERS), resonance Raman (RR), Stimulated Raman Scattering (SRS), Coherent Anti-Stokes Raman Scattering (CARS), Tip-Enhanced Raman Scattering (TERS). In fact, there are more than 20 various types of Raman spectroscopy techniques that have been reported in literature [9,21]. Most techniques are usually focused on boosting the otherwise quite weak Raman signal, which is one of the main weaknesses of the spontaneous Raman scattering. For example, the SERS-based molecular detection techniques have been employed to record Raman signals down to a single molecule level [22]. However, in terms of equipment price and operation simplicity, creating a clear advantage over the classic (spontaneous Raman) technique is still very challenging. For example, some Raman-based techniques employ tunable impulse lasers or atomic force microscopy platforms, which require e.g. stable environmental conditions, anti-vibration suspensions, powerful and stable power sources, precise adjustment and

alignment, long stabilization time, which cannot be easily or at a reasonable price translated to portable and effective detection solutions.

Raman spectroscopy for drug detection. Raman-based analytical techniques have been gradually implemented into drug discovery and development processes [8,23]. This includes process analytics, quality control, chemical identification, preformulation, solid form screening, bioanalysis, molecular biology research and diagnostics, characterization of raw materials and identification of counterfeit products, and formulation analytics during different phases of drug development. The analytical versatility of Raman spectroscopy methods allows for studying a wide variety of transparent, dense, colored samples in solid, semi-solid, suspension and solution forms.

Volumetric imaging. Raman spectroscopy is a powerful technique, which is using for volumetric microstructural characterization of various drug delivery systems, for the evaluation of drug loading methods and understanding cross-material interactions in the formulation. Raman chemical imaging has been used to determine the size distribution of active pharmaceutical ingredients (API) microparticles, to check tablets coating quality and variability and to determine the API distribution homogeneity in a composite formulated tablet [24–26]. This type of information can be extremely useful for the development of innovative drug products with continuous increasing of multi-material combinations and complexity of engineering structures [27–29]. Confocal Raman microscopy is useful for studying the distribution of components, but long signal scanning time and sample absorption might limit the applicability of the method. A few interesting approaches have been formulated to tackle these issues, for example, using different sample illumination strategies or employing specialized multifocal detectors [30–32]. However, these processes are usually extremely time consuming or include advanced optimization procedures.

State transformations. Raman spectroscopy has been widely used for studying phase transformations such as polymorphic changes, anhydrate − hydrate transitions and crystallization [33–37]. The crystallization kinetics of amorphous API prepared by different techniques can be investigated using the time resolved Raman spectroscopy [38]. Unlike a crystalline form, an amorphous form is characterized by the absence of a three-dimensional long-range order of molecular packing [39]. Therefore, amorphous forms are in a higher energetic state compared to their crystalline counterparts resulting in a faster dissolution rate and solubility [40]. During storage, it is necessary to stabilize a formulation in its amorphous form, however, it is also possible to spontaneously crystallize the formulation to a lower energy state. A common method to prepare solid dispersions is to add polymers to the API, which can form amorphous glass solutions [41]. In terms of manufacturing, the amount of polymer needed and, therefore, the polymer/drug ratio and a physical lid of a drug carrier need to be characterized and optimized. The reduced molecular mobility increases the formulation solubility and stability during the storage period. Furthermore, an interaction of water with solids is also critical and quite often can dramatically change their functionality [42]. There is an increasing interest to understand solid state transformations and dehydration pathways of hydrates (preventing unwanted solid-state transformations) due to their key influence on process-ability and storage [43]. Raman spectroscopy techniques with a broad sample illumination can provide a deep insight into the real-time anhydrate-to-hydrate transformation, i.e. reveal multiple solid-state forms and visualize uniformity of a sample during a complex dehydration process.

Crystallography. Identification of crystal faces is an important information that can explain properties and behavior of a crystalline material. Crystal orientation is one of the key characteristics of complex drugs, which affects properties such as solubility, stability, and a dissolution rate [44,45]. In order to understand chemical and physical properties, it is crucial to determine the crystal orientation with respect to a surface plane of a drug delivery device. Several studies focused on the identification of crystal faces using Raman spectroscopy have been reported [46–49]. However, until now there are no stand-alone Raman based system, that could create a sample map with quantitative information of the crystallographic orientation of the material.

Surface enhanced Raman spectroscopy. The development of sensitive, selective, portable and cheap sample analysis methods for quantitative detection of important molecules in complex media such as blood plasma, urine, salvia, milk, juice, waste water, etc. remains a challenging task [50–52]. A few major trends relevant to the current work can be summarized as follows: (i) miniaturization of optical sensor systems, and (ii) integration of miniature detectors with automated and compact sample pre-treatment platforms. Due to a recent progress in miniaturization of optical and electronic components, modern Raman spectrometers can be miniaturized too, which enables their integration with different analytical tools, e.g. for performing in situ Raman spectroscopy. Platforms that allow sample manipulation, filtration, pre-treatment, etc. prior to the detection of a target analyte, demonstrate great potential [53]. Such systems are usually known as Total Analysis Systems (TAS), and with further miniaturization of functional parts, introduction of microfluidics, electric and magnetic platforms – micro-TAS (μTAS). Advantages include high throughput due to compactness, massive parallelization, fast response because of short diffusion distances and small samples, fast heating, better process control, ease of use and low analyte volumes.

Raman spectroscopy allows one to tackle a wide variety of important analytical tasks due to its high selectivity. However, the analyte concentration range is usually limited to approximately 0.1 - 0.5M. This is because of an extremely small cross-section of inelastic scattered light, which is ~10^{14} and ~10^{10} times lower than the fluorescence and infrared absorption cross sections, respectively [54]. This severely constrains Raman spectroscopy in real-life applications. The SERS technique, on the other hand, can increase the Raman signal from an analyte by several orders of magnitude, which is particularly relevant for applications that require analyte detection in the μM-nM concentration range. To enhance the Raman signal, a nanostructured surface, usually gold or silver, is utilized in the detection process with a reported approximate (averaged over the substrate) electromagnetic enhancement factor (EF) of ~10^8 [55]. The origin of the SERS enhancement is related to the excitation of the so-called localized surface plasmon resonances (LSPR), and noble metal (e.g. silver, gold) nanostructures support LSPRs in the VIS-NIR spectral region [56].

Over the last two decades, major technological advancements in controlled micro- and nanofabrication techniques has facilitated the rapid development of nanostructured SERS-active materials [55]. One of the best examples is gold or silver metal-capped silicon nanopillar (NP) SERS substrates first reported by Schmidt et al. in 2012 [57]. The silver nanopillar (AgNP) structures can be further optimized to yield highly uniform SERS signal intensities across large surface areas, i.e. the recorded relative standard deviation is ~2.5% on the mm scale and ~7% on a 4” wafer scale, and an averaged SERS EF of >10^8 [58]. Another advantage of SERS is fluorescence quenching which is extremely relevant for a number of applications.

When dealing with multicomponent, real-life samples, a number of process parameters, e.g. sample pre-treatment or reproducibility of SERS measurements, play a crucial role in quantitative SERS [59,60]. Therefore, it is critical to develop methods that can eliminate the interfering compounds from the sample matrix, e.g. via controlled sample filtration, analyte segregation on a SERS substrate or surface wetting processes. By combining simple and effective sample pre-treatment techniques with SERS detection, selective, sensitive, rapid and quantitative determination of a wide range of analyte species can be achieved.

This work investigates the development process of complex, modular Raman system with possibility to be easily customized and to integrate additional subsystems for advanced analytical functionality. At the first stage of its evolution, the creation of embedded SERS-based centrifugal microfluidic platform and software package for application development is described. But being completely custom-made, modular and easily modifiable, the system is of great interest for complex and non-standard problems, required non-standard, innovative and often unique solutions. Also, all technical implementations for microstructural, fast kinetic and crystallographic drug characterization are described.

1.1 Aims of the PhD project

First, this work is a part of the "Total solution for High throughput surface enhanced Raman spectroscopy" (THOR) project funded by European Research Council (ERC). The main goal of the THOR project is to build a SERS-based sensing platform with integrated and automated sample pre-treatment capabilities for detecting the following analytes: (i) toxic melamine from milk samples, and (ii) p-coumaric acid produced by *E. coli* bacteria culture. To achieve this, a centrifugal disc-based microfluidic platform with an integrated SERS chip for molecular detection was combined with a custom-built Raman system. A few unique sample illumination and signal collection capabilities were developed and implemented in the THOR system: (i) the laser line-focus mode, and (ii) the laser wide-field mode.

Second, the PhD work is a part of drug delivery research activities within the center for Intelligent Drug delivery and sensing Using microcontainers and Nanomechanics (IDUN). The aim is to develop a system suitable for (i) Raman 3D imaging of drug loaded microcontainers, and for (ii) analysis of drug crystallization processes and (iii) hydrate systems, and (iv) implement 3D data visualization and analysis techniques. Specific objectives of the second part of the PhD project:

- Volumetric characterization of drug delivery systems (microcontainers, multilayered tablets), evaluation of supercritical CO_2 impregnation method ($scCO_2$) for loading of poorly soluble drugs (ketoprofen, naproxen) into confined polymer matrices of different sizes.
- Kinetics study of crystallization of amorphous APIs (ketoprofen and indomethacin), loaded into microcontainers, with respect on shape and size.
- Understand complex transformation pathways among various anhydrate–hydrate forms of nitrofurantoin monohydrate and theophylline crystals as a function of humidity and temperature.
- Develop and implement a polarized Raman microscopy technique for obtaining crystallographic characteristics of active pharmaceutical ingredients (tablets with

carbamazepine dihydrate) for assessment of crystal functionality, which is important for pharmaceutical research.

A major part of this PhD work was devoted to automation of electronic devices with a focus on task-specific, unique functionalities. A synchronized operation and control of more than 15 different devices (cameras, lasers, motorized stages, etc.) in the system was achieved using a custom-built software. The key software capabilities include: sample scanning, data manipulation and visualization in 2D/3D, chemometric analysis for identifying different types of molecules in a sample.

1.2 Outline of the thesis

The introductory part of the thesis is followed by Chapter 2, which briefly describes basics of the inelastic light scattering phenomena (the Raman effect), and information that a Raman spectrum provides.

In Chapter 3, Raman microscopes, their confocal characteristics and methods of collecting the Raman signal, are described. In addition, the chapter reviews in detail the THOR setup, i.e. microscope design, the laser-line focus illumination concept and the signal collection part. The THOR confocal properties that are important for volumetric drug imaging and the laser-line illumination approach suitable for kinetic studies of phase transformations in a solid crystals, are discussed.

In Chapter 4, surface-enhanced Raman spectroscopy (SERS) and a basic mechanism behind the enhancement of the Raman signal is discussed. In this chapter, the importance of SERS substrates is emphasized, and the main, nanopillar (NP)-based, SERS-active platform that was utilized in this work for molecular detection is described including a basic Ag or AuNP fabrication procedure. Finally, the laser line and wide-line sample illumination techniques that were employed in our SERS measurements are described in greater detail.

The impact of structural ordering in a material on the Raman scattering signal and advantages of polarized Raman spectroscopy for orientation study of crystals are presented in Chapter 5.

Chapter 6 describes the system automation processes, i.e. development of electronic submodules, custom-made control software, operation algorithms and analytical tools for data analysis.

Finally, all results and future work pathways are discussed in Chapters 7.

2 Raman spectroscopy

Raman spectroscopy is a widespread chemical analysis technique that can be utilized for studying a broad variety of materials, including inorganic compounds and living cells [61]. The Raman scattering spectroscopy method provides information about the vibrational modes of e.g. molecules, which can be associated with chemical bonds and then molecular chemical structure.
This chapter briefly describes the classical interpretation of the Raman scattering effect.

2.1 Classical theory of Raman Spectroscopy

The classical Rayleigh scattering model. Consider an oscillating Hertz dipole, i.e. a model of a radiating dipole in vacuum. It is known that the total intensity emitted in all directions by an electric dipole is expressed by the following equation [2]:

$$P = \frac{q^2 \omega^4 x_0^2}{12\pi\epsilon_0 c^3} \tag{2.1}$$

where ω - radiation frequency, x_0 - charge displacement from equilibrium position, q – charge.

Suppose that light (the electric field E_0 of the wave) is scattered by an oscillating electron of the atom with mass m, the displacement of which (x_0) is expressed from the equation of motion for a harmonic oscillator [2]:

$$x_0 = \frac{q_e E_0}{m(\omega_0^2 - \omega^2)} \tag{2.2}$$

Equations (2.1) and (2.2) yield:

$$P = \left(\frac{q_e^4}{12\pi\epsilon_0 c^3 m_e^2}\right)\left(\frac{\omega^4 E_0^2}{(\omega^2 - \omega_0^2)^2}\right) \tag{2.3}$$

In deriving this formula, the attenuation for the electronic vibration and the presence of many natural frequencies of the atom were not taken into account. As follows from the equation (2.3), the total intensity of the scattered light is proportional to the 4th power of its frequency and the square of the incident electric field. A similar dependence will be characteristic of the Raman scattering process.

A brief phenomenological description of the Raman scattering phenomenon is as follows. The equation (2.1) can be written as:

$$\frac{\partial P}{\partial \Omega} = \frac{\omega^4 |\boldsymbol{p}|^2}{12\pi\epsilon_0 c^3} \sin^2 \Theta \tag{2.4}$$

where Ω = Ω(θ,φ) - spatial angle from which the signal is collected, $|\mathbf{p}|^2$ - squared dipole moment modulus. A light wave interacting with a molecule polarizes it and sets electrons in motion. As a result,

the molecule becomes a new source of radiation at the same frequency as the original light wave (*Rayleigh scattering*). In the case of *Raman scattering*, the light wave interacts with the vibration of the molecule, which leads to radiation at other frequencies. For low intensities of the incident light, we can assume that the induced dipole moment is proportional to the electric component of the field:

$$\widetilde{\boldsymbol{p}} = \alpha(\omega_L, \omega_\upsilon)\widetilde{\boldsymbol{E}} \tag{2.5}$$

ω_L - frequency of the incident light, ω_ν - frequency of the scattered light, α - molecular polarizability.

It is important to note that in the derivation of this formula we did not take into account a number of important factors. *First*, in a general case, a substance that scatters light is anisotropic. In that case, α is a tensor of the second rank (represented by a 3 × 3 matrix).

$$\begin{pmatrix} p_x \\ p_y \\ p_z \end{pmatrix} = \begin{pmatrix} \alpha_{11}\alpha_{12}\alpha_{13} \\ \alpha_{21}\alpha_{22}\alpha_{23} \\ \alpha_{31}\alpha_{32}\alpha_{33} \end{pmatrix} \begin{pmatrix} E_x \\ E_y \\ E_z \end{pmatrix} \tag{2.6}$$

Second, for condensed matter it is important to distinguish between a local field acting on individual molecules of a substance and a mean field (macroscopic) corresponding to the electric field of a light wave. These fields differ due to the appearance of polarization charges in a substance, whose field also affects neighboring molecules. There are several models for converting a macroscopic field into a local one. We introduce the conversion factor described in [2]:

$$\widetilde{\boldsymbol{p}} = L_M^{\frac{1}{4}}\, \alpha(\omega_L, \omega_\upsilon)\widetilde{\boldsymbol{E}}$$

$$L_M^{\frac{1}{4}} = \frac{n_M^2 + 2}{3}$$

where n_M - refractive index. If we place an emitting dipole from a vacuum in a medium with a refractive index n_M, then according to [2], the radiation intensity of the dipole can be represented as:

$$\frac{\partial P}{\partial \Omega} = \frac{\omega^4 n_M \sqrt{L_M} |\boldsymbol{p}|^2}{12\pi\epsilon_0 c^3} \sin^2\Theta \tag{2.7}$$

The equation (2.7) shows that the scattering intensity for molecules will be higher in solution than in air.

Third, it is necessary to find a way to quantitatively describe the natural vibrations of a molecule in the framework of this theory. In this description, we will also follow the approach described in [2]. Imagine that radiation will interact only with a certain vibration of the molecule by the normal mode k with coordinate Q_k. A normal vibration can be called a molecular motion, in which the vibrations of atoms (functional groups) in a molecule occur at the same frequency. Normal coordinates are associated with natural (lengths of specific bonds, angles) linear transformation. Moreover, the coefficients at various natural coordinates reflect the share of this connection (or angle) in the normal oscillation. Sometimes one of the coefficients can be much larger compared to the other ones. In this case, it can be assumed that the normal vibration is due to the vibration of a certain bond (or valence angle) of the molecule. Otherwise, the vibrations of various parts of the molecule are mixed in a given normal vibration.

The simplest description of the Raman scattering phenomenon. A light wave with the frequency ω_L illuminates a molecule. The polarizability of the molecule in equilibrium state is α_L. If we assume that the molecular vibration introduces a small perturbation into the electronic structure of the molecule and its polarizability, we can consider Q_k (the coordinate of the normal mode) as a small parameter in the expansion of α_L in a power series:

$$\alpha_L(Q_k) = \alpha_L(0) + \left(\frac{\partial \alpha_L}{\partial Q_k}\right)_{Q_k=0} Q_k + \frac{1}{2}\left(\frac{\partial^2 \alpha_L}{\partial^2 Q_k}\right)_{Q_k=0} Q_k^2 + \cdots \quad (2.8)$$

A similar expression can be written for each of the nine components of the polarizability tensor. By analogy with the latter, we introduce the tensor R_k (ω_L), consisting of the components $\left(\frac{\partial \alpha_{ij}}{\partial Q_k}\right)_{Q_k=0}$. Leaving the linear terms, we can obtain the following expression for each of the components of the polarizability matrix:

$$\alpha_{ij}(Q_k) = \alpha_{ij}(0) + R_k^{ij}(\omega_L)_{Q_k=0} Q_k \quad (2.9)$$

Let the electric field of a light wave change harmoniously: $E = E_0 e^{-i\omega_L t}$. Then the expression for the induced dipole moment can be represented as follows:

$$p(t) = Re\left[\alpha_L(\omega_L, Q_k) E(\omega_L) e^{-i\omega_L t}\right] =$$

$$= Re\left[\alpha_L(\omega_L, 0) E(\omega_L) e^{-i\omega_L t}\right] + Q_k(t) Re\left[R_k(\omega_L) E(\omega_L) e^{-i\omega_L t}\right] =$$

$$= Re\left[\alpha_L(\omega_L, 0) E(\omega_L) e^{-i\omega_L t}\right] +$$

$$\frac{Q_k}{2} Re\left[R_k(\omega_L) E(\omega_L) e^{-i(\omega_L - \omega_K)t + i\Phi}\right] + \frac{Q_k}{2} Re\left[R_k(\omega_L) E(\omega_L) e^{-i(\omega_L + \omega_K)t - i\Phi}\right]$$

$$\underbrace{\frac{Q_k}{2} Re\left[R_k(\omega_L) E(\omega_L) e^{-i(\omega_L - \omega_K)t + i\Phi}\right]}_{\text{Anti-stokes component}} \quad \underbrace{\frac{Q_k}{2} Re\left[R_k(\omega_L) E(\omega_L) e^{-i(\omega_L + \omega_K)t - i\Phi}\right]}_{\text{Stokes component}}$$

where Φ is an arbitrary phase arising as a result of the delay of the Raman radiation compared to the incident wave. By using the last two expressions, as well as equation (2.5), it follows that:

$$\alpha_L(\omega_k) = \frac{Q_k}{2} R_k(\omega_L) \quad (2.10)$$

A necessary condition for the manifestation of the Raman band in the spectrum is a nonzero value of the derivative of the polarizability of the molecule with respect to the coordinate of the normal mode (also called reduced polarizability) $\left(\frac{\partial \alpha_{ij}}{\partial Q_k}\right)_{Q_k=0} \neq 0$.

It is important to note that some important features of Raman scattering cannot be explained within the framework of classical theory. For example, the intensity of the Stokes component usually exceeds the corresponding anti-Stokes component. This fact may seem to contradict the rule known from electromagnetic theory that the intensity of light scattering is proportional to the fourth power of the

wave number (or inversely proportional to the fourth power of the wavelength). This contradiction can be explained using the quantum-mechanical formalism.

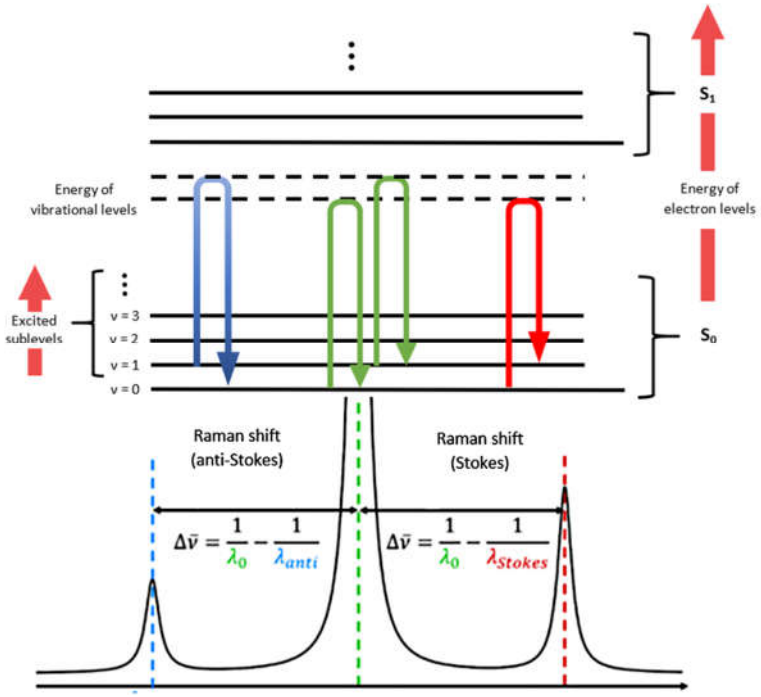

Figure 2.1: A diagram of the energy levels of a molecule with a schematic designation of *Rayleigh* (center) and *Raman scattering* (left: anti-Stokes, right: Stokes). The symbols S_0 and S_1 denote the unexcited and first excited vibrational sublevels. The dashed lines in the top diagram indicate a virtual state.

According to the basic concepts of quantum mechanics, molecules can occupy discrete vibrational energy levels [61] as shown in Fig. 2.1. By solving the Schrödinger equation, the vibrational energy (ε_v) for a harmonic oscillator is:

$$\varepsilon_v = \left(v + \frac{1}{2}\right) v_m \tag{2.11}$$

where v is the vibrational quantum number. In Raman spectroscopy, transitions with Δv = 1,2… are allowed. As for the transition probability, the most probable is the transition with Δv = 1.

In order to calculate the fraction of molecules having vibrational energy ε_v, the Maxwell – Boltzmann distribution can be employed. Then the Stokes (I_S) and anti-Stokes (I_{aS}) Raman scattering intensities are determined by the number of molecules available for a given transition at the starting vibrational sublevels N_S and N_{aS}:

$$\frac{I_S}{I_{aS}} = \left(\frac{v_0 - v_m}{v_0 + v_m}\right)^4 \frac{N_S}{N_{aS}} = \left(\frac{v_0 - v_m}{v_0 + v_m}\right)^4 \exp\left(\frac{\varepsilon_0 - \varepsilon_1}{kT}\right) \tag{2.12}$$

where ε_0 and ε_1 are the energy levels of the molecule before and after the transition, respectively, k and T are the Boltzmann constant and temperature. At room temperature, the transition from the state v = 0 to v = 1 has the highest probability to occur. This explains why the Stokes component displays significantly higher intensity compared to the anti-Stokes component.

2.2 Interpretation of a Raman spectra

A Raman spectrum can include qualitative and/or quantitative information. The Raman scattering spectrum is a plot of the scattered intensity versus the wavelengths at which the scattering occurs. The intensity of the Raman scattering signal is usually expressed in (photon) counts, which is then plotted versus wavenumber shifts (units of inverse length, cm^{-1}). By utilizing the cm^{-1} units, the position of the measured Raman modes is generally independent on the wavelength of the incident laser. In this way, any sample can be identified by simply comparing its Raman spectrum to a database of known Raman spectra.

The laser excitation wavelength and the Raman shift have the following relation:

$$\Delta_{Raman} = \frac{1}{\lambda_{Laser}} - \frac{1}{\lambda_{Raman}} \tag{2.13}$$

where λ_{laser} is the excitation wavelength and λ_{Raman} is the measured wavelength of a given peak. An example of a Raman spectrum is shown in Fig. 2.2.

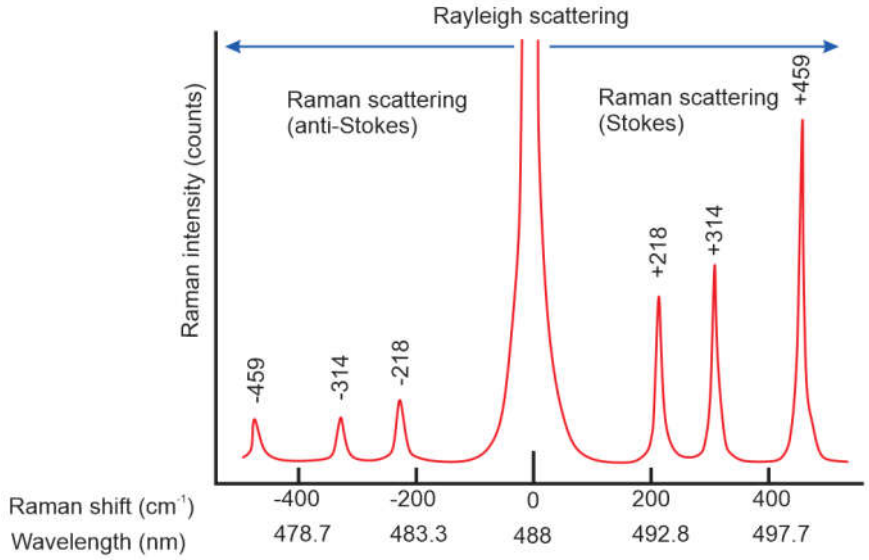

Figure 2.2: Raman spectrum of Carbon Tetrachloride (CCl_4) excited by laser radiation of λ_0=488 nm. The intensity of the Raman bands (in photon counts) plotted versus wavenumbers and wavelengths. The number above the peaks is the Raman shift in cm^{-1}.

Elastically-scattered light (*Rayleigh scattering*) carries the same energy as the incident radiation, thus the position of zero shift (0 cm^{-1}) in the spectrum is fixed to the Rayleigh line. In the case of the Raman Stokes scattering, the energy transfer from the pump laser to a molecule and emission of photons take place, which results in appearance of lines in the spectrum shifted to longer wavelengths. In the anti-Stokes Raman scattering, the scattered light carries more energy than the incident radiation and the spectrum is shifted to the opposite direction. The Stokes and anti-Stokes lines are located symmetrically about the Rayleigh line. However, at room temperature and at the vibration frequency of 1000 cm^{-1} the percentage of molecules in an excited vibrational state is around 0.7%. Therefore, the anti-Stokes peaks intensities are usually much lower [11].

As discussed previously, inelastic scattering results from the interaction of the incident radiation with the (vibrating) molecules of a given sample, which yields photons at different energies with respect to the laser excitation light.

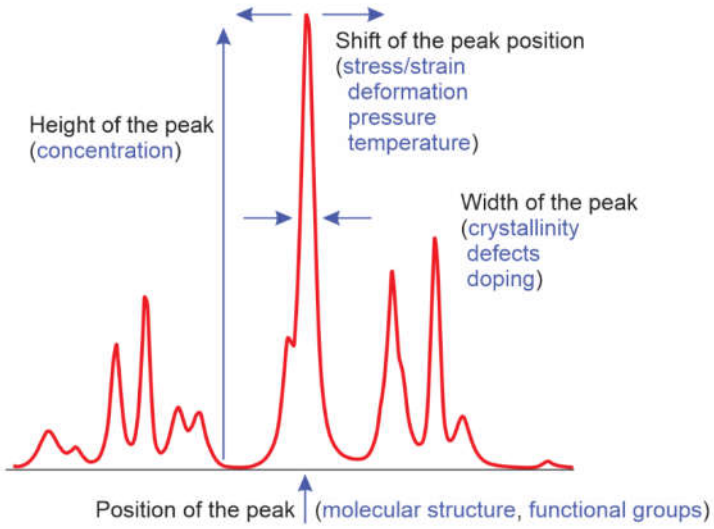

The position of each Raman peak corresponds to one of these energy shifts. The combination of peak positions and intensity provides information about a particular molecular vibration, and can be used to identify the type of bonds present in a compound. Changes in peak width, height or position, can inform about certain material modifications.

Figure 2.3: A typical Raman spectrum and a corresponding material information, which is used for identifying the type and quality of chemical bonds.

A unique combinations of interatomic bonds in a molecule yields a molecule-specific Raman spectrum, which makes Raman spectroscopy a perfect technique for identifying compounds. A Raman spectrum consists of a set of peaks, each associated with a vibrational mode (see Figure 2.4). Different types of functional groups of atoms (e.g. C=O, C-C, OH, CH_X, aromatic ring) as well as the molecular scaffold (skeleton) have unique vibrational modes, which lead to specific interactions with incident light and therefore, produce different Raman shifts. Skeletal vibrations are usually located at Raman shifts below 1800 cm^{-1} and along with other vibrations determine the region 300-1800 cm^{-1} as the "fingerprint" region of a substance that represents the most informative part of the spectrum for material identification. Nowadays, routines to perform a database search and peak characterization are available in commercial software packages. For example, one of them is the KnowItAll software (Bio-Rad Laboratories) and their associated databases, which are pretty good, informative, and have rich analytical possibilities [62].

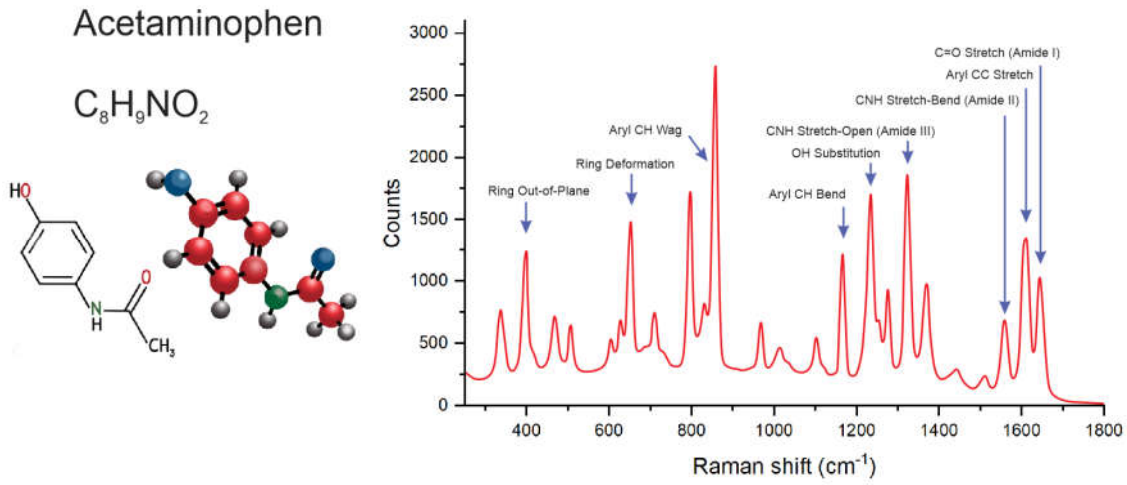

Figure 2.4: Left – the molecular structure, and right – the Raman spectrum of acetaminophen with mode assignments.

In the case of crystalline substance, Raman spectroscopy can give additional information about crystal structure: the degree of crystallization, state transformation, crystal orientation and distortion of crystal lattice (See Figure 2.5).

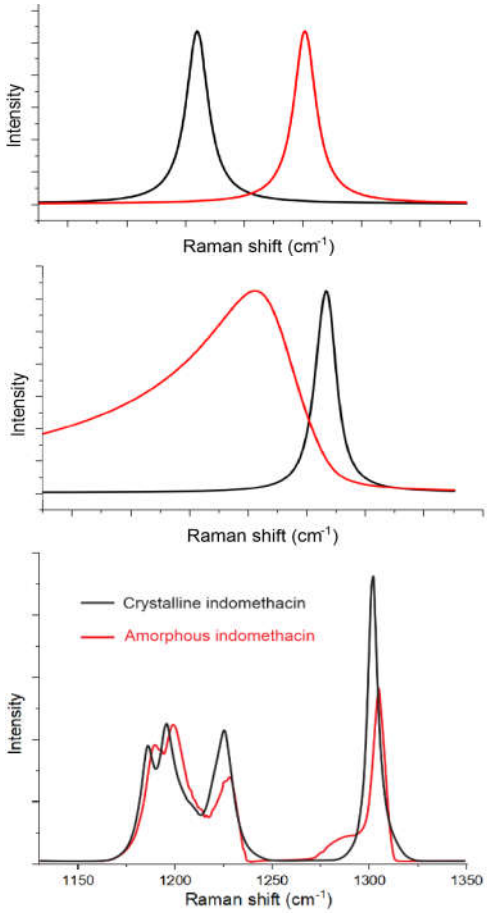

Frequency shift by applying pressure.
~ $1cm^{-1}$/kbar

As a result of lattice disturbance, asymmetric broadening and shift occur.

Crystallization of indomethacin from the amorphous state caused by the molecular mobility during storage.

Figure 2.5: Raman peaks transformations of crystalline materials after external influences.

Defects or damages induce changes in periodicity and symmetry, which might affect the crystal structure of a material. These effects lead to formation of new, broadening and/or asymmetrical reshaping of the existing Raman peaks [63]. Strain/stress changes the crystal lattice, which affects the lattice vibration energy of a material, and therefore, it can change Raman peak positions [64]. Solid-state molecule transformations are caused by a change in a lattice structure and/or molecular conformations, driven by minimization of energy states at certain environmental conditions. Materials with higher degree of crystallization are characterized by increased level of a three-dimensional long-range order of molecular packing, so Raman peaks become sharper and more intense [65].

3 Raman microscopy

By utilizing the same principles that scientists use to explore the most distant parts of the universe (through the telescope), chemical and biological processes at the nanoscale can be observed using microscopy. While modern microscopes generate multidimensional data (X, Y, Z, time, λ …), existing profiling methods simplify the study of various effects and processes. Raman spectroscopy can give an additional set of material characteristics, namely: chemical structure, molecular interactions, crystallinity, orientation, material deformation and many others.

Raman microscopy combines a Raman spectrometer and a standard optical microscope, which allows to make the Raman analysis at the microscopic level. In this part I will give a summary of the most important Raman spectrometer components and modules which were utilized in the assembly of the Raman system (e.g. THOR, see Chapter 4). A general diagram is shown in Figure 3.1:

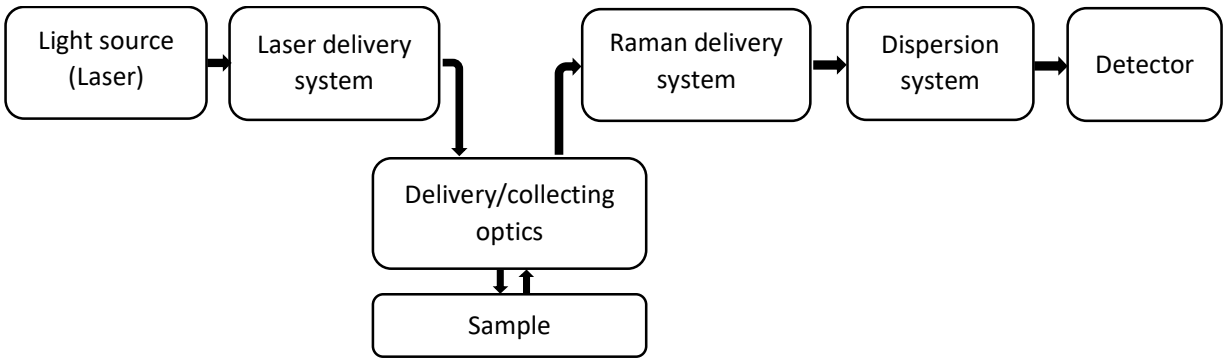

Figure 3.1: A general diagram of a Raman spectrometer. In most cases, a laser and Raman delivery systems are optional. In our Raman and SERS applications we used laser beam shaping optics, polarizers, beam splitters, analyzers for forming the proper incident excitation beam and extracting more information from the scattered radiation.

The most popular approach is shown below in Figure 3.2:

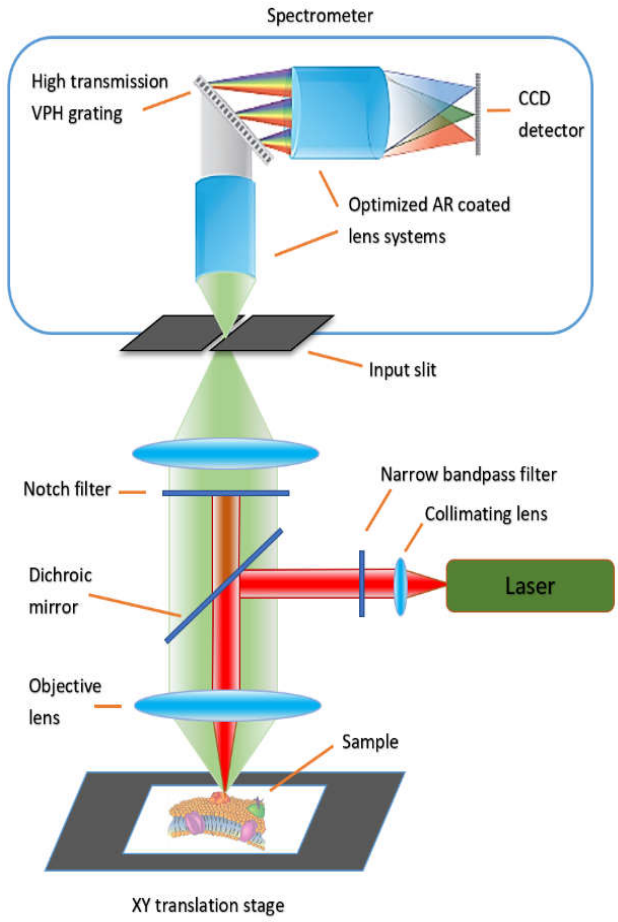

Figure 3.2: Basic structure of Raman microscope.

After a collimating lens, the parallel laser beam is "cleaned" using a narrow bandpass filter and guided through an objective, and then focused onto the sample. The Raman scattered light from the sample is collected using the same objective lens. The dichroic mirror reflects a part of the incident laser and transmits the Stokes-shifted Raman spectrum. The notch filter removes the laser light frequency, while an additional lens focuses the scattered light on the input slit of a spectrometer. Inside the spectrometer, the Raman spectrum is dispersed by a diffraction grating, and a special lens is used to focus the light on the CCD detector.

3.1 Confocal Raman microscopy

Combining Raman spectroscopy with confocal microscopy allows optimal spatial filtering for sample volume analysis. A spatial resolution down to 200nm laterally and 500nm vertically can be achieved using the visible light excitation wavelengths. In the following section, the basic construction principles of such systems is described which is also relevant to the Raman systems developed in this work.

3.1.1 Confocal microscopy

In the conventional wide-field microscopy, high-quality images can only be obtained from thin samples (a few millimeters in thickness). However, research often requires deeper profiling of areas, and imaging requires volumetric rendering techniques that are not available in conventional microscopes. The methods of confocal microscopy allow one to visualize slices of a multilayered sample.

A confocal microscope enables the user to obtain very sharp, higher contrast images. It differs from a "classical" optical microscope in the way that it captures only one object point at one moment in time. A complete image is built by scanning the object (e.g. moving a sample stage), see more detailed information in ref. [66–73]. In order to register only one point after an objective lens, it is necessary

to place a small size diaphragm/pinhole in the lens focal point. The red rays pass the diaphragm and are detected, while the blue rays are blocked, see Fig.3.3 b.

Another important improvement is the focused illumination approach. The illuminator focuses the light to the analyzed point. It can be done by using a second focusing system behind the object (object should be optically transparent), see Fig.3.3 c). As an alternative, the incident and reflected light can be focused by the same objective using a light splitting plate, see Fig.3.3 d).

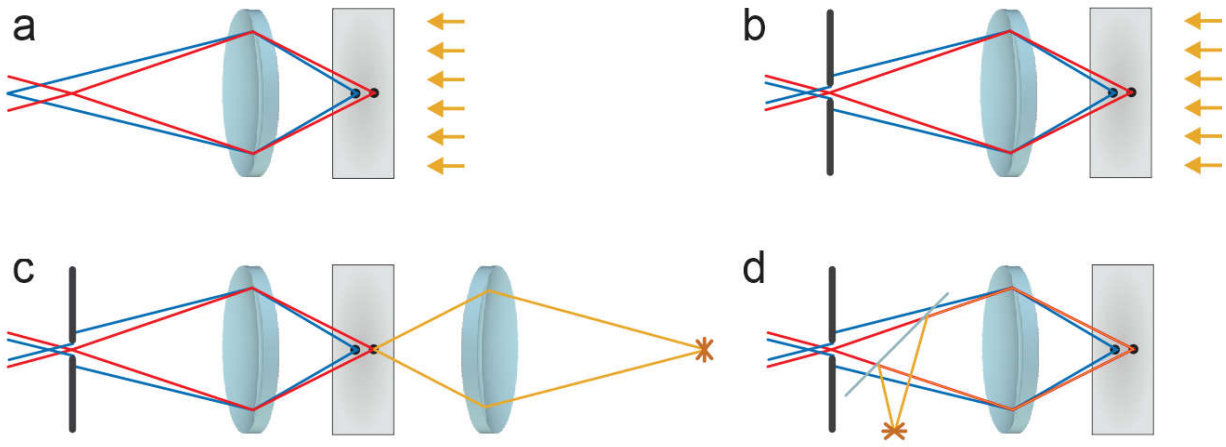

Figure 3.3: a) The light ray path in a conventional microscope. Light from different points reaches the detector. b) Applying a diaphragm allows to significantly reduce the background illumination from the outer points of the detection region. c) An image contrast enhancement by using the point back illumination approach. d) The configuration with the light beam splitter and one focusing objective can simplify the microscope design and adjustment process.

3.1.2 Resolution and contrast in confocal microscopy

It is qualitatively clear that the use of a confocal scheme should increase the contrast of an image. This is because the "parasitic" light from areas that surround the measured point is blocked and is not able to reach the detector. The image contrast can be explained using simple ray optics.
In conventional microscopy the point spread function (PSF) determines intensity distribution of the incident light in the lens focal plane, which is caused by Fraunhofer diffraction at the input diaphragm, see Fig. 3.4.

In a confocal microscope light passes through an objective twice. For a qualitative understanding, it is convenient to consider each PSF as the probability that a photon will hit a point with coordinates (x,y). Then confocal PSF is a product of independent probabilities and equals to:

$$p_{conf}(x,y) = p(x,y) \times p(x,y) \qquad (3.1)$$

Conventional PSF and confocal PSF are shown in Fig. 3.5.

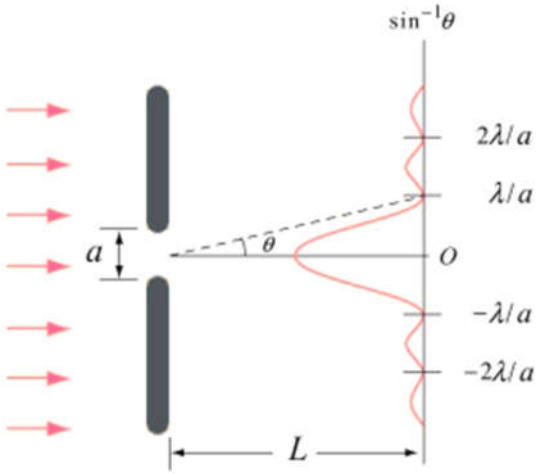

Figure 3.4: Fraunhofer diffraction in the focal plane

Using Rayleigh criteria for resolution (26% gap of the intensity maximum), the resolution in the confocal microscope increases, but not significantly. For the confocal microscope:

$$r_{conf} = 0.44\,\frac{\lambda}{NA} \tag{3.2}$$

while for the conventional microscope:

$$r_{reg} = 0.61\,\frac{\lambda}{NA} \tag{3.3}$$

Where λ - length of light wave, NA – numerical aperture of objective.

Intensity distribution along optical axis is:

$$r_{Z\,conf} = 1.5\,\frac{n\lambda}{NA^2} \tag{3.4}$$

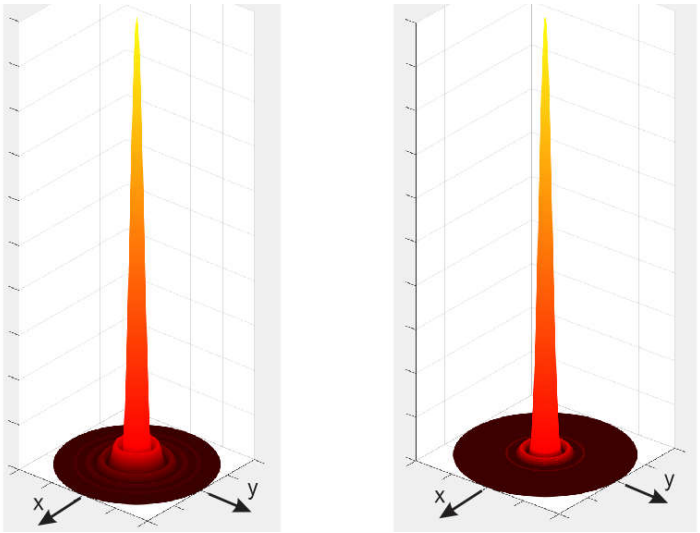

Figure 3.5 Conventional PSF (left) and confocal PSF (right).

In confocal microscopy there is 1.5 times resolution increase in X-Y plane, and higher resolution along Z axis, see Fig. 3.6.

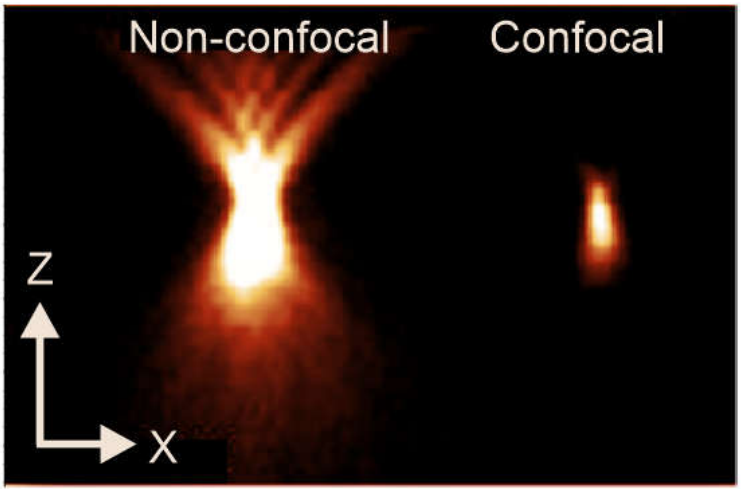

Figure 3.6 Light spreading around the focal point in a sample volume. Conventional (left) and confocal (right) schemes (adapted from olympus-lifescience.com).

In conventional microscopy the relation between maximums of the first and zero peaks is equal to 2%, while in confocal microscopy it is only 0.04%, i.e. the contrast is dramatically increased. This increase enables one to resolve objects with an intensity difference of up to 200:1. In Figure 3.7 we can see that it is impossible to detect a dim object with 200 times lower intensity compared to a bright object. However, the distance is larger than the Rayleigh Criterion says.

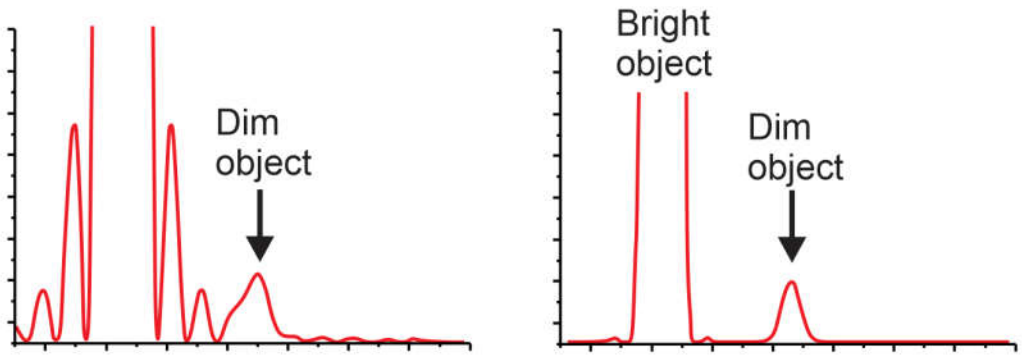

Figure 3.7 The light intensity distribution in the case of conventional (left) and confocal (right) microscope designs for the bright and dim objects with 200 times difference in the intensities.

3.1.3 Confocal schemes of Raman microscopes

It is also possible to implement the confocal scheme in a Raman microscope. In this case, the lateral resolution along X, Y axes is increased, and also along Z (depth). This enables image sectioning as a function of depth (along the Z-axis). There are several confocal schemes applicable to Raman microscopes.

Classic confocal scheme. The biggest advantage of a confocal Raman spectrometer is independent and individual control of spatial and spectral resolutions. This can be achieved by placing a pinhole diaphragm before a spectrometer slit. Pinholes with different diameters control the confocality level, and the input slit – spectral resolution of a spectrometer. This convenience causes some alignment difficulties via two diaphragms in order to get an optimal result.

Pseudo confocal scheme. In a simplified scheme the spatial resolution is determined by a combination of an input slit in one direction and the lateral resolution of CCD detector in another direction. These limitations of a spectrograph dictate the worse spatial resolution. However, a smaller number of optical elements provide much better total throughput of the system.

Hybrid confocal scheme. Both high throughput and classic confocal designs have their own benefits. That is why many confocal Raman microscopes are equipped with changeable slits and pinholes or hybrid combinations. On the same metallic plate a set of point and slit diaphragms can be placed, which can function as a confocal diaphragm or input slit of the spectrometer. Such hybrid realization combines benefits of each version and allows one to make fast switching between a high throughput and classic confocal modes.

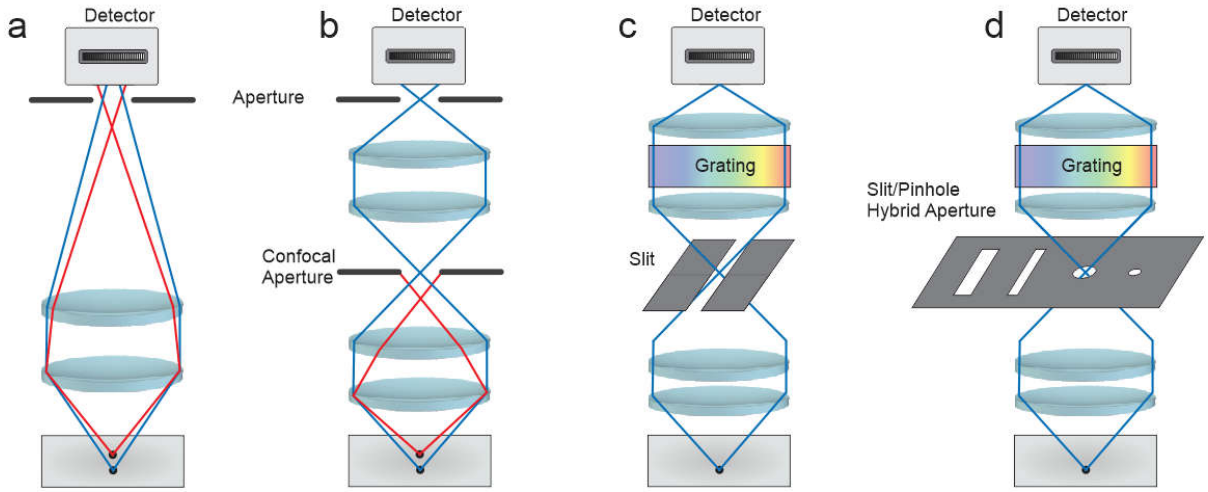

Figure 3.8: a) Conventional, b) confocal microscope optics, c) pseudo confocal microscope scheme, d) hybrid confocal microscope scheme with changeable slit and pinholes.

In the current Raman system (THOR) prototype, a pseudo confocal scheme with a possibility to select the level of confocality/throughput using software is realized, see Fig. 3.9 below.

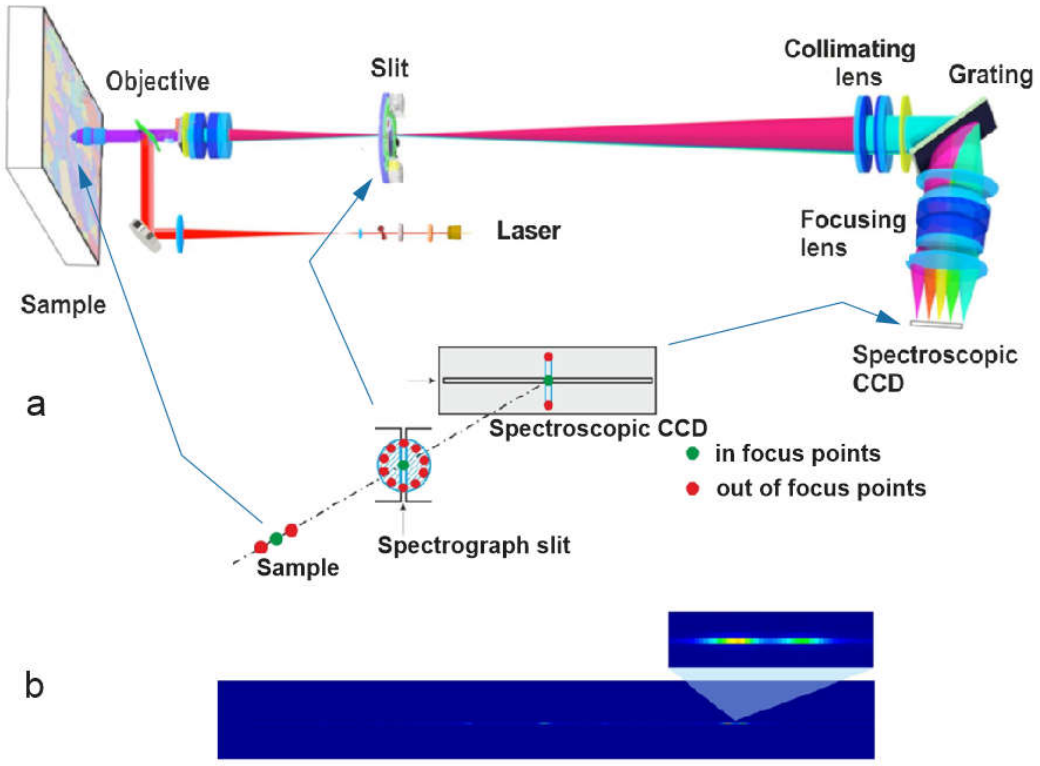

Figure 3.9: a) A slit based confocality principle. b) A typical image of the Raman signal from spectroscopic CCD in classic confocal scheme using a pinhole. The zoomed region shows the Raman spectrum compressed into one row on the CCD sensor

In Fig. 3.10 the Raman signal from silicon is shown. By selecting the central row N and desired number of the nearest rows ±M, software automatically calculates a summarized signal from rows N, N-1 … N-M, N+1 … N+M. A user of the system can easily define the confocality level and find a compromise between the scanning time and detail quality of the measured sample.

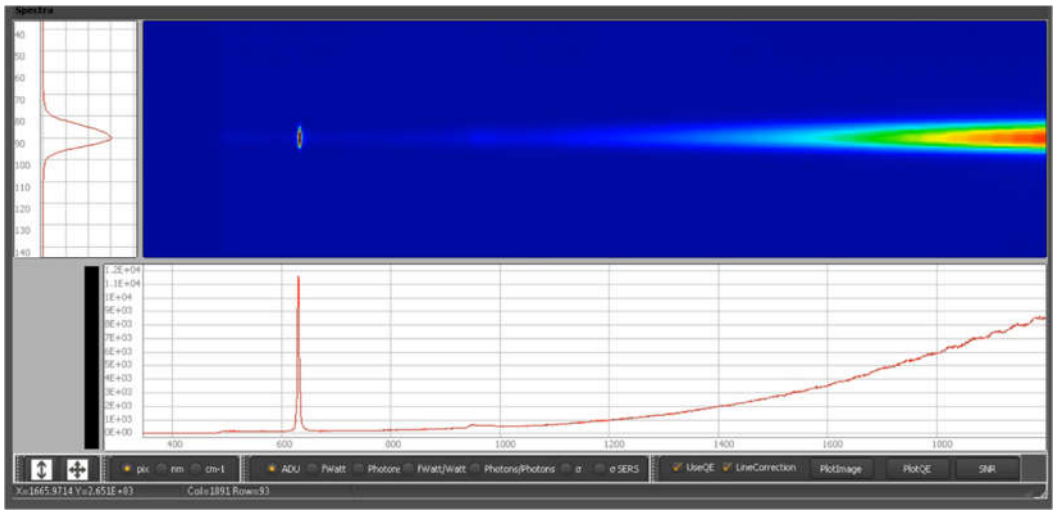

Figure 3.10: The Raman signal collected from a Si wafer surface using a pseudo confocal microscope scheme.

3.2 The basic THOR design and sample scanning techniques

3.2.1 2D-3D Raman scanning techniques

As a consequence of implementing the image contrast and resolution enhancement, a more complex sample scanning design is required [74,75]. The confocal signal filtering system allows the user to record the Raman signal emitted only from the focal plane. By adjusting the focus of an objective lens it is possible to measure the Raman signal distribution in any optical section along the z-axis without destroying the sample. The sample should be transparent or semi-transparent, so the incident light is able to reach the specified depth. However, even transparent objects scatter and absorb the incident light. In addition, reabsorption of the emitted Raman light limit possibilities of high-quality confocal microscopy with a depth of about 100 µm from the surface of the scanned object.
During the scanning in the XY plane, the detector registers a signal from the depth of a sample, which is defined by the focus alignment of the objective with the scanning plane and the pinhole diaphragm. Incremental movement of the scanning plane along the Z axis allows to obtain a series of contrast layer-by-layer images and to reconstruct the internal three-dimensional structure (3D) of the object under study. The scanning step size in the XY plane and the distance between Z slices define the volume of elemental volumetric element – voxel. Each voxel obtained during 3D Raman scanning contains a parametric information with Raman spectrum of the sample in the beam focus microvolume.

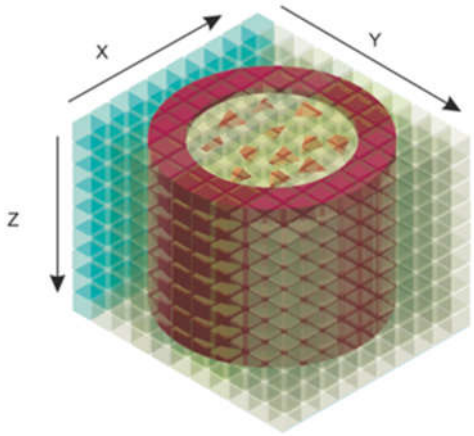

Figure 3.11: The division of the sample object into voxels.

There are two general methods of obtaining the Raman map in the XY plane: (i) laser beam scanning and (ii) XY microscope stage scanning.
In the first case, a system of mirrors moves the laser beam sequentially from one point to another in the XY plane. One mirror deflects the beam along the X axis, and the other along the Y axis, see Fig.3.12(a). Traditional laser scanning imaging and microscopy systems usually rely on bulky and high-power consuming galvanometer scanners [76,77]. However, the industry demands smaller and lower-power solutions, therefore, manufacturers are investigating alternative technologies. With the advent of micromechanical devices, the scanning MEMS (microelectromechanical system) mirrors are a convenient option, see Fig.3.12(b). These solutions are compact, low-cost, consume low power and are highly suitable for high-speed beam steering [78–81]. The “MEMS-in-the-lens architecture” is probably the current state-of-the-art approach, where standard scanning components can be replaced with an integrated MEMS device in a microscope objective [82].

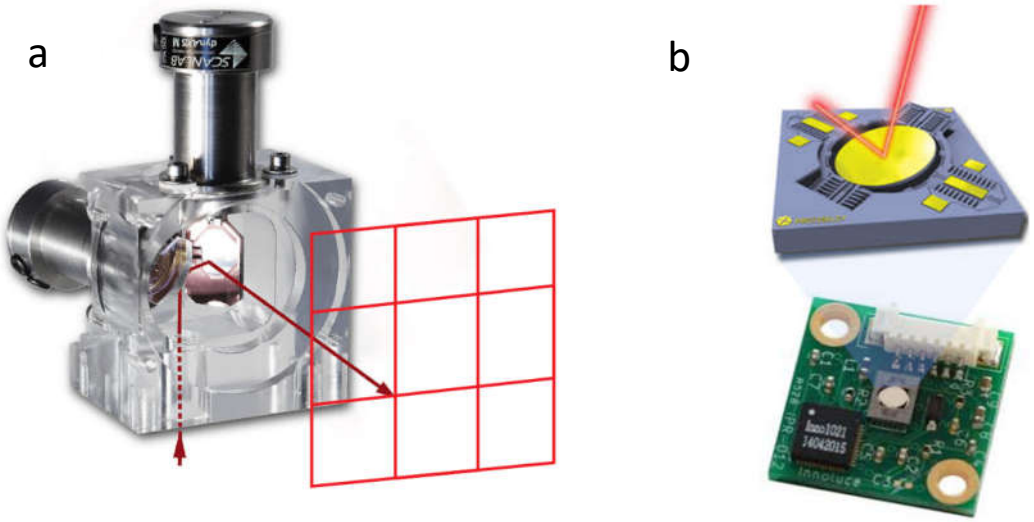

Figure 3.12: a) the dual axis Galvo-scanner with galvanometers and mirrors (dynAXIS, SCANLAB); b) MEMS scanning mirror (Preciseley Microtechnology Corporation).

A disadvantage of such scanning systems is that it introduces small changes in the laser beam. In order to avoid any beam distortions [77] or polarization changes induced by galvanometric optical scanner [83], it was decided to build a classical XY scanning system instead, which is based on linear motorized stages. In our design (e.g. THOR) the whole microscope is moving under a static sample, which provides the focal point replacement.

3.2.2 Microscope unit design

The THOR microscopic module features:

- Inverted configuration
- 3D Raman mapping (the sample is stationary)
- Bright field (reflection mode) sample surface analysis and acquisition of the Raman signal

The microscope design shown in Fig. 3.13 allows scanning in three dimensions without moving the sample. It consists of a microscope objective and two mirrors M1, M2, fixed on motorized linear stages with travel range of 25 mm in three XYZ directions. The idea is to always keep the light beam in a center of optics regardless of the relative position in which they are located. To do this, the objective can be moved along the Z-axis independently of the mirrors M1 and M2, the objective and the mirror M2 can be moved along the Y-axis independently of the mirror M1, and all of them can move as one unit along the X-axis. In this way a 3D scanning was organized by realizing the movement of the microscope and simultaneous maintaining the alignment of the incoming light beam.

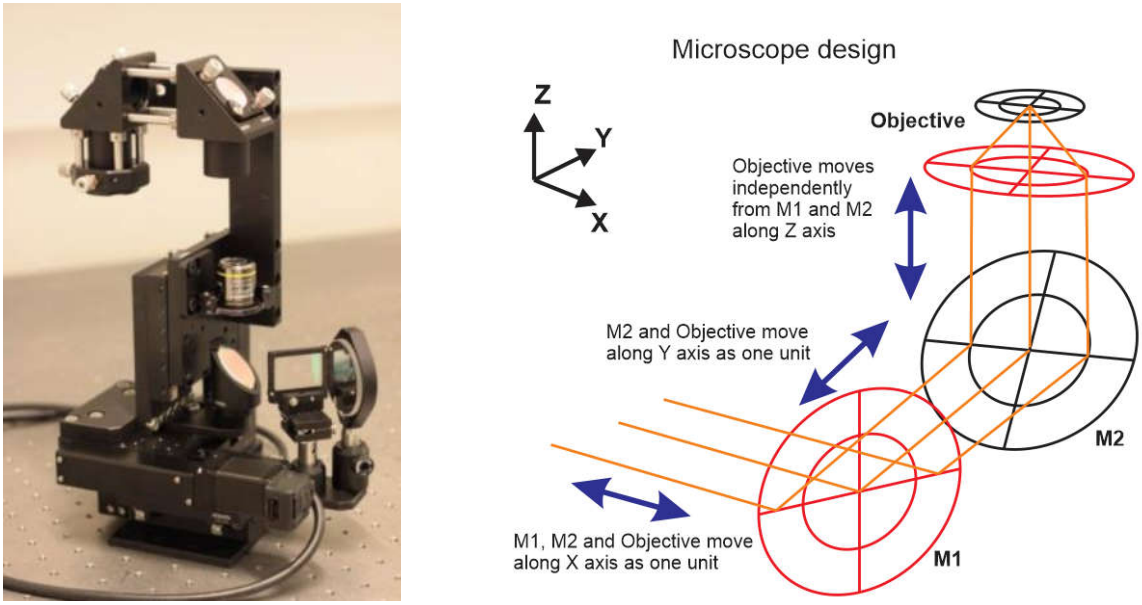

Figure 3.13: a) The THOR motorized XYZ microscope unit. b) A schematic description of the light path. The current design enables 3D Raman mapping without moving the sample. Microscope was custom designed and manufactured by Standa LTD, and now you can find it in the product catalog[1].

Microscope and laser delivery parts are separated from detection part with dichroic beamsplitter BS1, which only will pass the Stokes Raman signal, i.e. longer wavelengths compared to the incident laser light (see Figure 3.14).

The incoming laser beam reaches the microscope, reflecting off the BS1. Here it propagates through a pair of microscope mirrors to the objective and illuminates the sample.

The laser point or line-shaped beams are formed via the laser delivery part, which is then focused on a sample surface. All laser illumination modes are visible on a microscope CCD camera simultaneously with measured Raman spectra. This significantly simplifies the orientation on the sample surface and selecting the suitable areas for Raman measurements, which allows to make the fast probes without preliminary capturing images of the sample. This technique was implemented on the beamsplitter BS2 by combining the laser and visible light beams.

The back-scattered Raman signal is collected and collimated by the objective lens Ob, then reflected by M2 and BS2 through the BS1, edge filter Ed1 onto the slit lens F3. The entire optical path from a sample to the slit on the spectrograph is designed to transfer an image (in our case it is a line or a wide-field laser profile) in aberration corrected conditions. All additional details of the optical design with detailed descriptions of each component are shown in the paper 2.

[1] **8-0035 - Automated XYZ System for Microscopy -** http://www.standa.lt/products/catalog/custom_engineering?item=629&prod=automated_XYZ_microscopy_system

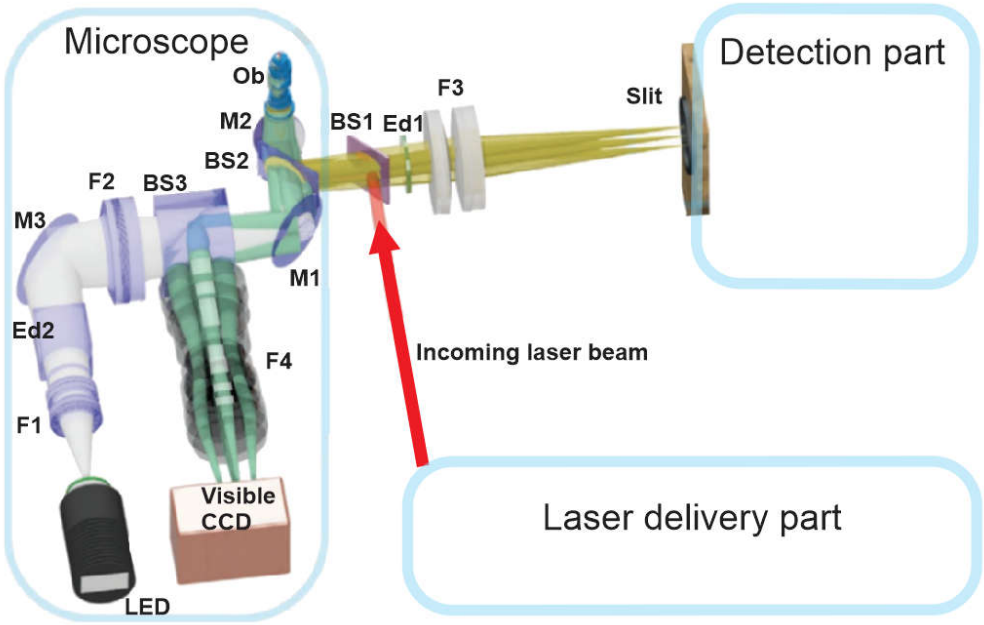

Figure 3.14: Microscope unit optics design with connections to the laser delivery and detection parts of the system.

Visible illumination.
A white-light emitting diode (LED) combined with an imaging CCD camera by a beamsplitter BS3, creates a reflected light illumination scheme [84].

The sample surface is imaged by the LED while collecting spectra, which allows visual control of the sample position and behavior during the measurement procedure. The emitted white light from the LED is collimated using lens F1, and passed through the edge filter Ed2, where the visible light is removed from the NIR spectrum part of the Raman spectrum (785-1000nm). The white-light beam is preliminary cuted off in 6 OD from NIR spectrum part of Raman shift by the edge filter Ed2 and then focused at the back focus of the objective by the lens F2. The beam splitter BS3 controls the incident and reflected light from the sample.

The visible CCD camera projection optics supports imaging of the whole microscope objective FOV with flat field visible light sample illumination, while commonly used Raman microscopes only cut the center part of the field of view.

All the aforementioned characteristics enable simultaneous real-time Raman measurements and sample visualization. The approach simplifies the Raman analysis process by allowing one to easily select relevant surface areas for the signal acquisition (Fig. 3.15).

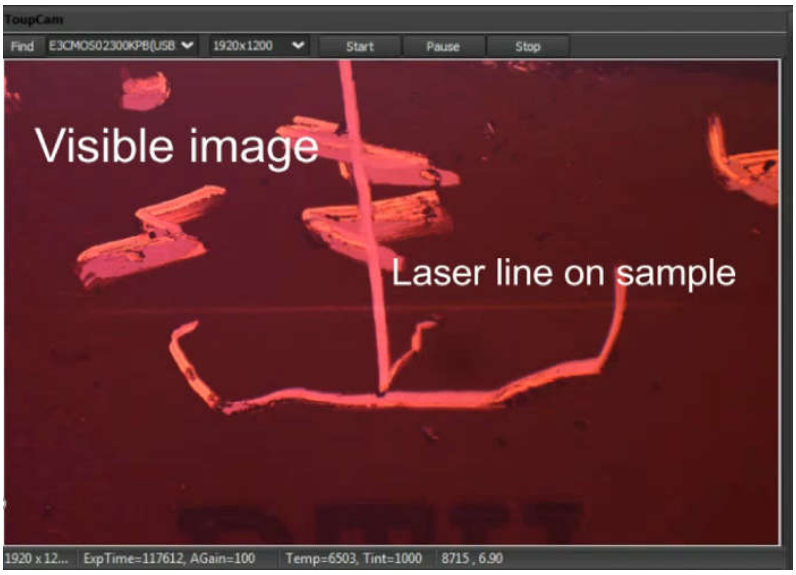

Figure 3.15: A visible image and a horizontal laser line on the sample surface can be simultaneously observed.

3.2.3 Spectrograph design

THOR system is aimed at recording extremely low molecular concentrations (sub-µM), the construction of the device should be highly optimized, and sensitivity - improved. One of the important solutions were self-designed aberration corrected imaging spectrograph (Fig. 3.16). It consists of five key components: slit with the height of 15mm, low NA collimation lenses F1, edge filter Ed1, transmittance volume phase holographic (VPH) grating and high NA focusing lens F2. A spectroscopic air-cooled CCD is using for Raman spectra registration. Collimating spectrograph objective F1 consists of a pair of two achromatic doublet lenses with total focal length 312 mm. A focusing objective was realized as a self-designed double-gauss type achromatic lens with aperture ratio f/2.6 and focal length 80mm. Spectral dispersion was realized on transmittance VPH grating placed between collimating and focusing lenses. The VPH grating has 1644 grooves per mm and first order diffraction efficiency around 78% at 850nm. This type of grating perfectly fits high sensitivity spectrograph construction requirements due to a sinusoidal grooves profile and low stray light background as a result. The spectrograph provides registration of Raman spectra from the laser wavelength of 785 nm in the range 350-2300 cm^{-1}. Total spectrograph magnification is -3.9x. Negative magnification helps to concentrate more scattering Raman intensity on a single CCD pixel size.

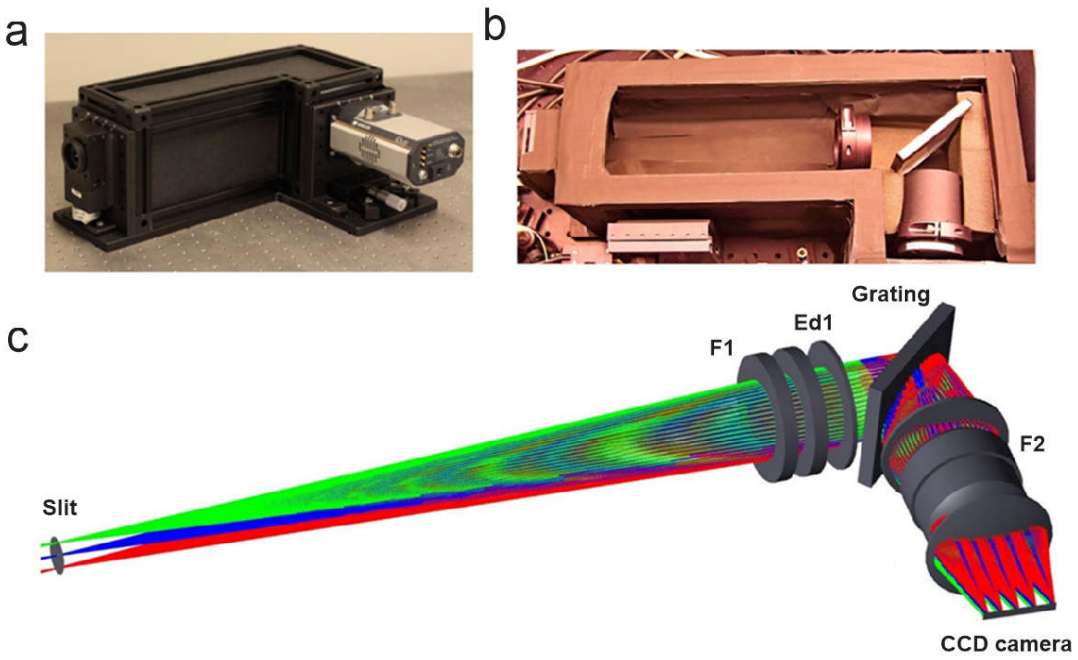

Figure 3.16: Aberration corrected spectrograph design. a) Photo of the spectrograph together with the coupled CCD, b) spectrograph inside view, c) optical design of the spectrograph.

3.2.4 3D study of microcontainers for oral drug delivery

A perfect application for evaluating the detection possibilities of our constructed system was depth volumetric studies of microcontainers for oral drug delivery. The microcontainers contained a polymer powder impregnated with anti-inflammatory drugs (see Figure 3.17). The more detailed information regarding origin and purpose of such microdevices is described in Paper 5. Signal acquisition details during the deep confocal measurements and data processing of multicomponent compounds are discussed in Paper 1. Here we will show the obtained data after confocal measurements and analysis possibilities of our system.

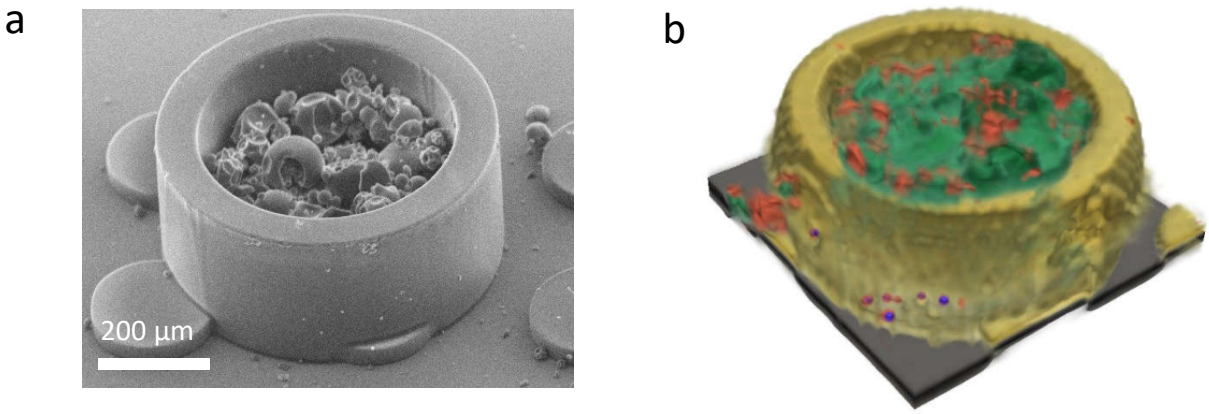

Figure 3.17: Microcontainer for oral drug delivery. a) image from electron scanning microscope, b) volumetric chemical imaging of a similar microcontainer made by Raman microscope.

As discussed previously, the focus change along the Z axis is achieved by moving the objective lens. A set of Raman maps/images (in the XY plane) obtained along the Z axis yield the three-dimensional distribution of materials, see Fig. 3.18.

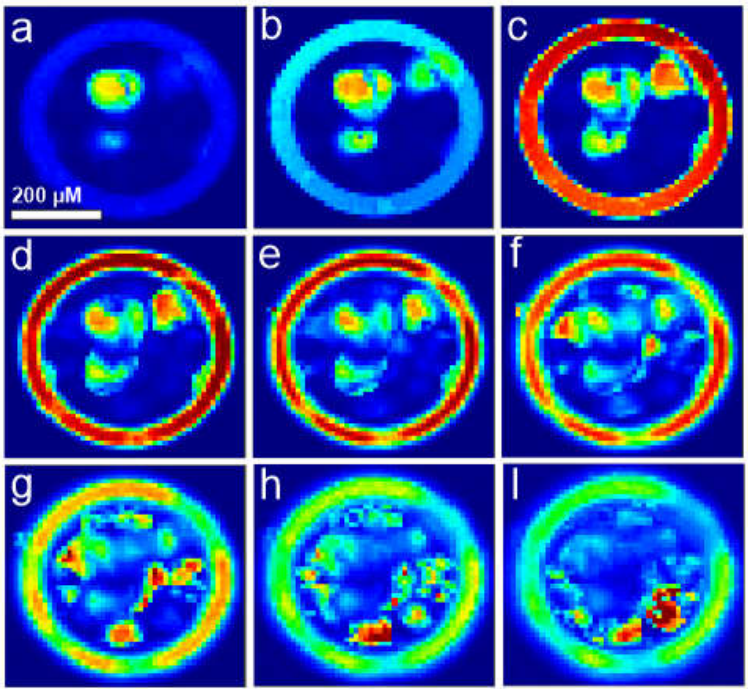

Figure 3.18: Images of XY cross sections from different sample depths with 10 µm interval (a – 0 µm, i – 80 µm). Color represents the intensity of Raman signal on the peak position 720 cm^{-1}.

During the three-dimensional scanning process the raw Raman data is collected in a four-dimensional array, where dimensions are wavelength, X, Y and Z coordinates. That means each voxel contains a vector of numbers, which represents a cumulative Raman spectrum of the materials located in the focused microvolume. The main task of Raman spectroscopy is to recognize each material (or selected one) and show its distribution map across the sample. Sometimes, in case of combinations of components with pure Raman spectra (where several peaks of different materials are not overlapped), it is possible to measure the concentration of each material by measuring the corresponding peak area (or just a height). But in general, the situation is much more complex and only chemometric mathematical methods of spectrum decomposition can solve such difficult task. There is a big variety of multivariate analytical tools, which can be used for multicomponent analysis – from elementary statistical methods to artificial neural networks [85,86]. In current version of THOR software, a non-negative least squares method was realized (more details in chapter 6.4). It allows one to work with libraries of spectra of pure materials and to very accurately calculate the concentrations of dozen components in thousands of spectra in less than a minute. Raw scanned data can also be exported to the CSV file for other methods testing using external software packages and toolboxes such as Matlab or python, where many methods are already implemented. This multivariate decomposition allows to recalculate and change the wavelength dimension of 2000 elements of spectra intensity by the components dimension with the few values (2 and more) of component concentrations.

While 3D visualization of component concentration distributions looks good for demonstration purposes, 2D cross-sections of an object are better suited for analysis. In our case of 4D data, positions in any two dimensions should be fixed, while intensities of two other dimensions can be plotted. In Figure 3.19 a) Z=90µm and Raman shift 720cm^{-1} are fixed and XY image is visualized. Software allows user to scroll any fixed position and change the cross-section view, or to open several views simultaneously. These Raman images are available in the form of two-dimensional images in XY, ZX and YZ planes, however it is also possible to plot wavelength versus any coordinate.

For 3D plots, data can be exported to a VTK file and visualized with 3-rd party software. In Figure 3.19 c) separated components are shown with different colors using an open-source multiple-platform application ParaView for interactive, scientific visualization.

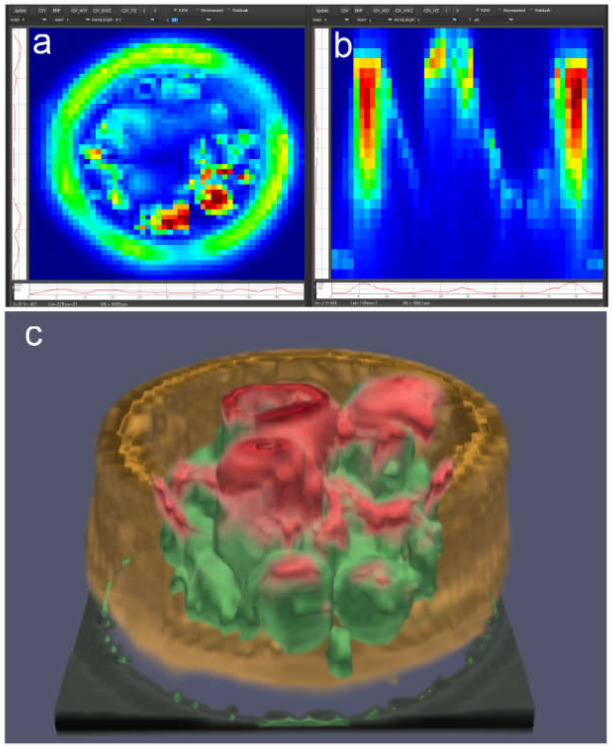

Figure 3.19: a) XY and b) XZ cross-sections of a microcontainer. Color represents the intensity level of Raman spectrum on selected peak position 720 cm^{-1} before multivariative analysis. c) 3D image of a microcontainer is reconstructed after the chemical decomposition of separate components. Each color represents a different material: red – drug, green – polymer, brown – SU-8 container wall, black - silicon substrate.

3.2.5 Fast Raman imaging using the laser line illumination

Spontaneous Raman scattering has a relatively low efficiency ($I_{Raman} \sim 10^{-7} - 10^{-11} \times I_{Laser}$) [87]. Therefore, frame exposition time is usually selected in a range from hundreds of milliseconds to hundreds of seconds for the systems where the broadband Raman spectrum is collected by the CCD camera.

Raman map measurements usually require collection of thousands spectra, in order to speed up the process of mapping, several methods were developed: direct Raman [88], line-focus [89] and line-scan [90]. The first two methods reshape the laser beam into a line or rectangle, which can cover a larger sample area, the last uses a scanning mirror to illuminate the line on a sample. The line-scan method requires much more laser power for each point compared to line-focus method [87]. The direct Raman method demonstrates the fastest measurement possibility at selected wavelength, however for the full spectrum measurements it requires the tunable filters based on the acousto-optic [87] or liquid-crystal devices [91].

Comparing these spontaneous Raman methods, the line-focus method is better suited for temperature sensitive samples, where local overheating plays an important role. It is especially suitable for SERS-based applications (see the THOR system). The line-focus capable system can greatly reduce the mapping time of SERS substrates.

The line-focus illumination probes the sample along the line-illuminated area simultaneously whereupon it is divided into hundreds of spectra by a large number of pixels using a CCD camera, see Fig. 3.20. The line-focus capable microscope with a detector matrix height of 256 pixels makes it possible to carry out measurements 256 times faster than a traditional point illumination Raman microscope.

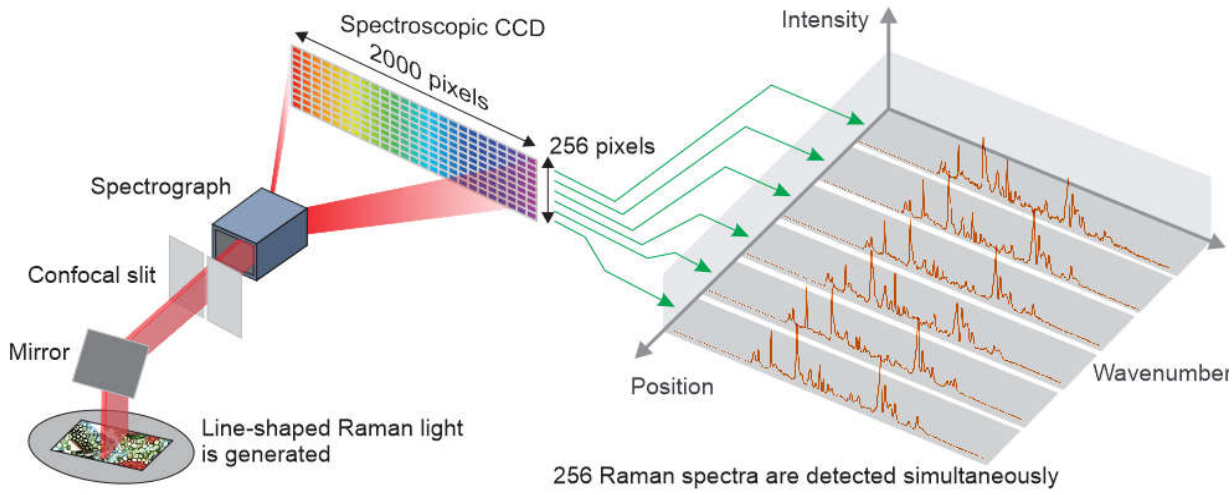

Figure 3.20: Line-shaped sample illumination and simultaneous detection of multiple spectra.

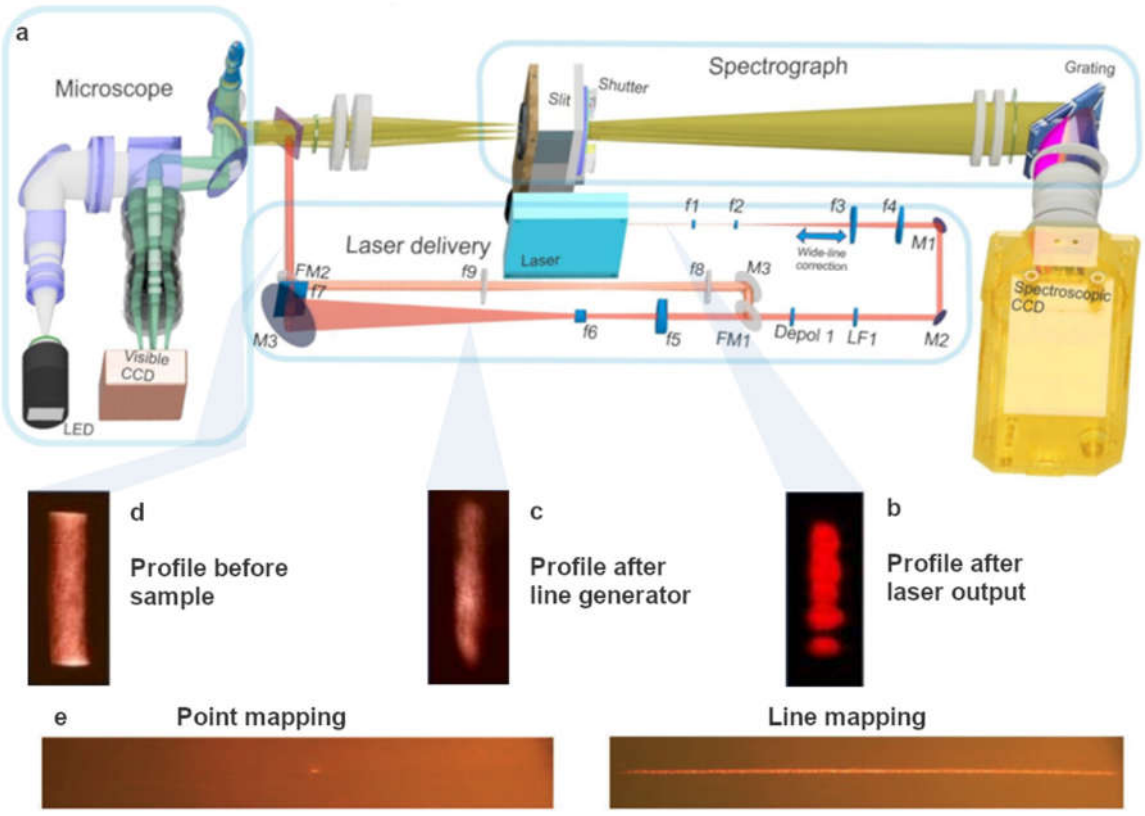

Figure 3.21: a) THOR optical construction. The connections of microscope, spectrograph parts and detailed laser delivery optical path with point/line illumination. b) laser beam profile at the laser output, c) laser beam profile after laser line genitor lens f6, d) laser beam profile before microscope objective, e) views of the point and line laser beams on the sample surface.

The laser beam delivery system is presented in Figure 3.21. The point and line illumination modes can be selected by switching the motorized flip mirrors FM1 and FM2. At line-focus mode a sample is illuminated with a 2.8 µm wide laser line using 10x magnification objective. The laser beam shape can be modified using a set of cylindrical lenses f1–f5.

We used a relatively low cost multimode high-power laser (785nm, 500mW) as an excitation source. The image of its beam profile is shown on Fig. 3.21 (b) which consists of five different spatial modes. Such mode distribution profile can be focused into a diffraction limited size in the vertical direction (y-axis). In order to create diffraction limited laser line profile on the sample we decided to use the x direction of the beam profile to control the width of laser line on the sample. Therefore, a line length should correspond to the vertical direction of the beam profile, which consists of five spatial modes. Laser line generator lens f6 works as mode mixer in the vertical direction. The result of mixing is highlighted in Fig. 3.21 (c) (after f6) and Fig. 3.21 (d) (after f7): the beam profile was transformed into homogeneous laser intensity distribution in the vertical direction. The variation of laser line intensity on the sample surface is around 20% (Fig.3.22).

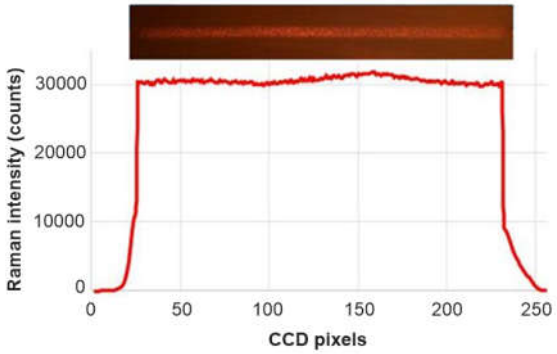

Figure 3.22: Uniformity of Raman intensity at 1641 cm^{-1} from BPE molecular response on SERS chip surface obtained at spectroscopic CCD after propagation through the laser beam delivery channel.

3.2.6 Laser line application for dehydration study of organic hydrates

In Paper 3 we proposed a fast line-focus hyperspectral Raman mapping method to study the dynamic processes of transformation pathways of organic hydrates during heating of drug particles. The particle of drug was aligned on a Linkam hot stage parallel to the laser line. A 1.8mm long laser line was focused along the length of the particle (Fig. 3.23). An exposure time of 8 seconds for the acquisition of 220 Raman spectra was used for all isothermal measurements, which allows simultaneous monitoring of the whole volume of the particle with good enough update frequency of

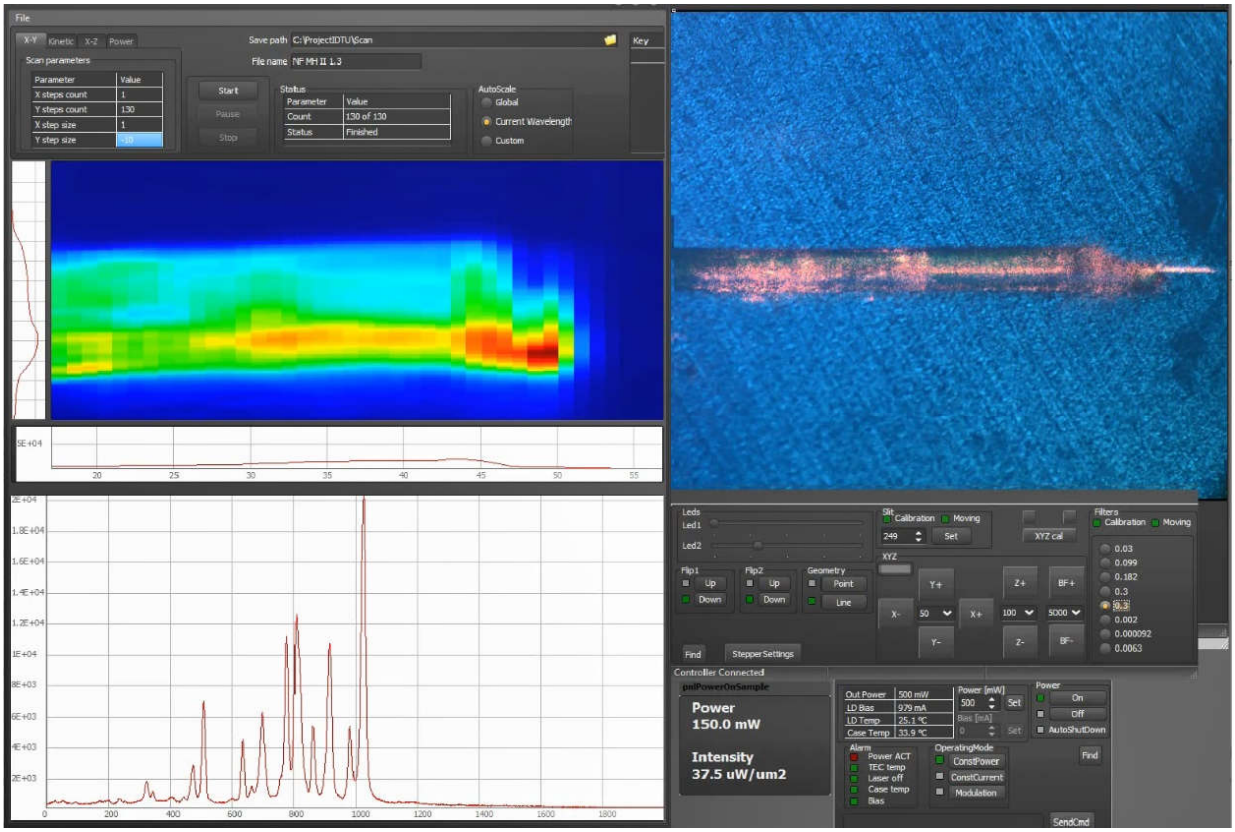

Figure 3.23: The single particle measurement process using line-focus illumination.

the frames. Chemical decomposition showed the overlapping forms of the drug that exist between the metastable intermediates as well as the stable anhydrous forms during dehydration (Fig. 3.24).

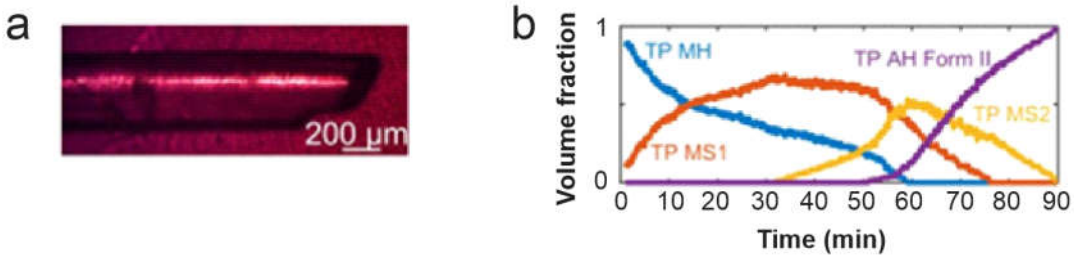

Figure 3.24: Decomposed results from the dehydration (50°C for 90 minutes) of a single particle of theophylline monohydrate (TP MH) to its stable anhydrous form II, where a) is an optical image of TP MH b) concentration profiles showing the dehydration of TP MH via two metastable intermediates to the stable anhydrous solid form.

Being able to perform Raman imaging on a single particle motivated the mapping of a real-life powder sample of nitrofurantoin monohydrate (NF MH II) with different shapes and sizes as shown in Figure 3.25. The full map 1170 µm x 2109 µm with 8 µm step-size was taken in 30 minutes.

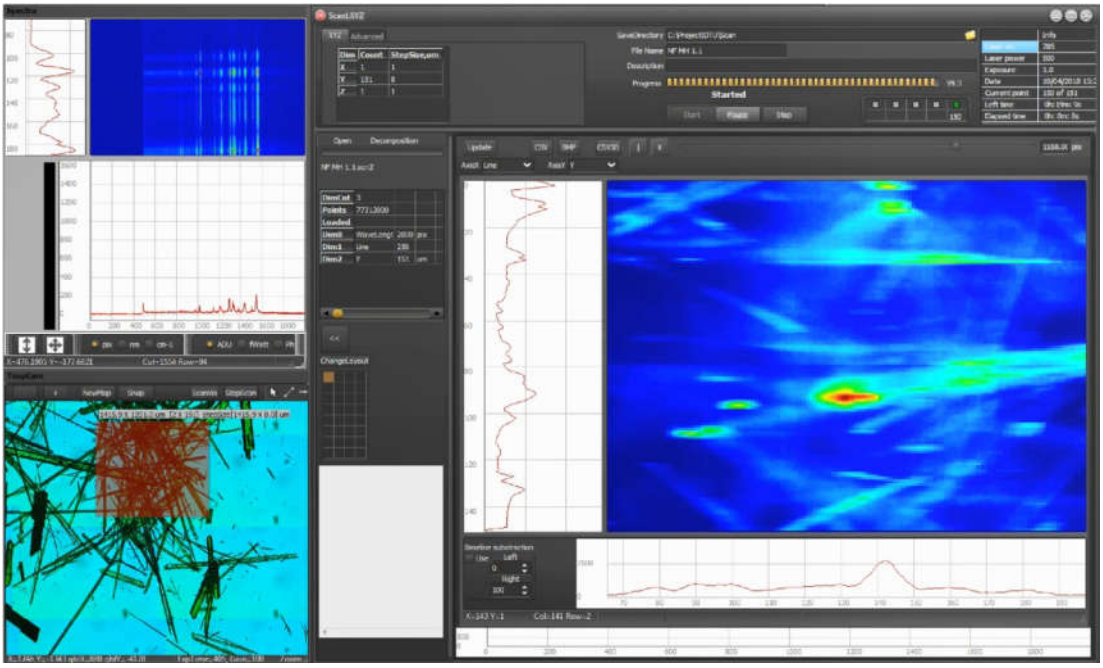

Figure 3.25: The nitrofurantoin particles were heated to 100 °C for ~5 minutes. Raman map represents the intensity of peak at 1558 cm^{-1} of the raw data before the decomposition procedure. Detailed chemical analysis and interpretation of the results were discussed in Paper 3.

In this study we showed the possibility of using a single particle as well as large areas of multiple particles with different sizes and shapes for determination of the multiple solid forms during a dehydration process. The physical stability of drugs and dependency on temperature and humidity have dramatic impact on drug properties, such as solubility, bioavailability, efficacy. This study was focusing on understanding the conditions of solid transformations with the future goal to control/prevent the appearance of unwanted metastable intermediates or control unexpected variations. Present work shows the possibility of structural resolution of different forms of drugs and

their tendency for phase transformations during relatively high temperatures. Overall, this method shows the ability for controlling material properties during development, manufacturing and storage.

4 Surface enhanced Raman spectroscopy

Raman spectroscopy is used as a fast, accurate and reliable method for determining the structure of matter, but the problem with this method is the rather small scattering cross section of ordinary molecules and, as a result, a rather weak signal. The sensitivity of Raman spectroscopy is improved by various methods such as resonant Raman scattering (RRS) [92], surface-enhanced Raman scattering (SERS)[93,94], tip-enhanced Raman scattering (TERS) [95,96] and coherent nonlinear optical effects: coherent anti-Stokes light scattering (CARS) [97] and stimulated Raman scattering (SRS) [98]. Compared to other methods, SERS is a simple and promising approach in solving the problems of increasing the effectiveness of the phenomenon and the intensity of the Raman signal, which will significantly extend the practical application of Raman spectroscopy in chemical analysis.

The first experiments on surface enhanced Raman scattering date back to 1974, when Fleischmann et al.[99] made studies of pyridine on roughened silver (Ag) electrodes. It was about 3 years before the concept of the SERS effect was described by the Van Duyne group [100] and Creighton group [101]. In 1997, significant interest in surface-enhanced Raman scattering was renewed with the publication of the first papers on the detection of single molecules [102,103].

The rapid development of SERS spectroscopy over the past 20 years was facilitated, firstly, by advances in the directed synthesis of nanostructured SERS-active materials [104,105], and secondly, by the development and improvement of Raman spectrometers. The work carried out all over the world in the field of SERS has a pronounced practical orientation, which indicates the need for further developments in this area and the high practical potential of such research.

4.1 General principles of SERS

The SERS effect consists in a huge increase in the effective cross section of Raman scattering of light by molecules adsorbed on the surface of nanoparticles of metals (mainly noble ones): silver, gold, copper.

SERS theoretically uses two mechanisms to increase the intensity of Raman scattering.

The first is an electromagnetic mechanism that occurs when the test substance is located near an enhanced electric field on the substrate surface. The light excites surface plasmons (charge density waves) in metal nanoparticles, which can resonate with electromagnetic Raman waves, amplifying them [104,105]. First of all, the SERS-amplification takes place due to the presence in the system of "the optical amplifier" - typically a metal nanostructures. (Fig. 4.1).

The occurrence of a signal can be represented as three stages:

- external radiation incident on the nanoparticle (NP) causes the conduction electrons to vibrate inside the NP; therefore, a strong electric field appears on the surface of the NP.

- an enhanced electric field is generated at the close proximity of two particles enveloped in a strong electric field.
- during the adsorption of analyte molecules in the gap between NPs an enhanced Raman effect is generated[106].

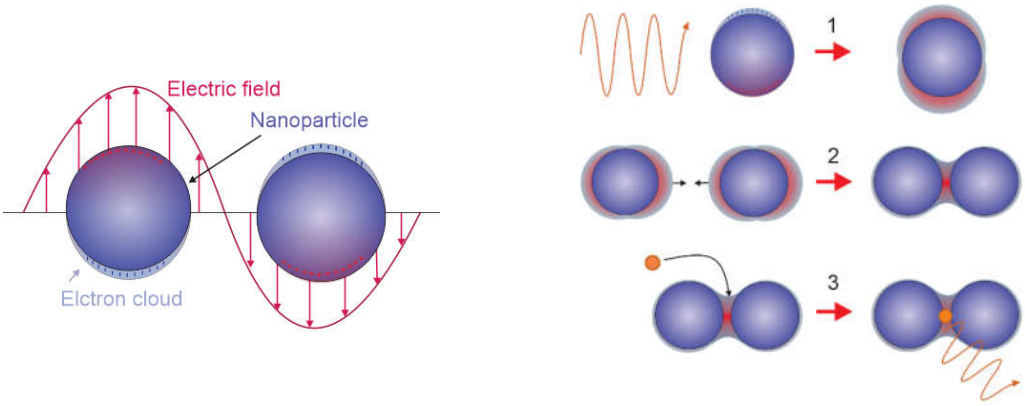

Figure 4.1: Left - collective vibrations of delocalized electrons in response to an external electric field E. Right - schematic concept of the electromagnetic enhancement mechanism of Raman scattering: 1 – External radiation incident on nanoparticles and causes conduction electron excitation, thus high electric field appears on the surface of nanoparticle. 2 – In the gap between two particles, covered with high electric field, an enhanced electric field is generated. 3 – After the adsorption of analyte molecule in the gap an enhanced Raman scattering is generated.

The second mechanism is a chemical (or sometimes - charge transfer) mechanism, which involves bonding a test material to the surface of a substrate. This bond increases the polarizability and, consequently, the intensity of Raman scattering. As described in the literature [50], due to the charge exchange between the substrate nanoparticles and the studied molecules, the scattering cross section of the molecules increases, which also increases the final Raman scattering intensity. It was shown that due to the electromagnetic mechanism, an amplification factor of the Raman scattering intensity of the order of 10^8 (amplification up to 10^{10} -10^{11} is possible, depending on the conditions [107]) is dominant in comparison with the chemical amplification mechanism, which gives a maximum gain of the order of 10^3, which has been reported in [93,108]. The degree of chemical enhancement of SERS depends on the strength of the bond between the molecule being determined and metal atoms on the surface of nanostructure. Thus, compounds with a higher affinity to the surface will be better adsorbed and have a more significant enhancement of the SERS signal, which increases the selectivity of the method [109].

Raman scattering can be considered as the result of two interrelated acts - excitation of an induced dipole and emission of a scattered dipole, arising as a result of the interaction of the molecule electrons with the field of the incident light wave. Under SERS conditions, scattering occurs mainly from a molecule located in close proximity to the surface of plasmonic metals, which have more excitation and emission options (Fig. 4.2).

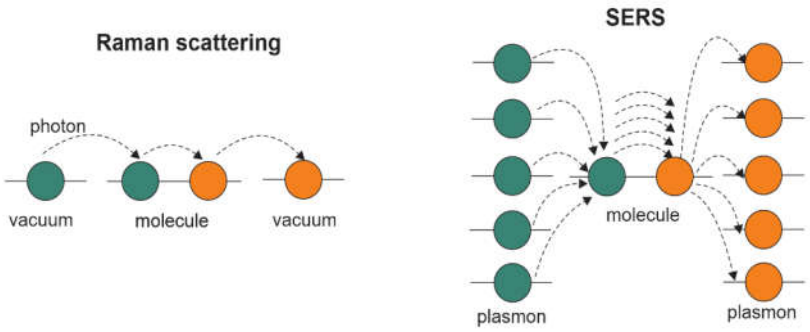

Figure 4.2: Schematic imaging of Raman scattering and SERS processes. While during spontaneous Raman scattering only internal electrons take part in the processes of excitation and emission, the much higher rates in the SERS process are dramatically enhanced by presence a large number of conduction electrons of the plasmonic metal.

Increasing number of transition paths is associated with the interaction of incident light with plasmon vibrations of metallic structures, in contrast to spontaneous Raman scattering in vacuum [110].

The adsorbed molecules are under the influence of the local electromagnetic field of the metal particles, which resonates with the incident light [111]. The observed SERS signal intensity depends on both incident and scattered radiation:

$$I_{SERS} = I_0(\omega_0)\, I'(\omega_0 - \omega_{vib}) = |E_0(\omega_0)|^2 |E'(\omega_0 - \omega_{vib})|^2 \qquad (4.1)$$

where I_{SERS}, I_0, I' – intensities of SERS, external radiation and group electrons vibrations, E_0, E' - the external electric field and the induced metal field, ω_0 and ω_{vib} - frequencies of incoming radiation and molecular vibrations of the analyte [50].

Consequently, the greatest amplification of the Raman signal is observed when the incoming radiation with a frequency ω_0 and scattered radiation with ($\omega_0 - \omega_{vib}$) are in resonance with the plasmonic band of the metal - the "surface amplifier". When performing $\omega_0 >> \omega_{vib}$ or $\omega_0 \approx (\omega_0 - \omega_{vib})$, the following approximation is widely used: $I_{SERS} \approx |E_0(\omega_0)|^4$. Since the strength of the electric field during interaction of two dipoles equals to $E(r) \sim r^{-3}$, then the intensity of the SERS signal depends on the distance between the molecule and the metal as $I_{SERS} \sim r^{-12}$ which is observed experimentally [22].

Thus, it can be assumed that the SERS effect is manifested due to the physical and geometric properties of the surface. An equally important aspect in SERS is the relative orientation of the molecule to the surface of the amplifier metal, since the vibrations of the molecule can be either in the plane, or at an angle, or perpendicular to the substrate surface [22].

To quantify the amplification of Raman signals, the enhancement factors (EF) are calculated [112]. Comparison of substrates from the point of view of their use as active materials is usually carried out according to the substrate EF, calculated by the formula:

$$EF = \frac{I_{SERS}/N_{surf}}{I_{Raman}/N_{Vol}} \qquad (4.2)$$

where $N_{Vol} = c_{Raman} \cdot V$ – number of molecules in volume V during measurements, N_{surf} – number of molecules adsorbed in the same volume at using SERS-active metallic surface.

An important aspect in the SERS method was the study of the so-called "hot spots" of the metal surface. "Hot spots" are small areas with a high-intensity enhancement of the local field, the cause of which is localized surface plasmon resonance. According to the theory, high local fields should appear in gaps between metal nanostructures (Fig. 4.3), for example, in aggregates of nanoparticles from dimers and trimers to complex structures formed by silver or gold nanospheres. The presence of "hot spots" on the metal surface makes a significant contribution to the enhancement of SERS, since resonance occurs near these regions, which makes it possible to record signals with enhancement of the order of 10^7 - 10^8 and up to ~ 10^{11}.

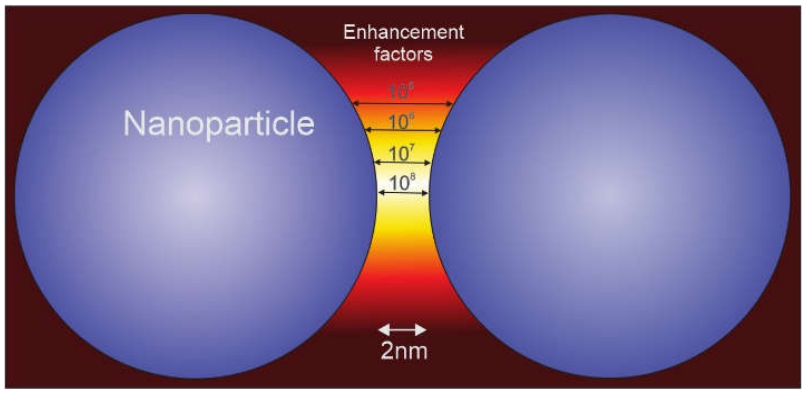

Figure 4.3: An illustration of a “hot-spot” in the gap between the nanoparticles and the enhancement factor dependency in the contact area (adopted from [113]).

It should be noted that the EF of the signal strongly depends on the distance between the metal surface and the molecule, which can adversely affect the reproducibility of experiments.

4.2 SERS spectroscopy applications

SERS spectroscopy opens new possibilities for lowering the detection limits of relevant analytes to pico- and femtomolar concentrations. The specificity of the analysis is achieved by registering SERS signals in the “fingerprint region” (400 – 2000 cm^{-1}), which are highly informative for the detection of individual compounds in mixtures of complex composition [114]. An obvious advantage of SERS spectroscopy is its sensitivity to minor changes in the structure and orientation of molecules. Due to all characteristics and low signal of water, SERS spectroscopy seems to be a good method for analyzing complex biological samples with no or minimal sample preparation. Also, SERS spectroscopy uses a wide range of excitation frequencies, which makes it possible to select an excitation source with minimal background autofluorescence and photodestruction of the sample, which is undoubtedly important for the analysis of biological objects.

The literature on SERS contains extensive and detailed information on the proposed amplification mechanisms of the Raman signal [111,115,116], methods for creating SERS-active materials [57,93,106,117], and a discussion of specific possibilities of using SERS spectroscopy in certain practical areas [50]: medical research and diagnostics [118–122], food [123–125] and pharmaceutical industries

[126], environment pollution monitoring [127,128], detection of explosives and chemical weapons [113], in judicial practice [129].

Currently, SERS spectroscopy is actively combined with in vivo imaging [130], microfluidic devices [131], and other techniques [132] that significantly increase the potential for practical application of SERS as a flexible and powerful analytical method. The advent of portable Raman spectrometers, diode lasers, and the improvement of optics make it possible to use SERS spectroscopy in the analysis of real objects outside the laboratory, which undoubtedly opens the new directions for research.

4.3 SERS substrates

Active research is currently underway to develop metal nanoscale structures that demonstrate plasmon properties. Since the discovery of the SERS effect, a large number of works have been presented with different methods of forming the various structures for SERS spectroscopy. SERS substrates can usually have two forms: a solid substrate with rough, porous or nanostructured surface, covered with a thin layer of SERS-active material, and nanoparticles dispersed in the liquid phase. While colloidal suspensions of nanoparticles require precise optimization of measurement parameter, such as the concentrations of aggregating agent and nanoparticles, their interaction time, solid SERS substrates do not require any stabilizing agents, which reduces the risk of background signal occurrence in the spectra and eliminates dependence on the dynamic aggregation process over time. Since the use of SERS is often hampered by low reproducibility of metal nanostructures and, hence, the poor reproducibility of SERS measurements, the main requirements for the SERS structures should fulfil a number of prerequisites:

- Metal nanoparticles should be placed periodically or regularly.
- Batch-to-batch manufacture reproducibility.
- Uniform enhancement over the entire surface or from batch to batch.
- Long term stability.
- Insensitivity to environmental influences such as temperature, moisture, light, oxygen.
- The SERS substrate must provide high gain, potentially up to single molecule detection, and simple preparation procedure.

Additionally, SERS substrates for sensing applications need to be manufactured in a uniform and reproducible fashion, resulting in spot-to-spot and batch-to-batch variations as low as possible.

Recently, the uniformity of a SERS signal using leaning gold nanopillar (AUNP) structures (Fig. 4.4) has been significantly improved. These AuNP structures exhibit a high SERS signal uniformity with variations around 2-3% of SERS signal intensity across a SERS chip surface [57].

The substrates were fabricated via a mask less RIE followed by a subsequent Au evaporation. The fabrication procedure is depicted in Figure 4.5. The RIE process relies on a combination of reactive gases (SF_6 and O_2), which are ionized in a reaction chamber through a strong electric field and then accelerated towards the Si substrate, etching the Si surface (Fig. 4.5 a, b). Careful tuning of the RIE process parameters allows a fine control over the density, shape and height of the AuNP. Other parameters that can be tuned are the chamber pressure, etching time and composition of reactive gases. To eliminate the background signal from reactive sulphur and fluoride species that remain after the etching process, it is very useful to perform a substrate cleaning procedure with an O_2 plasma. In

a subsequent step, Au metal caps are formed on the pillar tips through deposition of a thin metal film (225nm or 250nm for the different applications) via electron beam evaporation (Fig. 4.5 c). The formed AuNP are 50 – 80 nm wide and 400 - 600 nm tall.

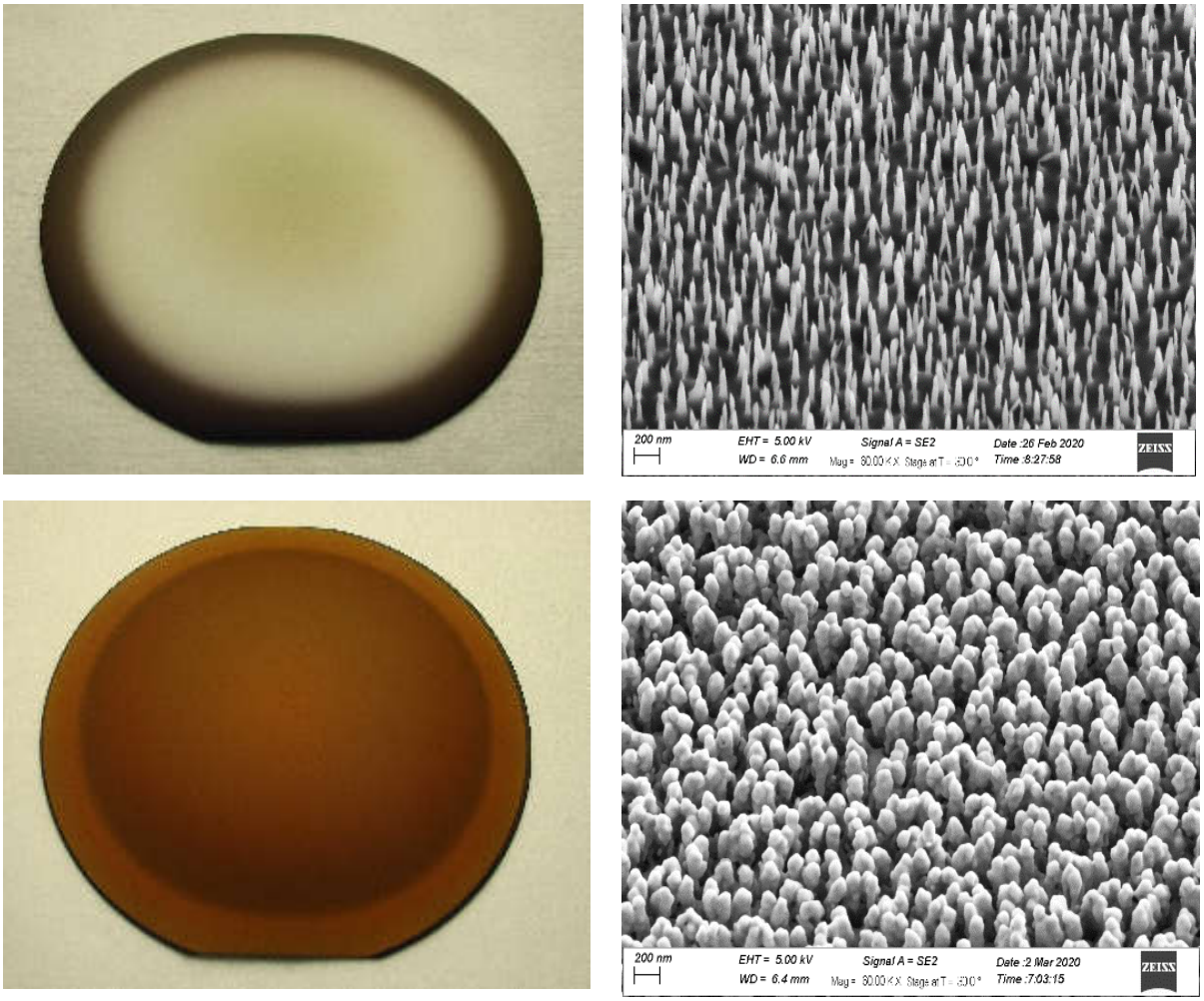

Figure 4.4: Looking at the fabricated substrates. Top - Sharp substrates after reactive ion etching; bottom - substrates after 250 nm Au deposition.

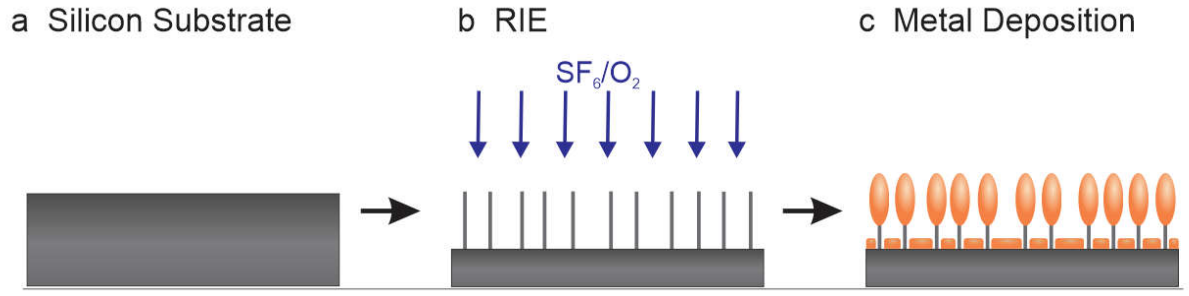

Figure 4.5: Fabrication process of AuNP. Nanopillars are formed on a Si substrate (a) through a RIE using the reactive gasses SF_6/O_2 (b). In a subsequent step Au caps are formed on the pillar tips and in-between pillars through electron beam deposition (c).

4.4 Line illumination optimization for SERS measurements

Technically, the signal collection should take advantage of the well-optimized manufacturing process of the SERS substrates. Surface scanning (mapping) is a very important step in quantitative analysis due to the necessity of averaging the signal from hot spots on the substrate. This procedure greatly reduces the error of molecular concentration determination. The larger an area of SERS chip is measured – the smaller quantification error and lower limit of detection will be reached. Taking into account the fact that the SERS signal, at low concentrations (less than 1 μM), is small and comparable to the substrate background, the exposure time of Raman signal collection can be around 0.1 sec. This means that the time required to collect a map with a surface area of 4x4 mm^2 will be around 3 days with laser spot diameter of 2.5 μm. This is an unbelievable time for Raman mapping and therefore users of commercial Raman systems usually increase the step size up to 10-50 μm. Hereby the total collection time decreases to 4.4 hours – 10 mins. However, such procedure leads to the 'losing' of hot spots on the SERS chip substarte.

Several techniques were designed to speed-up the process of spontaneous Raman measurement, which we mentioned in chapter 3.2.2. In terms of SERS experiments, it is important to take two constraints into account. First of all, the SERS substrate is normally a two-dimensional structure which does not require confocal properties. Secondly, SERS measurements require relatively low laser intensity on the sample (around 1-50 μW per μ^2). Therefore, we used the listed constraints and developed a technology called "wide-field mapping". This technology is similar to the line-focus mapping but the line width becomes 10-20 times broader. On the one hand, this leads to the increased speed of Raman mapping in three orders of magnitude compared to commonly used point focusing mapping without losing any hot spots. On the other hand, laser polarization becomes totally orthogonal to the sample surface which maximizes the efficiency of SERS enhancement compared to the point illumination measuring mode.

The specially designed laser delivery system, which implements point-, line- and wide-field laser illumination modes and aberration corrected Raman spectrograph, allows for highly accurate, sensitive and reliable measurements.

In the line-focus (LF) mode sample is illuminated by a diffraction limited laser line, the width of which is determined by a 10× microscope objective, a 785 nm laser wavelength and is equal to 2.8 μm (see chapter 3.2.2).

In the wide-line (WL) mode the width of laser line can be varied in a range from 2.8 to 64 μm via the position changing of a cylindrical lens f3 in the laser delivery unit (Fig. 4.6 a). Lens f3 works as a laser line/wide-field illumination tuner via its motorized movement through the optical beam axis ±7.5mm.

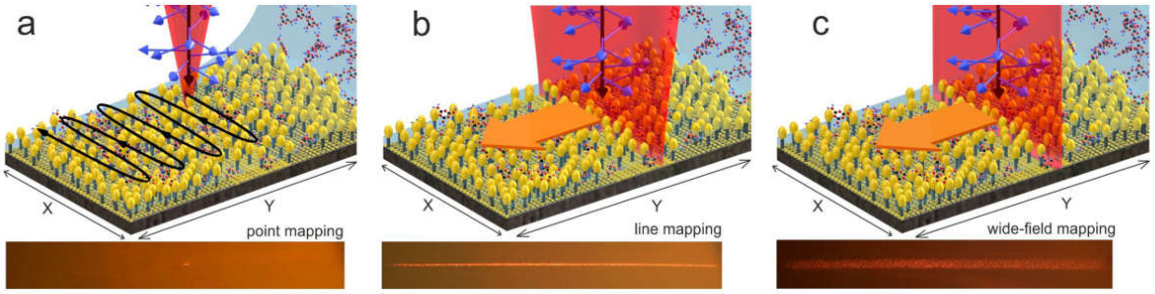

Figure 4.6: Point (a), line (b) and wide-line (c) schemes of sample illumination.

Due to the negative spectrograph magnification we are allowed to use a spectrograph slit size value of 100 µm and obtain a pixel limited spectral resolution of 2.5 cm^{-1}. Such resolution is more than enough for SERS studies where the smallest peak linewidth usually never becomes less than 10-15 cm^{-1}. Therefore, we experimentally determined that the maximum required slit size for the SERS measurements can be at the level of 400 µm, which corresponds to a spectral resolution of 15 cm^{-1} (see Fig. 4.7 a). SERS spectrum of BPE was chosen for spectral resolution test (see Fig. 4.7 b). A slit size of 400 µm corresponds to the 64 µm line width at sample focal plan using 10x microscope objective. It means that the maximum possible width of the laser wide-field illumination can be also 64 µm which is in 32 times broader than diffraction limited line width at equal laser excitation and objective magnification.

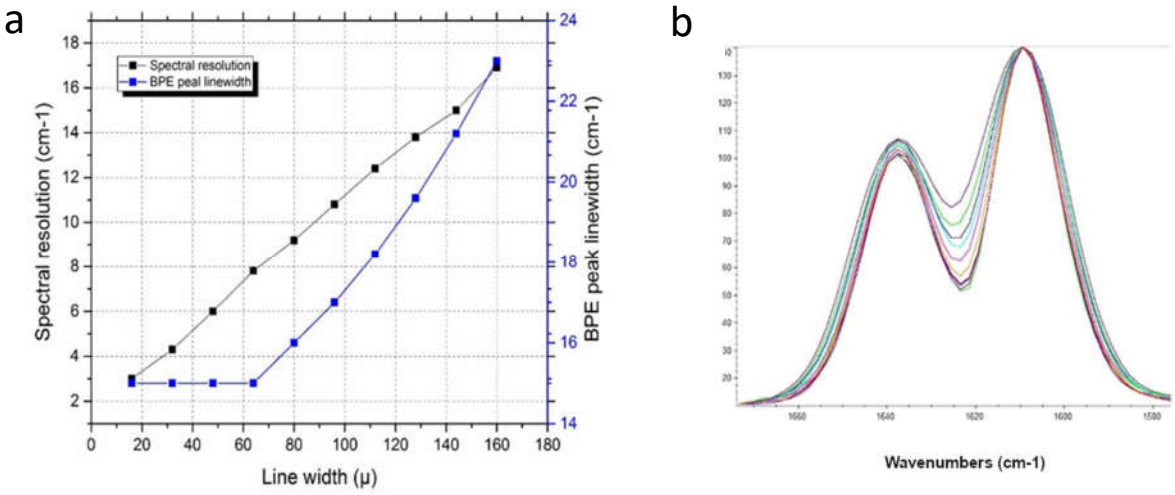

Figure 4.7: Resolution in wide-field mode.

To show SERS-optimized WL configuration benefits we compared obtained SERS spectra of BPE using all three illumination configurations (Fig. 4.8). As mentioned above, Raman mapping in point focusing mode can take many hours. A commonly used way of performing fast large surface area mapping in traditional point-focusing Raman microscopes is an X, Y net mapping procedure with increased lateral step size between points (see point mapping algorithm at the bottom of Fig. 4.8 (a). But, such solution leads to the big losses of mapped area (potential hot spots) between measured points. In the case of line/wide-field laser illumination (top and middle image on Fig. 4.8 (a) the sample surface is homogeneously illuminated and all hot spots are collected by the detector. A mapping algorithm was

realized via step by step movement of the line/wide-field with a step size equal to the line width. It becomes clear that line and especially wide-field mapping algorithms are able to scan sample surface much faster than commonly used point focusing technique. But, equally important is the fact that line/wide-field illumination does not lose any hotspots on the SERS surface which leads to a greatly increased signal-to-noise ratio (SNR) of measured sample. The results of SNR verification of SERS spectrum of BPE on nanopillar substrate are shown in Fig. 4.8 b. It is shown that system in wide field mode can provide SNR two orders of magnitude higher than the commercial system at equal measurement conditions: exposure time 0.1 sec, laser intensity 0.2 mW/µm.

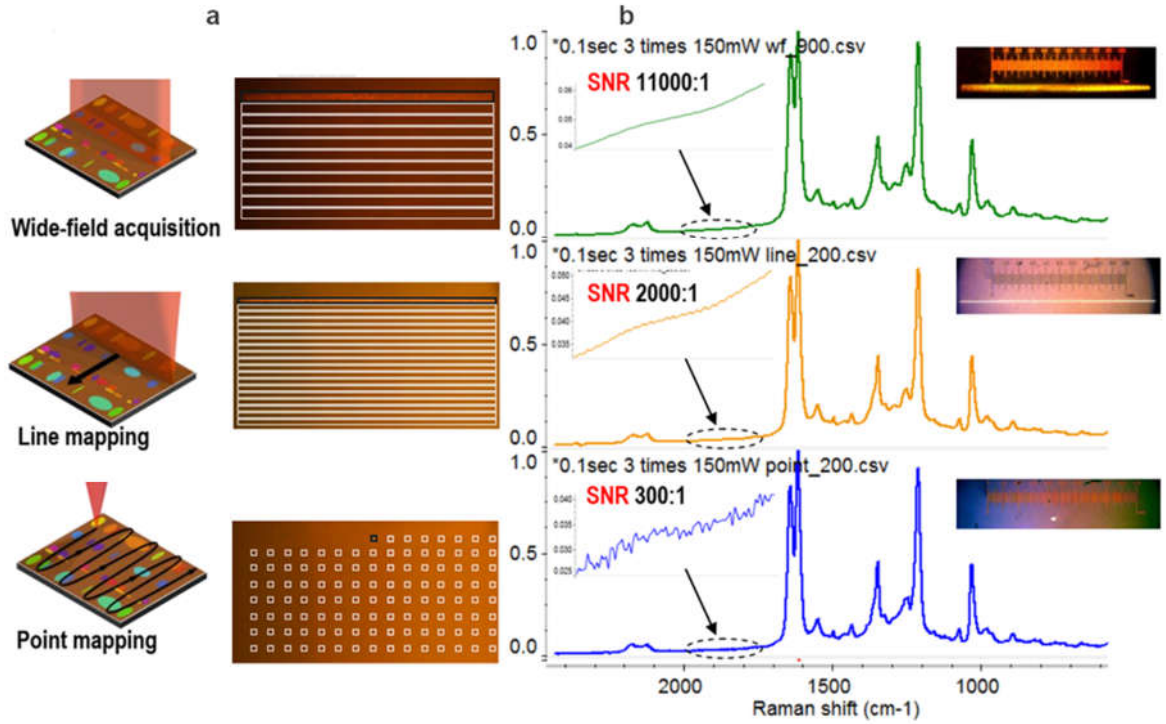

Figure 4.8: Laser illumination modes: (a) mapping algorithm at point-, line- and wide-field laser illumination modes, (b) SERS spectra of 10µM BPE measured on AuNP substrate at different laser illumination modes. All spectra were acquired at exposure time 0.1 seconds, laser intensity 0.2mW/µm of, excitation wavelength 785nm. SNR was calculated as the peak signal divided by root mean square (RMS) noise on the flat spectrum area 1800-2000 cm^{-1}.

4.5 SERS-based applications

There are a number of issues that make quantitative SERS very difficult. For example: poor SERS enhancement uniformity across large surface areas (> cm^2), the need for sample pretreatment like purification and separation, molecular and substrate functionalization, etc. In addition, the improvements in Raman microscope parameters such as sensitivity and SNR are very important for fast and reproducible SERS measurements.

In combination with a microfluidic platform (for detailed description see chapter 6.2) our system is able to provide precise sample manipulations and to cover a wide variety of applications. A number of cases using our nanopillar SERS chips and microfluidic platform are already described in [133–136]. In those studies, commercial high-end Raman devices for SERS detection were used (Fig. 4.9). In Paper 2

we presented application examples of melamine detection in raw milk and p-Coumaric acid (pHCA) production from E. coli bacteria culture. Compared to our previous results, obtained on commercial equipment, our system can detect analytes at much lower concentration level down to 1 µM (one order better) in case of melamine and pHCA detection, with a scanning speed three orders faster and without losing “hot spots” on the sample surface.

5 Polarized Raman spectroscopy

5.1 Basic methods of molecular orientation investigation

In this section, the main experimental methods for studying molecular orientations in a macroscopic phase are described. As an example, consider dye molecules inside a polymer. Quantitative description of molecular orientation is obtained via reconstruction of the orientation distribution function (ODF). It allows one to calculate a portion of molecules that are oriented in a certain direction with respect to a chosen direction in space. The ODF can be expressed as series for a certain set of known functions. Information of molecular orientations is then described in coefficients of the ODF. These coefficients are determined from the experimental data and are used to calculate the ODF. The number of expansion coefficients obtained experimentally dictate the accuracy of the ODF, i.e. larger number of expansion coefficients improves the ODF form [137].

The ODF decomposition coefficients can be obtained by various methods: wide-angle X-ray scattering (WAXS) [138], birefringence measurements [139], nuclear magnetic resonance (NMR) [140,141] , as well as Raman spectroscopy.

Each approach has its own advantages and disadvantages. Birefringence is an easy-to-use and convenient method that allows one to obtain object information, however, only averaged over an entire sample [142]. The use of the NMR method, on the other hand, is limited by high cost of the device. The WAXS method is the most accurate one. Compared to other methods, it generates the most accurate representation of the ODF, but it is only applicable for crystalline objects.

Among optical methods, fluorescence spectroscopy is used to solve a large class of problems. It allows to study the distribution of molecules that move freely within the phase under study [143]. The IR dichroism method allows calculating molecular orientation in both amorphous and crystalline phases [144]. This method allows to obtain only a single coefficient for the ODF, and therefore, the accuracy of predicting molecular orientations is significantly reduced. In addition, the object must be sufficiently transparent and thin for absorption measurements.

Polarization Raman spectroscopy (PRS) is a powerful method for studying molecular orientation [145]. Like IR dichroism, this method allows to analyze the ODF in both crystalline and amorphous samples.

The most general theory of molecular orientation using experimental data from PRS, is well developed and described in ref. [146,147]. Linearly polarized light polarized light may interact differently depends on a structural organization of molecules in a material and their relative orientation to the polarized light axis. For example, these orientation differences may indicate different polymorphic forms of the drug after crystallization, which is not achievable with depolarized light.

PRS can be particularly helpful in gaining information that is quite often complimentary to X-ray diffraction. Using vibrational spectroscopy, the following types of analyses can be done:

- Assign the vibrational modes, specifically the symmetry of the vibrational modes, and determine relative values of Raman tensor elements.
- Differentiate single crystal and polycrystalline materials.
- Identify and differentiate polymorphs and allotropes.
- Detect and characterize disorder and directionally varying strain.
- Determine orientation of a crystal or structure within a microelectronic or optical device.

5.2 Fundamentals of polarization Raman spectroscopy

For understanding the type of information, which can give us polarization Raman, recall equation (2.6). It expresses different components of the induced dipole moment (which define intensity of the Raman signal) with the tensor of molecule polarizability (Raman tensor) multiplied by the incident electric field components. The Raman tensor is predetermined by a relative position of atoms and the direction of bonds between them. Therefore, if the polarizability tensor of a material under the study is known, by using polarized light with different orientation angles we can more precisely characterize all vibration modes represented by peaks in measured Raman spectra. Usually, during Raman measurements, light is depolarized, which makes it possible to characterize the material composition independently on the relative orientation of a sample and a measurement system. By introducing a polarizer and an analyzer into an optical scheme of a spectrometer, it allows one to separate differently polarized components of light and determine their individual contribution to the resulting signal. The experimental set up is shown in Fig. 5.1 a. The incident laser light is linearly polarized using a polarizer. To select a certain component of the resulting signal, a second polarizer, called an analyzer, is placed directly in front of the detector.

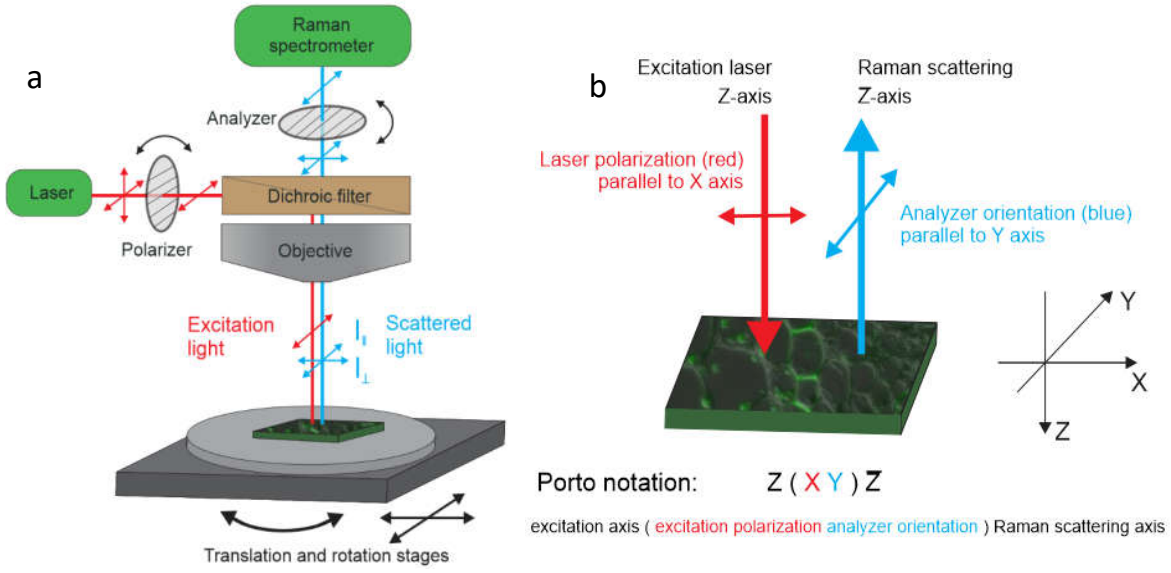

Figure 5.1: a) The experimental setup for studying molecular orientation using PRS. b) The Porto notation for freely oriented samples.

For annotation of the polarization conditions, a Porto notation was developed. It records the directions of incident laser beam and scattered light detection, as well as their polarizations, with respect to the sample orientation. [148]. The notation includes four terms:

a (b c) d

where:
a - direction of propagation of the incident laser
b - direction of polarization of the incident laser
c - direction of polarization of the scattered Raman
d - direction of detection of the scattered Raman

Figure 5.1 b gives an illustration of Porto's notation being applied in a back-scattering configuration of Raman microscope, where the overbar on the $\bar{Z}$ axis notation describes the reverse direction of scattered light detection. The terms inside the parenthesis explain the polarization direction of polarizer and analyzer. The terms outside the parenthesis explain the incident light path and scattering path.

The Raman scattering intensity I is dependent on the crystal symmetry, as well as the direction and polarization of the incident and collected light relative to the sample orientation. It is given by the relation:

$$\boldsymbol{I} \sim |\boldsymbol{\varepsilon_i} \cdot \boldsymbol{\mathfrak{R}} \cdot \boldsymbol{\varepsilon_s}|^2 \tag{5.1}$$

where $\boldsymbol{\mathfrak{R}}$ is the Raman tensor which depends on the crystal symmetry and on the particular vibrational mode, and ε_i and ε_s are the polarization vectors of the incoming and scattered light.

A Raman tensor is expressed by a matrix 3x3, and due to crystal formation properties, quite often it is sparse and contains symmetric elements (second-rank symmetric tensor) [149]. The symmetry point group of the crystal class defines non-zero and zero elements in the tensor, while their magnitudes are dictated by specific chemical bonds between atoms. There are 32 forms of Raman tensor determined for all types of crystals classes [149].

In order to find out whether a certain vibration mode appears in a Raman spectrum during its excitation with the fixed polarization, it is necessary to know the symmetry group of a sample molecule. The first material, which we selected for the crystal orientation study in paper 4 was silicon (Si). The main properties of Si were already studied in the literature [150–152], and it gave us a good starting point with pre-known portion of data for comparison and evaluation of our method at first stages of the system development. Silicon belongs to O_h crystal class, and its sole Raman active phonon mode at 520 cm^{-1} is triply degenerated and correspond to three Raman tensors:

$$\boldsymbol{\mathfrak{R}_x} = \begin{bmatrix} 0 & 0 & 0 \\ 0 & 0 & d \\ 0 & d & 0 \end{bmatrix}, \boldsymbol{\mathfrak{R}_y} = \begin{bmatrix} 0 & 0 & d \\ 0 & 0 & 0 \\ d & 0 & 0 \end{bmatrix}, \boldsymbol{\mathfrak{R}_z} = \begin{bmatrix} 0 & d & 0 \\ d & 0 & 0 \\ 0 & 0 & 0 \end{bmatrix} \tag{5.2}$$

Each normal vibrational mode is transformed by different symmetry operators (rotation, reflection, etc.) in a specific way, which depends on properties of a particular group. Orientation of a crystal can be described using three angles (Fig.5.2):

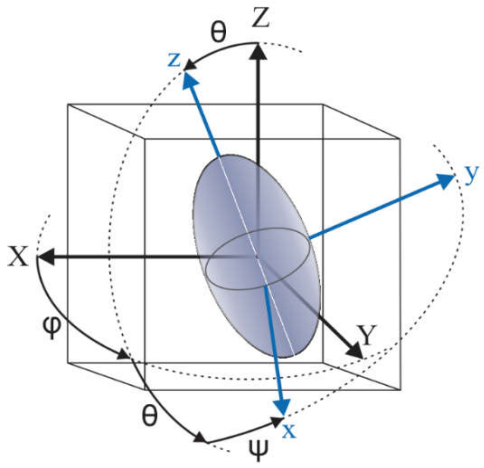

Figure 5.2: Schematic representation of a molecule oriented in a specific direction relative to the laboratory coordinate system. θ, ϕ, ψ are the Euler angles, which vary in the following ranges: $0 \leq \theta \leq \pi$, $0 \leq \phi \leq 2\pi$, $0 \leq \psi \leq \pi$.

Elements of the Raman scattering tensor are defined in the crystal coordinate system, therefore a rotation transformation of free-oriented crystal is expressed by applying a rotation matrix $\mathbf{\Phi}(\theta,\phi,\psi)$:

$$\mathfrak{R}(x,y,z) = \mathbf{\Phi}(\theta,\phi,\psi)\mathfrak{R}(X,Y,Z)\mathbf{\Phi}^{-1}(\theta,\phi,\psi) \tag{5.3}$$

where $\mathbf{\Phi}^{-1}(\theta,\phi,\psi)$ - inverse matrix, (X, Y, Z) – is the crystal coordinate system, (x, y, z) – the laboratory coordinate system.

The final Raman intensity can be rewritten as:

$$\boldsymbol{I}(\theta,\phi,\psi;\psi_i,\psi_s) \sim \sum_j \left|\boldsymbol{e_s}\,\mathbf{\Phi}^{\boldsymbol{T}}(\theta,\phi,\psi)\mathfrak{R}_j(X,Y,Z)\mathbf{\Phi}^{-1}(\theta,\phi,\psi)\boldsymbol{e_i}\right|^2 \tag{5.4}$$

where a sum over the all degenerate phonon modes takes place.

In order to check the quality of orientation determination and an error value, a simulation a testing dataset of the Raman intensity variation of Si wafers with cuts (100), (110) and (111) versus wafer rotation angle ψ was performed, as well as real measurements. The Raman intensity plots for the $Z(0\ 0)\bar{Z}$ detection configuration is shown in Figure 5.3. More detailed calculations and explanation of experimental steps are described in the supplementary notes in paper 4.

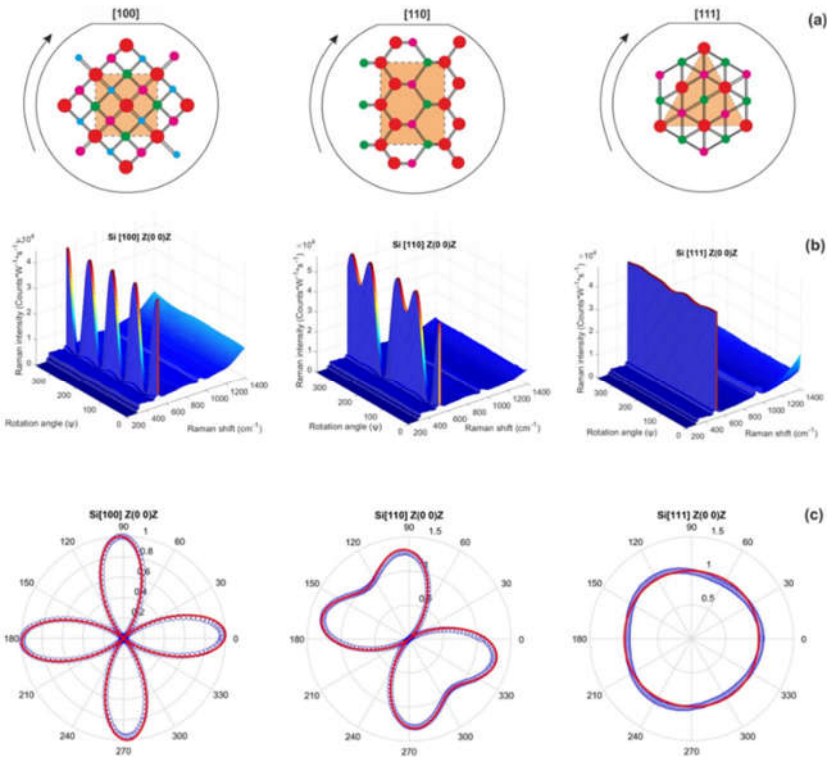

Figure 5.3: Si wafer rotation experiment. a) – Top view of Si unit cells with surface planes (100), (110), (111). b) – The corresponding Raman spectra versus wafer rotation angle ψ of each faces in detection configuration $Z(0\ 0)\bar{Z}$. c) – Intensity of Raman peak at 520 cm^{-1} (the sum of Si modes) versus the wafer rotation angle ψ.

Here we see several types of symmetry in the signal intensity versus rotation angle, which is not enough for the unambiguous angle determination. Since we aimed at creating a fast (ideally in a single shot mode) measurement method without sample rotation, a certain number of multi-configuration measurements is required at each step. The goal of the measurement procedure is to find a minimum number of detection configurations (channels), which can produce a unique set of intensities at any variation of rotation angles θ, ϕ, ψ.

The orientation determination procedure is performed by fitting the Euler angles, simulating Raman intensities for each channel, and minimizing the equation (in the least squares sense):

$$\left(\hat{\theta},\hat{\phi},\hat{\psi}\right) = argmin \sum_{i}\sum_{s}(\boldsymbol{I} - \boldsymbol{I}(\theta,\phi,\psi;\psi_i,\psi_s))^2 \tag{5.5}$$

where $\boldsymbol{I}$ – measured signal of each channel.

In the case of cubic symmetry of Si unit cell, the ambiguity of angles determination can be successfully resolved by introducing six on-axis and three off-axis detection channels (Fig.5.4). In order to describe Raman intensities in off-axis registration geometry, vector $\boldsymbol{e_s}$ is multiplied by rotation matrix **M** which results in $\boldsymbol{e'_s}$:

$$\boldsymbol{e'_s} = \mathbf{M}(\beta)\boldsymbol{e_s} \tag{5.6}$$

Matrix **M** depends on off-axis tilt angle β defining rotation of scattered light collection optics.

Further, by increasing the channel number up to 12 does not demonstrate any noticeable accuracy enhancement, so the decision was to work with nine registration channels in our system as a reasonable minimum for unambiguous measurement.

Figure 5.4: On-axis (a) and off-axis (b) detection schemes with normal sample illumination.

The Raman tensor model development and all steps of data processing: artifacts correction, objective numeric aperture (NA) compensation and sophisticated iterative algorithm of Euler angles fitting are out of author's responsibilities in the project, thus trey are not further described in this thesis.

5.3 Instrumental implementation of polarized Raman microscopy

In order to make the sample polarization investigation more informative and faster, the initial setup configuration was modified (see Fig. 5.5) to deliver two laser beams with orthogonal polarization orientations on the sample focal plane. Two illuminating channels, created by splitting the laser beam, was focused onto two separated, but closely to each other points. The scattered light was guided through the Wollaston Analyzer Unit (WAU), which splits the Raman beam into eight different channels with different polarization orientations (Figure 5.6). After the WAU splitter, the beams were coupled via a slit focusing lens to an imaging spectrograph. This is done in the same manner as the line-illuminated points during line-mapping experiments (Fig. 5.7).

After the scanning procedure, eight different maps from all channels can be overlapped and laterally shifted based on the distance between the points for further, precise data analysis.

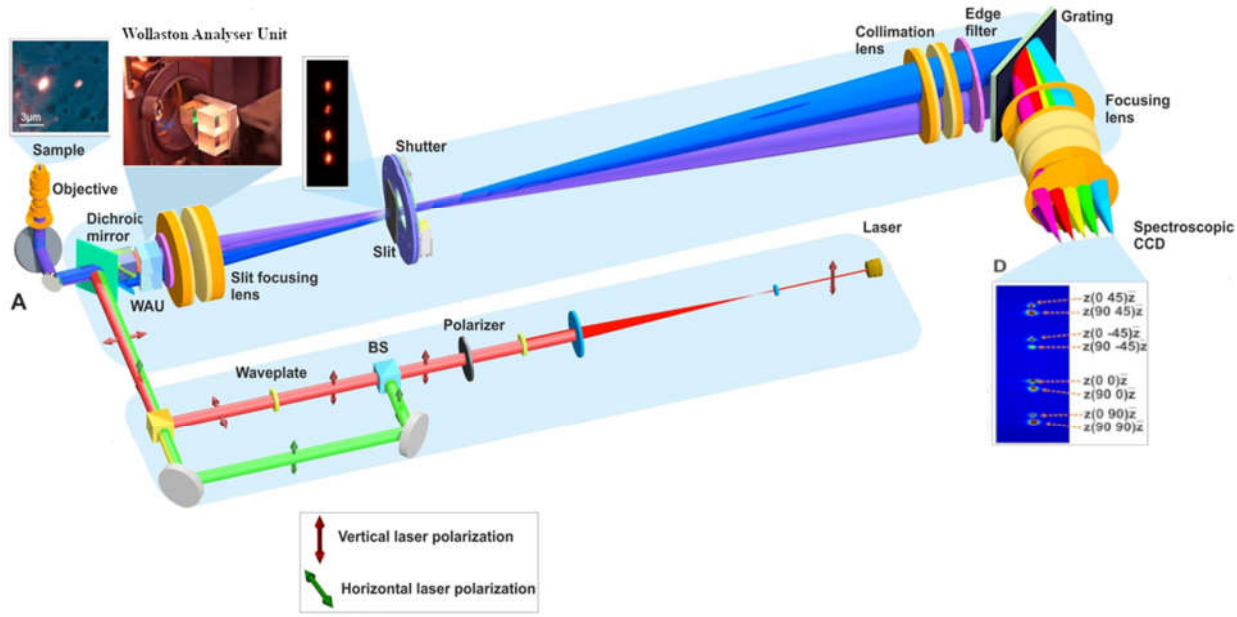

Figure 5.5. The THOR setup configuration for polarized measurements.

WAU is based on a beamsplitter, right-angle prism, λ/2 achromatic wave plate, which rotate a linear polarization by 45°, and two Wollaston prisms (see Fig.5.6). From each illuminated point on a sample, we obtain four separated beams with 0°, 90°, +45° and -45° polarization orientations. This sample illumination and light detection scheme allows one to make fast polarization dependent study without rotating the polarizer/analyzer and simultaneously provides eight Raman maps with various combinations of incident/scattered light polarizations (Fig.5.7, Fig.5.8).

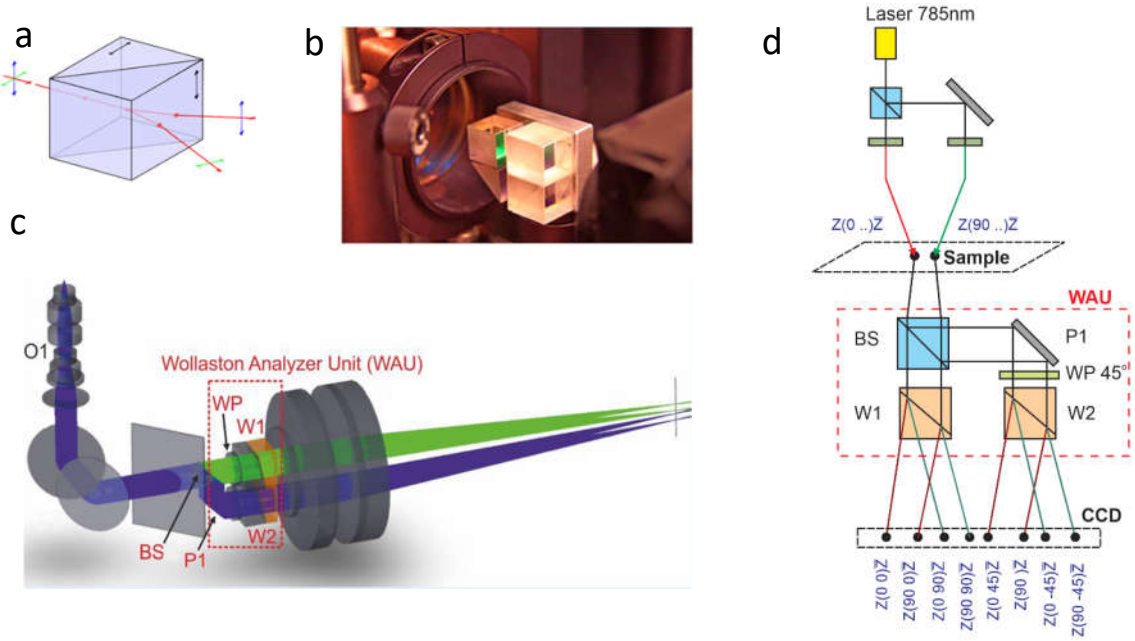

Figure 5.6. a) The Wollaston prism illustrates the depolarized light beam splitting to two orthogonal components; b) An assembled Wollaston Analyzer Unit; c) – Optical schematics of WAU. BS – beam splitter, P1 - right-angle prism, WP – λ/2 wave plate, W1 and W2 – Wollaston prisms, O1 – microscope

objective; d) – schematic representation of the sample illumination beams and their splitting via the WAU into 8 different detection channels.

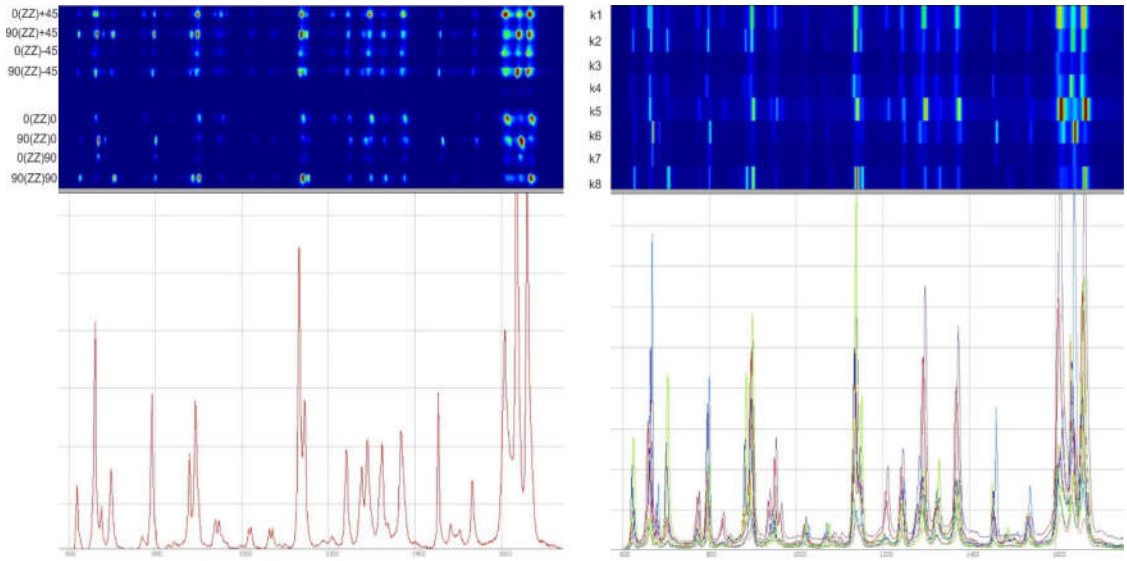

Figure 5.7: Simultaneous measurements of 8 channels with different combinations of polarizer-analyzer orientations. Top left – light distribution from multiple channels on the CCD area; top right – software separation and visualization of the binned data from each channel. Bottom left – spectra plot from a selected CCD row; bottom right – simultaneous visualization of the spectra from all (or selected) channels for quick analysis.

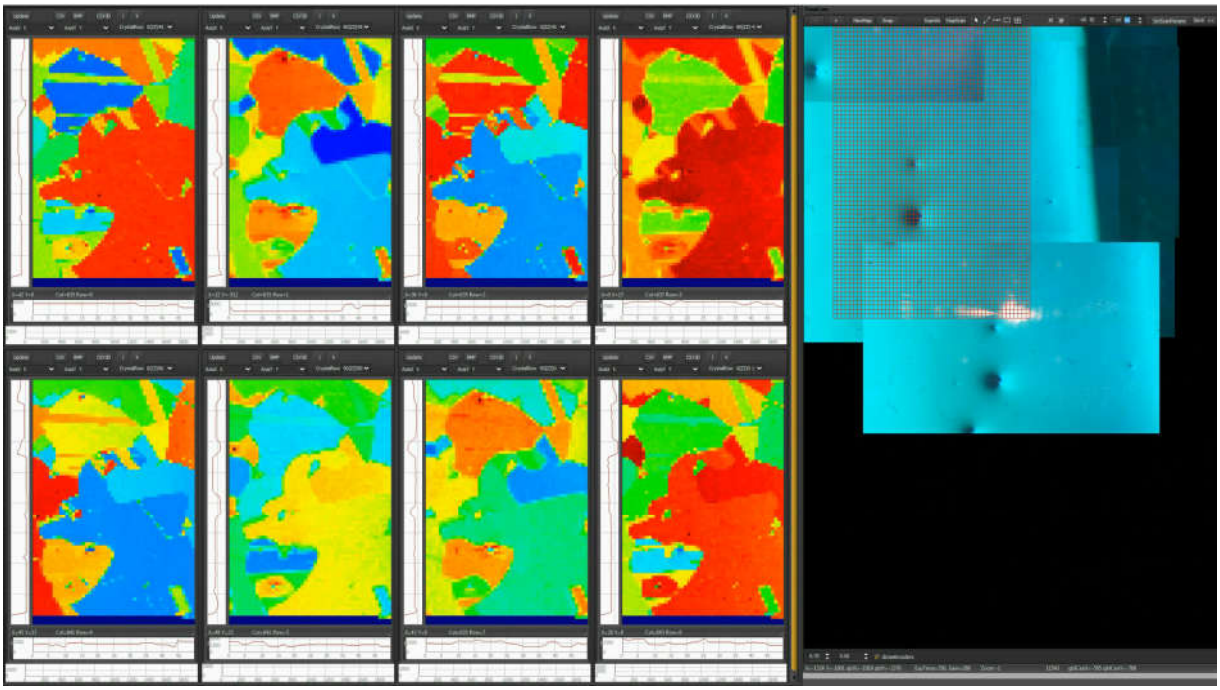

Figure 5.8: Simultaneous 8-channel polarization measurements of polycrystalline Si. Color maps represent the intensity of the Raman peak at 520 cm^{-1}.

Crystallographic orientation. In order to determine the crystal orientation without sample rotation, it requires multiple sample illumination channels at different laser polarizations and multiple detection

channels at multiple analyzer orientations. In Paper 4, crystallographic investigations using Raman spectroscopy system is described in detail. Here the aim is to highlight the fundamental principles of the system construction. Test measurements of Si wafers with (100), (110), (111), and later orientation fitting simulations showed the necessity to have not only on-axis channels, but also off-axis channels. For the cubic symmetry of Si crystals, the simulation with various numbers of channels yields the minimum numbers of 3 on-axis illumination channels, 6 on-axis and 3 off-axis registration channels.

For the fast orientation mapping two sample illumination layouts were implemented. In both cases three laser beams with polarization angles $\psi_1 = 0°$, $\psi_2 = 45°$ and $\psi_3 = 90°$ were used.

In a 2D layout, three differently polarized laser beams were created by splitting of the one beam with an excitation wavelength of 785 nm (Fig.5.9 a). The pattern with three periodical spots was formed on the sample focal plane. (Fig.5.9 c).

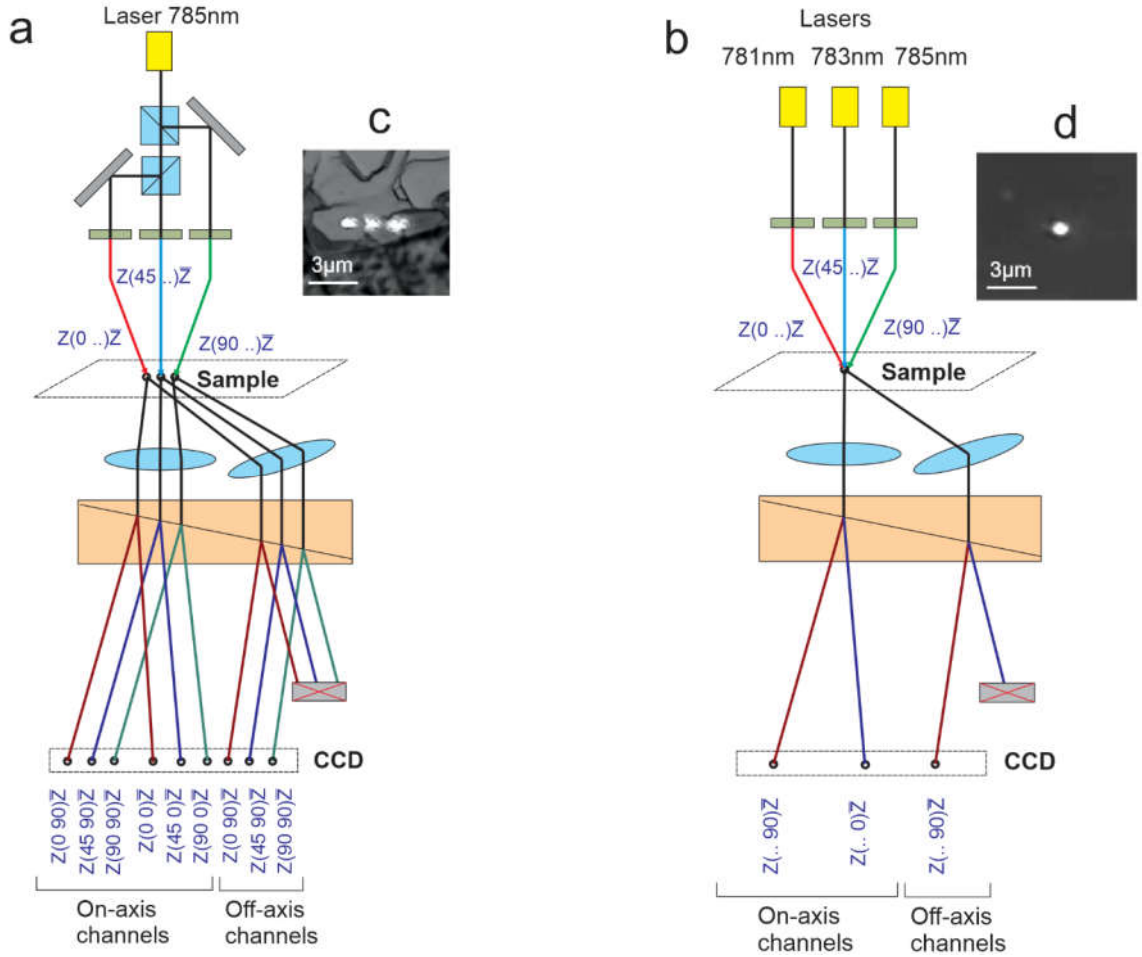

Figure 5.9: Schematic representation of simultaneous measurements with nine polarized Raman channels. a) The 2D illumination layout with three separated laser beams. b) The 3D illumination layout with combined laser beams. c-d) Microscopy images of the obtained laser spots.

In the 3D layout, the incident laser beams are created by three similar diode lasers, but stabilized at different temperatures and therefore operated at shifted wavelengths 781, 783 and 785 nm (Fig.5.9

b) and focused at one point on a sample surface (Fig.5.9 d). This illumination layout can only be used for materials with a low number of phonon modes since the spectra are overlapped in the registration channel. The wavelengths of the incident lasers can be fine-tuned in the range of a few nanometers by changing the working temperature. This shifts the recorded Raman modes by about 20 cm^{-1} or more, which is enough to separate the signals using software (Fig.5.10 b).

The key element in Raman delivery system is the WAU system, which splits the scattered signals on the orthogonal components and provides synchronous measurements at three different analyzer orientations: $\psi_s^1 = 0°$ and $\psi_s^2 = 90°$ on the main axis, and $\psi_s^{off\text{-}axis} = 90°$ on the side axis tilted by 45° to the sample plain.

In order to detect all channels, the system was equipped with two microscope objectives, focused at the same point, and a number of mirrors, which guided the off-axis light beam into the parallel position to the main on-axis beam without any polarization distortions (Fig. 5.10 a).

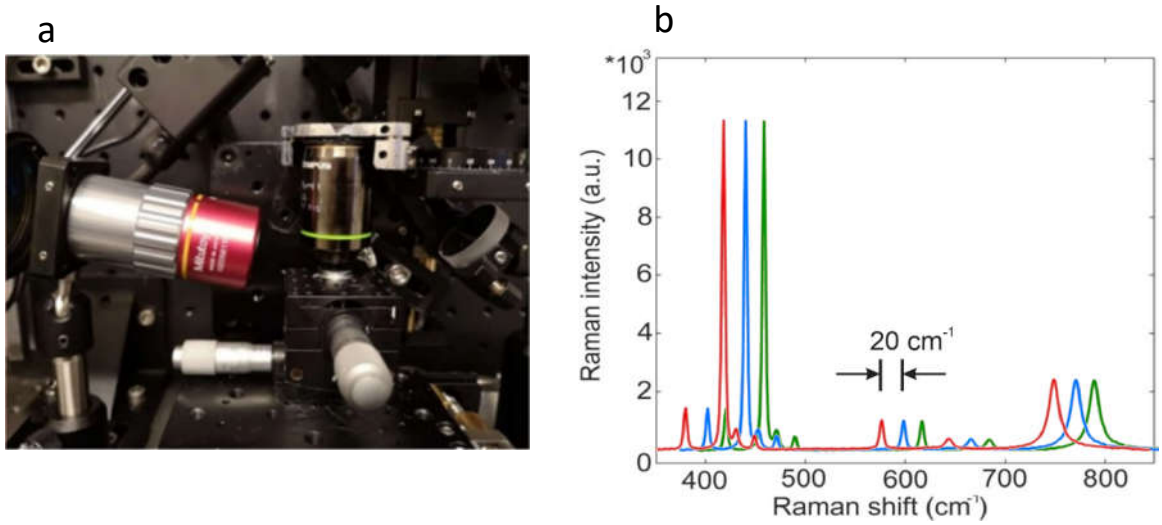

Figure 5.10: a) Two objective detection scheme. An additional channel is tilted by 45 degrees from the main axis. b) Three overlapped depolarized Raman spectra of polycrystalline sapphire shifted by 20 cm^{-1}.

5.4 Crystallographic orientation: applications

Paper 4 demonstrates several application examples of crystallographic orientation determination using the THOR setup: a polycrystalline Si solar cell 2D mapping, 3D mapping of a semitransparent polycrystalline sapphire samples that shows potential of these volumetric measurements, and a pharmaceutical tablet formulation surface mapping in order to determine the orientation of CBZ DH crystals on it.

Tableting using a direct compression is one of the most widespread approaches for manufacturing solid dosage forms [153]. However, there is a continuous progress towards developing more complex, multilayered tablets with different active ingredients and a smart dissolution behavior [154–156]. By performing fast PRS measurements, the current method for the first time shows that the orientation of particles could be determined using a bulk sample. This analytical technique can pave the way for

developing new drug delivery systems that involve materials with a particular crystal orientation for achieving desired disintegration and dissolution properties. The technique could be a useful tool in drug development and manufacturing processes.

6 Instrumentation. Electronics and control software

In this work, the aim was to develop a versatile Raman system with unique capabilities for Raman imaging and SERS-based applications. In this chapter, the basic electronics and software components that constitute the system are described. These components were developed with the following goals in mind:

(i) Imaging of drug-loaded microcontainers with the purpose to analyze and quantify 3D drug distribution.
(ii) Improve the Raman signal detection capability in terms of sensitivity and axial resolution for volumetric Raman chemical imaging where sample cooling and exponential depth dependent exposure corrections have been implemented.
(iii) Imaging of dehydration processes – the laser line-focus is required.
(iv) The laser-line focus technique for high throughput SERS-based molecular detection.
(v) A multichannel Raman microscopy system for 2D/3D orientation mapping.

First, the basic properties of the Raman system (THOR), that was develop e.g. for high-throughput SERS detection, see Fig. 6.1, are reviewed. The capabilities of the system were adopted to allow for the other aforementioned applications. The basic THOR system characteristics are:

- An integrated auto-sampler combined with a microfluidic lab-on-disc (LOD) centrifuge system. The LOD is designed to automate and simplify sample pretreatment procedures such as separation, mixing, and sample filtration using the Au/Ag NP SERS structures prior to the SERS detection of an analyte, i.e. melamine detection.
- A custom-made microscope (epi-detection) for the Raman/SERS signal mapping with a simultaneous visualization of the incident laser beam and a sample surface.
- A laser delivery system with three illumination modes: point-focus, line-focus and wide field.
- A custom-made, aberration corrected Raman spectrograph specifically designed to accommodate the line-focus and wide-field scanning modes.

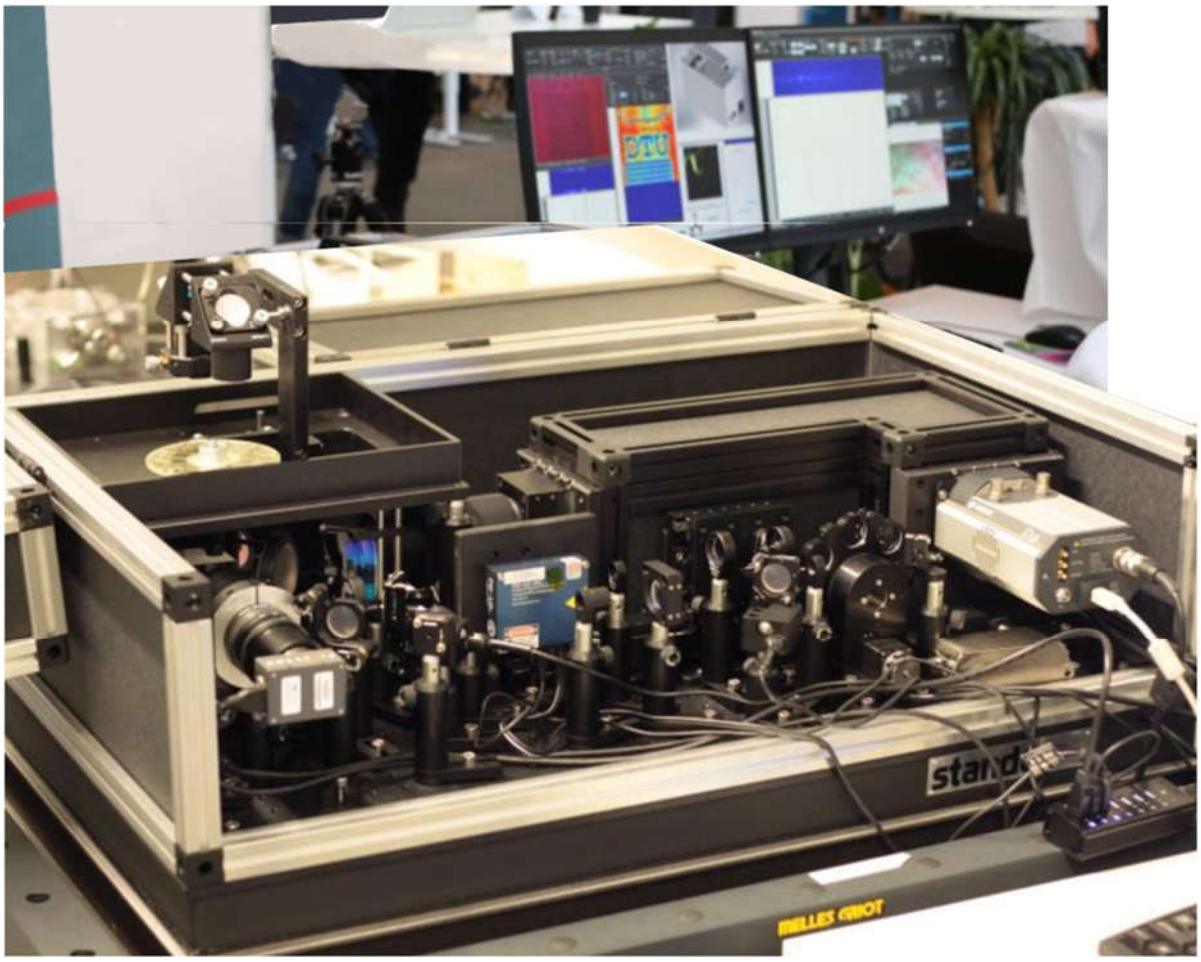

Figure 6.1: The THOR system internal and external view. In the operation mode, the THOR optics and sample compartment are closed.

A brief system summary. THOR is a home-built Raman imaging system, i.e. the laser delivery optics, microscope and spectrograph were assembled in-house. This offers advantages compared to commercial systems such as costs, improved sensitivity, flexibility, and a possibility to develop new, high-throughput Raman/SERS signal mapping techniques. Moreover, efficient conditions for the SERS signal detection using self-made optics, for example, depolarized laser illumination, in combination with fast Raman mapping techniques can be realized.

A more detailed overview of the laser beam delivery, microscope, the Raman scattering beam optical path and the spectrograph are given in Chapters 3-5. This chapter is focused on electronics and software, which enables the user to manipulate the samples, collect and analyze the data, and perform relevant data transformations for efficient visualization of obtained results.

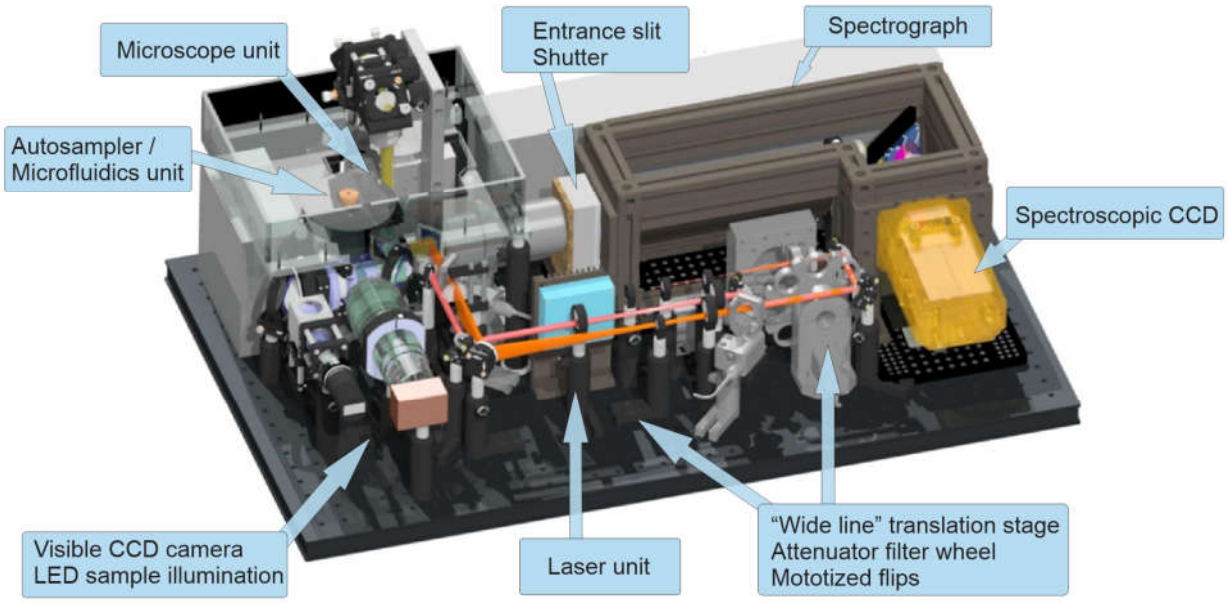

Figure 6.2 Electronic components location in the setup

All electronic components can be grouped in the following functional units:

1. The laser beam delivery unit
    - Laser source – LuxxMaster Compact Raman Boxx LML-785.OCB-FS / 785nm, 500mW, multimode, free space output, USB 2.0 (PD-LD Inc.)
    - Attenuator filter wheel – 8MRU-1WA / 8 positions, 1-inch filter holder (Standa Ltd.)
    - "Wide-line" translation stage - 8MT167M-25BS1 / 25mm travel range (Standa Ltd.)
    - Motorizes mirror flips (x2) - 8892-K-M / 1-inch mirror holder (Newport Corporation)
2. Detection unit
    - Spectroscopic CCD camera – Andor iDus 416 / Resolution 2000 x 256 pixels, Pixel Size 15x15 µm, Image Area 30x3.8 mm, 16 bit, TE Cooling Down to -95°C (Oxford Instruments)
    - Spectrograph entrance slit - 77736 Motor Driven Curved Slit Assembly / Hight 15 mm, Range 4µm - 2.0mm (Newport Corporation)
    - Spectrograph shutter - 87-208 C-mount Electrical Shutter / Aperture 20mm (Edmund Optics Inc.)
3. Microscope unit
    - XYZ translation stages (x3) – 8MT167S-25BS1 / 25mm travel range (Standa Ltd.)
    - Imaging CCD camera - E3CMOS02300KPB / Sensor 2.3Mpix/IMX249, resolution 1920x1200@30fps, USB 2.0 (ToupTek Photonics Co.)
    - Sample illumination source - MNWHL4 white light illumination unit with LED (Thorlabs)
4. Autosampler/microfluidics unit
    - Rotating motor – 320409 DC motor / speed 7750rpm, torque 107mNm, 90W, 48V, USB 2.0 (Maxon motor ag.)

- Motor controller - EPOS2 50/5 Digital positioning controller, 5 A, 11 - 50 VDC (Maxon motor ag.)
- Strobe lamp - L9455-11 Xenon flash lamp module, 5W (Hamamatsu)
- Strobe CMOS camera – PL-722CU-T / Sensor 2.3Mpix; global shutter; resolution 1920x1200; trigger Input - 1 optically Isolated, 5-12V DC; GPO/Strobe - 2 outputs, 3.3V and 1 optically isolated max 40V DC; GPI - 1 input, 3.3V; USB 3.0 (Pixelink, a Navitar Company)

5. Control unit
    - Custom built electronic controller for controlling and synchronizing all internal devices.

For a complete setup control, data acquisition, visualization and analysis a desktop multi-screen Windows-based software was built, see Fig.6.4. The source code is written in (i) Delphi using Embarcadero RAD studio 10.3, and (ii) C++ in the form of additional libraries. A complete source code is located in the GitHub repository[2].

The software consists of the five main modules:

- Microfluidics/auto-sampler module
- Navigation module
- Spectroscopy system control and data acquisition module
- Sample scanning and data visualization module
- Data analysis module

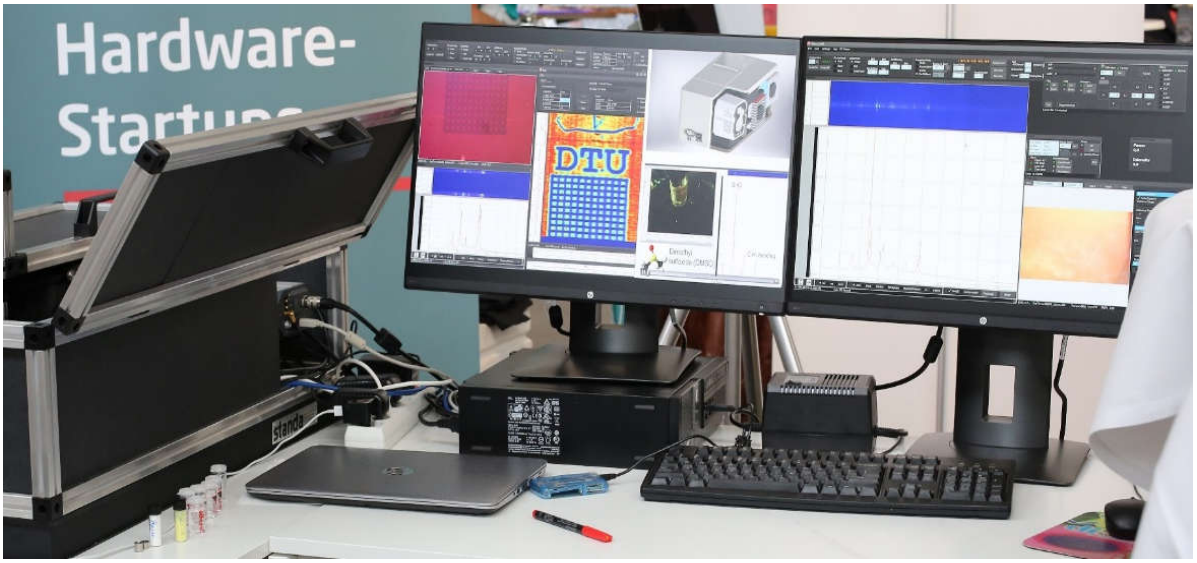

Figure 6.4: The software view of the THOR system.

[2] https://github.com/TravelDjaba/THOR

6.1 Control unit

Since the THOR system includes a big variety of devices obtained from different vendors, these devices are not optimized to work as one unit. In order to unify the system control and implement fast intranet synchronization between different devices, a custom control unit was designed and assembled, see an overview in Fig. 6.5.

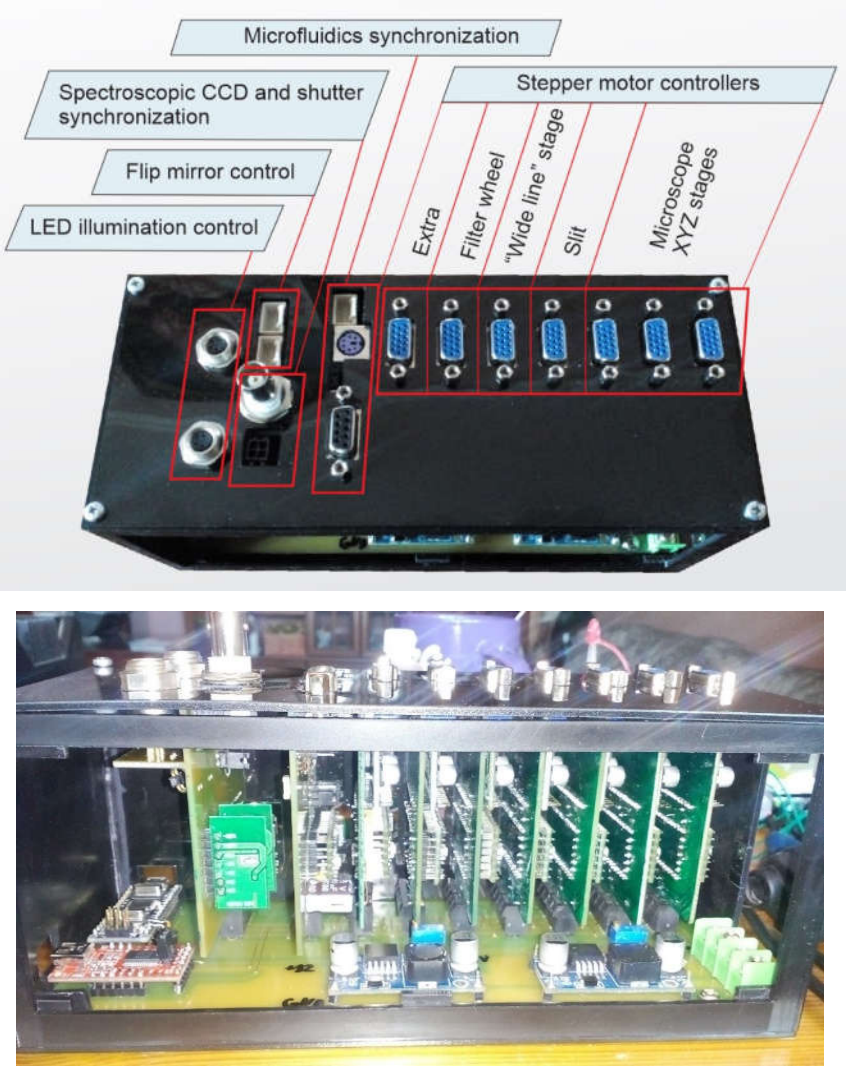

Figure 6.5: The THOR system control unit contains 9 slots for extension controllers. At the moment, 7 motor controllers, microfluidics controller and spectroscopy synchronization controller are used.

A brief summary of the control unit. The aim was to build a scalable platform in the form of a motherboard that can support any given number of extension modules. Each module operates a specific device. Therefore, the modules can be easily replaced, upgraded or changed depending on specific experimental goals, which require different functionalities. The designed motherboard provides power, communication and synchronization buses. New slots for additional modules can be added without any major modifications.

Three communication schemes with modules were tested and used. A brief list of advantages and disadvantages for each of the schemes can be summarized as follows:

Scheme 1. In this approach, one master controller acts as a gateway to PC and makes communication "arbitrage". Other controllers are connected to one shared line. The main advantage of this scheme is less wires, while the disadvantage is that one broken device blocks the line for another.

Scheme 2. One master controller, and slave controllers are connected to multiplexed lines. The major benefit is that a PC still "sees" all modules as one device. The master controller makes an arbitrage and provides multiplexing of the communication lines. The main disadvantage is that one broken slave controller introduces too many interruptions and occupies the line too often, which produces pauses and significantly reduces the communication speed.

Scheme 3. No master controller. Each controller directly communicates with a PC. The advantage is that it does not require software arbitrage and to use one controller. The disadvantage is that microcontrollers (of each module) has a slightly different firmware with a unique ID. This means that for each module the PC software should initiate a separate thread and, in some cases, provide multithread synchronization. At this point, this is a final, most stable version.

The importance of effective communication schemes. Consider a standard Raman scanning process using a relatively small size of e.g. 50x50x50 voxels and 1s exposure time. Then the whole Raman mapping process requires ~34 hours of a continuous system operation. In addition, the microscope stage movement between each exposure is approximately 0.3-0.5 s, which depends on step size. This adds another ~10-17 hours to the system operation time. Computer operation systems are not real-time systems, i.e. fast data transfer speed but low latency up to several hundred milliseconds. The whole cycle of a one point measurement is as follows: PC-to-camera message "start" – camera started measurement – camera finished – camera-to-PC message "Finished" – PC-to-microscope message "move" – microscope started movement – microscope finished – microscope-to-PC message "Finished". This contains four messages, which in some cases increases the experiment duration by the time that is required for microscope stage movement, which in our case is around 8-10 hours. Therefore, on the motherboard a synchronization bus with two lines – "clock" and "in use" is implemented. It helps to avoid the latency issue and efficiently save time (Fig. 6.6).

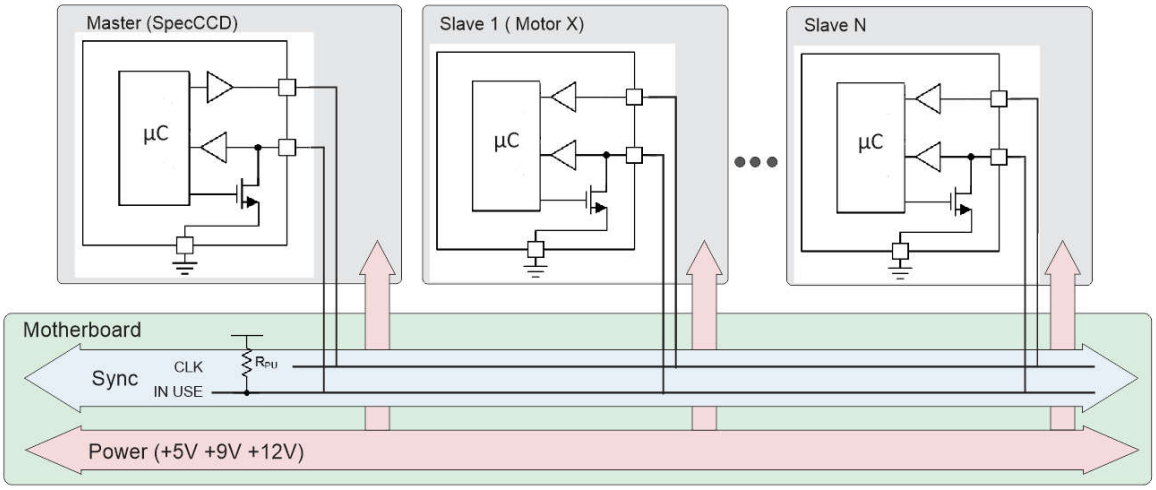

Figure 6.6: Modules interconnection in control unit.

Device designation. One device on the bus should be designated as a master, and the rest as slaves. The master is a device which drives the "clock" line (CLK). The slave's CLK pin is configured as an input

and just reads the state of this line. The line “in use” is pulled up to +3.3V. All microcontrollers are connected to this line with two pins, one is configured as an open drain output, another as an input.

Extension modules. There are three types of extension modules in the controller: (1) a stepper motor controller, (2) a microfluidic synchronization controller, and (3) an additional controller that controls all other devices from the spectroscopic part (e.g. motorized flip mirrors, spectroscopic CCD triggers, LED illumination). In the following, the last controller is referred to as a “spec” controller. The microfluidic controller does not participate in a scanning process, and therefore, it is described in the next chapter. The controllers (except the microfluidic controller) contain two working modes: a free mode and a fast scanning mode, and both support an operation with the synchronization bus.

All controllers have a first-in first-out (FIFO) command buffer with a depth for 32 commands. In the fast scanning mode after an impulse on a clock line, each controller executes next command from the buffer. The system software (the PC side) controls a number of the remaining commands and periodically loads a new portion of commands.

The “spec” controller functions as a master. Before the scanning process is initiated, the number of scans is loaded. At each scanning step it executes the following routine: (i) wait N milliseconds or generate a trigger impulse for a spectroscopic camera, and (ii) wait until a new frame is captured. After this, it generates an impulse on the clock line: all motor controllers that are connected to the synchronization bus pull down the “in use” line, and then execute the next command from its own command buffer. If the command buffer is empty, the controller keeps it in the low state until the software loads a new command. The master controller waits until all controllers finish their operations and then releases the “in use” line. In the next scanning step, this loop is repeated.

Debugging the scanning process. In order to debug the scanning and visualization processes, a specialized module was built (Fig. 6.7). The lists in the top row shows an actual state of command buffers of master and XYZ motor controllers. Below are lists of the commands for each controller, which the control software assembles before a new scan. Operator can manually add each new command, execute it one by one, run it automatically, and control the status of each controller.

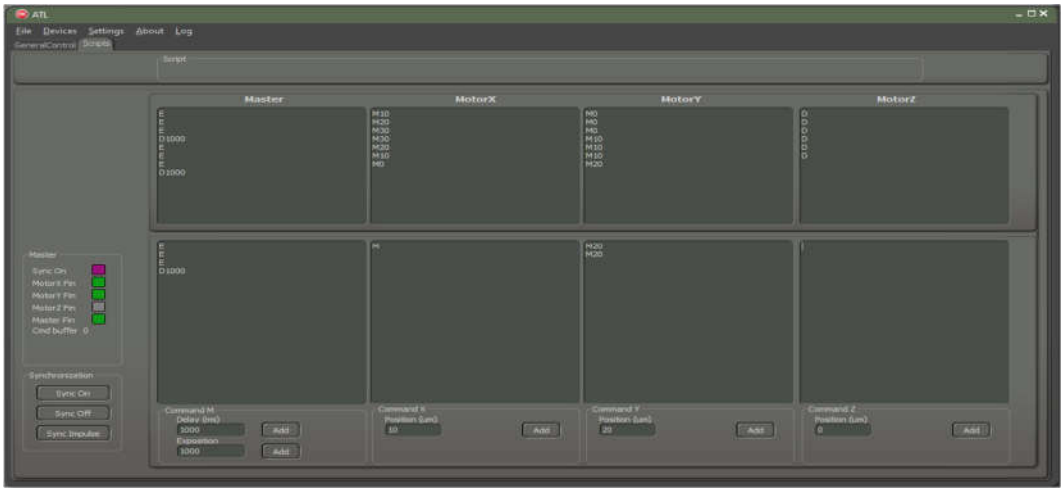

Figure 6.7: The debugging module for the fast scanning algorithm.

A universal bipolar motor controller for the THOR system. All linear and rotation stages as well as the motorized slit are operated via bipolar stepper motors. All have one or two mechanical or optical end-stops, different movement directions, and can operate at a different motor speed and current. Some

have an incremental encoder for a precise closed-loop movement control. In order to combine all these different motors, a universal bipolar motor controller was designed. The controller can handle industrial stages with any combination of parameters and sensors.

The motor controller is based on Teensy 3.2 development board [157] with MK20DX256VLH7 Cortex-M4 microcontroller, and ON Semiconductor's AMIS-30543 micro-stepping bipolar stepper motor driver [158], see Fig. 6.10. All the controller logic, communications and processing of sensor signals are situated in a microcontroller. The motor driver provides a convenient and fully programmable interface for a parameter setting and stepper motor operation. Using the serial peripheral interface (SPI), the microcontroller can control step mode, sleep, thermal and overcurrent warnings, adjust the limit for the peak-current on the fly as more/less torque or speed are required.

The controller specifications:

Motor type	Bipolar Stepper Motor
Current	132 mA to 3 A
Voltage	9-12V
Step division	full-step to 1/128-step (11 modes)
Maximum speed	35000 steps/s
Motion modes	move forward/backward, move to absolute or relative position, move with a continuous speed, acceleration and deceleration ramps, zero-position calibration
Control loop	Open loop, closed loop
Limit switches	Optocoupler, microswitch
Step loss compensation	Yes
Position encoder	Incremental quadrature encoder (TTL)
Communication interface	UART via USB
Synchronization	Input trigger, open-drain output
Motor connector	DB15F

The system frontend software. Each motorized device is controlled using a control board, which can be adjusted depending on a specific task, see Fig. 6.8. For example, a filter wheel can be rotated to previously defined positions by ticking a corresponding box. The spectrograph slit size can be defined by entering a required slit width in microns. In a simplest case, the microscope XYZ stage can be moved to a desired location by a selected number of microns.

The system backend software. On the software backend side, all motorized devices of the spectrometer are represented as unified motor controllers with identical control possibilities. However, it involves different parameters, which constitutes different functional behavior.

Communication with the controller takes place via a USB port by simulating a virtual COM port. The commands and data are sent in the form of an ASCII text for easier debugging. In the future, this format can be changed to a strict number of bytes for each command, data in a binary format, CRC-8 checksum and a better error control.

Figure 6.8: The system control board for motorized devices.

Controller setting window. In Fig. 6.9, a fine tuning of the system components and debugging is possible by loading a setting window. An operator can select a necessary motor controller and define all working parameters: current, speed and maximum speed, acceleration, select a micro-stepping mode, encoder type, forward or reverse movements. All new parameters are saved in a non-volatile flash memory of the microcontroller. The software displays a real-time stage position in step counts and encoder counts. Each position can be manually changed. An operator can move the stage by a certain number of steps relative to the current position or move it to an absolute (or "zero") position. The homing can be done by precisely moving to the left or right (if applicable) of the end-stop. Additional commands can be sent manually using command line at the bottom. If motor driver problems are encountered, an error is detected and the driver can be reset. The user can also change filter wheel predefined positions and give a description for each filter. Depending on a selected micro-stepping mode, the spectrometer slit size defined in micro-steps should also be converted to micro meters.

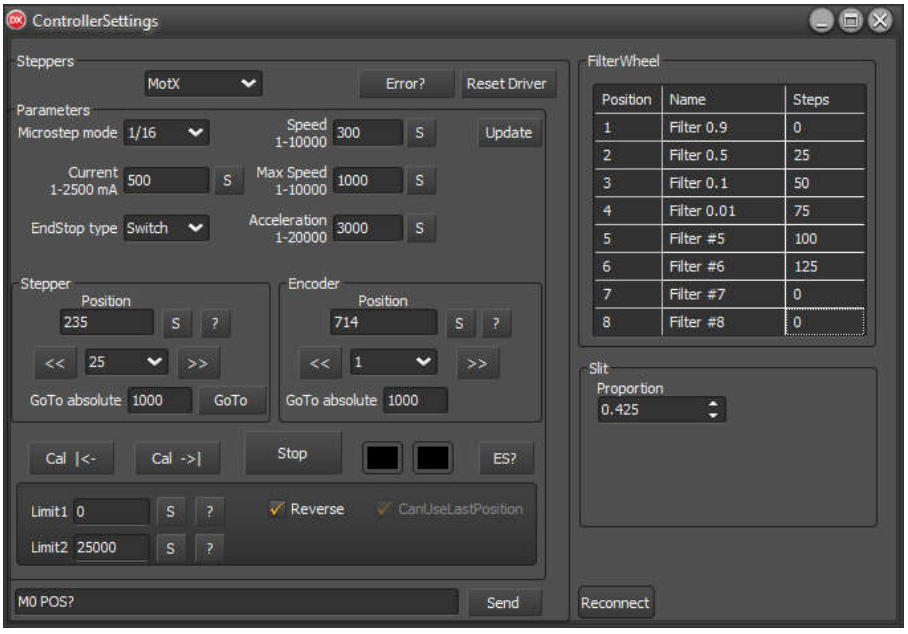

Figure 6.9: Left – the controller settings window for setting a motor controller configuration and predefined positions for a filter wheel stage; right – motorized filter wheel 8MRU-1WA (Standa)

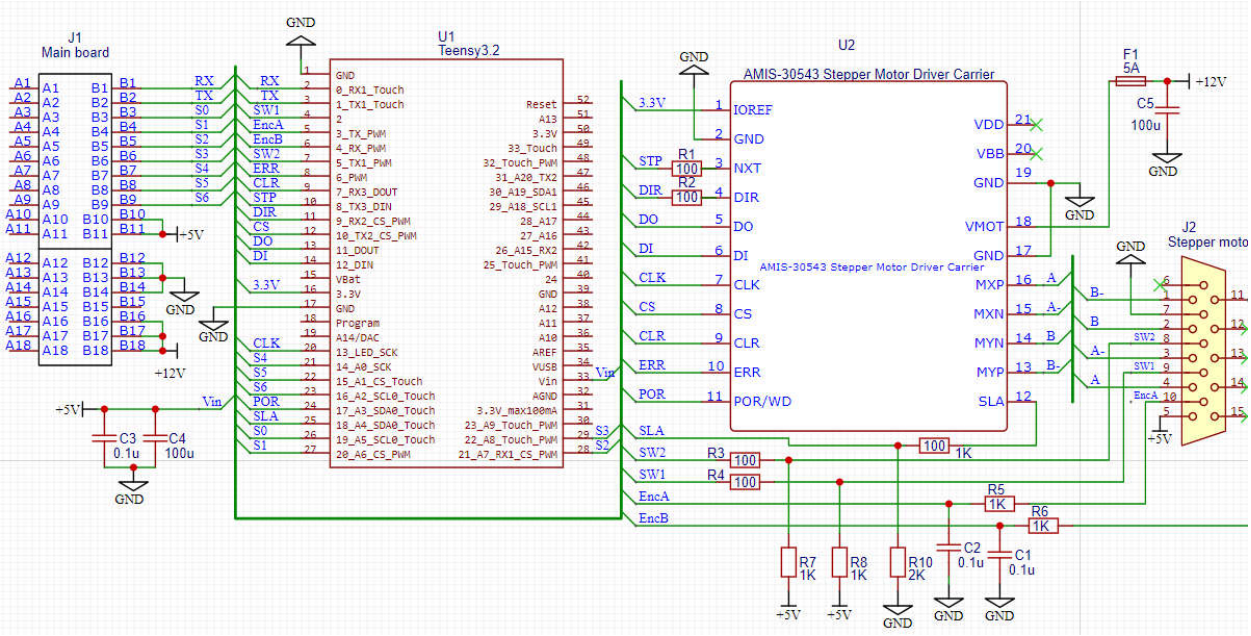

Figure 6.10: Schematic diagram of the motor controller.

"Spec" controller. It controls motorized flip mirrors, LED illumination, and in the fast scanning mode it synchronizes the spectroscopic camera-shutter operation with other controllers connected to the motherboard. There are 3 SMB (Sub Miniarture B) connectors on the Andor iDus416 spectroscopic camera: Fire, Ext Trig, Shutter, which are used for a frame exposition synchronization with external devices, and "Shutter" – is for an external shutter control, see Fig. 6.11.

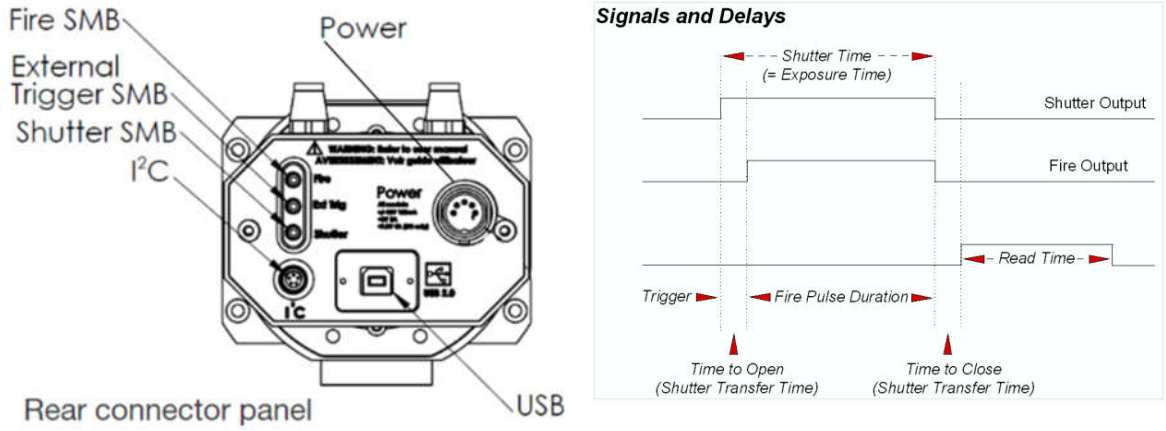

Figure 6.11: Left - external connections of Andor iDus416 camera; right – a diagram of a signal timing synchronization (datasheet information).

For the fast scanning algorithm, the sending an impulse to Trigger input is used to synchronize the start of the frame exposition, and detection of a falling signal on Fire output – for synchronization of the finish.

The controller is also based on Teensy 3.2 development board, the 74HCT244 is used as an 8-bit buffer/line driver for buffering synchronization lines of camera and shutter, as well as control motorized flip mirrors. The shutter line is bypassing the microcontroller, while signals on Trigger and

Fire lines are processed. During normal operation, the spectroscopic camera is using software triggering for operation, and these lines are out of consideration. But in a fast scanning mode a microcontroller in “spec” controller firstly generates a trigger impulse for CCD camera, and following a clock impulse for other modules of the system appears, only after falling edge of signal on Edge line, plus additional a 50ms delay of deactivation time of 87-208 C-mount Electrical Shutter (Edmund Optics).

Two LED sources can be connected to the controller. A continuous conduction mode inductive step-down converter PT4115 was selected as LED driver. It provides externally adjustable output current up to 1.2A and output power up to 30W. The PT4115 includes a power switch and an output current control circuit that uses an external resistor to set the nominal average output current. DIM input can be supplied either DC voltage or a PWM signal in wide range from 100 Hz to 20 kHz.

Schematic diagram is presented on Figure 6.12.

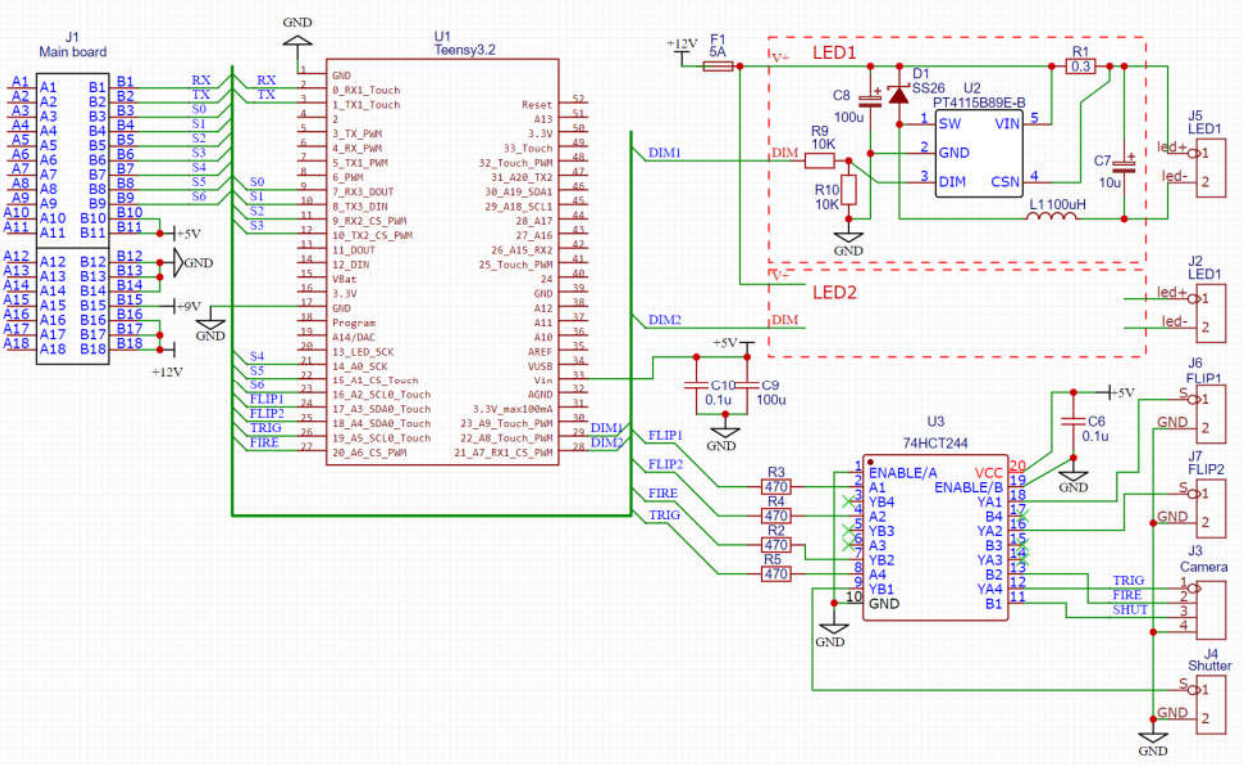

Figure 6.12: Schematic diagram of “spec” controller

6.2 Centrifugal microfluidic / autosampler unit

The task of quantitative chemical analysis is to determine the content of certain elements in the analyzed material, and the main requirement is that the results reflect the true content of these elements. Any analytical determination includes three stages: 1. sampling, 2. sample preparation, 3. measurement of the analytical signal as a function of the content of the target components in the sample. The total error in the results is equal to the sum of errors at each of its stages, and it requires minimization. Therefore, with the correct choice of the analysis method, the reliability of the results of chemical analysis largely depends on the correct sampling and preparation for analysis, since errors made at these stages lead to a distortion of the final results of chemical analysis even with the most careful implementation of this stage of the experiment. It can efficiently be done using microfluidic platforms, which can integrate all functions of analytical laboratory, including sample transport, sample pretreatment, precise dosing, mixing with reagents, separation, heating, titration and other operations in one device with a size of few centimeters. A microfluidic platform acts as a combination of functional elements that allow to implement certain actions with a sample, which can be easily combined with each other within the framework of certain technologies. By creating a different design of the fluidic channels, it is possible to implement centrifugation, filtration, valving, mixing, pneumatic pumping functional elements [159][160][161][162]. All these elements can efficiently work in an automated way without any human interference, and, due to the size, can create arrays of identical blocks, which allows to build the systems for multiple parallel measurements [163][164].

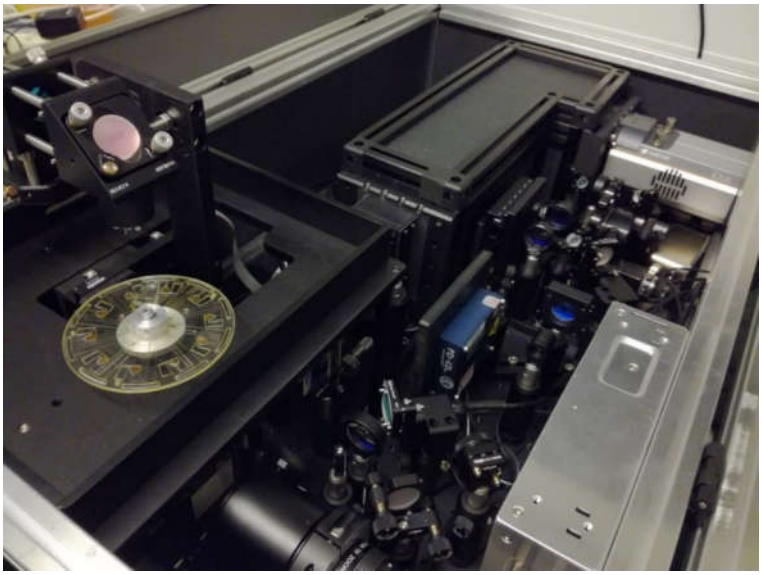

Figure 6.13: The centrifugal microfluidic disc unit implemented in the THOR system. The unit enables visualization of the sample pretreatment procedures and subsequent SERS measurements, e.g. for melamine detection in milk.

Microfluidic platforms can be classified depending on their liquid transport mechanism, i.e. capillary, force, centrifugal, electro-kinetic, and acoustical. Centrifugal platforms do not require any external pumping devices and tubing, which is important for miniaturization. Sample fluid manipulations are performed by utilizing inertial forces acting on fluids, which are promoted by rotation of the microfluidic disc platform [165]. A symmetrical disc layout allows one to operate several independent

systems (microfluidic units) that can involve different samples simultaneously. This makes it very practical for the point-of-care applications, where multiplex analysis of the sample is necessary.

The THOR system was equipped with a microfluidic lab-on-disc system (LoD) [131] [132], see Fig.6.13.

A fabrication overview of the microfluidic LoD system. An example of the LoD system in the form of a compact disc with embedded complex fluidic networks and integrated SERS substrates is shown in Fig. 6.14. The disc has a laminated structure and consists of multiple layers of laser cut polymer discs, i.e. poly(methyl metacrylate) (PMMA), injection molded polypropylene and pressure sensitive adhesive tape (PSA). The middle part contains molded patterns including chambers and channels for microfluidics, and the outer part represents a flat polymer surface suitable for SERS-based detection. Prior to assembly, spindle, liquid injection and alignment holes were cut in the polymer parts using a CO_2 laser. Next, ~4x8 mm^2 SERS chips were fixed in the sensing chamber using a PSA tape. Further, two polymer parts were integrated using a thermal bonding procedure. At a 4 kN bonding force and 1000°C temperature, the parts were pressed and left for cooling.

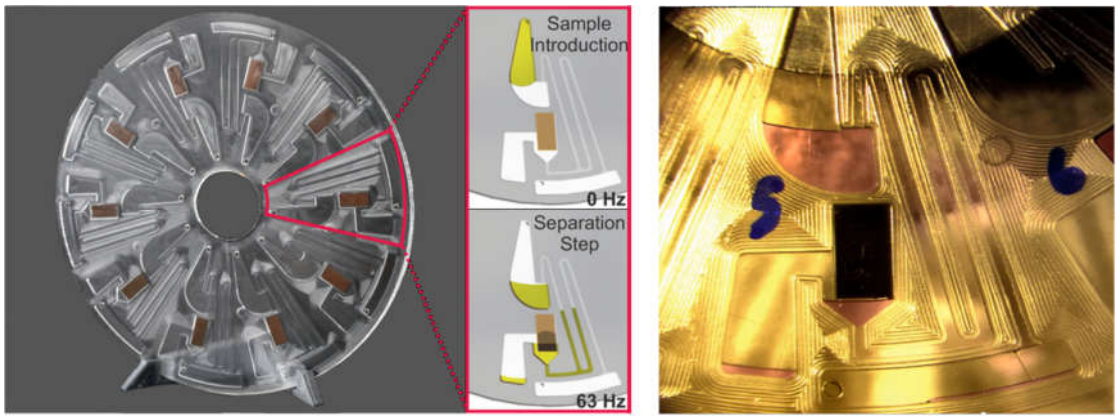

Figure 6.14: Microfluidic centrifugal disc system with integrated SERS substrates.

Software for the microfluidic module. For a real-time liquid flow monitoring at high disc rotation speeds, the liquid flow visualization unit is equipped with a synchronized strobe xenon lamp and a CCD camera. The microfluidic disc module and associated electronics are controlled using a custom-made software module, see the interface in Fig. 6.15. The microfluidic software module provides control of all key parameters: speed, acceleration, deceleration, rotation direction (important for shaking and mixing of the components), and timing cycles of the disc in order to automate sample pretreatment procedures. The software can be used to capture a picture or a video during the sample pretreatment process. The image acquisition is synchronized with the disc rotation frequency, i.e. the disc appears stationary while e.g. sample introduction, separation, and transport into the sensing chamber can be clearly observed. There is also a possibility to rotate the disc at a defined angle and use it as an autosampler in series of automated measurements. In this case, samples are located in specific positions at the same distance from the center of the disc.

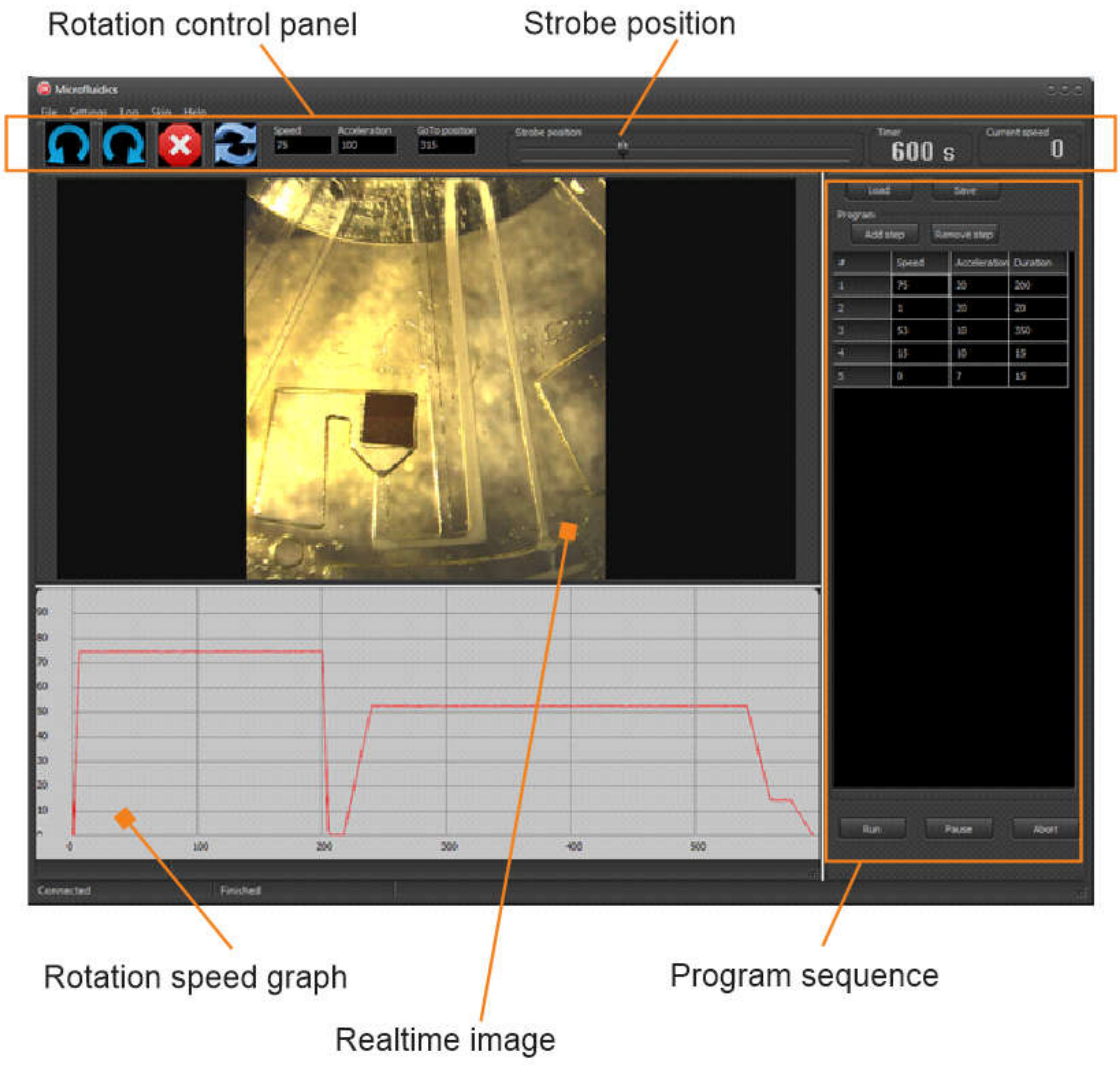

Figure 6.15: Software control for the centrifugal microfluidic disc module. The interface shows sample pretreatment steps for melamine detection in milk.

The main software window contains the following:

- Toolbox with basic disc rotation controls and a strobe light position.
- A real time image from a CCD camera.
- A dynamic speed graph with 1s update intervals.
- A panel for user-defined operation sequences.

The sample pretreatment procedure for the wicking based filtration of milk and subsequent detection of melamine using the SERS technique involves 5 steps:

1. *Centrifugation*. 37 µl of sample was injected into the loading chamber of the disc. This is followed by disc centrifugation at 75 rps (revolutions per second) for 200 seconds, acceleration - 20 rps. At this step, the milk solution is kept in the loading chamber and separated into two physical parts: (i) transparent liquid at the top and (ii) white-solid precipitate at the bottom.

2. *Transfer the sample to the sensing chamber*. The disc was brought to a stationary condition for 20 s. During this time, the transparent liquid in the loading chamber is soaked up towards the sensing chamber. Speed - 0 rps, duration – 20 s, acceleartion – 20 rps.
3. *The sample is intriduced onto the SERS substrate*. By accelerating the disc to 53 rps, the transparent aprt of the sample is relocated to the detecting chamber via capillary channels immersing the SERS chip. At this step, the SERS-active Au NP surface soaks the liquid where the NP-based nanofiltration takes place. After 350 s, the disc is brought to a stationary position. Speed - 53 rps, duration – 350 s, acceleartion – 10 rps.
4. *Transfer the sample to the waste chamber*. Consequently, the liquid in the sensing chamber is transferred back to the loading and waste chambers. The SERS chip is left to dry for subsequent SERS analysis. Speed - 25 rps, duration – 15 s, acceleartion – 10 rps.
5. *Finalization*. Speed - 0 rps, duration – 15 s, acceleartion – 7 rps.

The microfluidic disc module: a detailed description. A schematic representation of the integrated devices is shown in Fig. 6.16.

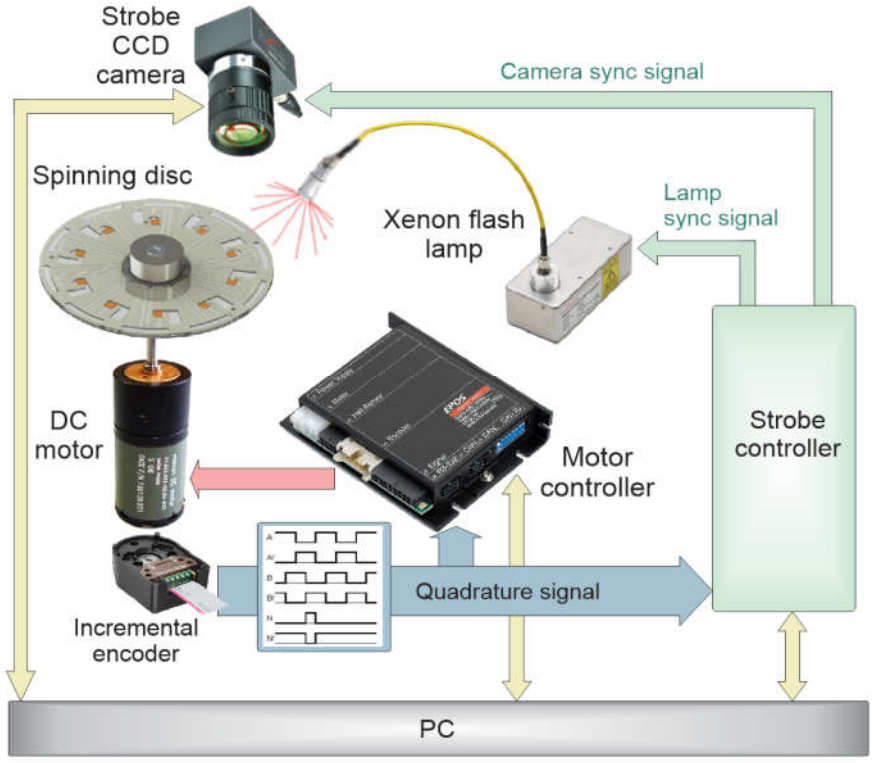

Figure 6.16: A schematic picture of the microfluidic disc module: devices, connections and device communication pathways.

Motion control. An industrial DC motor Maxon 320409 (7750rpm, 107mNm, 90W) with a specialized controller EPOS2 5/50 is utilized. For a precise positioning and speed control, the motor is integrated using a 3-channel incremental encoder. The company provides a software development kit (SDK) for the C++/LabVIEW/.Net custom control software development with a large set of functions for Microsoft Windows / Linux operating systems [141].

From the EPOS command library datasheet, the DC motor can operate in different working modes. The most relevant modes for our work:

Homing Mode (HM)

Profile Position Mode (PPM)

Profile Velocity Mode (PVM)

The HM mode allows one to calibrate the “zero” position of the encoder and fix the microfluidic disc on the motor shaft holder. In the PPM mode, the disc can be rotated to a defined position. Finally, the PVM mode controls all centrifugation parameters that are required for the experiment – speed, acceleration, and deceleration. During the sample pretreatment process development, all process parameters and operation modes can be accessed using the settings menu, see Fig. 6.17.

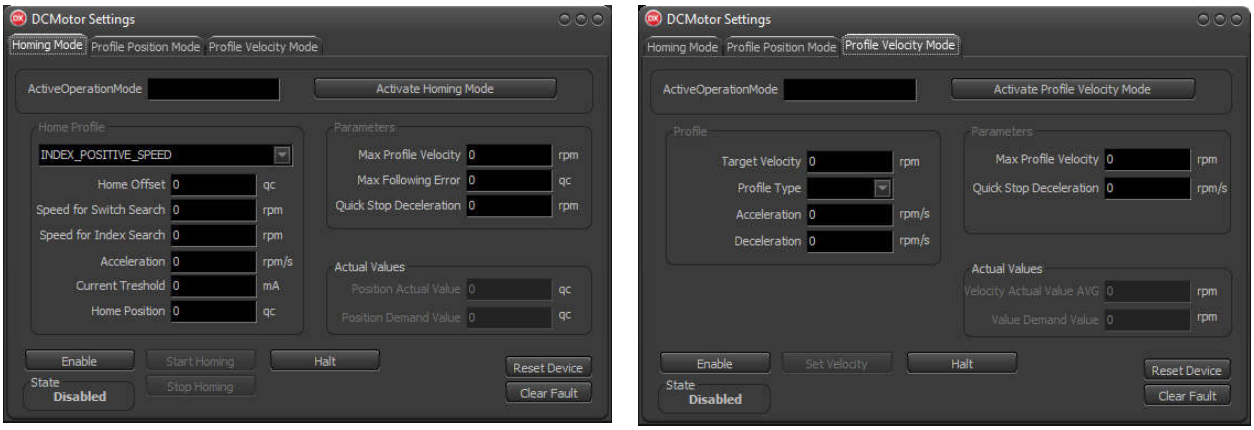

Figure 6.17: Settings of DC motor. Left – homing mode; right – profile velocity mode.

Imaging a fluid flow in the microfluidic disc. The imaging part of the microfluidic module consists of a CMOS camera (PL-722CU-T, supplied by Pixelink), lens (MVL8M23, Thorlabs), and a stroboscopic lamp (L9455-11, Hamamatsu). In order to synchronize the camera, flash lamp and the motor rotation frequency a designated controller was built. It is connected in-parallel to the encoder – controller signal bus and forms two triggering impulses: first – for the strobe lamp to illuminate the required region on the microfluidic disc and second - for the camera to capture an image. In such way a clear still image was captured each time the disc made a full revolution.

The rotary encoder has three differential lines: A, B, I, and provides 1000 impulses per revolution, see Fig. 6.18. Lines A and B form even quadrature impulses throughout the full turn. The synchronization controller is also based on Teensy 3.2 development board, like the other controllers. It has two 2-channel quadrature decoder/general purpose timers, and one is used for counting. Line I provides one pulse per revolution, and is used as a “0” reference point for the timer reset. Two outputs for the camera and flash lamp synchronization can be separately configured using software to provide synchronized impulses after reaching a certain counter value.

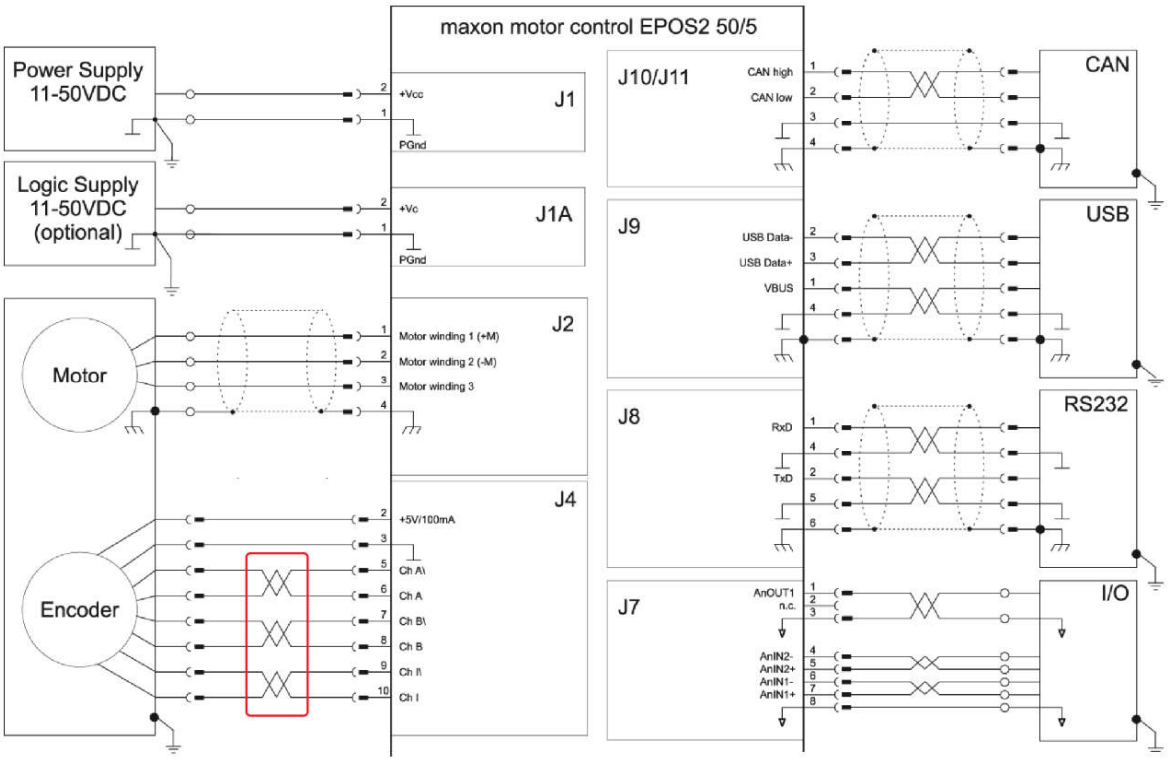

Figure 6.18: Connection lines for the DC motor and the encoder.

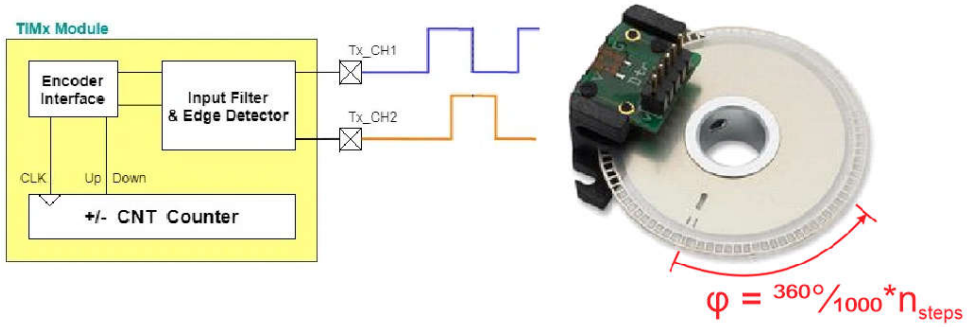

Figure 6.19: Formation of triggering impulses using the motor encoder.

PL-D722CU-T CMOS camera has external hardware trigger input and high frame rate up to 87 fps, which can be good for fast processes analysis. Global shutter allows all pixels have an exposure start and stop simultaneously, which corresponds to a real snapshot. All motion (as long as it is slower than the shutter) “freezes” in the image.

PixeLINK SDK allows one to work with the camera at a low level. By enabling triggering and changing parameters in the function PxLSetFeature(hCamera, FEATURE_TRIGGER, …), the current camera can operate in an automatic mode. It mainly uses three triggering types:

- A free running triggering. The camera acquires images continuously.
- Software triggering. The function PxLGetNextFrame() can be called, which triggers the camera to capture an image.

- Hardware triggering. By activating the trigger input of the machine vision connector, the camera acquires an image. This option was utilized in all experimental work.

Hardware triggering. The advantage of this option is that it does not depend on the code execution state. It operates as a master device and drives execution of other functions where the frame data is handled. At a high frame rate, the code execution speed is critical, especially for forming AVI video files using high-resolution images.

The fabricated synchronization module is an extension card, which was added to the main controller unit board, see a schematic diagram in Figure 6.20. There are three essential parts: a quadruple differential line receiver for digital data transmission AM26LS32AC, a microcontroller and a quad buffer/line driver 74HCT125.

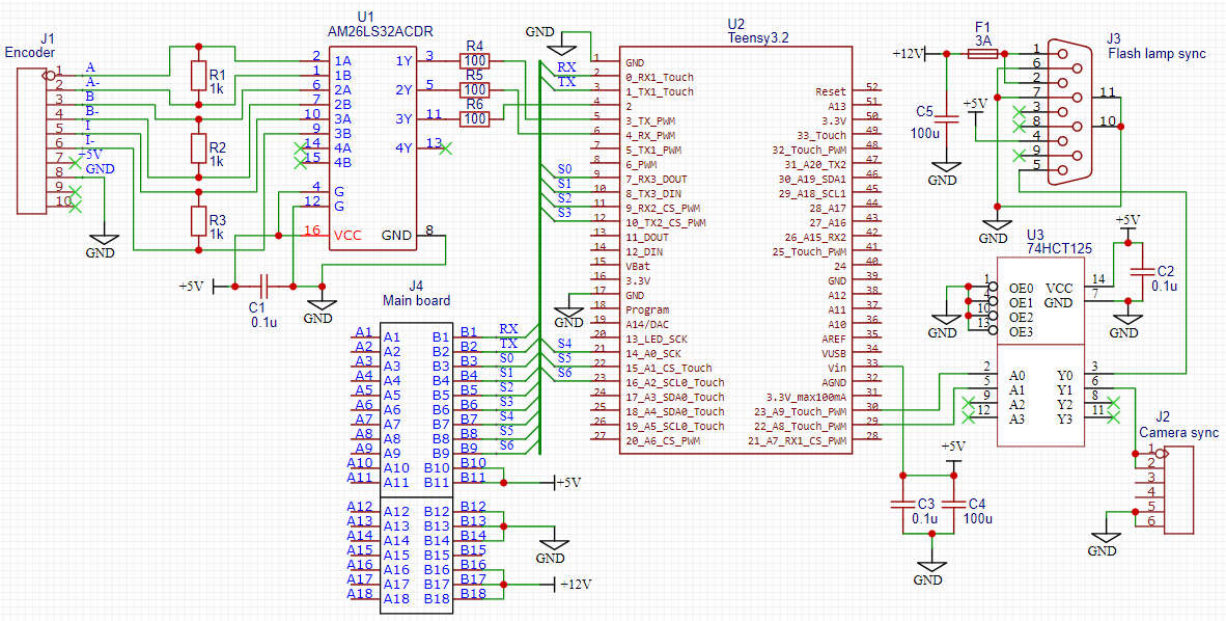

Figure 6.20: Schematic diagram of the strobe controller

6.3 Imaging and navigation

For a convenient sample handling, a flexible sample navigation system was designed and built. In the so-called exploring mode, it allows one to quickly explore a sample surface outside the field of view. New image regions can be displayed by simply dragging the mouse pointer over an imaging window. All standard imaging microscopes, with a possible exception of e.g. expensive Zeiss or Leica systems, produce only an actual image from the field of view of a visible camera. The sample imaging approach implemented in the THOR system allows one to save all previously explored regions in the form of image sections (tiles) with unique IDs and coordinates, and then project these regions on a global sample map. It is also possible to return to any previously explored region and perform spectroscopic analysis.

After an initial microscope XYZ-stage calibration, the system obtains global coordinates of the current microscope position from the stage encoders. The stages produce a 25x25mm scanning range in the XY plane, and a 25mm range in the Z dimension. Depending on the magnification (e.g. 5x, 10x, 20x,

etc.), each objective provides a different field of view, which needs to be pre-calibrated. After this, all image sections can be scaled and positioned correctly.

System combines the both sides of a map processing: collection part, where the new tiles are forming from camera images with respect to the global microscope position, and visualization part with the forming a map of a visible region with the proper scaling.

The THOR image navigation system has a global zoom of x1/2, x1/4, x1/8, etc. as well. A screen can fit 1, 4, 16, 64, etc. tiles, which are located side by side (negative zoom). An image from a visible camera is always centered and placed on a top layer, and shows a real-time view of the sample surface. The tiles of all previously explored regions are displayed on a background layer. A positive zoom e.g. x2, x4 allows one to only see a central (zoomed) part of the real-time image, see an example in Fig.6.21.

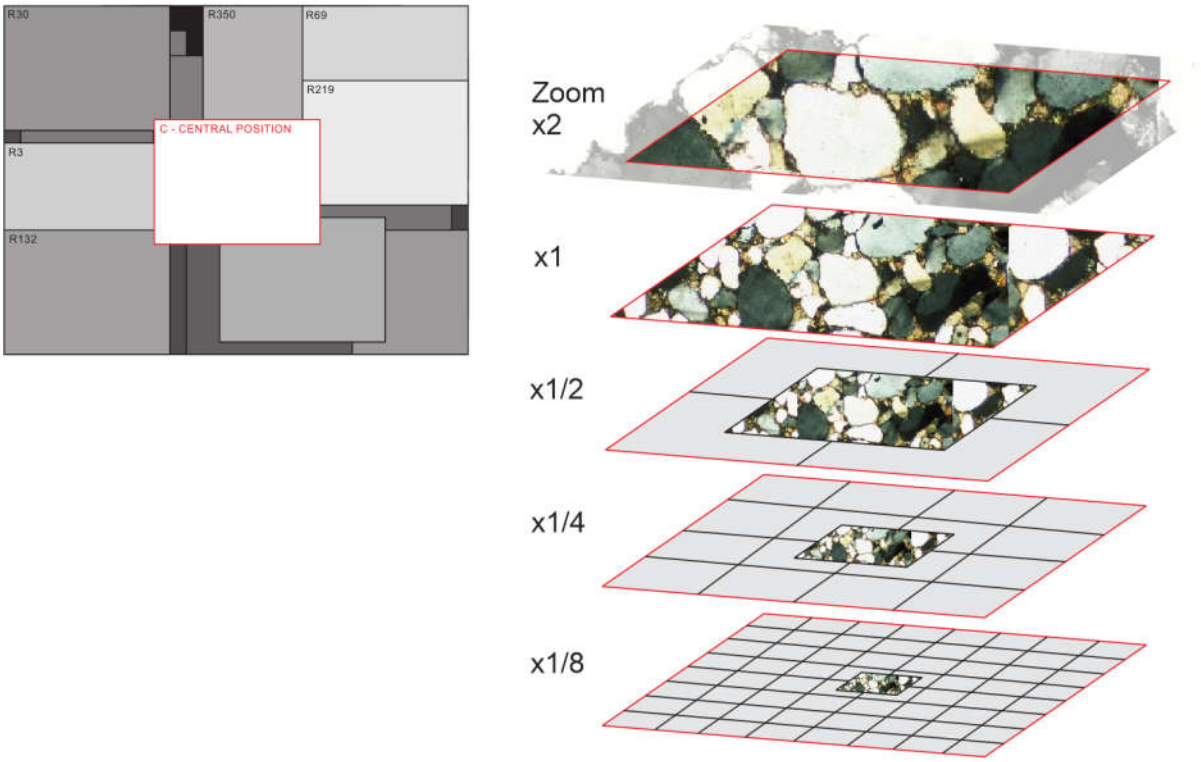

Figure 6.21: Left - Representing the entire surface image using separate image sections (tiles); right – the tile scaling and projection on the image canvas in the navigation window.

The image navigation system: details. Unlike most global imaging systems (GIS), which save the tiles of the map for all discrete zoom levels and give to user only necessary sets, our system works only with the most detailed tiles and rescale them on a map each time for any zoom. It is highly optimized for fast operation by using different scrolling and zooming options. Images from the central region are cached in one big layer, which is redrawn or rescaled after each operation. In the case of a negative zoom, empty regions are filled using corresponding image sections (if any) from the local temporary files location. All captured image sections are saved in a temporary folder as PNG images with specific filenames. The filename information and global coordinates of top left and bottom right corners is located in the list of all captured tiles, which corresponds to the current sample.

In the case of positive zoom, first, the cached layer is rescaled. This quickly yields a proper low-resolution image. Afterwards, all regions are updated to the resolution, which is necessary for the current zoom level.

If a sample surface is explored without utilizing the zoom option, the cached layer is moved and empty regions are filled as previously described. At each new location, a new image section is captured and a new descriptive information is added. This way the sample surface view can be expanded. Each image section (tile) has a global coordinate, which is fixed to an absolute position of the stage. The sample movement and an image section drawing is performed using the local window coordinates, which are converted to global coordinates. If an image needs to be redrawn, the process is reversed. The image coordinate calculation and drawing algorithms are flexible and support any rescaling of the working window.

Once the XY-stage and camera operation is synchronized, it allows one to stitch neighboring data sets and makes possible to have a larger field of view at high magnification. It is also possible to automatically scan a selected region and acquire a high-resolution image of up to several hundred megapixels.

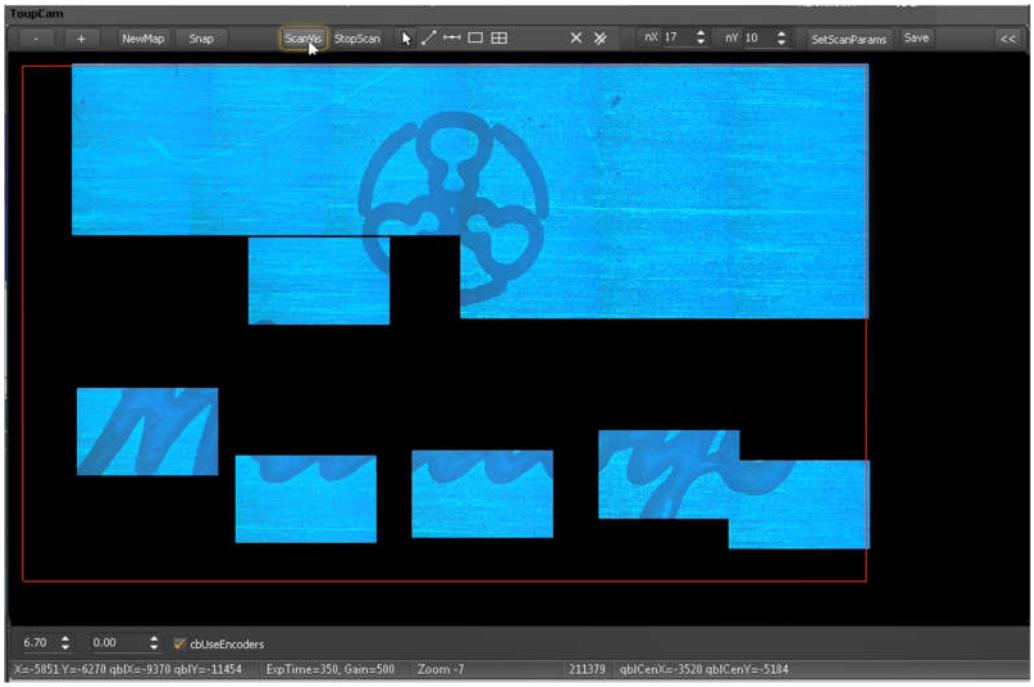

Figure 6.22: Image sections (tiles) can be acquired either sequentially or at selected locations. The tiles are then used to produce a large sample surface image. Each tile represents a full field of view of a 10X magnification objective.

The image navigation software includes a set of basic options e.g. a scale bar tool, different drawing possibilities, etc., see an example in Figure 6.23. Scale bars are defined via a selected objective magnification lens and are adjusted automatically if the image is rescaled. By using a scanning grid tool, the user can select an area for Raman mapping. Basic scanning parameters: (1) a number of steps in each direction and (2) a step size. These parameters are sent to the scanning module. During the mapping procedure, the Raman signal is acquired from each of the grid-defined locations (crosses) and a Raman map can be produced, see the bottom of Figure 6.23.

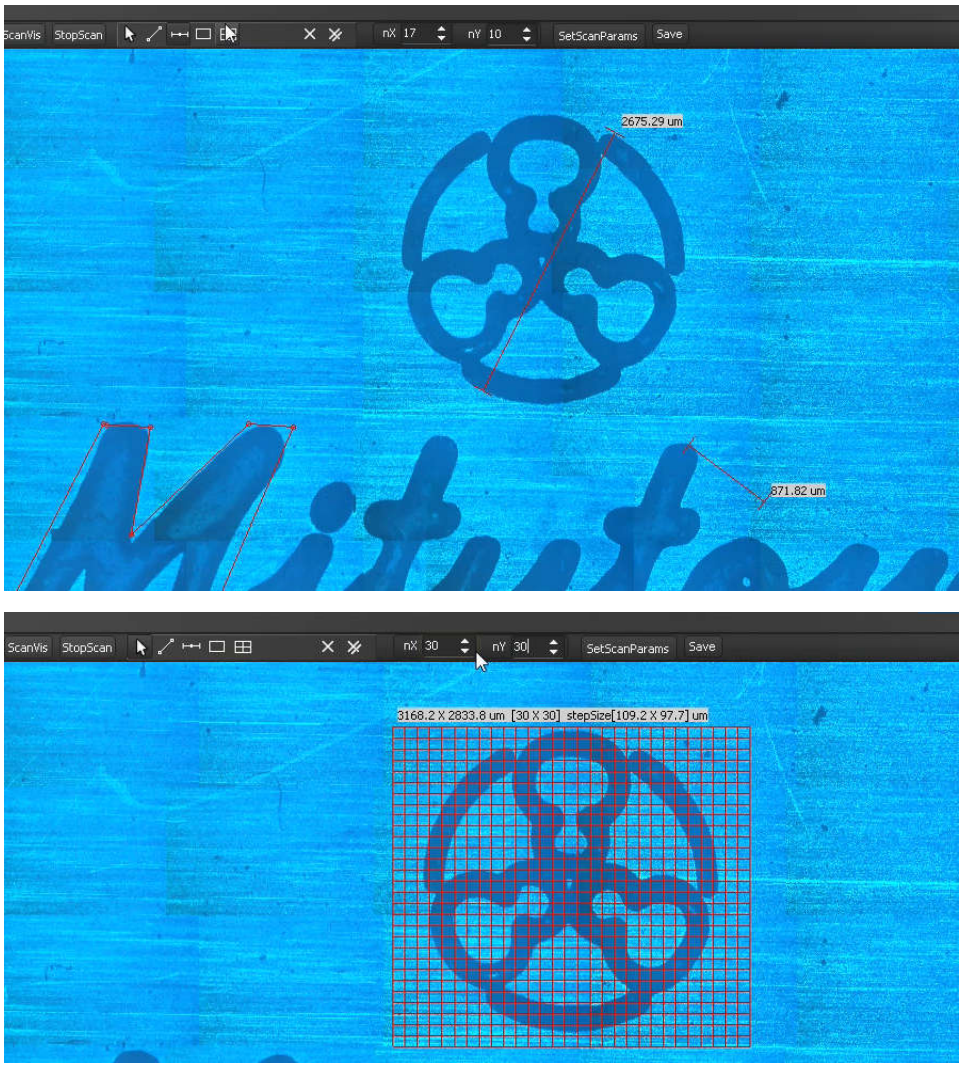

Figure 6.23: Top – an example of using scale bars and drawing tools; bottom – the scanning grid.

6.4 Data acquisition and visualization

As a detector, a spectroscopic CCD camera Andor iDus416 is used. The main properties are: (1) a back-illuminated CCD, deep-depletion with anti-fringing, (2) a low dark current sensor with 2000 x 256 active pixels 15 x 15 µm in size, (3) cooling temperature down to -70°C, (4) peak QE of up to 95% and (5) optimized to work in the near-infrared spectral range.

A full control of the camera was integrated into a custom-built software using Andor SDK. Most of the device controls are placed on separate floating panels, which can be rearranged depending on the operator preferences and needs. All positions can be saved as a named layout.

The most frequently used controls and features of iDus416 are placed on one wide panel. The user can control the following: detector temperature and an operation of the cooling fan, shutter working mode: auto, always open, always closed; readout modes: full resolution image, full vertical binning (FVB), single track, multitrack; different types of hardware and software binning modes; readout

modes: single, accumulate, kinetic, run till abort; readout and digitizing parameters: readout rates and preamplifier gain. See a standard working window in Fig.6.24.

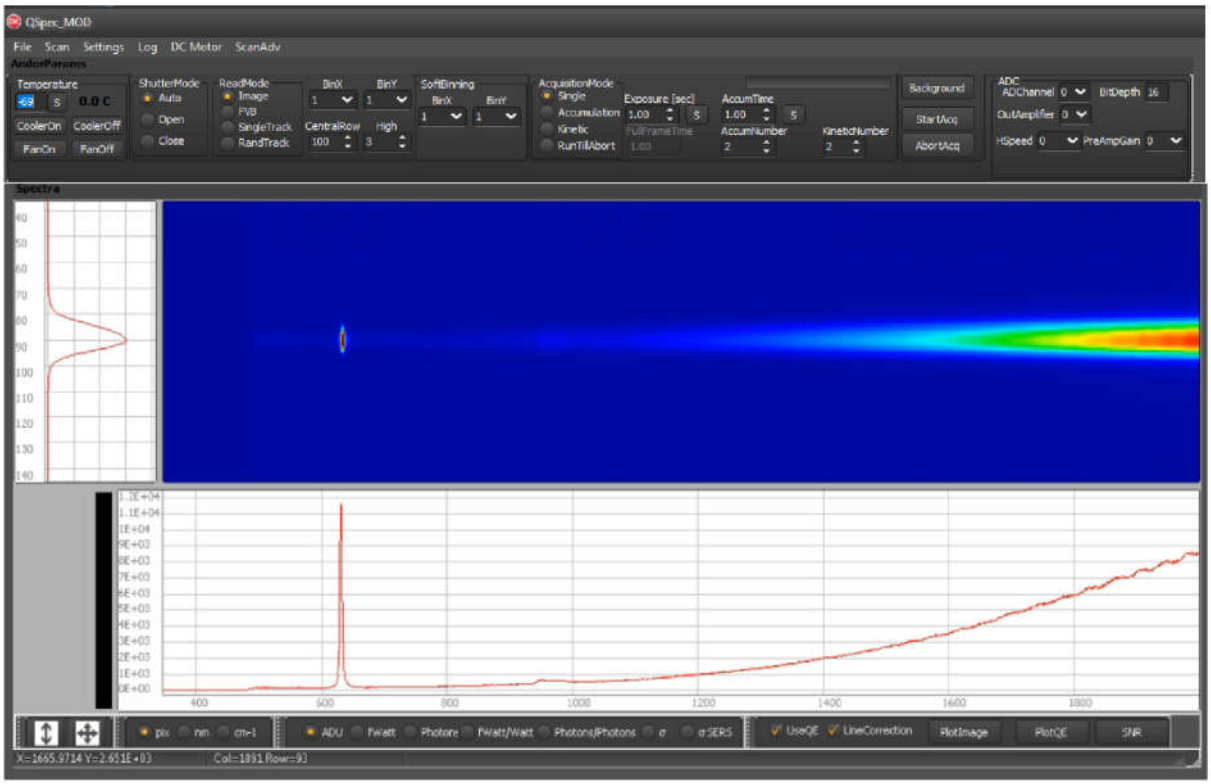

Figure 6.24: The camera control and data visualization windows.

This system uses four readout modes for reading data from a CCD camera (Fig. 6.25):

- A full resolution image allows to get the signal from each single pixel, which gives the full picture of the light distribution on the CCD matrix.
- At full vertical binning mode the charges of the pixels from each column are combined (or binned). In such way the CCD chip is using as a linear sensor with one signal value for each column.
- The random multi-track mode allows to define several horizontal tracks on the CCD area and separately obtain data from each of them. A user can define height and offset of each track in a way to match the light pattern produced on the CCD chip by a Wollaston Analyzer Unit.
- The single-track mode, as a very popular variation of a random multi-track mode, is separated to an additional category, and allows one to get a signal from closely positioned rows. This is useful for pseudo-confocal measurements.

A resulting image intensities can be represented in grayscale or different color palettes.

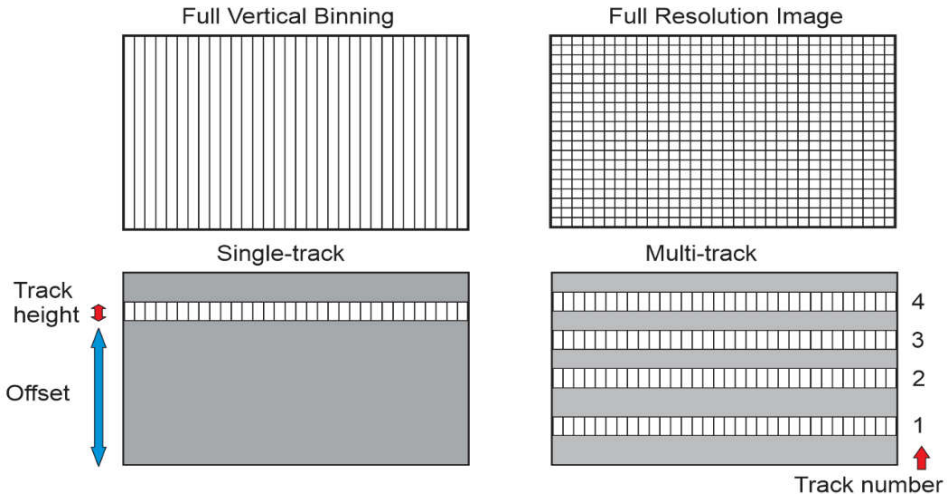

Figure 6.25: Different binning patterns.

In order to provide a convenient way for spectroscopic data monitoring and analysis, a flexible module to view and manipulate spectra was created. The center image in Fig.6.27 shows a signal intensity as acquired by the CCD matrix. By clicking any pixel in the image, two cross sections on the left side and the bottom are shown. The vertical one shows the signal distribution across rows of the selected column, and the horizontal one displays an actual Raman spectrum from a selected column.

In the multi-track mode, it is possible to select a number of tracks, define each offset and track height, and select a desired color. For example, the laser line-focus scanning mode utilizes data from an entire image, since each row contains data from the next point (due to the laser line illumination).

By dragging and zooming the left and bottom graphs in vertical and horizontal directions, it is possible in an intuitive way to change the contrast level of the central image and observe it at a detailed level. The x-axis can be shown as CCD pixels, nanometers, or inverse centimeters. Intensity of the Raman spectrum can be "corrected" by taking into account the quantum efficiency of the CCD camera. Also, in the laser line scanning mode, the intensity of each row can be corrected by measuring the non-homogeneous laser intensity distribution along the line. The laser control is integrated into the software and allows one to operate the laser at a constant power, constant current modes, monitor output power, laser diode bias, and temperature (Fig.6.26).

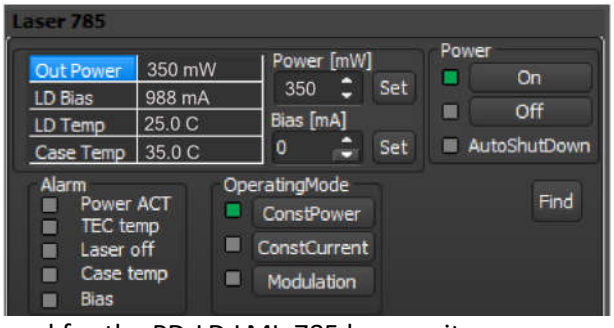

Figure 6.26: A control panel for the PD-LD LML-785 laser unit.

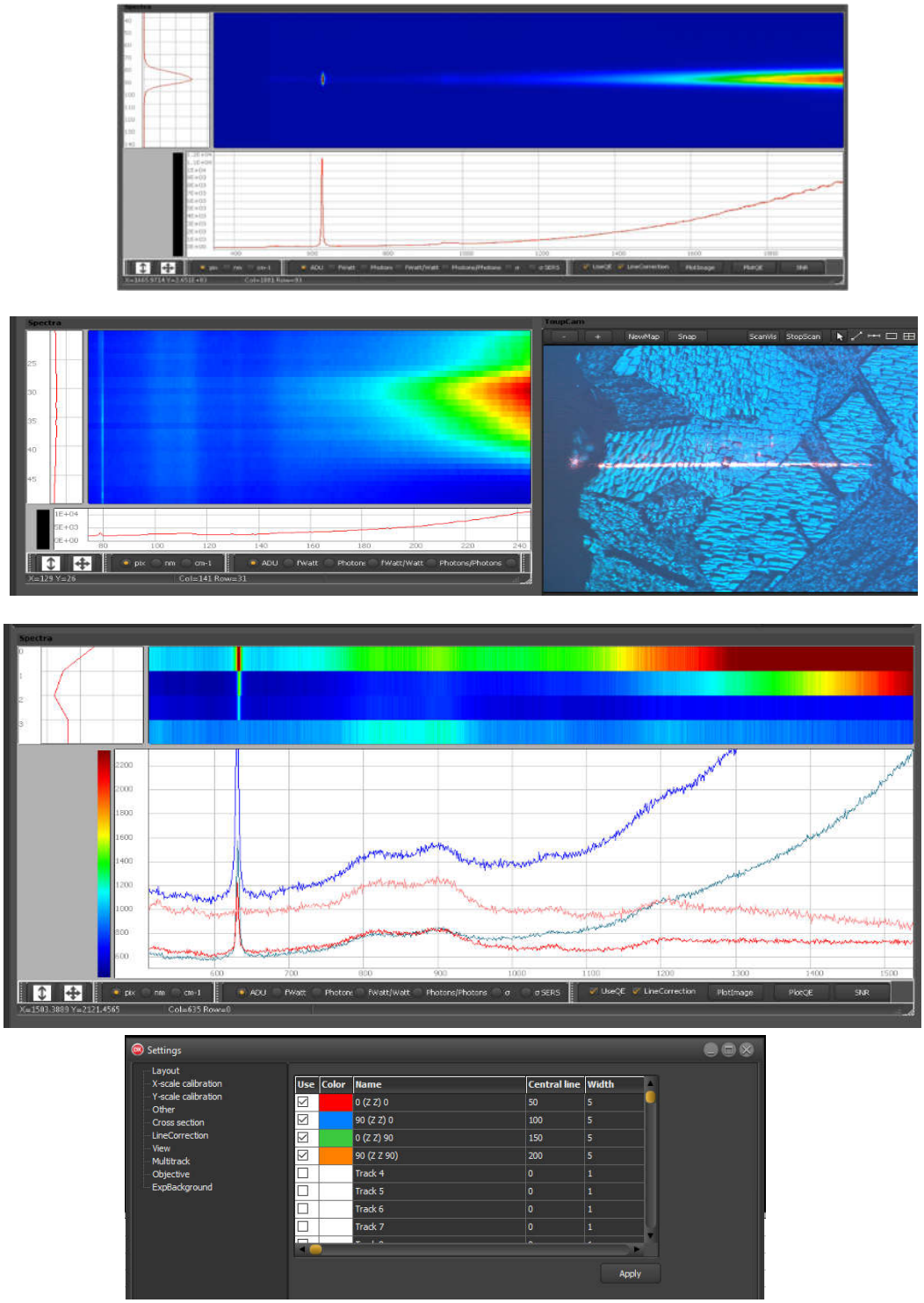

Figure 6.27: An example of the custom-built software for working with different binning patterns data visualization.

3D Raman mapping. Large varieties of Raman spectroscopy based applications require knowledge about material 3D distribution, e.g. to analyze different drug mixtures in loaded microcontainers. The custom-built Raman system described in this work provides a big variety of scanning possibilities. The implemented advanced scanning algorithm uses a recursive method for multidimensional scanning,

which at least theoretically allows one to increase the number of dimensions to infinity, see an example in Figure 6.28. In practice, the developed method never utilized more than five dimensions: wavelength, X, Y, Z and polarization.

Scanning dimensions:

- Wavelength
- X
- Y
- Z
- Rotation
- Polarization
- Time
- Laser power
- Other ….

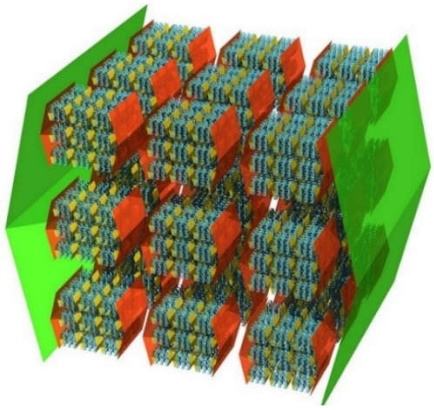

Figure 6.28: The image illustrates a hyper-dimensional scanning array.

The scanning module allows one to create an arbitrary sequence of scanning parameters: volumetric X, Y, Z scanning, sample rotation, kinetic measurements, etc. It is not a problem to connect an additional device, for example, Linkam heating stage and use its temperature as a new parameter for the scanner. For some parameters, e.g. in the case of X-Y scanning, it makes sense to utilize a "ZigZag" option, which reduces the scanning time, see an example in Fig. 6.29.

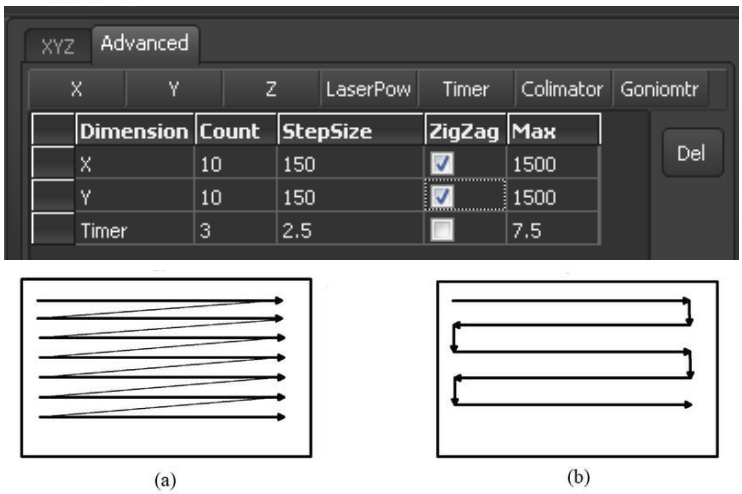

Figure 6.29: Top – an example of a standard scanning configuration; bottom – normal (a) and "ZigZag" (b) scanning options.

In order to tackle complex Raman mapping application, a Multidimensional Viewer was created. It is designed to work as a standalone application for data post processing. It can be easily integrated into the scanner module for data visualization in real-time. It is optimized for a fast and safe multi-thread operation. A user can select a number of windows to visualize a set of 2D cross sections that are required for sample analysis, see an example in Fig.6.30.

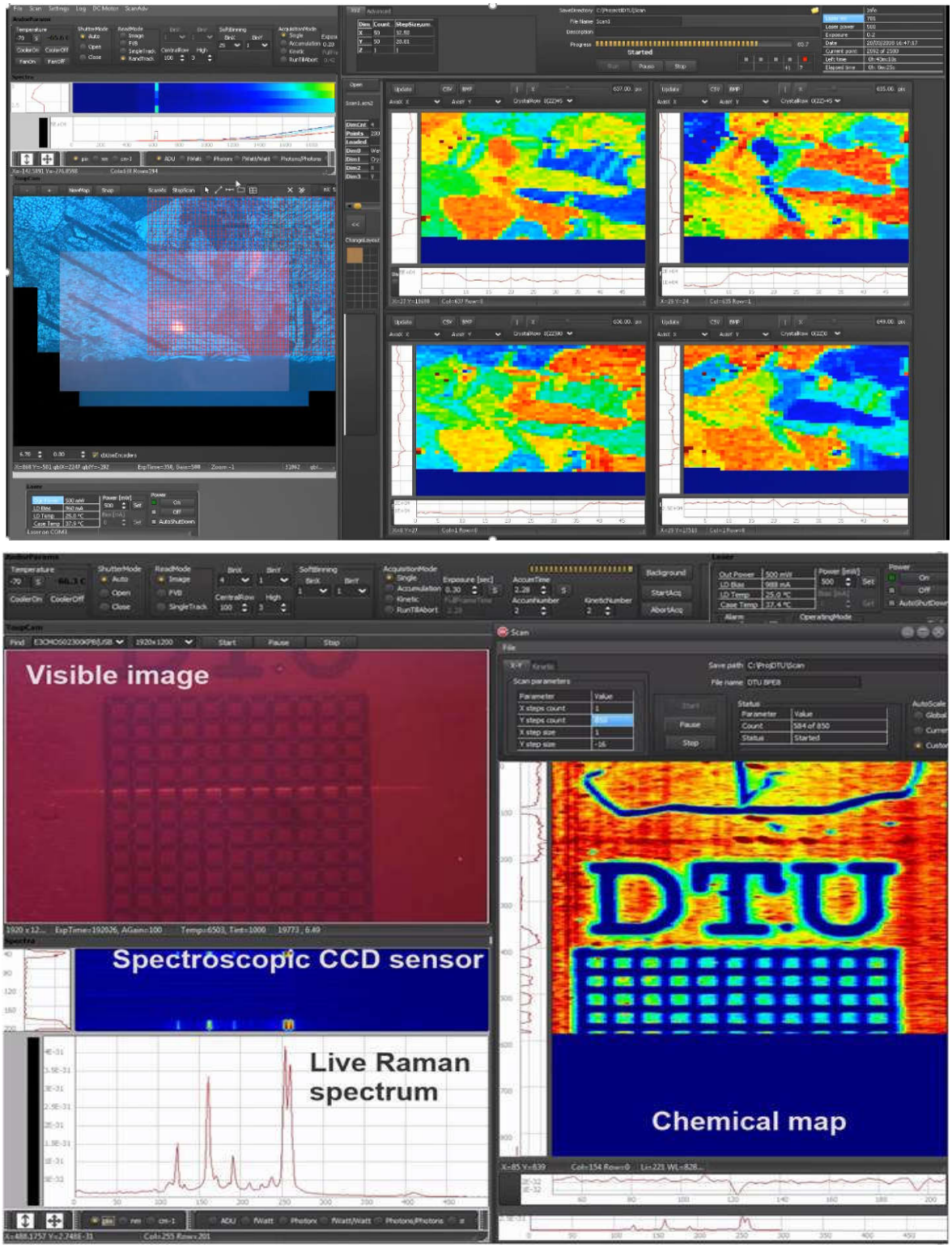

Figure 6.30: Top – A 4-channel scanning of polycrystalline Si. Each view shows a XY cross section for a different light polarization value and the 520 cm-1 wavelength peak position; bottom – line scanning of the laser engraved SERS chip with deposited BPE (trans-1,2-bis(4-pyridyl)ethylene. The BPE concentration is 10 µM.

The user can select any layout of views for data analysis: 1x1, 2x1, … 4x3, 4x4… by just selecting a necessary configuration of cells in a table, see Fig.6.31.

Each view is an independent component, which can extract data from the scanned hyper-array and visualize it. It consists of an intensity map with vertical and horizontal cross section graphs of a selected column and row on the map, a Raman spectrum at a selected point, and an instrumental toolbar. Using the toolbar a user can select two dimensions for the main axes for the intensity map visualization. In the case of other dimensions, a user needs to select a fixed point on each of the dimensions. In the case of the wavelength dimension, it is possible to select a necessary point by clicking the interesting peak on the Raman spectrum graph.

The toolbar can be used to save intensity maps as BMP images or CSV files. In addition, it is possible to export the data using the most common combinations of dimensions as CSV files for further analysis using commercial programs e.g. Matlab. The dimension combinations e.g. dim0+dim1+dim2, dim1+dim2+dim3, dim0+dim1+dim2+dim3 correspond to wavelength (W) – X-Y, X-Y-Z, W-X-Y-Z. If the post data analysis is required, for example, chemical decomposition, new hyper-arrays can be created displaying results of the analysis. Switching between the initial RAW and internal hyper-array format is also implemented.

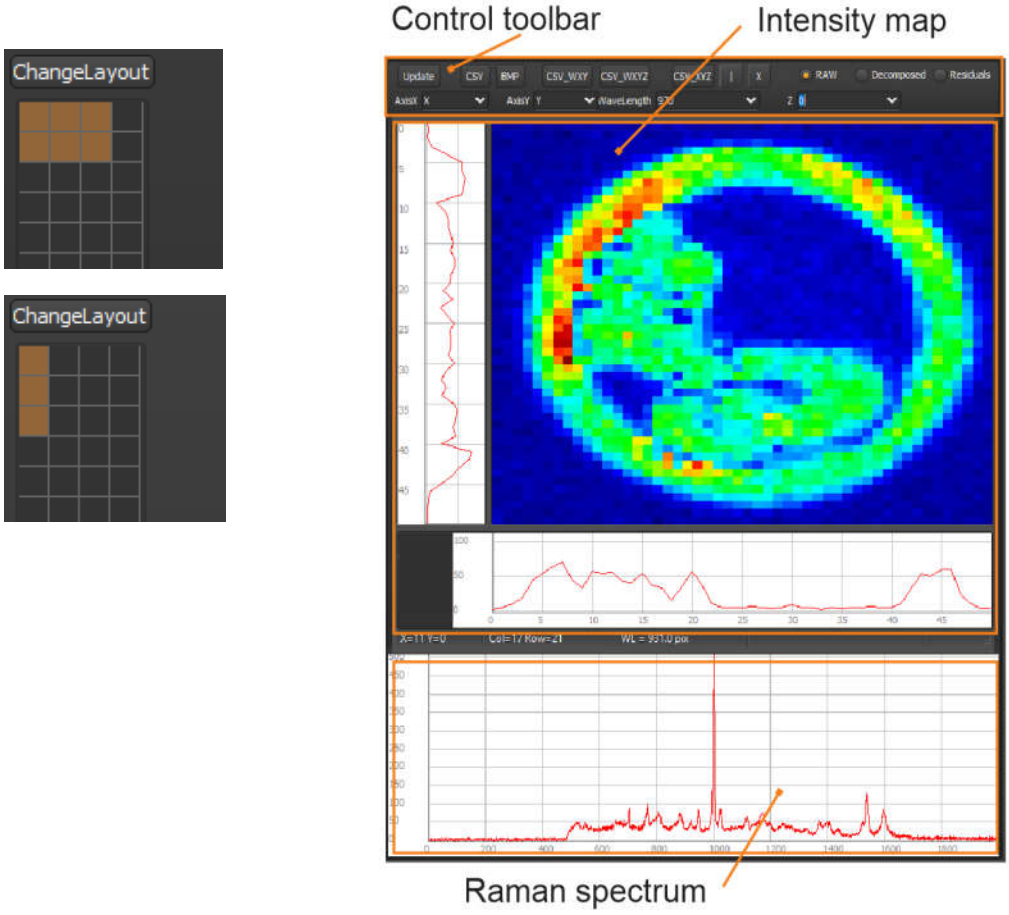

Figure 6.31: Left – a layout of the selection panel; right – a cross section of a drug-loaded microcontainer.

The viewer includes a few integrated routines for fast data preprocessing and analysis. All Raman spectra from the acquired Raman map can be smoothed using the Savitzky-Golay filter with a specified polynomial order and a frame length [166]. In addition, Raman spectra can be background corrected using the rolling-circle filter [167], see Figure 6.32.

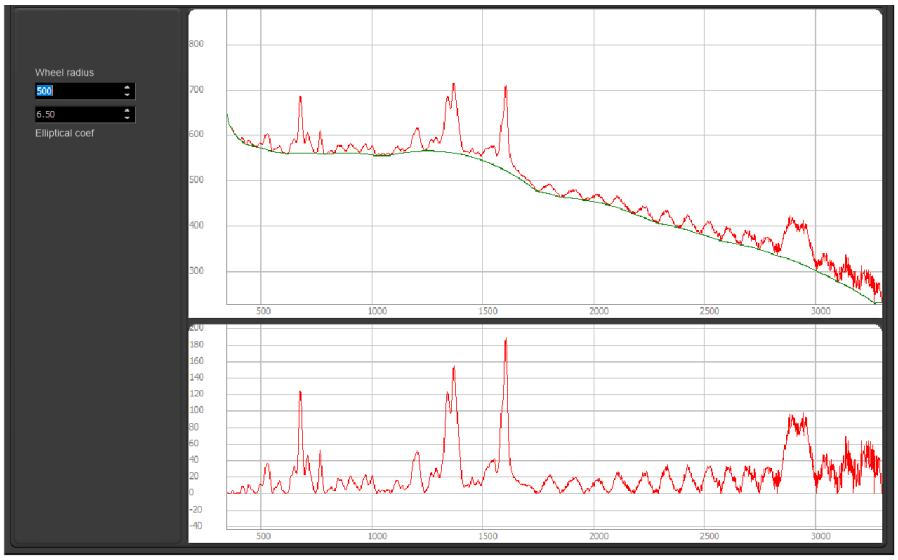

Figure 6.32: The example illustrates background correction using the rolling-circle filter.

In addition, the viewer includes a non-negative least square (NNLS) analysis system for chemical decomposition of complex, multicomponent samples [168][85]. In many cases, where different components of the sample do not chemically react, it is possible to completely separate their contribution to the total recorded Raman spectrum by using specialized mathematical algorithms. As a first step, it is often reasonable to estimate a number of components in a sample and visualize the component distribution. In the decomposition library window, the user can search the material library. Raman spectra of pure materials can be used to analyze an experimentally obtained Raman map of material mixture.

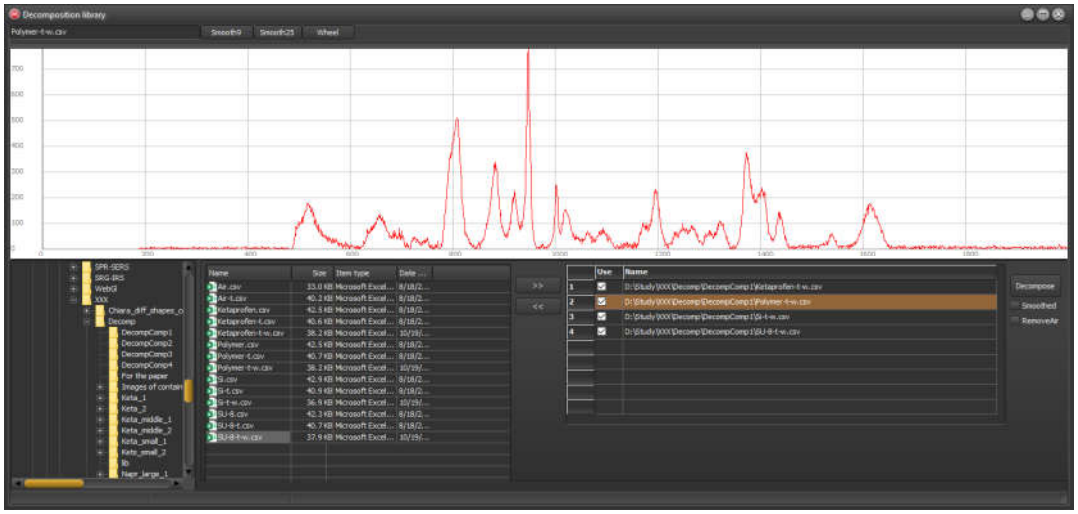

Figure 6.33: A library of known materials with premeasured Raman spectra can assist in analyzing an unknown, experimentally obtained material mixture, e.g. a drug-loaded microcontainer.

Figure 6.34 shows a complex sample – microcarrier for drug delivery, filled with mixed materials. For simultaneous and more visual analysis, it is very comfortable to place the views of the different materials in such way, that each row corresponds to a different material.

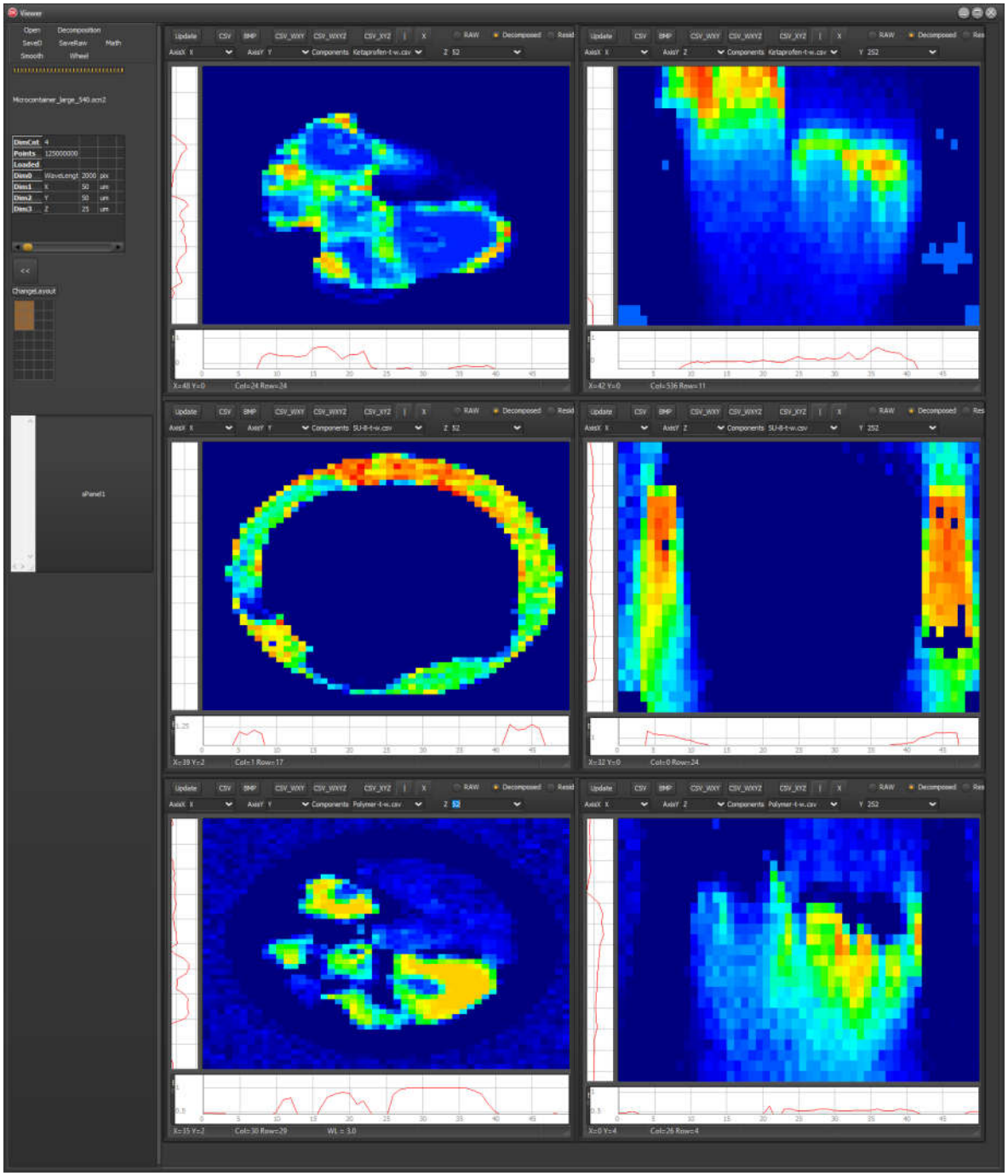

Figure 6.34: The results show chemical decomposition of SU-8 microcontainers (500 µm in diameter and 225 µm in height) filled with PVP polymer and ketoprofen. The top row are XY and XZ cross sections displaying the ketoprofen distribution, the middle row – SU-8, bottom row – PVP. All XY cross sections are obtained at a depth of 50 µm, and the XZ cross sections are from the middle of the microcontainer (250 µm).

7 Conclusions and future perspectives

In this work, we first developed a highly sensitive spectrograph, optimized for the NIR spectral range. In paper I and partially in paper V we demonstrated an improved Raman signal detection for applications aimed at quality control of multilayered, multicomponent drug carriers, where volumetric material analysis plays an important role. In the case of drug loaded microcontainers (~300 µm in size), detecting the Raman signal at a sample depth >100 µm is a very challenging task for most commercial Raman spectrometers. The developed spectrograph was able to extract the signal down to a depth of ~200 µm, and the obtained data can be used for constructing detailed Raman maps in 3D for chemometric analysis and studying distribution of drugs in a microcontainer.

In the next step, the Raman system was modified for SERS-based molecular detection. Quantitative detection of trace amounts of analytes using a SERS substrate often requires acquiring the SERS signal from large surface areas (>1 mm2). Classic point-by-point measurements lead to prolonged signal collection times which is a major constrain since this might affect the stability of a sample, e.g. due to solvent evaporation. In order to circumvent this, different sample laser illumination modes were implemented and tested. The laser beam delivery was modified to support two geometries: the laser-line and wide-line illumination modes. The laser line mode produces a diffraction-limited (~2.9 µm in width) laser line (>2 mm in length) which can be expanded (up to ~64 µm) to produce the wide-line illumination mode at the expense of reduced spectral resolution, which in this case is increased to ~8cm^{-1}.

In paper II, the performance of the setup was evaluated in terms of signal-to-noise ratios for different illumination configurations by measuring 10 µM of BPE deposited on AuNP SERS substrates. The obtained improvements in SNRs for the laser-line and the wide-line modes are 13 and 68 times, respectively. The laser-line mode illuminates a bigger surface area, which increases the surface mapping process by ~2 orders of magnitude depending on the vertical resolution of a spectroscopic CCD camera (in our setup this value is 256). In the wide-line mode, one row in a CCD camera collects the signal from approximately 8.2x64 µm surface area, which is more than 100 times larger compared to a diffraction limited point (~2.5 µm in size). In conclusion, both sample illumination techniques can significantly reduce the surface mapping time, and in particular, the wide-line mode can be used to probe a large SERS substrate area, e.g. 4x4 mm, in a reasonable amount of time. This is not the case in the classic point illumination mode where only a limited number of surface points are examined. Probing an entire surface, with no gaps, is particularly important at low analyte concentrations since the probability of located molecules in the electromagnetic hot spots is significantly reduced.

In paper III, the laser-line illumination mode was utilized in kinetic studies of dehydration processes of organic hydrates. Heat induced phase transformations in nitrofurantoin monohydrate and theophylline crystals were studied. Chemical maps and concentration profiles obtained using the laser-line illumination mode provided valuable insights into dehydration pathways and dynamics of metastable intermediate states. The method is highly suitable for the pharmaceutical industry for assessing quality of particulate materials.

In paper IV, theoretical considerations for determining crystal orientation using Raman spectroscopy were presented. In order to determine crystal orientation and avoid possible ambiguities in some crystal symmetries, the study established a minimum required number of incident laser beams with different polarizations and incident angles. The method was utilized to investigate a tablet containing polyvinylpyrrolidone (PVP) and carbamazepine dihydrate (CBZD), where the CBZD orientation map was obtained. This illustrates the potential for the Raman crystallography method, which can provide insight into the crystal face functionality in pharmaceutical research and material science in general. As a 2D application example, a polycrystalline Si solar cell was studied, and the results were compared

to the well-established EBSD method. The results showed the average miss-orientation value of around 2.1° and a presence of several artifacts. As a 3D application example, a semitransparent polycrystalline sapphire sample with 5-40 µm grain size was investigated. A 3D reconstruction of grains with determined orientation was successfully demonstrated. However, the spectral data from the depth of >50 µm shows an increased level of artifacts due to multi-reflection effects from grain borders and absorption, which makes these type of samples very challenging for orientation studies.
In summary, the developed THOR system (see the table below) is a versatile device with a user-friendly, functional navigation and a convenient scanning algorithm where synchronized operation of multiple devices and a sample pretreatment module were integrated into a unified system. In particular, the implemented navigation system can also be utilized in other microscopic or e.g. cartographic applications, where the area map needs to be constructed and immediately used. The new sample illumination modes offer significantly increased surface scanning speeds, better SNRs and advantageous functionalities e.g. for SERS applications. New optics and spectrograph design schemes enabled Raman imaging of drug-loaded microcontainers at a depth of ~200 µm where the acquired Raman data can be used to build a volumetric distribution of drug mixtures in 3D.
The developed Raman polarization measurement system illustrates that the Raman method can be successfully utilized to determine crystal orientations in a number of tested samples. These techniques were transferred to the start-up company LightNovo ApS where the aim is to evolve existing algorithms and instrumentation and build a system that could compete with the EBSD technique, and potentially, X-ray diffraction crystallography. However, preferences of the crystallographic community will dictate the use and successful implementation of this new technology.

THOR specifications

General parameters	
Lasers	
Multimode (wavelength 785nm, power 0.5W)	Default
Multimode (wavelength 680nm, power 0.3W)	Option
Laser safety	Class 1 (standard)
Replaceable options	
Simultaneous multi-laser usage	Option
Autosampler	Integrated with centrifugal microfluidic unit
Spectroscopic CCD	Andor iDus 416
Objectives	5x, 10x, 20x, 40x
Microscopy module	
Travel range	25 x 25 x 25 mm
Accuracy	0.1um
Computer Interface	USB 3.0
Software	Acquisition and analysis modules QSpec
Reflected visible microscopy operation	Simultaneously with Raman measurements
Laser beam configurations	Point / diffraction-limited line / wide line
Polarization measurements	Depolarized or multichannel polarized (0(ZZ)0, 0(ZZ)90, 90(ZZ)0, 90(ZZ)90, 0(ZZ)45, 0(ZZ)45, 90(ZZ)-45, 90(ZZ)-45 by default)

Spectral parameters	
Spectral range from 785nm laser	350 – 2300 cm^{-1}
Spectral range from 680nm laser	2200 – 4300 cm^{-1}
Spectral resolution	2 - 4 cm^{-1} (FWHM)
Sensitivity or Signal to Noise Ratio (SNR)	

SNR at point illumination	2000:1
SNR at line illumination	15000:1
SNR at wide-field illumination	40000:1
Wavenumber Accuracy	±1.5 cm^{-1}
Lateral spatial resolution (x, y)	Diffraction limited
Confocal spatial resolution (z)	Diffraction limited

Physical parameters	
Weight	15 kg
Temperature range	20-40 C°
Spectrometer dimensions	40 x 32 x 28 cm
Sample compartment dimensions	15 x 15 x 10 cm

References

[1] D.A. Long, The Raman effect: a unified treatment of the theory of Raman scattering by molecules. 2002, 2002. https://doi.org/10.1002/0470845767.

[2] P. Vandenabeele, Practical Raman Spectroscopy - An Introduction, 2013. https://doi.org/10.1002/9781119961284.

[3] J.P. MATHIEU, Fundamentals of molecular spectra, in: Optics, 1975. https://doi.org/10.1016/b978-0-08-017157-9.50021-7.

[4] M. Schmitt, J. Popp, Raman spectroscopy at the beginning of the twenty-first century, J. Raman Spectrosc. (2006). https://doi.org/10.1002/jrs.1486.

[5] X. Zhu, T. Xu, Q. Lin, Y. Duan, Technical development of raman spectroscopy: From instrumental to advanced combined technologies, Appl. Spectrosc. Rev. (2014). https://doi.org/10.1080/05704928.2013.798801.

[6] L. Gao, H. Zhao, T. Li, P. Huo, D. Chen, B. Liu, Atomic force microscopy based tip-enhanced Raman spectroscopy in biology, Int. J. Mol. Sci. (2018). https://doi.org/10.3390/ijms19041193.

[7] A.A.E. Saleh, D.K. Angell, J.A. Dionne, Electron- And light-induced stimulated Raman spectroscopy for nanoscale molecular mapping, Phys. Rev. B. (2020). https://doi.org/10.1103/PhysRevB.102.085406.

[8] A. Paudel, D. Raijada, J. Rantanen, Raman spectroscopy in pharmaceutical product design, Adv. Drug Deliv. Rev. (2015). https://doi.org/10.1016/j.addr.2015.04.003.

[9] D.W. Shipp, F. Sinjab, I. Notingher, Raman spectroscopy: techniques and applications in the life sciences, Adv. Opt. Photonics. (2017). https://doi.org/10.1364/aop.9.000315.

[10] L.P. Choo-Smith, H.G.M. Edwards, H.P. Endtz, J.M. Kros, F. Heule, H. Barr, J.S. Robinson, H.A. Bruining, G.J. Puppels, Medical applications of Raman spectroscopy: From proof of principle to clinical implementation, Biopolym. - Biospectroscopy Sect. (2002). https://doi.org/10.1002/bip.10064.

[11] R.L. McCreery, Raman Spectroscopy for Chemical Analysis, 2005. https://doi.org/10.1002/0471721646.

[12] M.T.T. Pacheco, L.M. Moreira, Raman spectroscopy: New perspectives for its clinical application in diagnosis, Photomed. Laser Surg. (2013). https://doi.org/10.1089/pho.2013.9873.

[13] P. Vandenabeele, H.G.M. Edwards, L. Moens, A decade of Raman spectroscopy in art and archeology, Chem. Rev. (2007). https://doi.org/10.1021/cr068036i.

[14] M.D. Hargreaves, K. Page, T. Munshi, R. Tomsett, G. Lynch, H.G.M. Edwards, Analysis of seized drugs using portable Raman spectroscopy in an airport environment - A proof of principle study, J. Raman Spectrosc. (2008). https://doi.org/10.1002/jrs.1926.

[15] M. Liszewska, B. Bartosewicz, B. Budner, B.J. Jankiewicz, Raman and SERS spectroscopies in the detection of hazardous materials, in: URSI 2018 - Balt. URSI Symp., 2018. https://doi.org/10.23919/URSI.2018.8406758.

[16] A. Hakonen, K. Wu, M. Stenbæk Schmidt, P.O. Andersson, A. Boisen, T. Rindzevicius, Detecting forensic substances using commercially available SERS substrates and handheld Raman spectrometers, Talanta. (2018). https://doi.org/10.1016/j.talanta.2018.07.009.

[17] J.I.S. da S. de Jesus, R. Löbenberg, N.A. Bou-Chacra, Raman spectroscopy for quantitative analysis in the pharmaceutical industry, J. Pharm. Pharm. Sci. (2020). https://doi.org/10.18433/jpps30649.

[18] L.L. Chandler, B. Huang, T. Mu, A smart handheld Raman spectrometer with cloud and AI deep learning algorithm for mixture analysis, in: 2019. https://doi.org/10.1117/12.2519139.

[19] Thermo Fisher Scientific, Cloud-enabled FTIR Spectroscopy, (2018). https://www.thermofisher.com/dk/en/home/industrial/spectroscopy-elemental-isotope-analysis/molecular-spectroscopy/fourier-transform-infrared-ftir-spectroscopy/cloud-enabled-ftir-spectroscopy.html?cid=fl-msd-ftircloud.

[20] SpaceX, Starlink Mission, SpaceX.Com. (2019). https://www.spacex.com/news/2019/05/24/starlink-mission.

[21] R.R. Jones, D.C. Hooper, L. Zhang, D. Wolverson, V.K. Valev, Raman Techniques: Fundamentals and Frontiers, Nanoscale Res. Lett. (2019). https://doi.org/10.1186/s11671-019-3039-2.

[22] B. Pettinger, Single-molecule surface- and tip-enhanced Raman spectroscopy, Mol. Phys. (2010). https://doi.org/10.1080/00268976.2010.506891.

[23] K. Buckley, A.G. Ryder, Applications of Raman Spectroscopy in Biopharmaceutical Manufacturing: A Short Review, Appl. Spectrosc. (2017). https://doi.org/10.1177/0003702817703270.

[24] P.Y. Sacré, P. Lebrun, P.F. Chavez, C. De Bleye, L. Netchacovitch, E. Rozet, R. Klinkenberg, B. Streel, P. Hubert, E. Ziemons, A new criterion to assess distributional homogeneity in hyperspectral images of solid pharmaceutical dosage forms, Anal. Chim. Acta. (2014). https://doi.org/10.1016/j.aca.2014.02.014.

[25] S. Romero-Torres, J.D. Pérez-Ramos, K.R. Morris, E.R. Grant, Raman spectroscopic measurement of tablet-to-tablet coating variability, J. Pharm. Biomed. Anal. (2005). https://doi.org/10.1016/j.jpba.2005.01.007.

[26] A. Kuriyama, Y. Ozaki, Assessment of active pharmaceutical ingredient particle size in tablets by Raman chemical imaging validated using polystyrene microsphere size standards, AAPS PharmSciTech. (2014). https://doi.org/10.1208/s12249-013-0064-9.

[27] L.H. Nielsen, S.S. Keller, A. Boisen, Microfabricated devices for oral drug delivery, Lab Chip. (2018). https://doi.org/10.1039/c8lc00408k.

[28] N. Scoutaris, M.R. Alexander, P.R. Gellert, C.J. Roberts, Inkjet printing as a novel medicine formulation technique, J. Control. Release. (2011). https://doi.org/10.1016/j.jconrel.2011.07.033.

[29] M.A. Yessine, J.C. Leroux, Membrane-destabilizing polyanions: Interaction with lipid bilayers and endosomal escape of biomacromolecules, Adv. Drug Deliv. Rev. (2004). https://doi.org/10.1016/j.addr.2003.10.039.

[30] W. Hauswald, R. Förster, J. Popp, R. Heintzmann, Thermal illumination limits in 3D Raman

microscopy: A comparison of different sample illumination strategies to obtain maximum imaging speed, PLoS One. (2019). https://doi.org/10.1371/journal.pone.0220824.

[31] K. Mochizuki, T. Lee, K. Fujita, Accelerating image acquisition in line-illumination raman microscopy, in: Opt. InfoBase Conf. Pap., 2017.

[32] L. Kong, M. Navas-Moreno, J.W. Chan, Fast Confocal Raman Imaging Using a 2-D Multifocal Array for Parallel Hyperspectral Detection, Anal. Chem. (2016). https://doi.org/10.1021/acs.analchem.5b03707.

[33] J.B. Nanubolu, J.C. Burley, Investigating the recrystallization behavior of amorphous paracetamol by variable temperature Raman studies and surface raman mapping, Mol. Pharm. (2012). https://doi.org/10.1021/mp300035g.

[34] A. Hédoux, Y. Guinet, M. Descamps, The contribution of Raman spectroscopy to the analysis of phase transformations in pharmaceutical compounds, Int. J. Pharm. (2011). https://doi.org/10.1016/j.ijpharm.2011.01.031.

[35] N. Chieng, T. Rades, J. Aaltonen, An overview of recent studies on the analysis of pharmaceutical polymorphs, J. Pharm. Biomed. Anal. (2011). https://doi.org/10.1016/j.jpba.2010.12.020.

[36] F. Tian, J.A. Zeitler, C.J. Strachan, D.J. Saville, K.C. Gordon, T. Rades, Characterizing the conversion kinetics of carbamazepine polymorphs to the dihydrate in aqueous suspension using Raman spectroscopy, J. Pharm. Biomed. Anal. (2006). https://doi.org/10.1016/j.jpba.2005.07.030.

[37] T. Gnutzmann, R. Kahlau, S. Scheifler, F. Friedrichs, E.A. Rössler, K. Rademann, F. Emmerling, Crystal growth rates and molecular dynamics of nifedipine, CrystEngComm. (2013). https://doi.org/10.1039/c2ce26911b.

[38] W. Sinclair, M. Leane, G. Clarke, A. Dennis, M. Tobyn, P. Timmins, Physical stability and recrystallization kinetics of amorphous ibipinabant drug product by Fourier transform Raman spectroscopy, J. Pharm. Sci. (2011). https://doi.org/10.1002/jps.22658.

[39] B.C. Hancock, G. Zografi, Characteristics and Significance of the Amorphous State in Pharmaceutical Systems, J. Pharm. Sci. 86 (1997) 1. https://doi.org/10.1021/js9601896.

[40] G.E. Granero, G.L. Amidon, Stability of valacyclovir: Implications for its oral bioavailability, Int. J. Pharm. 317 (2006) 14–18. https://doi.org/10.1016/J.IJPHARM.2006.01.050.

[41] S. Bertoni, B. Albertini, L. Ferraro, S. Beggiato, A. Dalpiaz, N. Passerini, Exploring the use of spray congealing to produce solid dispersions with enhanced indomethacin bioavailability: In vitro characterization and in vivo study, Eur. J. Pharm. Biopharm. 139 (2019) 132–141. https://doi.org/10.1016/j.ejpb.2019.03.020.

[42] V.N. Makatun, L.N. Shchegrov, State of Water in Inorganic Crystal Hydrates and the Characteristic Features of Their Dehydration, Russ. Chem. Rev. (1972). https://doi.org/10.1070/rc1972v041n11abeh002102.

[43] K. Higashi, K. Ueda, K. Moribe, Recent progress of structural study of polymorphic pharmaceutical drugs, Adv. Drug Deliv. Rev. (2017). https://doi.org/10.1016/j.addr.2016.12.001.

[44] E. Hadjittofis, M.A. Isbell, V. Karde, S. Varghese, C. Ghoroi, J.Y.Y. Heng, Influences of Crystal Anisotropy in Pharmaceutical Process Development, Pharm. Res. (2018). https://doi.org/10.1007/s11095-018-2374-9.

[45] S. Datta, D.J.W. Grant, Crystal structures of drugs: Advances in determination, prediction and engineering, Nat. Rev. Drug Discov. (2004). https://doi.org/10.1038/nrd1280.

[46] T.K. Wijethunga, J. Stojaković, M.A. Bellucci, X. Chen, A.S. Myerson, B.L. Trout, General Method for the Identification of Crystal Faces Using Raman Spectroscopy Combined with Machine Learning and Application to the Epitaxial Growth of Acetaminophen, Langmuir. (2018). https://doi.org/10.1021/acs.langmuir.8b01791.

[47] K. Moriyama, N. Furuno, N. Yamakawa, Crystal face identification by Raman microscopy for assessment of crystal habit of a drug, Int. J. Pharm. (2015). https://doi.org/10.1016/j.ijpharm.2015.01.031.

[48] J. Hübner, T. Deckert-Gaudig, J. Glorian, V. Deckert, D. Spitzer, Surface characterization of nanoscale co-crystals enabled through tip enhanced Raman spectroscopy, Nanoscale. (2020). https://doi.org/10.1039/d0nr00397b.

[49] P.R. Carey, Raman crystallography and other biochemical applications of raman microscopy, in: Annu. Rev. Phys. Chem., 2006. https://doi.org/10.1146/annurev.physchem.57.032905.104521.

[50] S. Schlücker, Surface-enhanced raman spectroscopy: Concepts and chemical applications, Angew. Chemie - Int. Ed. (2014). https://doi.org/10.1002/anie.201205748.

[51] T.M. Cotton, J. -H Kim, G.D. Chumanov, Application of surface-enhanced Raman spectroscopy to biological systems, J. Raman Spectrosc. (1991). https://doi.org/10.1002/jrs.1250221203.

[52] K.C. Bantz, A.F. Meyer, N.J. Wittenberg, H. Im, Ö. Kurtuluş, S.H. Lee, N.C. Lindquist, S.H. Oh, C.L. Haynes, Recent progress in SERS biosensing, Phys. Chem. Chem. Phys. (2011). https://doi.org/10.1039/c0cp01841d.

[53] C.T. Culbertson, T.G. Mickleburgh, S.A. Stewart-James, K.A. Sellens, M. Pressnall, Micro total analysis systems: Fundamental advances and biological applications, Anal. Chem. (2014). https://doi.org/10.1021/ac403688g.

[54] K. Kneipp, H. Kneipp, I. Itzkan, R.R. Dasari, M.S. Feld, Ultrasensitive Chemical Analysis by Raman Spectroscopy, Chem. Rev. (1999). https://doi.org/10.1021/cr980133r.

[55] R. Pilot, R. Signorini, C. Durante, L. Orian, M. Bhamidipati, L. Fabris, A review on surface-enhanced Raman scattering, Biosensors. (2019). https://doi.org/10.3390/bios9020057.

[56] S. Kawata, T. Ichimura, A. Taguchi, Y. Kumamoto, Nano-Raman scattering microscopy: Resolution and enhancement, Chem. Rev. (2017). https://doi.org/10.1021/acs.chemrev.6b00560.

[57] M.S. Schmidt, J. Hübner, A. Boisen, Large area fabrication of leaning silicon nanopillars for Surface Enhanced Raman Spectroscopy, Adv. Mater. (2012). https://doi.org/10.1002/adma.201103496.

[58] K. Wu, T. Rindzevicius, M.S. Schmidt, A.H. Thilsted, A. Boisen, Optimizing silver-capped silicon nanopillars to simultaneously realize macroscopic, practical-level SERS signal reproducibility

and high enhancement at low costs, J. Raman Spectrosc. (2017). https://doi.org/10.1002/jrs.5255.

[59] L.B. Laurentius, A.C. Crawford, T.S. Mulvihill, J.H. Granger, R. Robinson, J.S. Spencer, D. Chatterjee, K.E. Hanson, M.D. Porter, Importance of specimen pretreatment for the low-level detection of mycobacterial lipoarabinomannan in human serum, Analyst. (2017). https://doi.org/10.1039/c6an02109c.

[60] R. Panneerselvam, G.K. Liu, Y.H. Wang, J.Y. Liu, S.Y. Ding, J.F. Li, D.Y. Wu, Z.Q. Tian, Surface-enhanced Raman spectroscopy: Bottlenecks and future directions, Chem. Commun. (2017). https://doi.org/10.1039/c7cc05979e.

[61] H.G.M. Edwards, Modern techniques in Raman spectroscopy, New York, 1997. https://doi.org/10.1016/s1386-1425(97)00063-2.

[62] B.F. Adar, S. Volume, M.S. Workshop, Introduction to Interpretation of Raman Spectra Using Database Searching and Functional Group Detection and Identification, Spectroscopy. (2016).

[63] S. Nakashima, H. Harima, Characterization of Defects in SiC Crystals by Raman Scattering, in: 2004. https://doi.org/10.1007/978-3-642-18870-1_24.

[64] P. Meszmer, R.D. Rodriguez, E. Sheremet, D.R.T. Zahn, B. Wunderle, Stress imaging in structural challenging MEMS with high sensitivity using micro-Raman spectroscopy, Microelectron. Reliab. (2017). https://doi.org/10.1016/j.microrel.2017.10.010.

[65] A. Heinz, C.J. Strachan, K.C. Gordon, T. Rades, Analysis of solid-state transformations of pharmaceutical compounds using vibrational spectroscopy, J. Pharm. Pharmacol. (2009). https://doi.org/10.1211/jpp/61.08.0001.

[66] T. Wilson, Scanning optical microscopy, Scanning. (1985). https://doi.org/10.1002/sca.4950070203.

[67] R.H. Webb, Confocal optical microscopy, Reports Prog. Phys. (1996). https://doi.org/10.1088/0034-4885/59/3/003.

[68] Confocal Microscopy : Basic Concepts, Nikon Microsc. (2014).

[69] J.B. Pawley, Fundamental and practical limits in confocal light microscopy, Scanning. (1991). https://doi.org/10.1002/sca.4950130205.

[70] Electronic light microscopy: Techniques in modern biomedical microscopy, edited by David Shotten, Wiley-Liss, New York, 1992, 355 pp, $89.95, Mol. Reprod. Dev. (1994). https://doi.org/10.1002/mrd.1080370418.

[71] R.H. Webb, Theoretical basis of confocal microscopy, Methods Enzymol. (1999). https://doi.org/10.1016/S0076-6879(99)07003-2.

[72] W.H. Wehrmacher, Light and electron microscopy., Arch. Phys. Med. Rehabil. (1983). https://doi.org/10.1016/0022-0981(93)90059-w.

[73] B. Amos, G. McConnell, T. Wilson, Confocal microscopy, in: Compr. Biophys., 2012. https://doi.org/10.1016/B978-0-12-374920-8.00203-4.

[74] D.S. Goodman, Theory and Practice of Scanning Optical Microscopy, J. Opt. Soc. Am. A. (1987). https://doi.org/10.1364/josaa.4.000551.

[75] K. Carlsson, P.E. Danielsson, A. Liljeborg, L. Majlöf, R. Lenz, N. Åslund, Three-dimensional microscopy using a confocal laser scanning microscope, Opt. Lett. (1985). https://doi.org/10.1364/ol.10.000053.

[76] G.F. Marshall, J. Montagu, Galvanometric and Resonant Scanners, in: Handb. Opt. Laser Scanning, 2018. https://doi.org/10.1201/9781315218243-8.

[77] Y. Li, Beam deflection and scanning by two-mirror and two-axis systems of different architectures: A unified approach, Appl. Opt. (2008). https://doi.org/10.1364/AO.47.005976.

[78] M.K. Stefan Richter, Carsten Wehe, Uwe Wolf, Thomas Nobis, Lars-Christian Wittig, Philipp Huebner, Alexander Froeber, Gerhard Krampert, Dirk Thiele, Joerg Muetze, Integrated confocal imaging system, SPIE OPTO. Proceeding (2019). https://doi.org/10.1117/12.2514552.

[79] Y. Zhao, W.J. Eldridge, J.R. Maher, S. Kim, M. Crose, M. Ibrahim, H. Levinson, A. Wax, Dual-axis optical coherence tomography for deep tissue imaging, Opt. Lett. (2017). https://doi.org/10.1364/ol.42.002302.

[80] C. Yin, A.K. Glaser, S.Y. Leigh, Y. Chen, L. Wei, P.C.S. Pillai, M.C. Rosenberg, S. Abeytunge, G. Peterson, C. Glazowski, N. Sanai, M.J. Mandella, M. Rajadhyaksha, J.T.C. Liu, Miniature in vivo MEMS-based line-scanned dual-axis confocal microscope for point-of-care pathology, Biomed. Opt. Express. (2016). https://doi.org/10.1364/boe.7.000251.

[81] C.D. Lu, M.F. Kraus, B. Potsaid, J.J. Liu, W. Choi, V. Jayaraman, A.E. Cable, J. Hornegger, J.S. Duker, J.G. Fujimoto, Handheld ultrahigh speed swept source optical coherence tomography instrument using a MEMS scanning mirror, Biomed. Opt. Express. (2014). https://doi.org/10.1364/boe.5.000293.

[82] T. Liu, M. Rajadhyaksha, D.L. Dickensheets, MEMS-in-the-lens architecture for a miniature high-NA laser scanning microscope, Light Sci. Appl. (2019). https://doi.org/10.1038/s41377-019-0167-5.

[83] G. Anzolin, A. Gardelein, M. Jofre, G. Molina-Terriza, M.W. Mitchell, Polarization change induced by a galvanometric optical scanner, J. Opt. Soc. Am. A. (2010). https://doi.org/10.1364/josaa.27.001946.

[84] D.B. Murphy, M.W. Davidson, Fundamentals of Light Microscopy and Electronic Imaging: Second Edition, 2012. https://doi.org/10.1002/9781118382905.

[85] J.W. Einax, M.J. Adams: Chemometrics in Analytical Spectroscopy, 2nd edition, Anal. Bioanal. Chem. (2005). https://doi.org/10.1007/s00216-005-3181-9.

[86] H. Mark, J. Workman, Chemometrics in Spectroscopy, 2007. https://doi.org/10.1016/B978-0-12-374024-3.X5000-4.

[87] Y. Ozeki, F. Dake, S. Kajiyama, K. Fukui, K. Itoh, Analysis and experimental assessment of the sensitivity of stimulated Raman scattering microscopy, Opt. Express. (2009). https://doi.org/10.1364/oe.17.003651.

[88] J. Ling, S.D. Weitman, M.A. Miller, R. V. Moore, A.C. Bovik, Direct Raman imaging techniques for study of the subcellular distribution of a drug, Appl. Opt. (2002). https://doi.org/10.1364/ao.41.006006.

[89] A.F. Palonpon, J. Ando, H. Yamakoshi, K. Dodo, M. Sodeoka, S. Kawata, K. Fujita, Raman and

SERS microscopy for molecular imaging of live cells, Nat. Protoc. (2013). https://doi.org/10.1038/nprot.2013.030.

[90] C.J. De Grauw, C. Otto, J. Greve, Line-scan Raman microspectrometry for biological applications, Appl. Spectrosc. (1997). https://doi.org/10.1366/0003702971939587.

[91] H. Li, W. Luo, G. Li, G. Zhang, P. Zhang, C. Li, Y. Gu, A practical wide-field Raman imaging method with high spectral and spatial resolution, Rev. Sci. Instrum. (2018). https://doi.org/10.1063/1.5041529.

[92] E. Smith, G. Dent, Modern Raman Spectroscopy - A Practical Approach, 2005. https://doi.org/10.1002/0470011831.

[93] B. Sharma, R.R. Frontiera, A.-I. Henry, E. Ringe, R.P. Van Duyne, SERS: Materials, applications, and the future Background and mechanism, 2012. https://doi.org/10.1016/S1369-7021(12)70017-2.

[94] D. Cialla, A. März, R. Böhme, F. Theil, K. Weber, M. Schmitt, J. Popp, Surface-enhanced Raman spectroscopy (SERS): Progress and trends, Anal. Bioanal. Chem. (2012). https://doi.org/10.1007/s00216-011-5631-x.

[95] R. Zhang, Y. Zhang, Z.C. Dong, S. Jiang, C. Zhang, L.G. Chen, L. Zhang, Y. Liao, J. Aizpurua, Y. Luo, J.L. Yang, J.G. Hou, Chemical mapping of a single molecule by plasmon-enhanced Raman scattering, Nature. (2013). https://doi.org/10.1038/nature12151.

[96] M.D. Sonntag, J.M. Klingsporn, L.K. Garibay, J.M. Roberts, J.A. Dieringer, T. Seideman, K.A. Scheidt, L. Jensen, G.C. Schatz, R.P. Van Duyne, Single-molecule tip-enhanced Raman spectroscopy, J. Phys. Chem. C. (2012). https://doi.org/10.1021/jp209982h.

[97] J.X. Cheng, X.S. Xie, Coherent anti-Stokes Raman scattering microscopy: Instrumentation, theory, and applications, J. Phys. Chem. B. (2004). https://doi.org/10.1021/jp035693v.

[98] R.C. Prince, R.R. Frontiera, E.O. Potma, Stimulated Raman scattering: From bulk to nano, Chem. Rev. (2017). https://doi.org/10.1021/acs.chemrev.6b00545.

[99] M. Fleischmann, P.J. Hendra, A.J. McQuillan, Raman spectra of pyridine adsorbed at a silver electrode, Chem. Phys. Lett. (1974). https://doi.org/10.1016/0009-2614(74)85388-1.

[100] D.L. Jeanmaire, R.P. Van Duyne, Surface raman spectroelectrochemistry. Part I. Heterocyclic, aromatic, and aliphatic amines adsorbed on the anodized silver electrode, J. Electroanal. Chem. (1977). https://doi.org/10.1016/S0022-0728(77)80224-6.

[101] M.G. Albrecht, J.A. Creighton, Anomalously Intense Raman Spectra of Pyridine at a Silver Electrode, J. Am. Chem. Soc. (1977). https://doi.org/10.1021/ja00457a071.

[102] K. Kneipp, Y. Wang, H. Kneipp, L.T. Perelman, I. Itzkan, R.R. Dasari, M.S. Feld, Single molecule detection using surface-enhanced raman scattering (SERS), Phys. Rev. Lett. (1997). https://doi.org/10.1103/PhysRevLett.78.1667.

[103] S. Nie, S.R. Emory, Probing single molecules and single nanoparticles by surface-enhanced Raman scattering, Science (80-.). (1997). https://doi.org/10.1126/science.275.5303.1102.

[104] M. Fan, G.F.S. Andrade, A.G. Brolo, A review on the fabrication of substrates for surface enhanced Raman spectroscopy and their applications in analytical chemistry, Anal. Chim. Acta. (2011). https://doi.org/10.1016/j.aca.2011.03.002.

[105] M. Jahn, S. Patze, I.J. Hidi, R. Knipper, A.I. Radu, A. Mühlig, S. Yüksel, V. Peksa, K. Weber, T. Mayerhöfer, D. Cialla-May, J. Popp, Plasmonic nanostructures for surface enhanced spectroscopic methods, Analyst. (2016). https://doi.org/10.1039/c5an02057c.

[106] S. Fateixa, H.I.S. Nogueira, T. Trindade, Hybrid nanostructures for SERS: Materials development and chemical detection, Phys. Chem. Chem. Phys. (2015). https://doi.org/10.1039/c5cp01032b.

[107] G.C. Schatz, M.A. Young, R.P. Van Duyne, Electromagnetic mechanism of SERS, Top. Appl. Phys. (2006). https://doi.org/10.1007/11663898_2.

[108] L. Jensen, C.M. Aikens, G.C. Schatz, Electronic structure methods for studying surface-enhanced Raman scattering, Chem. Soc. Rev. (2008). https://doi.org/10.1039/b706023h.

[109] N.S. Chong, K. Donthula, R.A. Davies, W.H. Ilsley, B.G. Ooi, Significance of chemical enhancement effects in surface-enhanced Raman scattering (SERS) signals of aniline and aminobiphenyl isomers, Vib. Spectrosc. (2015). https://doi.org/10.1016/j.vibspec.2015.09.002.

[110] Y.S. Yamamoto, Y. Ozaki, T. Itoh, Recent progress and frontiers in the electromagnetic mechanism of surface-enhanced Raman scattering, J. Photochem. Photobiol. C Photochem. Rev. (2014). https://doi.org/10.1016/j.jphotochemrev.2014.10.001.

[111] T. Itoh, H. Yoshikawa, K. Yoshida, V. Biju, M. Ishikawa, Evaluation of electromagnetic enhancement of surface enhanced hyper Raman scattering using plasmonic properties of binary active sites in single Ag nanoaggregates, J. Chem. Phys. (2009). https://doi.org/10.1063/1.3146788.

[112] E.C. Le Ru, E. Blackie, M. Meyer, P.G. Etchegoint, Surface enhanced raman scattering enhancement factors: A comprehensive study, J. Phys. Chem. C. (2007). https://doi.org/10.1021/jp0687908.

[113] A. Hakonen, P.O. Andersson, M. Stenbæk Schmidt, T. Rindzevicius, M. Käll, Explosive and chemical threat detection by surface-enhanced Raman scattering: A review, Anal. Chim. Acta. (2015). https://doi.org/10.1016/j.aca.2015.04.010.

[114] J.M. Chalmers, P.R. Griffiths, Handbook of Vibrational Spectroscopy: Theory and Instrumentation (Vol.1), J. Am. Chem. Soc. (2002). https://doi.org/10.1021/ja025228w.

[115] Y.S. Yamamoto, M. Ishikawa, Y. Ozaki, T. Itoh, Fundamental studies on enhancement and blinking mechanism of surface-enhanced Raman scattering (SERS) and basic applications of SERS biological sensing, Front. Phys. (2014). https://doi.org/10.1007/s11467-013-0347-3.

[116] Y.S. Yamamoto, T. Itoh, Why and how do the shapes of surface-enhanced Raman scattering spectra change? Recent progress from mechanistic studies, J. Raman Spectrosc. (2016). https://doi.org/10.1002/jrs.4874.

[117] U.Y. Qazi, R. Javaid, A Review on Metal Nanostructures: Preparation Methods and Their Potential Applications, Adv. Nanoparticles. (2016). https://doi.org/10.4236/anp.2016.51004.

[118] S. McAughtrie, K. Faulds, D. Graham, Surface enhanced Raman spectroscopy (SERS): Potential applications for disease detection and treatment, J. Photochem. Photobiol. C Photochem. Rev. (2014). https://doi.org/10.1016/j.jphotochemrev.2014.09.002.

[119] A. Bonifacio, S. Cervo, V. Sergo, Label-free surface-enhanced Raman spectroscopy of biofluids: Fundamental aspects and diagnostic applications, Anal. Bioanal. Chem. (2015). https://doi.org/10.1007/s00216-015-8697-z.

[120] Z.A. Nima, A. Biswas, I.S. Bayer, F.D. Hardcastle, D. Perry, A. Ghosh, E. Dervishi, A.S. Biris, Applications of surface-enhanced Raman scattering in advanced bio-medical technologies and diagnostics, Drug Metab. Rev. (2014). https://doi.org/10.3109/03602532.2013.873451.

[121] A. Samanta, S. Jana, R.K. Das, Y.T. Chang, Biocompatible surface-enhanced Raman scattering nanotags for in vivo cancer detection, Nanomedicine. (2014). https://doi.org/10.2217/nnm.13.222.

[122] W.R. Premasiri, P. Lemler, Y. Chen, Y. Gebregziabher, L.D. Ziegler, SERS Analysis of Bacteria, Human Blood, and Cancer Cells: a Metabolomic and Diagnostic Tool, in: Front. Surface-Enhanced Raman Scatt. Single Nanoparticles Single Cells, 2014. https://doi.org/10.1002/9781118703601.ch12.

[123] L. He, Recent developments in Raman spectroscopy for the detection of food chemical hazards, in: Food Chem. Hazard Detect. Dev. Appl. New Technol., 2014. https://doi.org/10.1002/9781118488553.ch6.

[124] W. Liao, X. Lu, Determination of chemical hazards in foods using surface-enhanced Raman spectroscopy coupled with advanced separation techniques, Trends Food Sci. Technol. (2016). https://doi.org/10.1016/j.tifs.2016.05.020.

[125] J. Zheng, L. He, Surface-Enhanced Raman Spectroscopy for the Chemical Analysis of Food, Compr. Rev. Food Sci. Food Saf. (2014). https://doi.org/10.1111/1541-4337.12062.

[126] T. Vankeirsbilck, A. Vercauteren, W. Baeyens, G. Van der Weken, F. Verpoort, G. Vergote, J.P. Remon, Applications of Raman spectroscopy in pharmaceutical analysis, TrAC - Trends Anal. Chem. (2002). https://doi.org/10.1016/S0165-9936(02)01208-6.

[127] R.A. Álvarez-Puebla, L.M. Liz-Marzán, Environmental applications of plasmon assisted Raman scattering, Energy Environ. Sci. (2010). https://doi.org/10.1039/c002437f.

[128] D.W. Li, W.L. Zhai, Y.T. Li, Y.T. Long, Recent progress in surface enhanced Raman spectroscopy for the detection of environmental pollutants, Microchim. Acta. (2014). https://doi.org/10.1007/s00604-013-1115-3.

[129] C. Muehlethaler, M. Leona, J.R. Lombardi, Review of Surface Enhanced Raman Scattering Applications in Forensic Science, Anal. Chem. (2016). https://doi.org/10.1021/acs.analchem.5b04131.

[130] S. Wachsmann-Hogiu, T. Weeks, T. Huser, Chemical analysis in vivo and in vitro by Raman spectroscopy-from single cells to humans, Curr. Opin. Biotechnol. (2009). https://doi.org/10.1016/j.copbio.2009.02.006.

[131] S.H. Yazdi, I.M. White, A nanoporous optofluidic microsystem for highly sensitive and repeatable surface enhanced Raman spectroscopy detection, Biomicrofluidics. (2012). https://doi.org/10.1063/1.3677369.

[132] Y. Zhang, S. Zhao, J. Zheng, L. He, Surface-enhanced Raman spectroscopy (SERS) combined techniques for high-performance detection and characterization, TrAC - Trends Anal. Chem. (2017). https://doi.org/10.1016/j.trac.2017.02.006.

[133] L. Morelli, K. Zór, C.B. Jendresen, T. Rindzevicius, M.S. Schmidt, A.T. Nielsen, A. Boisen, Surface Enhanced Raman Scattering for Quantification of p-Coumaric Acid Produced by Escherichia coli, Anal. Chem. (2017). https://doi.org/10.1021/acs.analchem.6b04428.

[134] L. Morelli, L. Serioli, F.A. Centorbi, C.B. Jendresen, M. Matteucci, O. Ilchenko, D. Demarchi, A.T. Nielsen, K. Zór, A. Boisen, Injection molded lab-on-a-disc platform for screening of genetically modified: E. coli using liquid-liquid extraction and surface enhanced Raman scattering, Lab Chip. (2018). https://doi.org/10.1039/c7lc01217a.

[135] O. Durucan, T. Rindzevicius, M.S. Schmidt, M. Matteucci, A. Boisen, Nanopillar Filters for Surface-Enhanced Raman Spectroscopy, ACS Sensors. (2017). https://doi.org/10.1021/acssensors.7b00499.

[136] K. Sanger, O. Durucan, K. Wu, A.H. Thilsted, A. Heiskanen, T. Rindzevicius, M.S. Schmidt, K. Zór, A. Boisen, Large-Scale, Lithography-Free Production of Transparent Nanostructured Surface for Dual-Functional Electrochemical and SERS Sensing, ACS Sensors. (2017). https://doi.org/10.1021/acssensors.7b00783.

[137] M. Tanaka, R.J. Young, Review Polarised Raman spectroscopy for the study of molecular orientation distributions in polymers, J. Mater. Sci. (2006). https://doi.org/10.1007/s10853-006-6595-7.

[138] R.-J. Roe, Methods of X-ray and neutron scattering in polymer science, Oxford Univ. Press New York. (2000).

[139] H. de Vries, A new approach to the continuum theory of birefringence of oriented polymers, Colloid Polym. Sci. Kolloid Zeitschrift Zeitschrift Für Polym. (1979). https://doi.org/10.1007/BF01382363.

[140] P. Spegt, B. Meurer, C. Hornick, G. Weill, Molecular Orientation in Stretched Poly(Vinyl Alcohol). I. Nmr Anisotropy and Birefringence., J. Polym. Sci. Part A-2, Polym. Phys. 23 (1985) 315–325. https://doi.org/10.1002/pol.1985.180230207.

[141] M. Botev, P. Judeinstein, R. Neffati, J. Rault, Orientation of amorphous chains in polyamide-6 fibers through 2H-NMR, Macromolecules. (1996). https://doi.org/10.1021/ma960436s.

[142] M.E.R. Robinson, D.I. Bower, W.F. Maddams, Molecular Orientation in Poly(Vinyl Chloride) Studied By Raman Spectroscopy and Birefringence Measurements., J Polym Sci Polym Phys Ed. 16 (1978) 2115–2138. https://doi.org/10.1002/pol.1978.180161203.

[143] J.H. Nobbs, D.I. Bower, I.M. Ward, D. Patterson, A study of the orientations of fluorescent molecules incorporated in uniaxially oriented poly(ethylene terephthalate) tapes, Polymer (Guildf). (1974). https://doi.org/10.1016/0032-3861(74)90126-8.

[144] J.H. Nobbs, D.I. Bower, I.M. Ward, Comparison of Polarized Fluorescence With Polarized Raman and Infrared Dichroism Measures of Orientation in Uniaxially Drawn Poly(Ethylene Terephthalate)., J Polym Sci Polym Phys Ed. 17 (1979) 259–272. https://doi.org/10.1002/pol.1979.180170206.

[145] D.I. Bower, D.A. Jarvis, I.M. Ward, Molecular orientation in biaxially oriented sheets of poly(ethylene terephthalate). I. Characterization of orientation and comparison with models, J. Polym. Sci. Part B Polym. Phys. (1986). https://doi.org/10.1002/polb.1986.090240706.

[146] Nomura S., Kawai H., General description of orientation factors in terms of expansion of

orientation distribution function in a series of spherical harmonics, J Polym Sci Part A-2 Polym Phys. 8 (1970) 383–400. https://doi.org/10.1002/pol.1970.160080305.

[147] D.I. Bower, Investigation of Molecular Orientation Distributions By Polarized Raman Scattering and Polarized Fluorescence., J Polym Sci Part A-2 Polym Phys. 10 (1972) 2135–2153. https://doi.org/10.1002/pol.1972.180101103.

[148] T.C. Damen, S.P.S. Porto, B. Tell, Raman effect in zinc oxide, Phys. Rev. (1966). https://doi.org/10.1103/PhysRev.142.570.

[149] R. Loudon, The Raman effect in crystals, Adv. Phys. (1964). https://doi.org/10.1080/00018736400101051.

[150] K. Mizoguchi, S.I. Nakashima, Determination of crystallographic orientations in silicon films by Raman-microprobe polarization measurements, J. Appl. Phys. (1989). https://doi.org/10.1063/1.342787.

[151] Z.Q. Lu, T. Quinn, H.S. Reehal, Polarization-dependent Raman spectra of thin crystalline silicon films, J. Appl. Phys. (2005). https://doi.org/10.1063/1.1844613.

[152] U. Ramabadran, B. Roughani, Intensity analysis of polarized Raman spectra for off axis single crystal silicon, Mater. Sci. Eng. B Solid-State Mater. Adv. Technol. (2018). https://doi.org/10.1016/j.mseb.2017.12.040.

[153] M. Otsuka, Effects of environmental temperature and compression energy on polymorphic transformation during tabletting, Drug Dev. Ind. Pharm. (1993). https://doi.org/10.3109/03639049309047191.

[154] M. Efentakis, S. Politis, Comparative evaluation of various structures in polymer controlled drug delivery systems and the effect of their morphology and characteristics on drug release, Eur. Polym. J. (2006). https://doi.org/10.1016/j.eurpolymj.2005.11.009.

[155] P. Shende, C. Shrawne, R.S. Gaud, Multi-layer tablet: Current scenario and recent advances, Int. J. Drug Deliv. (2012). https://doi.org/10.5138/ijdd.v4i4.845.

[156] R. Yokoyama, G. Kimura, J. Huwyler, K.I. Hosoya, M. Puchkov, Impact of insoluble separation layer mechanical properties on disintegration and dissolution kinetics of multilayer tablets, Pharmaceutics. (2020). https://doi.org/10.3390/pharmaceutics12060495.

[157] Teensy 3.2 USB Development Board, (n.d.). https://www.pjrc.com/store/teensy32.html.

[158] AMIS-30543 Stepper Motor Driver Carrier, (n.d.). https://www.pololu.com/product/2970.

[159] M. La, S.J. Park, H.W. Kim, J.J. Park, K.T. Ahn, S.M. Ryew, D.S. Kim, A centrifugal force-based serpentine micromixer (CSM) on a plastic lab-on-A-disk for biochemical assays, Microfluid. Nanofluidics. (2013). https://doi.org/10.1007/s10404-012-1127-z.

[160] R. Gorkin, L. Clime, M. Madou, H. Kido, Pneumatic pumping in centrifugal microfluidic platforms, Microfluid. Nanofluidics. (2010). https://doi.org/10.1007/s10404-010-0571-x.

[161] J. Siegrist, R. Gorkin, L. Clime, E. Roy, R. Peytavi, H. Kido, M. Bergeron, T. Veres, M. Madou, Serial siphon valving for centrifugal microfluidic platforms, Microfluid. Nanofluidics. (2010). https://doi.org/10.1007/s10404-009-0523-5.

[162] E.J. Templeton, E.D. Salin, A novel filtration method integrated on centrifugal microfluidic

devices, Microfluid. Nanofluidics. (2014). https://doi.org/10.1007/s10404-013-1293-7.

[163] G.M. Whitesides, The origins and the future of microfluidics, Nature. (2006). https://doi.org/10.1038/nature05058.

[164] T.M. Squires, S.R. Quake, Microfluidics: Fluid physics at the nanoliter scale, Rev. Mod. Phys. (2005). https://doi.org/10.1103/RevModPhys.77.977.

[165] U. Demirci, A. Khademhosseini, R. Langer, J. Blander, Microfluidic technologies for human health, 2012. https://doi.org/10.1142/8469.

[166] M. Člupek, P. Matějka, K. Volka, Noise reduction in Raman spectra: Finite impulse response filtration versus Savitzky-Golay smoothing, J. Raman Spectrosc. (2007). https://doi.org/10.1002/jrs.1747.

[167] N.N. Brandt, O.O. Brovko, A.Y. Chikishev, O.D. Paraschuk, Optimization of the rolling-circle filter for Raman background subtraction, Appl. Spectrosc. (2006). https://doi.org/10.1366/000370206776342553.

[168] D. Kim, S. Sra, I.S. Dhillon, A non-monotonic method for large-scale non-negative least squares, Optim. Methods Softw. (2013). https://doi.org/10.1080/10556788.2012.656368.

Appendix: Publications

Paper I

Volumetric Raman Chemical Imaging of Drug Delivery Systems

R. Slipets, O. Ilchenko, C. Mazzoni, F. Tentor, L.H. Nielsen, and A. Boisen

Journal of Raman Spectroscopy. 2020

Received: 7 November 2019 | Revised: 4 February 2020 | Accepted: 25 February 2020

DOI: 10.1002/jrs.5869

RESEARCH ARTICLE

Journal of RAMAN SPECTROSCOPY WILEY

Volumetric Raman chemical imaging of drug delivery systems

Roman Slipets | Oleksii Ilchenko | Chiara Mazzoni | Fabio Tentor | Line Hagner Nielsen | Anja Boisen

The Danish National Research Foundation and Villum Foundation's Center for Intelligent Drug Delivery and Sensing Using Microcontainers and Nanomechanics (IDUN)—Department of Health Technology, Technical University of Denmark, Kongens Lyngby, Denmark

Correspondence
Oleksii Ilchenko, The Danish National Research Foundation and Villum Foundation's Center for Intelligent Drug Delivery and Sensing Using Microcontainers and Nanomechanics (IDUN)—Department of Health Technology, Technical University of Denmark, Kongens Lyngby, Denmark.
Email: olil@nanotech.dtu.dk

Funding information
Villum Fonden, Grant/Award Number: 9301; Danish National Research Foundation, Grant/Award Number: DNRF122

Abstract

The ability to image drug distribution inside a several hundred micron thick polymer matrix, encapsulated by a protective coating, would greatly contribute to the understanding of the performance and shortcomings of drug delivery devices. Here, we present an experimental framework for deep volumetric Raman imaging (dVRI), where common challenges such as low Raman cross section, fluorescence, and low transparency of samples are overcome. We apply dVRI to a selection of drug delivery forms, tablets with thin protective coatings and drug-loaded microdevices. We demonstrate three-dimensional visualization of the different drug/polymeric materials, constituting a drug delivery device, with imaging depth of 225 μm.

KEYWORDS

chemometrics, decomposition, drug delivery systems, Raman imaging, volumetric mapping

1 | INTRODUCTION

Three-dimensional (3D) confocal Raman mapping is one of the most promising techniques to study the chemical composition of complex organic[1] and inorganic materials.[2] The common way to present Raman data is based on peak intensity visualization. However, this method leads to artifacts in the visualization of chemical responses due to overlapping of the spectral profiles from different compounds.[3] In order to overcome this problem, several chemometric approaches have been developed.[4–8] It has recently been demonstrated that quantitative volumetric Raman imaging can be applied to cell culture samples[1] where a vertex component analysis (VCA) algorithm is used.[9] However, quantitative volumetric Raman imaging is still a state-of-the-art technique with few reported applications, mostly due to interference from molecular fluorescence,[10] limited sample transparency at the laser excitation wavelength,[11,12] complexity of chemometric analysis,[13] and low Raman scattering cross section of the chemical components.[4] Herein, we demonstrate that these obstacles can be overcome, using tablets with thin protective coatings and drug-loaded polymeric microcontainers (MCs) as challenging test cases. MCs are cylindrical microdevices with only the top side open, fabricated in the epoxy polymer SU-8.[14] It has been shown that MCs improve oral bioavailability of model drugs due to their unidirectional release.[15,16] Our studied MCs are loaded with a polymer matrix (polyvinylpyrrolidone [PVP]) and a drug (i.e., ketoprofen, naproxen) and used for oral drug delivery.[15] The MC material, SU-8 is highly fluorescent[17] and the MC cavity, loaded with the PVP/drug matrix (low optical transparency), is approximately 225 μm deep.[15]

The molecular fluorescence of the drug compounds can be suppressed in several ways.[18] However, the most proper and common techniques like Kerr-gated Raman,[19] ultraviolet Raman,[20] and near-infrared (NIR) Fourier transform (FT) Raman[21] are not well applicable to the diffraction limited deep volumetric Raman imaging (dVRI) due to the limitation connected with confocality or penetration depth. The most appropriate solution is the usage of NIR lasers (780, 785, and 830 nm) as excitation sources.[13] For the sole purpose of suppressing sample fluorescence, Nd:YAG lasers with 1,064-nm excitation wavelength are a very attractive solution;[22] however, the Raman scattering cross section becomes usually too low for dVRI. In this situation, where the fluorescence of drug systems takes place, we decided to use NIR laser with wavelength of 785 nm.

Different drug systems have previously been imaged with Raman spectroscopy. However, the transparency is limited, even when using a laser at 785-nm excitation wavelength.[23] Using a commercially available Raman microscope equipped with 785-nm laser excitation, we were able to scan only the top 15 μm of MCs.[24] It is important to mention that in-depth Raman mapping is also limited by off-axis laser refraction effects leading to Raman signal attenuation and decreased axial resolution.[25–28] The usual way of addressing this problem is to increase the laser power and/or the exposure time. However, the latter leads to an unrealistic total time of 3D map acquisition (>3 days). Increasing the laser power, instead, overheats and burns the sample.

Herein, we present an efficient solution to solve the previously discussed problems of dVRI of samples that manifest fluorescence and low transparency. This result was achieved by the development of a confocal Raman microscope with high Raman signal throughput, optimization of sample mapping method, and further chemometric hyperspectral data analysis based on non-negative least squares (NNLS).[3] Preliminary experimental results were shown in our previous study.[29] Here, we present a detailed description of the optical and analytical solutions implemented in the dVRI method.

2 | INSTRUMENTATION

For dVRI, an optical setup should have diffraction limited confocal performance, high throughput from sample to detector, and spectral resolution limited within a spectroscopic sensor pixel size.

To match the required conditions, we designed and constructed a high throughput confocal Raman microscope based on an on-axis lens type spectrograph (Figure 1a). Design of the optics was performed in Zemax Optics Studio 18.9. As an excitation source, a single mode frequency stabilized laser from Thorlabs LP785-SAV50 (785 nm, 50 mW) was used. Lenses f1 and f2 were used as a beam expander for the proper fit between the diameter of the laser beam and the microscope objective pupil lens. A Zeiss objective 100×/0.75 HD DIC was used.

A detailed description of the microscope's *X*, *Y*, and *Z* scanning procedures has been reported earlier.[13]

The collimated Raman beam from the microscope objective is propagated through the dichroic mirror Dm1 and the edge filter Ed1 and focused on the spectrograph slit by the Lens f3. The spectrograph consists of fused silica transmitting grating (averaged diffraction efficiency 96%), collimating Lens f4 and focusing Lens f5 (see details in Ilchenko et al.[13]). As an imaging sensor, we used an NIR enhanced deep cooling charge-coupled device (CCD; Andor iDus416).

Due to the aberration corrected Raman system design, diffraction limited axial resolution was reached without a classical pinhole.[13] The confocal mode was organized in a cross slit geometry in which, the vertical slit orientation was implemented in the entrance of the spectrometer, and the horizontal slit orientation was organized on the spectroscopic CCD focal plane by the readout of the selected rows. An example of a typical Raman spectrum measured with our system is shown in Figure 1b. In the zoomed region, it is possible to observe that the Raman spectrum is compressed into one row on a spectroscopic sensor. Due to the absence of moving parts, extra mirrors and the usage of custom aberration corrected optics with NIR coatings, high total Raman system throughput (from sample to detector) was reached at the level of 91%.[30]

3 | METHODS

To address the problem of the Raman signal attenuation taking place in tablets and MCs, we designed and constructed a highly sensitive confocal Raman microscope (Figure 1a). However, even in this case, we verified that the Raman signal attenuation at an MC depth of 100 μm was significant, and consequently, the system was insufficient for mapping the total depth of the MC (225 μm). As a solution, we decided to increase the laser power delivered to the sample from 5 to 30 mW. To efficiently remove the heat generated by the laser, a Peltier cooling system of the sample holder was implemented. The temperature was kept at 8°C during all 3D mapping experiments. The 3D mapping was organized so that the first mapped axis dimension was *Z*, the second—*X*, and the third—*Y* (Figure 1c). This approach provided a more

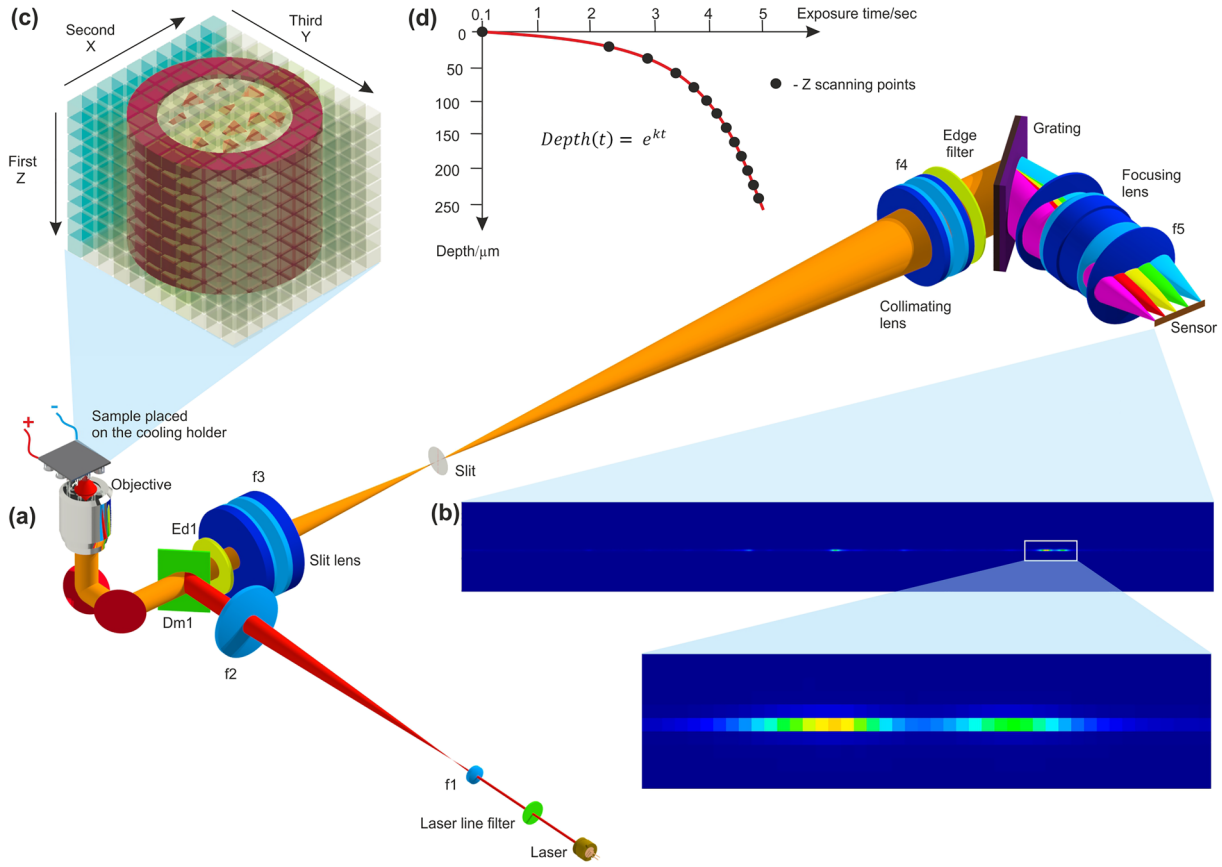

FIGURE 1 Volumetric Raman mapping (deep volumetric Raman imaging) system. (a) Optical design of the Raman microscope, (b) example of an image from the spectroscopic charge-coupled device (CCD) Raman signal; the zoomed region shows that the spectrum is compressed into one row on the CCD sensor, (c) $Z \rightarrow X \rightarrow Y$ mapping algorithm applied to the microcontainer measurements for a more homogeneous heat distribution, (d) depth dependent acquisition algorithm, which exponentially increases the exposure time for each mapping z-stack

homogeneous heat distribution through the volume of tablets and MCs in comparison with a traditional mapping where the laser is kept at one z-stack for much longer time.

In order to maintain the signal-to-noise ratio of Raman spectra captured at different depths in the same value range, we performed a depth dependent acquisition algorithm, which exponentially increases the exposure time for each z-stack mapped (Figure 1d).

All of the presented volumetric Raman maps were measured at the following conditions: The exposure time per point varied from 0.1 to 3 s (exponentially scaled depending on the mapping depth), the CCD was operated in a single track mode with vertical beaning equal to 4 pixels. The step size was 6 and 12 μm in lateral and axial dimensions, respectively; 3D map dimensions were 50 × 50 × 25 pixels or 300 × 300 × 300 μm. The total measurement time per map was equal to 26 hr. All spectra were background corrected using rolling-circle filter[31] (circle radius was 300 cm^{-1}). Savitzky–Golay filtering algorithm was applied for data smoothing.[32] All acquisition and data analysis procedures including NNLS were realized in our own software written in Delphi.

4 | RESULTS

As a demonstration example of the performance of dVRI, we used a pharmaceutical tablet consisting of a cellulose matrix (Figure 2). The depth dependent exponential decay of the intensity of the Raman spectrum of cellulose (Figure 2a [red line]) is shown in Figure 2b (orange line). The Raman signal intensity after exponential exposure time correction is shown in Figure 2b (blue line). In a homogenous medium, the presented dependence should have a constant Raman intensity versus tablet depth. The deviation from constant dependence behavior was caused by inhomogeneity of material compression at the stage of tablet production.[33] Nevertheless, we demonstrated that applied correction can significantly improve signal-to-noise ratio in-depth dependent Raman mapping. The depth cross section and the dVRI map of titanium dioxide

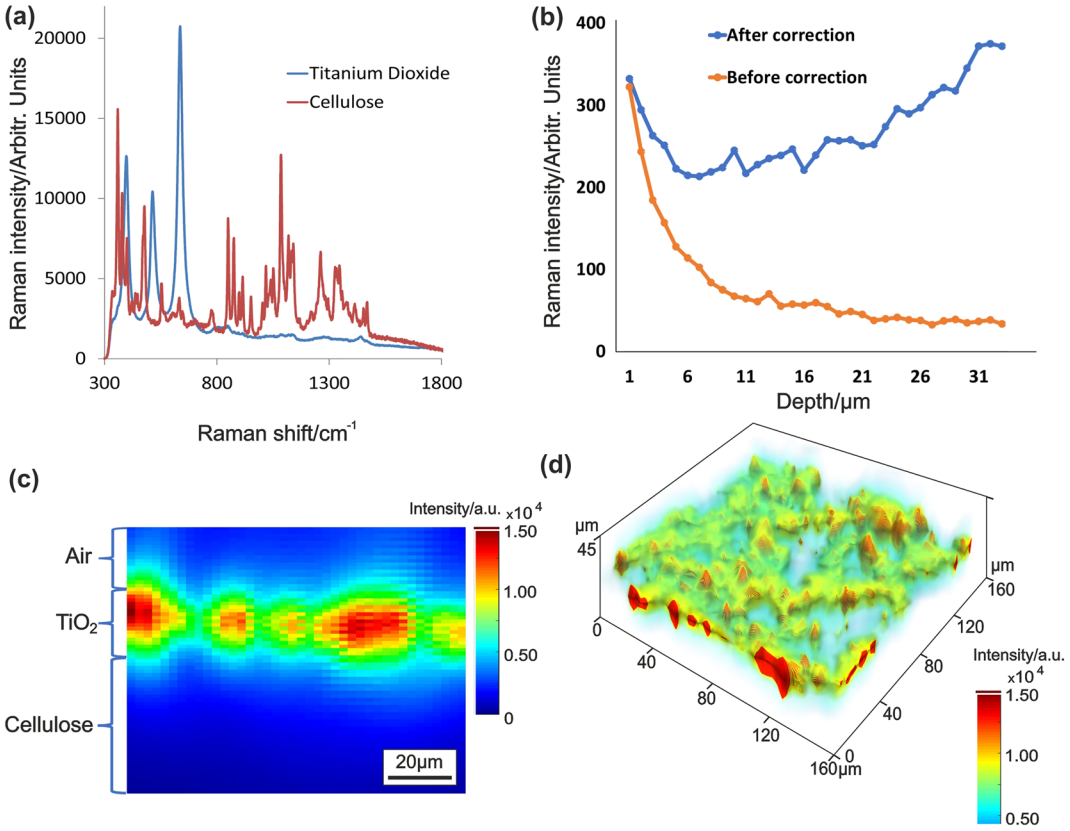

FIGURE 2 Deep volumetric Raman imaging (dVRi) of a pharmaceutical tablet. (a) Raman spectra of a model tablet consisting of titanium dioxide coating and cellulose, (b) depth dependent Raman intensity profile of the tablet matrix (cellulose) before (orange line) and after (blue line) exponential correction, (c) depth cross section of the cellulose tablet coated with titanium dioxide, (d) dVRI map of titanium dioxide coating represented at peak intensity of Eg mode (635 cm^{-1}) with an imaging depth of 45 μm

coating on the surface of the cellulose tablet represented at peak intensity of Eg mode (635 cm^{-1}) and is shown on Figure 2c,d (Movie S1). It is possible to observe small titanium dioxide clusters on the surface of the tablet. This result demonstrates that dVRi is applicable for coating thickness determination, as well as for verification of coating homogeneity. Such information is crucial and can be used to optimize a tablet manufacturing process.

As an example of dVRi applicability for multicomponent polymeric devices for drug delivery, we demonstrate results obtained on MCs. Ketoprofen and naproxen are poorly soluble drugs, and it was of utmost important to evaluate their solid state once loaded into MCs. The solid state influences the dissolution of the drugs. For the purpose of chemical decomposition, we measured Raman spectra of the pure chemical components presented in the MCs (Figure S1a). Following this, we identified the peak positions of amorphous and crystalline drug (ketoprofen), PVP, SU-8, and Si with minimum peak overlapping. The selected peaks are 1,000, 1,688, 932.5, 809, and 520 cm^{-1}, respectively.

The Raman intensity-based 3D plots are shown in Figure S1b. We do not present a map of crystalline ketoprofen as the response of crystalline drug was not observed in the Raman map. The problem of overlapping Raman peaks prevents the use of univariate data analysis to map the distribution of components: Ketoprofen, PVP, and Si responses are all present on the walls of the MCs (Figure S1a,b). Drawing conclusions on the drug distribution is thereby not possible. To solve this issue, a chemometric hyperspectral data analysis was applied.

Species contributions in multicomponent mixtures can be determined from the spectral data using different chemometric techniques.[4,8,9] Most algorithms are based on the fact that the recorded spectra are the weighted sum of pure components spectra present in the investigated mixture. Based on this assumption, the unfolded data matrix **X** may be decomposed into a concentration matrix **C** and a spectral matrix $\mathbf{S}^{T}$

$$X = CS^{T} + E \quad (1)$$

where **E** is the residual matrix (Figure 3a).

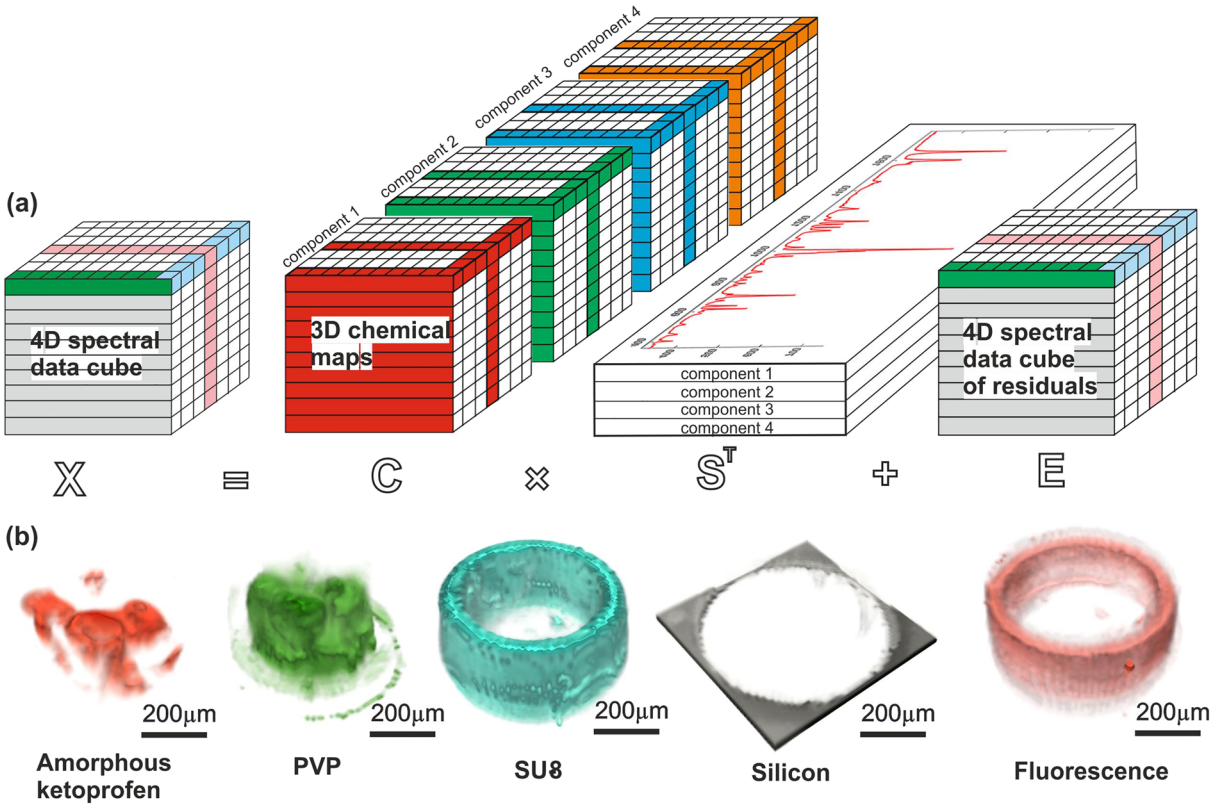

FIGURE 3 Volumetric chemical imaging. (a) Illustration of the nonnegative least squares (NNLS) algorithm for the decomposition of hyperspectral Raman data into normalized chemical responses, (b) volumetric chemical maps of MCs components (amorphous ketoprofen, PVP, SU-8, and Si) built after NNLS analysis. The volumetric distribution of fluorescence is shown to the right

When the pure spectrum of each component is known, their concentration can be obtained directly using a classical least squares (CLS) approach[3]:

$$C = DS(S^TS)^{-1} \quad (2)$$

The limitation of CLS lies in the assumption that the separately measured pure spectra of the chemical components $\mathbf{S}^T$ have identical profiles in the mixture (experimentally measured matrix **D**).[3] In the case of the MCs analysis, we were able to (a) measure the pure spectra of each component (Figure S1a) and (b) demonstrate that there were no chemical interactions occurring between components in the loaded MCs. Therefore, CLS algorithm was a perfect solution for our case study. The LS was limited with two constrains, applied to the matrix **C**: nonnegativity and normalization. Such algorithm is usually called NNLS analysis.[3] As an extra component, in $\mathbf{S}^T$, we also included a spectrum generated from the lenses of the microscope objective. Finally, we obtained 3D plots of the normalized distributions of amorphous ketoprofen, PVP, SU-8, and Si (Figure 3b). Microscope objective response was excluded from the normalization procedure because it is not involved in the set of chemical components of MCs. Comparing with the 3D maps obtained by the peak intensity (Figure S1b), NNLS decomposed maps of MCs components were clearly separated and ready for distribution analysis.

Because the acquired spectral data set (matrix **X**) was background corrected, the presence of fluorescence was subtracted from the impact into the decomposition result. However, the residuals obtained after the background subtraction were used for the representation of the distribution of fluorescence response (see pink image on Figure 3b). It mainly represents the fluorescence from SU-8 and fluorescent impurities outside of the MC.

In Figure 4a, we present the combined volumetric chemical maps of the MCs components. It is possible to conclude that (a) PVP was homogeneously distributed throughout the MCs, (b) amorphous ketoprofen was deposited on the top of MCs walls and over the surface of PVP, (c) no signal from crystalline ketoprofen was recorded as we obtained zero values from the crystalline ketoprofen channel, and (d) the Si substrate response was recorded only at the bottom of the map. More visual information can be obtained from Movie S2.

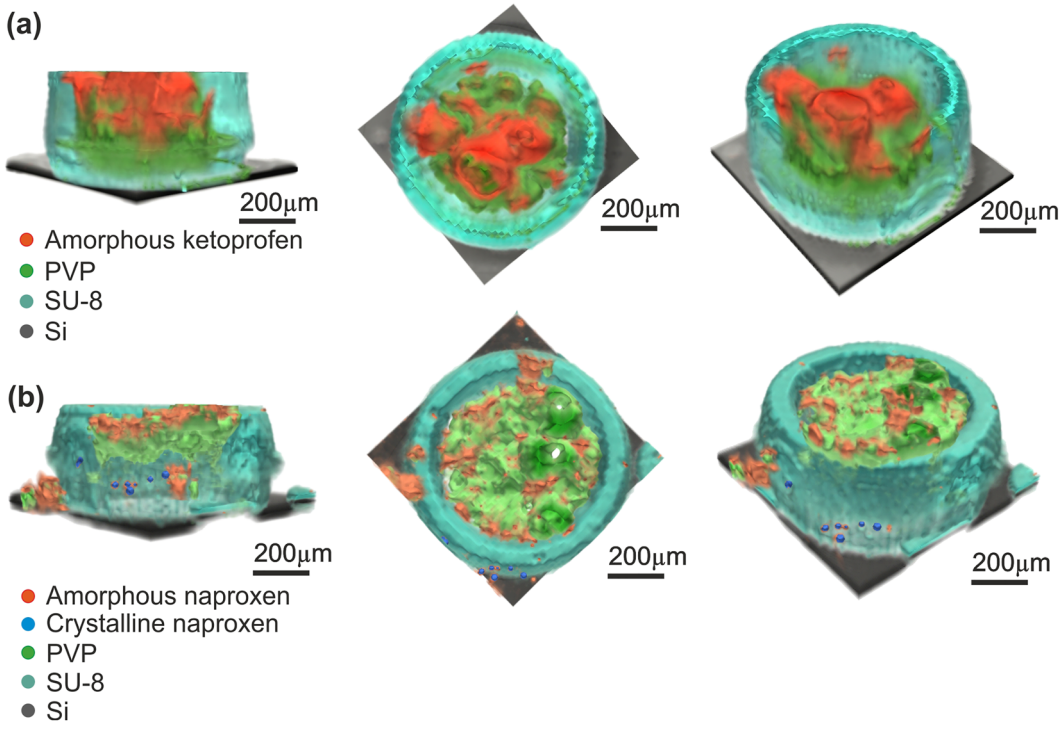

FIGURE 4 Combined volumetric chemical maps of MCs loaded with ketoprofen (a) and naproxen (b) are shown from different rotation angles

The universality of the developed method for highly sensitive volumetric Raman chemical imaging of fluorescent and highly absorptive samples was tested on several drugs and MCs with different dimensions in our previous study.[29] As an example, the distribution of naproxen loaded into the polymer matrix is shown on Figure 4b (Movie S3). In this case, naproxen was concentrated on the top of the MCs, with limited penetration into the PVP matrix. A minor amount of crystalline drug was observed outside the MCs (Figure 4b). It is important to notice that we were not able to distinguish crystalline naproxen in our previous work[29] due to incomplete methodology of dVRi. In particular, fluorescence impact (see Figure 3b) was not taken into account.

5 | CONCLUSIONS

Volumetric Raman chemical imaging method with improved Raman signal detection has been developed and applied for monitoring the coating thickness on pharmaceutical tablets and the distribution of different components in a drug-loaded polymer matrix in MCs for oral drug delivery of poorly soluble drugs. According to the location and the solid state of the drug, it is therefore possible to better understand and predict its release in vitro and/or in vivo. A confocal Raman microscope with improved sensitivity and diffraction limited axial resolution was developed for this purpose. For efficient mapping of the absorptive MCs material, exponential depth dependent exposure correction was applied, and the sample was kept under continuous cooling for efficient heat removal. The obtained 3D Raman maps of MCs have been decomposed into chemical volumetric images by the usage of NNLS analysis, where the signal of fluorescence was extracted from background correction as an individual contribution. Crucial information on the distribution/state of drugs in the polymer matrix (PVP) in MCs material (SU-8) was hereby obtained.

ACKNOWLEDGEMENTS

The authors would like to acknowledge the Center for Intelligent Drug Delivery and Sensing Using Microcontainers and Nanomechanics (IDUN) whose research is funded by the Danish National Research Foundation (DNRF122) and Villum Fonden (Grant 9301).

CONFLICT OF INTEREST

The authors declare no competing financial interest.

ORCID

Oleksii Ilchenko https://orcid.org/0000-0002-2150-895X

REFERENCES

[1] C. Kallepitis, M. S. Bergholt, M. M. Mazo, V. Leonardo, S. C. Skaalure, S. A. Maynard, M. M. Stevens, *Nat. Commun.* . https://doi.org/10.1038/ncomms14843
[2] A. Zoubir, *Raman Imaging*, Vol. 168, Springer Berlin Heidelberg, Berlin, Heidelberg **2012**, vol.
[3] O. O. Ilchenko, Y. V. Pilgun, A. S. Reynt, A. M. Kutsyk, *Ukr. J. Phys.* **2016**, *61*, 519.
[4] K. C. Gordon, C. M. McGoverin, *Int. J. Pharm.* **2011**, *417*, 151.
[5] B. Vajna, G. Patyi, Z. Nagy, A. Bódis, A. Farkas, G. Marosi, *J. Raman Spectrosc.* **2011**, *42*, 1977.
[6] Y. Roggo, K. Degardin, P. Margot, *Talanta* **2010**, *81*, 988.
[7] J. Jaumot, A. de Juan, R. Tauler, *Chemom. Intel. Lab. Syst.* **2015**, *140*, 1.
[8] A. de Juan, R. Tauler, *Anal. Chim. Acta* **2003**, *500*, 195.
[9] J. M. P. Nascimento, J. M. B. Dias, *IEEE Trans. Geosci. Remote Sens.* **2005**, *43*, 898.
[10] D. Wei, S. Chen, Q. Liu, *Appl. Spectrosc. Rev.* **2015**, *50*, 387.
[11] N. J. Everall, *Analyst* **2010**, *135*, 2512.
[12] N. J. Everall, *Appl. Spectrosc.* **2000**, *54*, 1515.
[13] O. Ilchenko, Y. Pilgun, T. Makhnii, R. Slipets, A. Reynt, A. Kutsyk, D. Slobodianiuk, A. Koliada, D. Krasnenkov, V. Kukharskyy, *Vib. Spectrosc.* **2016**, *83*, 180.
[14] J. Nagstrup, S. Keller, K. Almdal, A. Boisen, *Microelectron. Eng.* **2011**, *88*, 2342.
[15] C. Mazzoni, F. Tentor, S. A. Strindberg, L. H. Nielsen, S. S. Keller, T. S. Alstrøm, C. Gundlach, A. Müllertz, P. Marizza, A. Boisen, *J. Control. Release* **2017**, *268*, 343.
[16] L. H. Nielsen, A. Melero, S. S. Keller, J. Jacobsen, T. Garrigues, T. Rades, A. Müllertz, A. Boisen, *Int. J. Pharm.* **2016**, *504*, 98.
[17] A. Qualtieri, T. Stomeo, L. Martiradonna, R. Cingolani, M. De, *Lithography*, InTech **2010**.
[18] A. C. De Luca, M. Mazilu, A. Riches, C. S. Herrington, K. Dholakia, *Anal. Chem.* **2010**, *82*, 738.
[19] P. Matousek, M. Towrie, C. Ma, W. M. Kwok, D. Phillips, W. T. Toner, A. W. Parker, *J. Raman Spectrosc.* **2001**, *32*, 983.
[20] S. Asher, C. Johnson, *Science (80-.)* **1984**, *225*, 311.
[21] J. Pironon, J. Sawatzki, D. J.*Geochim. Cosmochim. Acta* **1991**, *55*, 3885.
[22] A. P. Oliveira, R. A. Bitar, L. Silveira, R. A. Zângaro, A. A. Martin, *Photomed. Laser Surg.* **2006**, *24*, 348.
[23] C. Adlhart, W. Baschong, *Int. J. Cosmet. Sci.* **2011**, *33*, 527.
[24] M. Chiara, T. Fabio, A. Anastasia, J. Rasmus, M. Jacob, S. Roman, I. Oleksii, K. S. N. Line, B. Anja, *Distribution and quantitative analyses of poorly water soluble drugs loaded by supercritical CO2 impregnation in microcontainers with different sizes*, 2018 CRS annual meeting, New York **2018**.
[25] N. J. Everall, *Appl. Spectrosc. Vol. 54, Issue 6, pp. 773–782* **2000**, *54*, 773.
[26] J. L. Bruneel, J. C. Lassègues, C. Sourisseau, *J. Raman Spectrosc.* **2002**, *33*, 815.
[27] C. Sourisseau, P. Maraval, *Appl. Spectrosc. Vol. 57, Issue 11, pp. 1324–1332* **2003**, *57*, 1324.
[28] G. Gouadec, L. Bellot-Gurlet, D. Baron, P. Colomban, **2012**, pp. 85–118.
[29] C. Mazzoni, F. Tentor, A. Antalaki, R. D. Jacobsen, J. Mortensen, R. Slipets, O. Ilchenko, S. S. Keller, L. H. Nielsen, A. Boisen, *ACS Biomater Sci. Eng.* **2019**, *5*, 2935.
[30] O. Ilchenko, *Nat. Commun. 10*, 1. https://doi.org/10.1038/s41467-019-13504-8
[31] N. N. Brandt, O. O. Brovko, A. Y. Chikishev, O. D. Paraschuk, *Appl. Spectrosc.* **2006**, *60*, 288.
[32] M. Člupek, P. Matějka, K. Volka, *J. Raman Spectrosc.* **2007**, *38*, 1174.
[33] I. C. Sinka, J. C. Cunningham, A. Zavaliangos, *J. Pharm. Sci.* **2004**, *93*, 2040.

SUPPORTING INFORMATION

Additional supporting information may be found online in the Supporting Information section at the end of this article.

How to cite this article: Slipets R, Ilchenko O, Mazzoni C, Tentor F, Nielsen LH, Boisen A. Volumetric Raman chemical imaging of drug delivery systems. *J Raman Spectrosc*. 2020;1–7. https://doi.org/10.1002/jrs.5869

Supporting Information

Volumetric Raman chemical imaging of drug delivery systems

Roman Slipets, Oleksii Ilchenko*, Chiara Mazzoni, Fabio Tentor, Line Hagner Nielsen, Anja Boisen

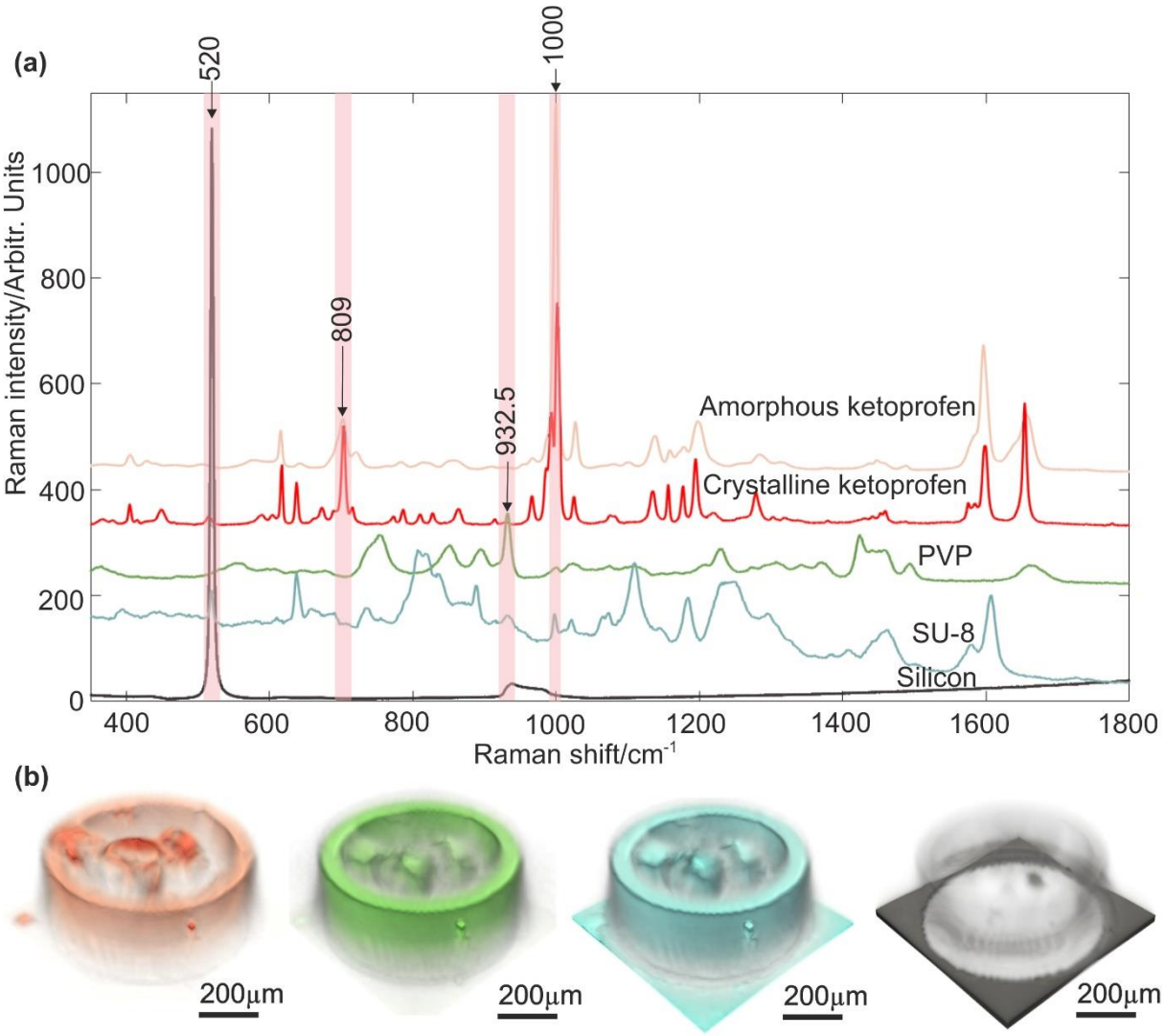

Figure S1. (a) Raman spectra of MCs components (amorphous and crystalline ketoprofen, PVP, SU-8 and Si), (b) volumetric Raman maps of peak intensity distribution of MCs components (pink - amorphous ketoprofen peak at 1000cm^{-1}, green – PVP peak at 932.5cm^{-1}, blue – SU-8 peak at 809cm^{-1}, black – silicon peak at 520cm^{-1}). Peak positions representing MCs components are shown on Fig. 1Sa.

Paper II

Wide Line Surface-Enhanced Raman Scattering Mapping

O. Ilchenko, **R. Slipets**, T. Rindzevicius, O. Durucan, L. Morelli, M.S. Schmidt, K. Wu, and A. Boisen

Advanced Materials Technologies. 2020

ADVANCED MATERIALS TECHNOLOGIES
www.advmattechnol.de

Wide Line Surface-Enhanced Raman Scattering Mapping

Oleksii Ilchenko, Roman Slipets, Tomas Rindzevicius, Onur Durucan, Lidia Morelli, Michael S. Schmidt, Kaiyu Wu, and Anja Boisen*

Surface-enhanced Raman spectroscopy (SERS)-based molecular detection at extremely low concentrations often relies on mapping of a SERS substrate. This yields a large number (>1000) of SERS spectra that can improve the limit of detection; however, the signal collection time is a major constraint. In this work, a wide line (WL) laser focusing technique aimed at fast mapping of SERS substrates is presented. The WL technique enables acquisition of thousands of SERS spectra in a few seconds without missing any of the electromagnetic "hot spots" in the illuminated area. In addition, the SERS signal averaging across the line in the WL mode displays extremely high signal-to-noise ratios. The advantages of the WL technique for SERS-based sensing are verified using different analyte molecules, that is, p-coumaric acid and melamine. Results show that the limit of detection can be improved by one order of magnitude compared to results obtained using a commercial Raman microscope.

1. Introduction

Surface-enhanced Raman spectroscopy (SERS) is a well-established analytical tool in various biosensing applications that allows detection of analytes down to the single molecule level.[1,2] It has been shown that the dominant part contributing to SERS is the electromagnetic (EM) enhancement mechanism,[3,4] which is based on extreme amplification and localization of the incoming optical field by metal nanoparticles that support localized surface plasmon resonance (LSPR).[3] Efficient LSPR coupling between nanoparticles leads to EM enhancement factors $>10^8$. Sites containing highly confined optical fields in the vicinity of metallic nanostructures are often referred to as the EM "hot spots."[5,6]

For SERS, despite its phenomenal sensitivity, reliable quantification of target molecules has been hindered by i) non-uniform nature of the plasmonic near fields, ii) fluctuation in the SERS signal intensities due to unspecific binding,[7] and iii) poor wafer-to-wafer reproducibility and uniformity of SERS substrates.[8] To circumvent these issues, large area SERS mapping is an advantageous approach for obtaining statistically reliable and reproducible results which significantly improves limit of detection (LoD).[8–12] The method is particularly relevant for quantification of low-abundance molecules, for example, at sub-nanomolar concentrations where recording large SERS maps also greatly reduces the error of estimated molecular concentrations.[10,13,14] Typically, if Raman active molecules display high affinities toward a SERS surface, satisfactory SERS signals can be obtained. However, a multitude of important molecules, such as p-coumaric acid[15] and glucose[16] do not bind to nanoplasmonic surfaces. In these cases, obtaining reliable SERS spectra already at concentrations <1 µM is a challenging task. The SERS signal intensity is low and typically comparable to the SERS substrate background originating from, for example, surface contaminants. Here, large area SERS mapping is highly suitable. However, the Raman signal collection time is still a major constrain. For example, if we use the following conditions: exposure time t = 0.1 s, diffraction limited step size, 785 nm laser excitation wavelength, and a 10× magnification objective, the time required to measure the surface area of, for example, ≈20 mm^2 is around 7.7 days (step = (0.66*0.785 µm)/0.3 = 1.73 µm). Since this is practically impossible, the SERS map acquisition step size is usually increased to 10–100 µm, which still leads to a collection time of 32–3.2 h, respectively. Decreasing the step size might be counterproductive since at ultra-low analyte concentrations (<nM), the probability for a target molecule to be situated in the EM "hot spot" is extremely low, that is, most "hot spots" are unoccupied. This leads to a very few detectable points on a SERS surface. Even though statistical interpretation of such SERS data has been theoretically investigated,[13] fast acquisition of SERS signals over a large surface area with a diffraction limited step size is still challenging and has not yet been addressed.

There are three basic fast Raman mapping methods developed for spontaneous Raman scattering applications: line-focus (LF),[17–20] line-scan (LS),[21–23] and direct Raman or wide-field (WF) Raman.[24–27] All three techniques require an imaging design of the Raman setup with an aberration corrected spectrograph for simultaneous acquisition of spectra from multiple points on a sample through a laser line illumination. However, the LF technique produces a static image of a laser line on a sample, and therefore, it requires a lower laser power density compared to a dynamic movement of the laser focus point in the LS technique.[21] Since the LS method utilizes extremely high laser powers, typically ≈5–100 mW focused into

Dr. O. Ilchenko, R. Slipets, Dr. T. Rindzevicius, Dr. O. Durucan, Dr. L. Morelli, Dr. M. S. Schmidt, Dr. K. Wu, Prof. A. Boisen
The Danish National Research Foundation and Villum Foundation's Center for Intelligent Drug Delivery and Sensing Using Microcontainers and Nanomechanics (IDUN)
Department of Health Technology
Technical University of Denmark
Ørsteds Plads Building 345C, Kgs. Lyngby 2800, Denmark
E-mail: olil@dtu.dk

The ORCID identification number(s) for the author(s) of this article can be found under https://doi.org/10.1002/admt.201900999.

DOI: 10.1002/admt.201900999

a diffraction limited spot, the technique is generally not suitable for SERS-based sensing applications. In SERS, in order to minimize photo-induced effects and thermal processes, a laser power on the order of ≈10 μW at the sample is generally preferred.[28] In the WF Raman technique, an acousto-optic tunable filter (AOTF),[29] instead of a spectrometer, can be used to collect spectra. The technique is capable of simultaneously acquiring a 2D Raman map at a selected Raman shift, and the spectral scanning is performed via AOTF. However, there are a few limitations. First, the laser intensity should be homogeneously distributed on the sampled area, which is a significant experimental challenge. Second, the spectral resolution is usually quite low (10–40 cm^{-1}) and is highly wavelength dependent. Third, the tuning range and transparency of AOTFs is limited to ≈100 nm in the near IR range. WF Raman technique can also be realized by the use of fiber optic bundles with a so-called "round to slit" configuration whereby a wide area of a sample can be covered simultaneously.[30] This method provides high spectral resolution. However, due to the space between fibers in the bundle and addition of optical elements in the system, this method leads to a reduced lateral resolution and decreased signal throughput. Since, the use of fiber optic bundles for Raman signal detection is challenging to combine with sample mapping, this technique is not well suited for microscopy applications.

All the aforementioned methods have been aimed at spontaneous Raman scattering measurements, and the techniques are not directly suitable/designed for SERS-based sensing applications. First of all, a SERS substrate is usually a 2D nanoplasmonic surface; hence, confocal properties of the Raman system can be omitted. Moreover, with respect to SERS, a fast Raman mapping should be able to 1) simultaneously target multiple EM "hot spots" across a large SERS substrate surface area (≈mm^2); 2) perform SERS measurements at a relatively low laser power density, that is, ≈1–50 μW $μm^{-2}$ at a sample; 3) integrate a depolarized laser illumination mode which is important for probing all randomly oriented "hot spots."

In this work, we implemented all the aforementioned criteria and developed a new SERS substrate mapping technique termed wide line (WL) SERS. The WL-SERS method is based on the diffraction limited line (DLL) Raman mapping, where the width of a laser line is increased by at least an order of magnitude. This leads to a reduced spatial resolving power; however, a given SERS substrate area can be imaged 33 600 times faster compared to using a classical point focus SERS mapping mode. The performance of the WL-SERS method is illustrated by mapping the Raman signal of p-coumaric acid and melamine deposited on gold-coated silicon nanopillar (AuNP) SERS substrates with LSPR optimized for near-IR range,[8] where detection limit and signal-to-noise ratio are significantly improved.

2. Results and Discussion

2.1. Wide-Line SERS Microscope

A schematic illustration of the WL-SERS experimental setup is shown in **Figure 1**a. The main parts are the following:

(i) Laser beam delivery system where the laser point focus, DLL, and WL laser illumination modes are implemented.
(ii) Custom-made, epi-detection-based microscope for simultaneously obtaining an optical image and a laser beam illumination profile on the surface of the SERS substrate.
(iii) Raman beam delivery system capable of projecting an aberration-corrected laser line image onto a spectroscopic imaging sensor.

The optical paths of laser beam delivery, microscope, and Raman scattering were designed using the Zemax Optic Studio 19.4 software package. The optomechanical design of the setup was performed using Autodesk Inventor 2019. Custom-designed mechanical parts were milled from aluminum and combined with commercially available optomechanical parts.

2.1.1. Laser Beam Delivery

The laser beam delivery layout consists of two geometries: the first geometry is a point illumination mode (Figure 1b), and the second geometry is for producing the DLL and WL sample illumination modes (see Figures 1c and 1d, respectively). A pair of motorized flip mirrors are used for switching between point and DLL/WL illumination modes. The DLL-focus mode is achieved when a sample is illuminated by a diffraction limited laser line, that is, d_{DLL} = 2.8 μm in width using a 785 nm laser excitation wavelength and 10× magnification lens. The WL mode is obtained by expanding the width of the laser line, that is, d_{WL} > 2.8 μm and up to 64 μm, which is achieved by adjusting the position of a cylindrical lens f3 in the laser delivery path (see Figure 1a). The laser beam profile is modified using a set of cylindrical lenses f1–f5, including laser line generator lens f6. Detailed description of beam modification in laser beam delivery system was described in our recent work.[31]

In this work, we utilized a multimode high-power laser (785 nm, P_{max} ≈ 500 mW) with a line-shaped beam output profile as an excitation source. The obtained distribution of the laser intensity in the DLL and WL modes is shown in Figures 1c and 1d, respectively. Since the laser output profile consists of multiple modes, ≈15–20% variation in the laser intensity across the entire length of the focused laser line ($L_{DLL/WL}$ ≈ 2 mm) at the sample focal plane was observed. The variation was corrected by normalizing the laser intensity at each pixel on the CCD camera.

In order to image the entire ≈2 mm long DLL/WL laser profile on a sample, the aperture for the laser beam (after a lens f7) was designed to fit the field of view (FOV = 2.2 mm) of the 10× near-infrared (NIR) microscope objective. A WL-SERS high-speed Raman mapping of 100 μM trans-1,2-bis (4-pyridyl) ethylene (BPE) in ethanol solution deposited on the AuNP substrate, displaying only minor aberrations, is shown in Movie S1, Supporting Information.

2.1.2. Microscope Construction

One of the main components in the Raman microscope is a dichroic beamsplitter (BS) that reflects the incident laser

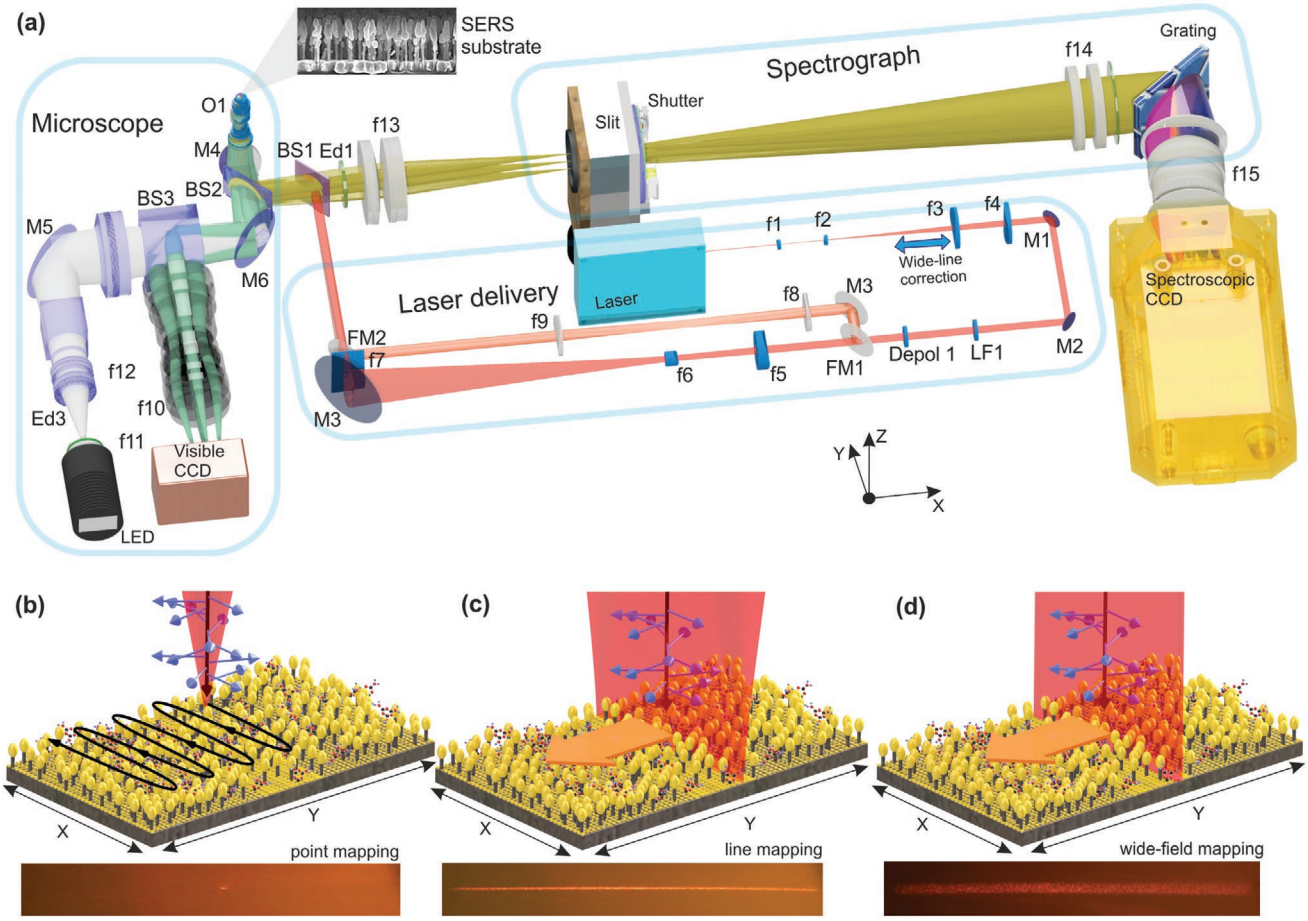

Figure 1. WL SERS microscope: a) WL SERS microscope optical design, b) point, c) DLL, and d) WL laser illumination modes in SERS microscope. The orientation of EM vectors (blue arrows in (b)–(d)) represents depolarized laser irradiation. Laser polarization in WL mode is parallel to the surface of the SERS chip.

wavelength (785 nm) and transmits the Stokes-shifted Raman spectrum. In this case, the laser beam is reflected from BS1 (Figure 1a) and guided through a set of mirrors into the 10× microscope objective, and then focused on the SERS chip surface in either the point, DLL, or WL illumination mode (see Figure 1b–d).

The sample surface is imaged by a camera while collecting SERS spectra, which simplifies the measurement procedure. This was realized by combining the incident laser beam with visible light from a light emitting diode (LED) using BS2 (Figure 1a). To ensure that the white light source is not contributing to the recorded SERS spectra in the 785–1000 nm wavelength range, the NIR emission from the LED source was suppressed (on the order $\approx 10^6$) by an edge filter (Ed3).

An example of the WL-SERS surface scanning process is shown in Movie S1, Supporting Information. The camera projection optics is designed to enable imaging of the entire microscope objective FOV with a homogeneous sample illumination. This is usually not the case for most commercial Raman microscopes that only utilize the central part of FOV.

2.1.3. Raman Beam Delivery

The back-scattered Raman signal is collected and collimated into a parallel beam using a 10× NIR microscope objective O1 (see Figure 1a). The beam is then reflected by a mirror M4, BS2, and propagates through BS1, Ed1, and the lens f13. The optical path from sample to spectrograph slit is designed to transmit an aberration-free image of the DLL or WL laser profile. This is achieved by combining a low numerical aperture (NA) collimating lens with a high NA focusing lens in the imaging spectrograph. The low NA collimating lens f14 allows one to insert the lens f13 with equal NA. Therefore, the focal length of f13 (113 mm) is sufficiently long for delivering the DLL/WL image from the sample surface to the slit, and with correct input angles at the spectrometer. In this way, beam cutting inside the spectrograph is avoided. Alternatively, the image delivery can be obtained using two intermediate lenses between a microscope objective and a lens; however, this leads to losses in the Raman signal and increases aberrations.[19,20]

Due to the low NA of the slit and collimating lenses, even at d_{slit} = 100 µm slit, the pixel size limited spectral resolution is ≈1.8–2.5 cm^{-1} throughout the Raman Stokes shift range of 350–2200 cm^{-1}.

Optomechanical design and photograph of the constructed WL-SERS system is shown in Figure S1, Supporting Information. The modification of the laser beam profile in WL mode during propagation through the laser beam delivery optical path is shown in Figure S2, Supporting Information.

2.2. Beam Polarization Parameters

The LSPR excitations that generate the EM "hot spots" in the AuNP structures depend on the polarization of the incident field.[32] Since AuNP clusters display random orientations,[8] which is often the case for SERS substrates,[33] illuminating a SERS substrate by a depolarized laser beam leads to more efficient excitation of the EM "hot spots," that is, achieving higher surface-averaged EM field enhancement factors (EFs), leading to stronger SERS signals since $I_{SERS} \propto |\mathbf{E}|^4$.[32] The influence of a depolarized laser excitation on different nanoparticle clusters was investigated using COMSOL software package (see **Figure 2**a,b). The electric field distribution around different nanoparticle clusters shown in Figure 2b indicates that more "hot spots" are generated using two incident polarizations. Furthermore, the calculated ratios of surface averaged electrical field EF $R_{<EEF>}^4$ and absorption R_{Abs} between orthogonal and linear polarizations for different nanoparticle configurations, shown in Figure 2a, indicate that depolarized excitation is beneficial for obtaining higher SERS signals without introducing additional heat which could cause desorption and decomposition of analytes.

To verify this experimentally, we decided to implement depolarized or circular irradiation in our WL microscope. However, the control of the laser polarization state becomes a challenging task when the angle of linear polarization differs from 0° and 90° with respect to the coordinate system shown in Figure 1a.[34] In Figure S3, Supporting Information, we present polarization simulation results obtained in Zemax Optics Studio for the laser polarization propagation after beam reflection from mirrors. Simulation was performed at three different input polarization angles: 0°, 90°, and 45° for linear polarization (Figure S3b, Supporting Information). It is clear that polarization states 0° and 90° orientation propagate without linear phase (LA) anisotropy effects on dielectric mirrors and dichroic filters. However, if the angle of polarization differs from 0° or 90°, LP anisotropy takes place, which is shown in Figure S3b, Supporting Information. As a result, linear polarization becomes elliptical. It is important to notice that the type of dielectric or interference coating also has an effect on the LP anisotropy.

Polarization analysis was also performed for circular input polarization (see bottom images in Figure S3b, Supporting Information). Here, we see that LP anisotropy leads to the transformation of circular polarization into elliptical on the sample focal plane. Therefore, the summarized polarization state will have a preferred orientation which will affect our depolarization experiment.

Figure 2c illustrates laser beam path in WL mode obtained in Zemax Optics Studio. Figure 2d represents polarization analysis in wide line mode from four differently oriented input polarizations (0°, 45°, 90°, and 135°). Such combination of polarization orientations makes it possible to simulate a quazi-depolarized laser beam, after propagation through a liquid crystal polymer depolarizer from Thorlabs (cat. number DPP25-B) named Depol 1 in Figure 1a. LP anisotropy becomes significant for input polarization components, which differ from 0° and 90°.[34] Polarization simulation analysis also shows that this effect takes place at the edges of the line. However, polarization artifacts are at the level of a few degrees and can thus be neglected.

In order to check system polarization artifacts generated in the Raman beam delivery path, we performed additional polarization analysis in Zemax Optics Studio (see Figure S3c,d, Supporting Information). Our signal collection setup was designed in a way so that it has no LP anisotropy for any input linear polarization. An example, with 45° orientation of polarization, is shown in Figure S3d, Supporting Information. Due to the presence of a dichroic filter in the beam path, the signal is influenced by linear amplitude (LA) anisotropy, where S and P components of EM wave transmit with different efficiency

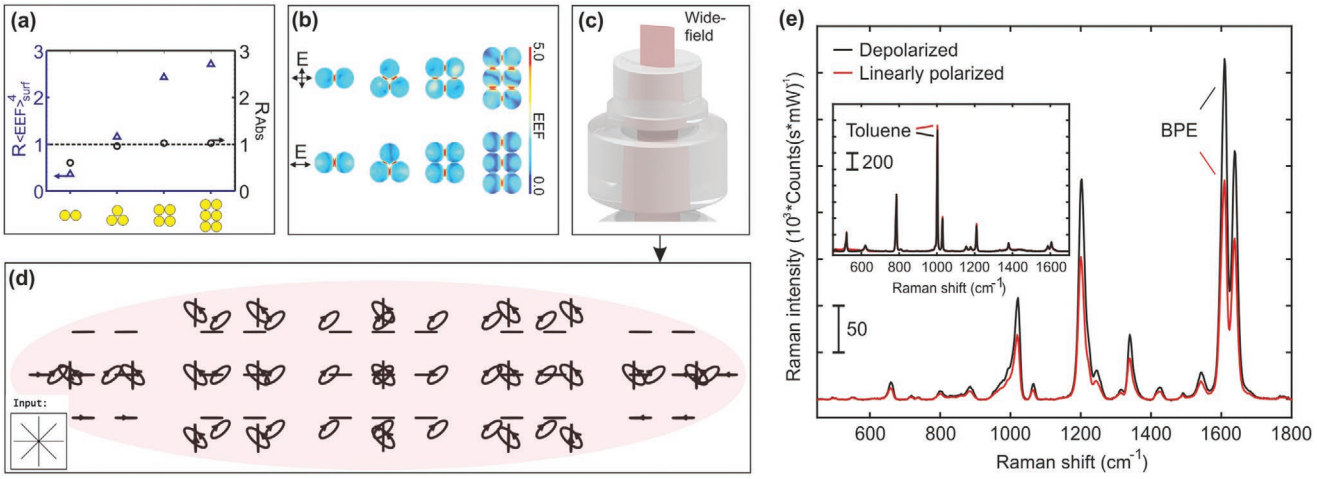

Figure 2. Depolarized laser excitation impact on SERS efficiency. a) Calculated ratios of surface averaged electrical field EF $R_{<EEF>}^4$ and absorption R_{Abs} between orthogonal and linear polarizations for different nanoparticle configurations under same irradiance; b) simulated electric field distribution around nanoparticle clusters under orthogonal and linear incident polarizations with same irradiance; c) illustration of the laser beam path in WL mode obtained in Zemax Optics Studio; d) polarization analysis in WL mode performed in Zemax Optics Studio (depolarization effect from depolarizer was simulated as a mixture of four differently oriented EM waves); e) the enhancement of BPE SERS signal obtained on NP substrate by changing from linearly polarized (red line) to depolarized (black line) laser excitation condition The insert graph demonstrates optical system independency to the orientation of laser polarization on the sample of liquid toluene.

through the filter. This effect leads to a tilt of polarization with a maximum angle of 2° in the entire spectral range of the Raman stokes shift.

Therefore, the most critical part of signal collection with regard to polarization orientation sensitivity is the diffraction grating (named as grating in Figure 1a). It is important to notice that our spectrograph is based on a low polarization dependent transmitting fused silica diffraction grating from Ibsen Photonics (cat. number RAMAN NIR-1500-908). Due to low polarization dependency of the grating, we were able to carry out quantitative Raman intensity comparison between polarized and depolarized experiments as described below.

A depolarizer (Depol 1) was introduced into the laser beam delivery part of the WL-SERS setup (see Figure 1a). The depolarizer was fixed on a manual flip mount. A difference between polarized and depolarized laser excitation cases was realized by inserting Depol 1 into the laser beam path. First, we evaluated that the setup is insensitive to the polarization of the incident field by recording Raman spectra of toluene in a cuvette using the i) linearly polarized and ii) depolarized WL illumination modes. Both spectra display virtually identical Raman mode intensities (see the inset in Figure 2e). In order to be sure that the Raman beam delivery optical path is insensitive to the polarization orientation, we also verified that a Raman spectrum of toluene has virtually identical intensities at different laser polarizations. Next, SERS spectrum of 10 μM BPE deposited on the AuNP surface was recorded in the depolarized WL mode and it shows ≈50% increase in the SERS intensity compared to the linearly polarized WL case (see Figure 2e).

It is important to notice that simulations in Comsol (Figure 2a,b) were done under the assumption that depolarized light is formed as a mixture of two orthogonally polarized beams. However, the depolarizer produces multiple randomly polarized beams. For a correct comparison with simulation results, we repeated an experiment with two orthogonally polarized beams focused on the sample as shown in Figure S4a, Supporting Information. The orientation of the half wave plate placed before polarized beam splitter can equalize the intensity between orthogonal beams recombined on the second non-polarized beam splitter. By rotation of the half wave plate we can change polarization parameters in the sample focal plane from the linear polarized case to the case with two orthogonally polarized laser beams. In such geometry, equal total intensity is maintained automatically in both experiments. This experiment demonstrated similar increase in the SERS intensity of BPE compared to the linearly polarized case (around ≈50%) as shown in Figure 2e. For simplicity of optics, all further depolarized experiments were done with the use of depolarizer Depol 1.

2.3. Signal-to-Noise Ratio Comparison

Pixel limited spectral resolution of the WL SERS system is ≈1.8–2.5 cm^{-1}. A relationship between d_{slit} and spectral resolution of the setup was evaluated using 100 μM of BPE deposited on the AuNP SERS substrates (see **Figure 3**a). The peak width of the 1602 cm^{-1} BPE mode is ≈10–15 cm^{-1}. It means that the spectral resolution obtained at d_{slit} = 100 μm can be reduced by a factor of ≈4. At d_{slit} = 400 μm, the spectral resolution is

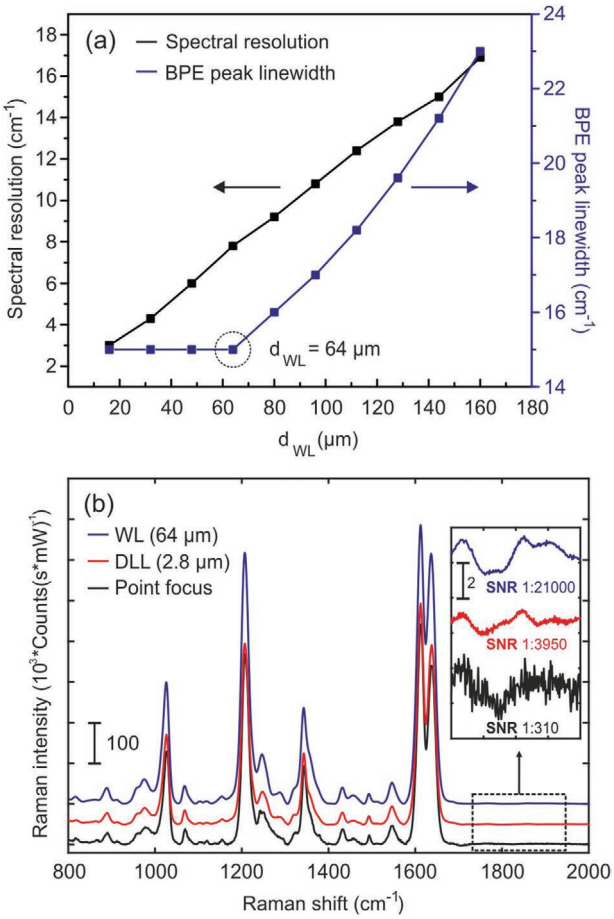

Figure 3. a) Spectral resolution test in WL mode. Black plot: spectral resolution dependence versus line thickness; blue plot: the linewidth of BPE peak with central position 1602 cm^{-1} versus line thickness. b) Comparison of SERS microscope laser illumination modes. a) SERS spectra of BPE (10 μM concentration) measured on Au nanopillars substrate at point (black), DL line (red), and WL (blue) illumination modes; b) zoomed spectra in the range 1750–1950 cm^{-1} for SNR demonstration. All presented spectra were acquired at equal conditions: 0.2 mW $μm^{-1}$ of laser intensity, laser wavelength 785 nm, exposure time 0.1 s, 10× magnification microscope objective. SNR was measured as signal divided on RMS noise.

≈8 cm^{-1}, which corresponds to d_{WL} ≈ 64 μm (L_{WL} ≈ 2 mm) at the sample focal plane when using a 10× microscope objective. Therefore, the maximum possible width of a laser line in the WL illumination mode is 64 μm, which is ≈22 times broader compared to the diffraction limited line width (d_{DLL}). It is important to mention that such line widening only becomes possible if the spectral resolution of the spectrometer is higher than the expected spectral line width of the Raman peaks.

The performance of the setup in terms of signal-to-noise ratios (SNR) has been evaluated for the point, DLL, and WL focus modes, by measuring 10 μM of BPE deposited on the AuNP substrates in a droplet with volume 5 μL (see Figure 3b). Results show that the WL mode yields a two orders of magnitude higher SNR compared to the point focus mode under the same measurement condition: 10× magnification lens, 0.1 s exposure time, 0.2 mW $μm^{-2}$ irradiance, 400 μm slit size, ≈8 cm^{-1} spectral resolution (see also Movie S2, Supporting Information).

This can be explained by calculating laser illumination surface areas for the three cases ($L_{DLL/WL} \approx 2$ mm), which are ≈25 μm^2, ≈6000 μm^2 ($d_{DLL} = 2.8$ μm), and ≈128 000 μm^2 ($d_{WL} = 64$ μm) for the point, DLL, and WL illuminations, respectively. The ratios between point/DLL and point/WL illumination areas are 1:240 and 1:5120, respectively. The improvement in SNRs can be calculated as a square root of these ratios which yields 15 and 72 times higher SNRs for the two cases. Experimentally obtained SNR ratios are: point: 1:310; DLL: 1:3950; and WL: 1:21 000 (see Figure 3b). The measured improvements in SNRs for the DLL and WL modes are 13 and 68 times, respectively, which is in good agreement with the calculated values. The difference in values can be explained by several sources of errors. First, point and WL areas can differ from the calculated values. Second, corrections for signal attenuation on the edges of the WL can be applied with wrong coefficients. It is important to notice that CCD pixels across spectral dimension were not averaged by post processing or CCD binning in both point and WL modes.

Performance of our system can be compared with existing commercially available Raman line-focus microscopes. Fundamentally, they should provide SNR at the same level as we demonstrate for DLL focus mode. Our system would have an advantage when the WL mode is applied. Based on the calculations presented above, SNR will be improved 5.2 times in WL mode compared to DLL mode.

2.4. p-Coumaric Acid Detection

p-Coumaric acid (pHCA) is a precursor of phenolic compounds which are extremely important for food[35] and cosmetics industries.[36] It has been shown previously that pHCA produced by genetically engineered *Escherichia coli* cultures can be quantitatively detected using the point-focus-based SERS mapping technique with a reported detection limit (LoD) of 10 μM of pHCA in ethanol.[15] We used an x–y step size of 100 μm to map the AuNP SERS surfaces. In order to demonstrate the performance of the WL-SERS method, different concentrations of pHCA down to 1 μM in ethanol were deposited on the AuNP substrates and detected using both 1) the point focus and 2) WL illumination modes for comparison (see results in **Figure 4**).

In point focus mode, 8 × 10 points (80 spectra, step size 263 μm in X direction, 423 μm in Y direction) for each SERS map were collected at 0.2 s per point exposure time, that is, 16 s per SERS map. A schematic illustration of the data acquisition process and averaged pHCA SERS spectra is shown in Figure 4a–c, and the process is visualized in Movie S3, Supporting Information. The estimated LoD of pHCA using the 1187 cm^{-1} and 1610 cm^{-1} vibrational mode intensities is ≈10 μM, which is in accordance with the aforementioned study.[15]

Next, SERS spectra from the same samples were recorded using the WL illumination mode (see Figure 4d–f). The WL field is scanned in the y-direction with a step size equal to the width of the WL profile, that is, $d_{WL} = 64$ μm in this case (see Movie S4, Supporting Information). A SERS map for each concentration of pHCA is collected using 80 steps at 0.2 s exposure/step (16 s per map). Note, the total exposure time for each SERS map is the same as in the point-focus case. The obtained averaged SERS spectra for the WL mode are shown in Figure 4e. In this case, the same characteristic pHCA vibrational peaks are resolved well even at a concentration of 1 μM.

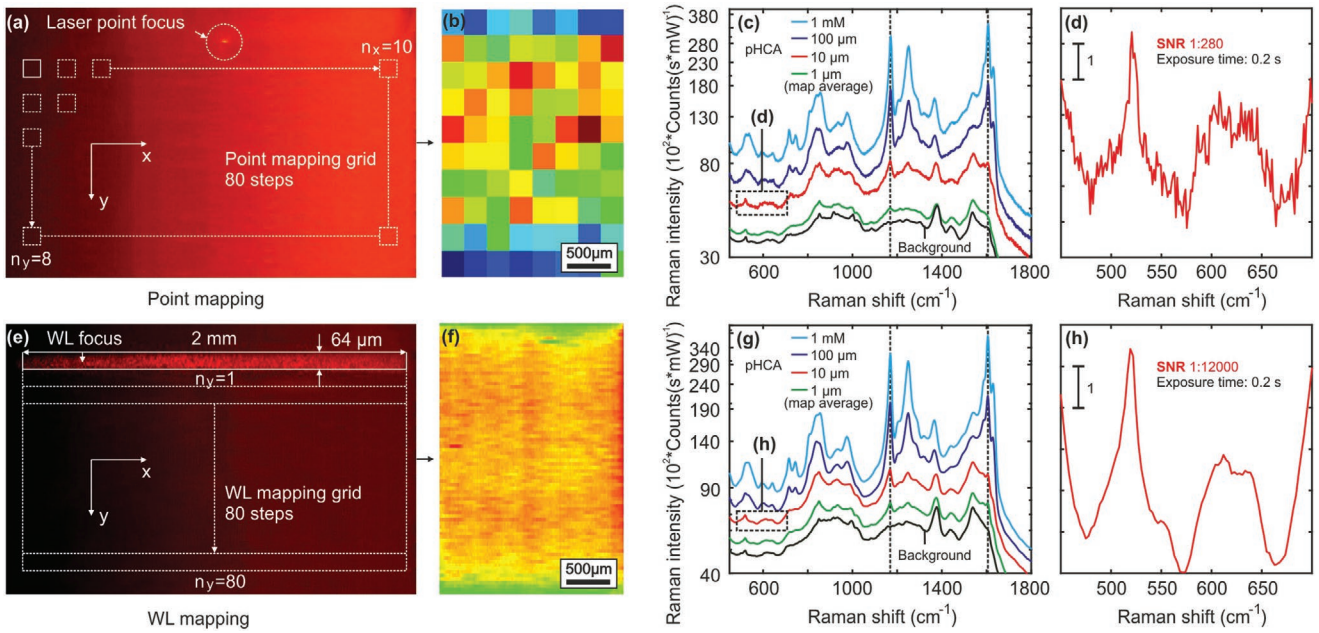

Figure 4. pHCA detection at point and WL illumination modes. a,e) Illustration of mapping algorithms at point and WL laser illumination, respectively; b,f) SERS maps of pHCA represented at peak position 1604 cm^{-1} for point and WL laser illumination modes, respectively; c,g) SERS spectra of pHCA at different concentrations on Au nanopillars substrate measured with SERS microscope at point and WL illumination modes, respectively; d,h) zoomed spectrum region of pHCA at 10 μM concentration obtained at point and WL illumination modes, respectively. Point and WL illumination SERS spectra were acquired at equal conditions: 0.2 mW μm^{-2} of laser irradiance, laser wavelength 785 nm, exposure time 0.2 s, 10× magnification microscope objective.

The results show that the WL-SERS method is highly suitable for molecular detection where both the SNR and LoD can be significantly boosted compared to the standard laser point-focus mode. In the illustrated pHCA case, the SNR and LoD are improved by a factor of ≈43 and 10, respectively.

2.5. Melamine Detection

Melamine is a nitrogen-rich chemical that has received much attention in recent years owing to a series of highly publicized food safety incidents.[37] Several melamine detection methods have been developed.[38] SERS-based detection is considered a promising technique; however, the LoD needs to be further decreased.[11] We measured melamine using a microfluidics platform. Melamine was spiked into raw milk at concentrations 1, 20, 40, 60, 80, 100, 150, and 200 ppm. Samples with different concentrations were placed into different positions on a SERS disk and centrifuged according to the rotation algorithm described in our previous work.[11,39]

At the end of the centrifugation process, each SERS chip was scanned in WL mode. Raman mapping was performed on the entire SERS chip surface with 0.2 s exposure time per WL; step size in *Y*-direction was equal to 15 µm. Total exposure time per map was 80 s. Collected SERS maps with dimensions (*X*, *Y*, wavenumber) were averaged through the *X* axis.

Averaged Raman maps for different melamine concentrations are presented in **Figure 5**a. Graphical representation of melamine peak intensity distribution at wavenumber 674 cm^{-1} along the SERS chip length is presented in Figure 5b. Similar to the pHCA case, we were able to detect the melamine peak at 1 ppm concentration level (Figure 5c). LoD obtained on commercial research-grade point mapping Raman microscope using equal sample pretreatment procedures was at the level of 10 ppm.[11] We consider this result an important achievement toward the development of a highly sensitive melamine detection method.

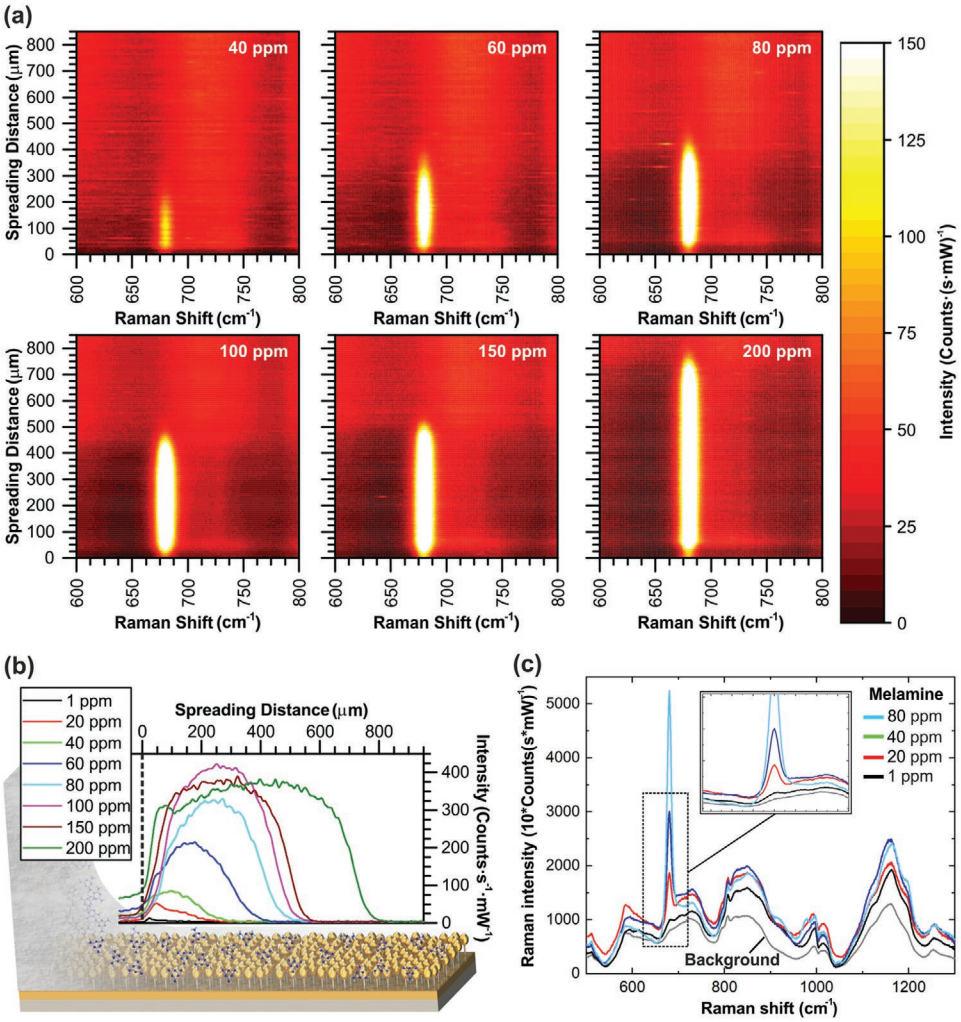

Figure 5. Melamine detection at WL illumination mode. a) Spreading distance versus Raman maps representing the distribution of melamine vibrational mode (673 cm^{-1}) through the SERS chip surface as a function of concentration (experimental parameters: 0.2 mW $µm^{-2}$ of laser irradiance, laser wavelength 785 nm, step size 15 µm, width of line 15 µm, exposure time per WL 0.2 s, 10× magnification microscope objective); b) graphical representation of melamine distribution though the SERS chip surface at different concentrations; c) SERS spectra of melamine at different concentrations on Au nanopillars substrate measured with SERS microscope at WL illumination mode. Characteristic peak of melamine is shown by dotted line (678 cm^{-1}).

3. Conclusion

We have developed a WL SERS microscope which provides improved sensitivity of molecular detection from SERS substrates. The system can operate in point, DL line, and WL laser focusing modes. Summarizing optical novelty of the setup, we can highlight two key benefits. First, WL illumination technique provides 8 cm^{-1} spectral resolution in the case of a sample illumination area of 2100 × 64 μm. At such conditions, the spatial resolving power of the microscope is reduced; however, the SERS substrate surface can be scanned three orders faster than the point-focus mode without losing any "hot spots." Second, laser polarization was designed to be parallel to the sample surface and randomly polarized in the WL illumination mode. Such condition provides the most efficient way of surface plasmon excitation on the NP SERS substrate.

Based on our previous results obtained on high-end commercial Raman equipment, we can conclude that a WL SERS microscope can provide at least one order lower LoD in WL mapping mode compared to the point mapping mode at equal exposure times.

Supporting Information

Supporting Information is available from the Wiley Online Library or from the author.

Acknowledgements

This work was financially supported by the European Research Council Proof of Concept grant (713474-THOR), European Research Council under the European Union's Seventh Framework Program (FP7/2007–2013) (Grant no. 320535-HERMES), and the IDUN Center of Excellence (Grant no. DNRF122) funded by the Danish National Research Foundation and the Villum Foundation (Grant No. 9301).

Conflict of Interest

The authors declare no conflict of interest.

Keywords

depolarized light, fast mapping, line-focus illumination, plasmon excitation, surface-enhanced Raman scattering

Received: November 6, 2019
Revised: March 7, 2020
Published online:

[1] S. Laing, L. E. Jamieson, K. Faulds, D. Graham, *Nat. Rev. Chem.* **2017**, *1*, 0060.
[2] A.-I. Henry, B. Sharma, M. F. Cardinal, D. Kurouski, R. P. Van Duyne, *Anal. Chem.* **2016**, *88*, 6638.
[3] S.-Y. Ding, E.-M. You, Z.-Q. Tian, M. Moskovits, *Chem. Soc. Rev.* **2017**, *46*, 4042.
[4] M. Kerker, *Acc. Chem. Res.* **1984**, *17*, 271.
[5] H. Wei, H. Xu, *Nanoscale* **2013**, *5*, 10794.
[6] S. M. Asiala, Z. D. Schultz, *Analyst* **2011**, *136*, 4472.
[7] L. Seballos, N. Richards, D. J. Stevens, M. Patel, L. Kapitzky, S. Lokey, G. Millhauser, J. Z. Zhang, *Chem. Phys. Lett.* **2007**, *447*, 335.
[8] M. S. Schmidt, J. Hübner, A. Boisen, *Adv. Mater.* **2012**, *24*, OP11.
[9] K. Wu, T. Rindzevicius, M. S. Schmidt, K. B. Mogensen, A. Hakonen, A. Boisen, *J. Phys. Chem. C* **2015**, *119*, 2053.
[10] J. Yang, M. Palla, F. G. Bosco, T. Rindzevicius, T. S. Alstrøm, M. S. Schmidt, A. Boisen, J. Ju, Q. Lin, *ACS Nano* **2013**, *7*, 5350.
[11] O. Durucan, T. Rindzevicius, M. S. Schmidt, M. Matteucci, A. Boisen, *ACS Sens.* **2017**, *2*, 1400.
[12] L. Morelli, L. Serioli, F. A. Centorbi, C. B. Jendresen, M. Matteucci, O. Ilchenko, D. Demarchi, A. T. Nielsen, K. Zór, A. Boisen, *Lab Chip* **2018**, *18*, 869.
[13] M. Palla, F. G. Bosco, J. Yang, T. Rindzevicius, T. S. Alstrom, M. S. Schmidt, Q. Lin, J. Ju, A. Boisen, *RSC Adv.* **2015**, *5*, 85845.
[14] J. Yang, M. Palla, F. G. Bosco, M. S. Schmidt, T. Rindzevicius, A. Boisen, J. Ju, Q. Lin, in *The 17th Int. Conf. Solid-State Sensors, Actuators and Microsystems (TRANSDUCERS EUROSENSORS XXVII)*, IEEE, Piscataway, NJ **2013**, pp. 1799–1802.
[15] L. Morelli, K. Zór, C. B. Jendresen, T. Rindzevicius, M. S. Schmidt, A. T. Nielsen, A. Boisen, *Anal. Chem.* **2017**, *89*, 3981.
[16] O. Lyandres, J. M. Yuen, N. C. Shah, R. P. VanDuyne, J. T. Walsh, M. R. Glucksberg, *Diabetes Technol. Ther.* **2008**, *10*, 257.
[17] K. A. Christensen, M. D. Morris, *Appl. Spectrosc.* **1998**, *52*, 1145.
[18] M. Ivanda, K. Furić, *Appl. Opt.* **1992**, *31*, 6371.
[19] A. F. Palonpon, J. Ando, H. Yamakoshi, K. Dodo, M. Sodeoka, S. Kawata, K. Fujita, *Nat. Protoc.* **2013**, *8*, 677.
[20] O. Ilchenko, Y. Pilgun, T. Makhnii, R. Slipets, A. Reynt, A. Kutsyk, D. Slobodianiuk, A. Koliada, D. Krasnenkov, V. Kukharskyy, *Vib. Spectrosc.* **2016**, *83*, 180.
[21] C. Otto, C. J. De Grauw, J. Greve, *Appl. Spectrosc.* **1997**, *51*, 1607.
[22] S. Deng, L. Liu, Z. Liu, Z. Shen, G. Li, Y. He, *Appl. Opt.* **2012**, *51*, 3701.
[23] J. Qi, W.-C. Shih, *Appl. Opt.* **2014**, *53*, 2881.
[24] J. Ling, S. D. Weitman, M. A. Miller, R. V. Moore, A. C. Bovik, *Appl. Opt.* **2002**, *41*, 6006.
[25] S. Schlücker, M. D. Schaeberle, S. W. Huffman, I. W. Levin, *Anal. Chem.* **2003**, *75*, 4312.
[26] A. Papour, J. H. Kwak, Z. Taylor, B. Wu, O. Stafsudd, W. Grundfest, *Biomed. Opt. Express* **2015**, *6*, 3892.
[27] H. R. Morris, C. C. Hoyt, P. Miller, P. J. Treado, *Appl. Spectrosc.* **1996**, *50*, 805.
[28] F. Svedberg, Y. Alaverdyan, P. Johansson, M. Käll, *J. Phys. Chem. B* **2006**, *110*, 25671.
[29] N. Gupta, R. Dahmani, *Spectrochim. Acta, Part A* **2000**, *56*, 1453.
[30] K. Shin, H. Chung, *Analyst* **2013**, *138*, 3335.
[31] P. O. Okeyo, O. Ilchenko, R. Slipets, P. E. Larsen, A. Boisen, T. Rades, J. Rantanen, *Sci. Rep.* **2019**, *9*, 7525.
[32] K. Wu, T. Rindzevicius, M. S. Schmidt, K. B. Mogensen, S. Xiao, A. Boisen, *Opt. Express* **2015**, *23*, 12965.
[33] K. Wu, T. Li, M. S. Schmidt, T. Rindzevicius, A. Boisen, S. Ndoni, *Adv. Funct. Mater.* **2018**, *28*, 1704818.
[34] O. Ilchenko, Y. Pilgun, A. Kutsyk, F. Bachmann, R. Slipets, M. Todeschini, P. O. Okeyo, H. F. Poulsen, A. Boisen, *Nat. Commun.* **2019**, *10*, 5555.
[35] N. Balasundram, K. Sundram, S. Samman, *Food Chem.* **2006**, *99*, 191.
[36] A. Ribeiro, M. Estanqueiro, M. Oliveira, J. Sousa Lobo, *Cosmetics* **2015**, *2*, 48.
[37] K. Rovina, S. Siddiquee, *J. Food Compos. Anal.* **2015**, *43*, 25.
[38] Y. Lu, Y. Xia, G. Liu, M. Pan, M. Li, N. A. Lee, S. Wang, *Crit. Rev. Anal. Chem.* **2017**, *47*, 51.
[39] O. Durucan, K. Wu, M. Viehrig, T. Rindzevicius, A. Boisen, *ACS Sens.* **2018**, *3*, 2492.

ADVANCED MATERIALS TECHNOLOGIES

Supporting Information

for *Adv. Mater. Technol.*, DOI: 10.1002/admt.201900999

Wide Line Surface-Enhanced Raman Scattering Mapping

Oleksii Ilchenko, Roman Slipets, Tomas Rindzevicius, Onur Durucan, Lidia Morelli, Michael S. Schmidt, Kaiyu Wu, and Anja Boisen*

Supporting Information

Wide line surface-enhanced Raman scattering mapping

Oleksii Ilchenko, Roman Slipets, Tomas Rindzevicius, Onur Durucan, Lidia Morelli, Michael S. Schmidt, Kaiyu Wu and Anja Boisen*

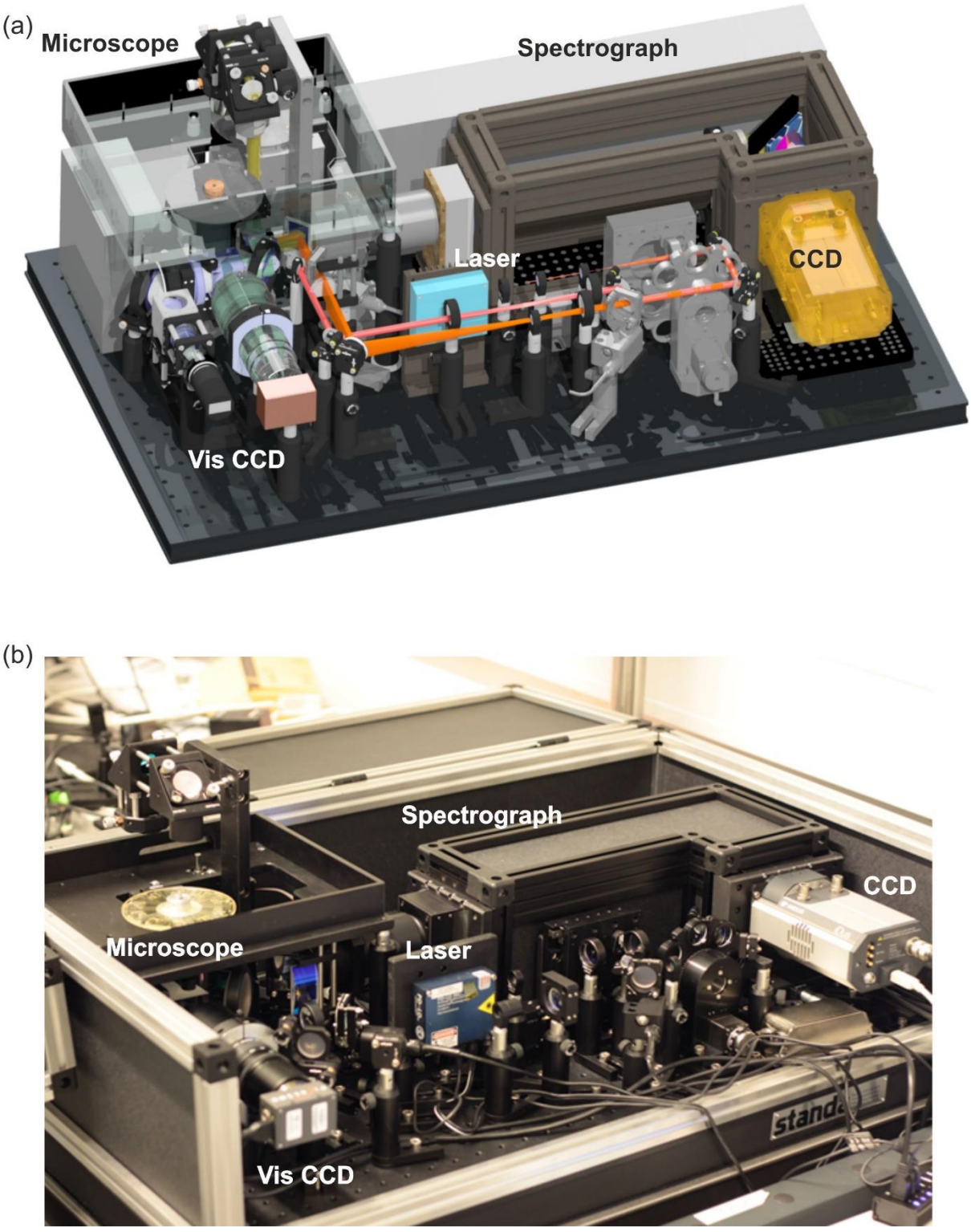

Figure S1. Optomechanical design (a) and photograph of constructed wide-line SERS microscope (b).

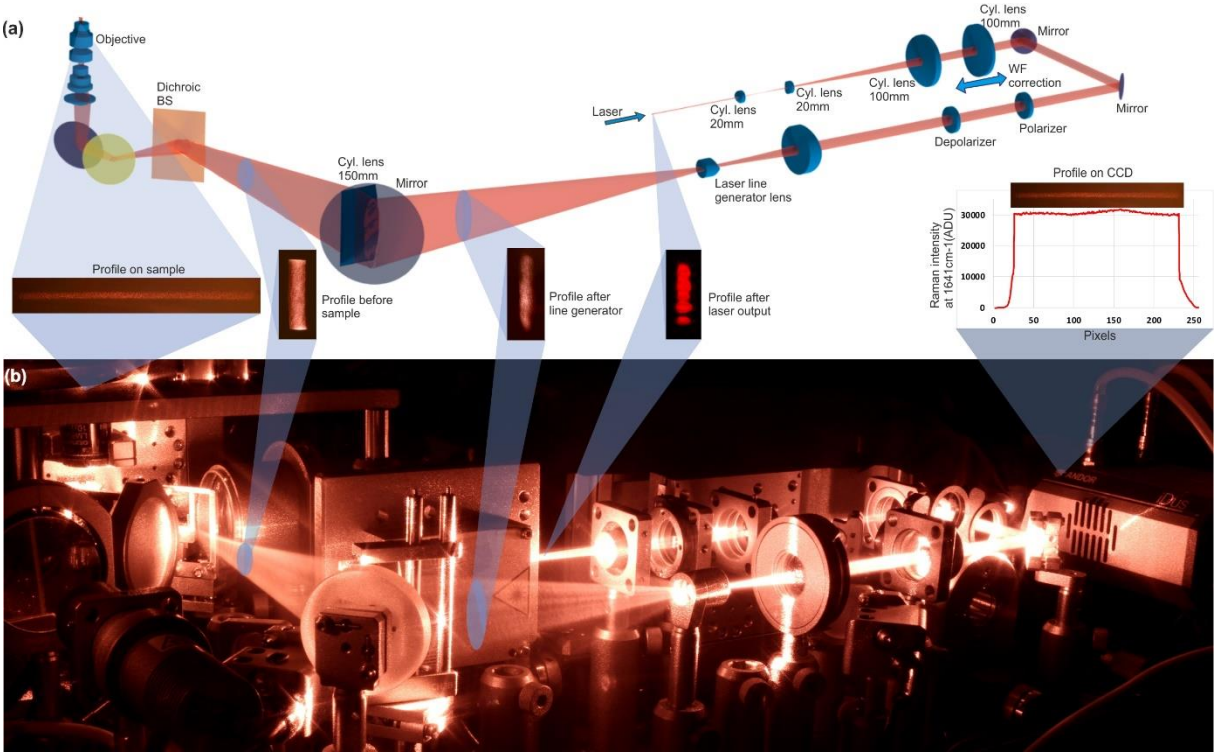

Figure S2. Optomechanical design (a) and photograph (b) of constructed wide-line SERS microscope. Inserted images demonstrate the modification of laser beam profile during the propagation through the laser beam delivery optical path.

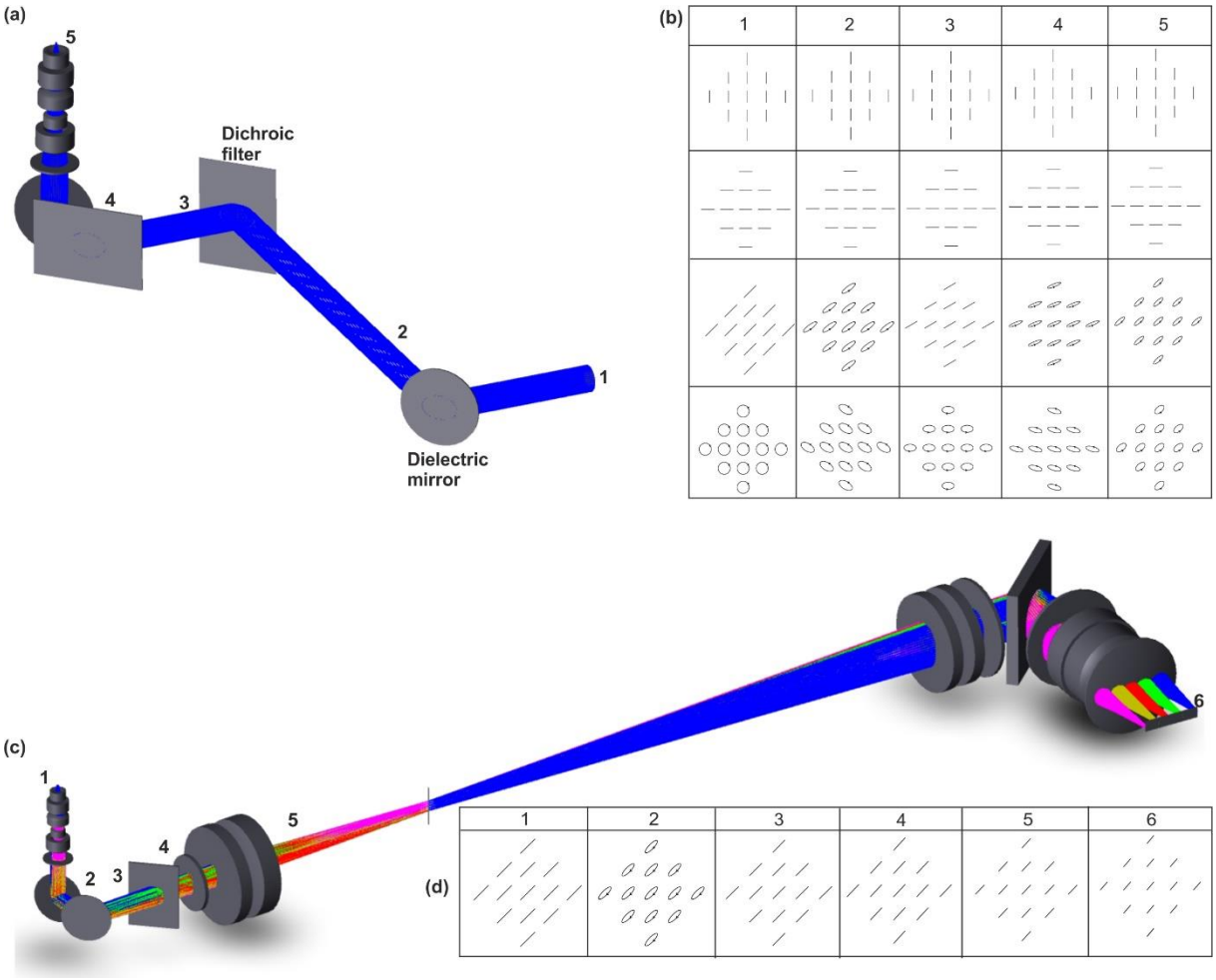

Figure S3. Polarization analysis for laser and Raman beams. (a) Optical schema of laser beam delivery system, **(b)** laser beam delivery system analyzed on laser polarization propagation with input orientation of 0°, 90°, 45° and circular polarization; (c) optical schema of Raman beam delivery system; (d) Raman beam delivery system analyzed on Raman polarization propagation with input orientation of 45°. Points 1 and 3 demonstrate the polarization state of Raman beam before and after compensation of phase shift between S and P components of electromagnetic wave. Compensation was realized by the proper orientation of mirrors between microscope objective and dichroic filter.

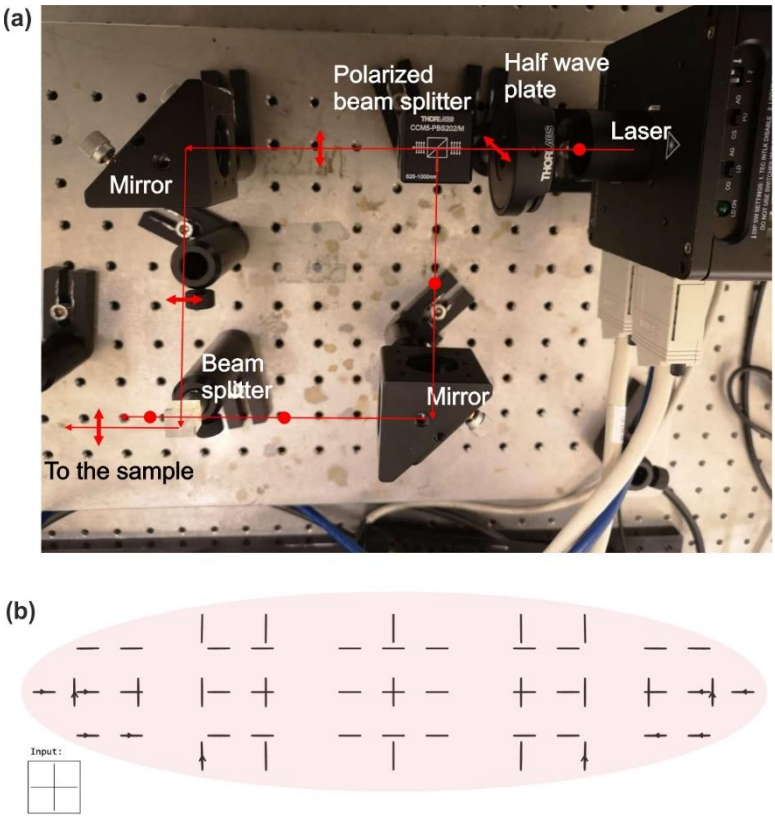

Figure S4. Depolarization experiment. **(a)** Optomechanical realization of orthogonally polarized laser beams; **(b)** polarization analysis in WL mode performed in Zemax Optics Studio for two orthogonally polarized input EM waves.

Paper III

Imaging of Dehydration in Particulate Matter Using Raman Line-Focus Microscopy

P.O. Okeyo, O. Ilchenko, R. Slipets, P.E. Larsen, A. Boisen, T. Rades, and J. Rantanen

Scientific Reports 9 (1). 2019

SCIENTIFIC REPORTS

OPEN

Imaging of dehydration in particulate matter using Raman line-focus microscopy

Received: 13 December 2018
Accepted: 29 April 2019
Published online: 17 May 2019

Peter Ouma Okeyo[1,2,3], Oleksii Ilchenko[2,3], Roman Slipets[2,3], Peter Emil Larsen[2,3], Anja Boisen[2,3], Thomas Rades[1] & Jukka Rantanen[1]

Crystalline solids can incorporate water molecules into their crystal lattice causing a dramatic impact on their properties. This explains the increasing interest in understanding the dehydration pathways of these solids. However, the classical thermal analytical techniques cannot spatially resolve the dehydration pathway of organic hydrates at the single particle level. We have developed a new method for imaging the dehydration of organic hydrates using Raman line-focus microscopy during heating of a particle. Based on this approach, we propose a new metastable intermediate of theophylline monohydrate during the three-step dehydration process of this system and further, we visualize the complex nature of the three-step dehydration pathway of nitrofurantoin monohydrate to its stable anhydrous form. A Raman line-focus mapping option was applied for fast simultaneous mapping of differently sized and shaped particles of nitrofurantoin monohydrate, revealing the appearance of multiple solid-state forms and the non-uniformity of this particle system during the complex dehydration process. This method provides an in-depth understanding of phase transformations and can be used to explain practical industrial challenges related to variations in the quality of particulate materials.

Interactions of water with solids are critical for most materials and can have a dramatic impact on their functionality[1]. In the pharmaceutical industry, the majority of the products are marketed as solid dosage forms. Approximately one-third of the existing drug compounds are estimated to have the ability to form hydrates that have different physio-chemical properties in comparison to their anhydrous counterparts[2]. There is an increasing interest in understanding the dehydration pathways of hydrates because of their key importance to processability and storage (preventing unwanted solid-state transformations)[3]. The dehydration of an organic hydrate, when exposed to an external stress such as temperature, pressure or humidity, can result in a mixture of solid-state forms making it challenging to reveal and track metastable intermediates[4]. This has inspired the development of several mechanistic schemes[5] for the classification of hydrates and most notably among them is the Rouen 96 model by Petit and Coquerel[6]. Rouen 96 assumes that every dehydration process results in the evacuation of water from the crystal structure and the formation of new anhydrous material (NAM) with the optional reorganization of the NAM. Two general classes describe the dehydration pathway and the evolution of NAM in relation to the stable hydrate and the anhydrous product. Class I assumes that the stable anhydrous form has a completely different crystal structure to its stable hydrate, whereas Class II describes the topotactic relationship between the hydrate and the dehydrated product. The Rouen 96 model is based on inorganic materials, that have well-defined pathways of dehydration, but real-life organic material particles contain imperfections resulting in cases, where multiple and crossing pathways can occur simultaneously in the same particle. Morris and Rodriguez-Hornedo also proposed a general structural classification for hydrates due to the location of water in channels or isolated sites in the crystal structure[7].

Standard solid-state analytical techniques including differential scanning calorimetry (DSC), thermal gravimetric analysis (TGA) and x-ray powder diffraction (XRPD) are commonly used to study the dehydration of

[1]Department of Pharmacy, University of Copenhagen, Universitetsparken 2, 2100, Copenhagen, Denmark. [2]The Danish National Research Foundation and Villum Foundation's Center for Intelligent Drug Delivery and Sensing Using Microcontainers and Nanomechanics (IDUN), Department of Health Technology, Technical University of Denmark, Ørsted Plads, 2800 Kgs Lyngby, Denmark. [3]Department of Health Technology, Technical University of Denmark, Ørsted Plads, 2800, Kgs Lyngby, Denmark. Correspondence and requests for materials should be addressed to O.I. (email: olil@dtu.dk) or J.R. (email: jukka.rantanen@sund.ku.dk)

organic hydrates[8]. These methods typically require a minimum of a few milligrams of the sample, which means that the analysis is based on several particles and does not consider differences between single particles. In addition, DSC and modulated DSC have a limited sensitivity to observe subtle thermal events, such as the appearance of metastable intermediates or complex overlapping thermal events[9]. Revealing metastable intermediates is of great pharmaceutical importance since they have different physical properties and are known to be more soluble than their stable counterparts[10]. Spectroscopic techniques such as Raman and near-infrared spectroscopy (NIR) are used at different stages of the drug development process and are well suited to monitor hydrate formation and dehydration during processing, but require long measurement times; risking dehydration on the hydrate[11,12]. Computational approaches have recently been used in order to determine the structural changes during dehydration and to identify an amorphous intermediate of ampicillin trihydrate[13]. These approaches provide a molecular-level understanding of dehydration pathways; however, they require experimental methods to confirm.

Herein, we report the use of Raman line-focus microscopy to visualize, at a single particle level, the dehydration pathway of two model drugs; theophylline monohydrate (TP MH) and nitrofurantoin monohydrate (NF MH II). We employ multivariate curve resolution (MCR)[14,15] and non-negative least squares (NNLS) in the data analysis in order to reveal their metastable solid-state intermediates, and to determine the dehydration pathways of TP MH and NF MH II.

Results

The solid-state analytical methods applied in this study confirmed the solid-state form of the model compounds of TP to be TP monohydrate (CSD refcode: THEOPH01), TP AH form II (CSD refcode: BAPLOT01) and NF to be NF MH II (CSD refcode: HAXBUD) and NF AH β (CSD refcode: LABJON02) (see Supplementary Figs 1, 2). The thermogram from TGA of TP MH revealed a 9% (one mole of water per mole of drug) weight loss between 55–80 °C. This weight loss occurred as a one-step process when using a heating rate of 10 °C/min. The DSC thermogram of TP MH dehydration resulted in a broad endotherm between 63–95 °C indicative of a channel hydrate[16]. In comparison, the thermogram from TGA analysis of NF MH II revealed a weight loss of 7% (one mole of water per mole of drug) at a heating rate of 10 °C/min. DSC results of NF MH II showed a sharp endotherm between 110–140 °C. The shape of the DSC thermogram from TP MH is suggesting that the dehydration process is a two-step process[17]. Supplementary Figs 3 and 4 show the variable temperature XRPD (VT-XRPD) results for the dehydration of TP MH and NF MH II. The diffractograms of both drugs showed the presence of the intermediate forms, but they were highly overlapped making it challenging to discern the distinct peaks for both drugs. An attempt was made to identify the subtle difference in peaks; however, preferred orientation played a dominating role in these measurements, as both drugs are needle-like in shape. Additionally, the time needed to collect an XRPD pattern is still relatively high and it proved to be a challenge to capture these short-lived solid-state species with the VT-XRPD approach. Our Raman line-focus method circumvents these challenges.

Measurement setup. In order to visualise the dehydration pathway of TP MH and NF MH II during heating an in-house built Raman line-focus microscope (Fig. 1) was used (see "Methods section"). Temperature and time-dependent Raman measurements were performed in combination with a Linkam hot stage (FTIR600 stage, T95 Linksys controller) in order to image the single particle of the drug during heating. A single particle was fixed with an aluminium clamp to ensure that the particle was immobile during the measurements. The 1.8 mm laser line was illuminated on the particle during collection of the Raman spectra yielding 220 spatially separated spectra per measurement. The optical images of the crystal(s) were collected simultaneously (Supplementary Figs 5, 6). One of the main benefits of using hydrates in these experiments is due to the physical change in the particles from transparent to opaque as a result of dehydration. This is due to the formation of nucleation events that are occurring on the surface of the particle resulting in the formation of small-sized crystallites that can be seen visually using optical microscopy by the formation of dark regions[18]. The measured multiple single particles of NF were recrystallized from NF AH β spiked with multiple single particles (different shapes and sizes) of NF MH I, NF AH α and NF AH β. A depolariser was used in order to eliminate particle orientation as a contributing factor to all the experiments.

Experimental solid-state characterisation of TP and NF. It is challenging to obtain pure Raman spectra of the metastable intermediates as they overlap with their stable counterparts. It is equally challenging to capture these short-lived species with diffraction-based methods as shown by our VT-XRPD results and typically, synchrotron-based radiation is needed to observe these intermediates[19]. Therefore, in order to confirm the presence of the metastable intermediates of TP and NF, multiple isothermal experiments between 45–130 °C 90 minutes (each experiment) were conducted using only a single particle per experiment and the residual intensity maps were calculated from the raw Raman spectra taking into account the stable forms[20,21]. This was a critical step in the experiments because by subtracting the stable hydrate and anhydrous responses from the hyperspectral Raman data we were able to study the dynamics of only the metastable intermediates of TP and NF. This is a method that has previously been applied to studying multicomponent systems (see refs[16,17]).

In order to understand the dynamics of the metastable intermediates of the model particles, concentration profiles and maps were obtained from the Raman data using MCR and NNLS. The isothermal dehydration of a single particle of TP MH was conducted from 45–65 °C for 90 minutes (each experiment) using the Raman line-focus setup and the hot-stage (Fig. 2a). These experiments showed the complex dehydration pathway of TP MH and they revealed a new metastable intermediate (TP MS2). The concentration profiles at 50 °C for 90 minutes obtained after MCR analysis of the hyperspectral Raman data showed an initial decrease in the concentration of TP MH accompanied by a simultaneous increase in the concentration of TP MS1 (Fig. 2b). The decrease of TP MS1 is followed by an increase in the concentration of TP MS2 via two steps after 32 min of the dehydration

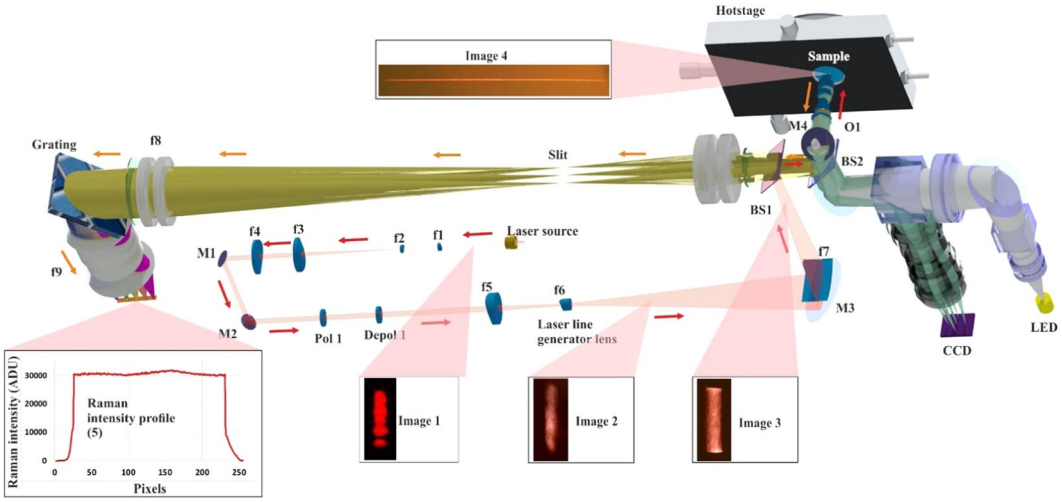

Figure 1. Optical setup of the in-house built Raman line-focus microscope. Where BS – beam splitter, O – microscope objective, M – mirror, f – cylindrical lens, Pol – polariser, Depol – depolariser, LED – light-emitting diode, CCD- visible camera. Image 1 is the laser beam profile from the multimode laser source (785 nm), Image 2 is the laser beam profile after the laser line generator lens (f6), Image 3 is from the laser beam profile before the microscope objective (O1), Image 4 is from the laser beam profile on a given sample (after passing through O1) and the Raman intensity profile (5).

process at 50 °C. TP AH form II increases in concentration up to the end of the experiment in a mixture with TP MS2. Reported literature has shown that the dehydration pathway of TP MH to TP AH form II includes only one metastable intermediate, which we refer to as TP MS1; however, to the best of our knowledge, we are the first to experimentally reveal TP MS2. The concentration profiles were able to highlight the overlap of the solid-state forms during dehydration, but do not give information with regard to the spatial location of both intermediates in the TP particle; hence, chemical concentration maps were needed.

In order to visualise the heterogeneous distribution of the four solid-state forms of TP from its single particle, NNLS was applied on the Raman data to obtain four chemical concentration maps of TP (Fig. 2c1–4). The TP MH map showed specific regions in the single particle (0.02–0.38 mm, 0.48–0.72 mm, and 0.75–1.13 mm) with high concentrations of TP MH and this is due to local defects that were present in the particle. TP MH and TP MS1 appear at the same time as in the concentration profile but are located spatially in different parts of the particle. This level of spatially resolved information cannot be obtained with DSC and TGA, as they require bulk samples for analysis. Fig. 2c1–2 show that TP MH and TP MS1 overlap and diffuse throughout the particle at the end of the experiment at the 'defect-rich' areas. After 30 minutes, a gradual decrease in the concentration of TP MS1 as it spreads throughout the particle. For 45 minutes, TP MS1 and TP MS2 were overlapping in different concentration profiles. This could be linked to their structural similarity as shown by the recorded Raman spectra and potentially a small energy barrier that exists between these two metastable forms. The concentration profile and map show that TP AH form II appears after 50 minutes when both metastable intermediates of TP were present in varying concentrations.

Raman spectra of the four different solid-state forms of TP were obtained during previously described experiments from the MCR analysis. The spectral changes during dehydration are shown in Fig. 2d1–4. A comparison between TP MH and TP AH form II showed two peaks (1690 and 1730 cm^{-1}), indicative of TP AH form II and are due to C=O, C=N and C=C stretching modes[22]. This is indicative of the loss of hydrogen bonding[23] related to the water molecules present in TP MH. As shown in Fig. 2d2–3, the spectral regions 500–750 cm^{-1} (C–C aliphatic chain vibrations) and 1650–1750 cm^{-1} are where the most differences were noted between the spectra of the four forms. The Raman spectra of TP MS1 and TP MS2 differed in the regions around 1150 cm^{-1}, 1230 cm^{-1}, and 1750 cm^{-1} due to deformation of the imidazole and pyrimidine ring. This deformation is critical in revealing the small structural differences between the metastable intermediates even though they are overlapping during dehydration[24]. The crystal structures of TP MH and TP AH form II are published[25]. To the best of our knowledge, we are the first to publish the mid-frequency Raman spectra of TP MS1 and TP MS2. However, their structures have not been determined due to their metastable nature.

The isothermal experiments (45, 50, 60, and 65 °C) demonstrated the solid-state transformation between TP MS1 and TPMS2 (Fig. 2e1–4), where it should be noted that the result in the Fig. 2e2 is from another TP MH particle than the result presented in the Fig. 2b. The stable forms were taken into account, however, in the Fig. 2e1–4 only the metastable intermediates have been plotted. Both metastable intermediates are highly overlapped in the isothermal conditions 50–65 °C. At 45 °C, only TP MS1 was observed, but at 50, 60 and 65 °C both TP MS1 and TP MS2 were observed. The appearance of TP MS1 and TPMS2 is slower at 45 and 50 °C and faster at a 60 and 65 °C. At each isothermal condition, the dehydration profiles of the metastable forms are different with only TP MS1 appearing at 45 °C, but TP MS2 appearing at 50, 60 and 65 °C. TP MS2 appears at the same time as TP MS1 at 60 °C and before TP MS 1 at 65 °C.

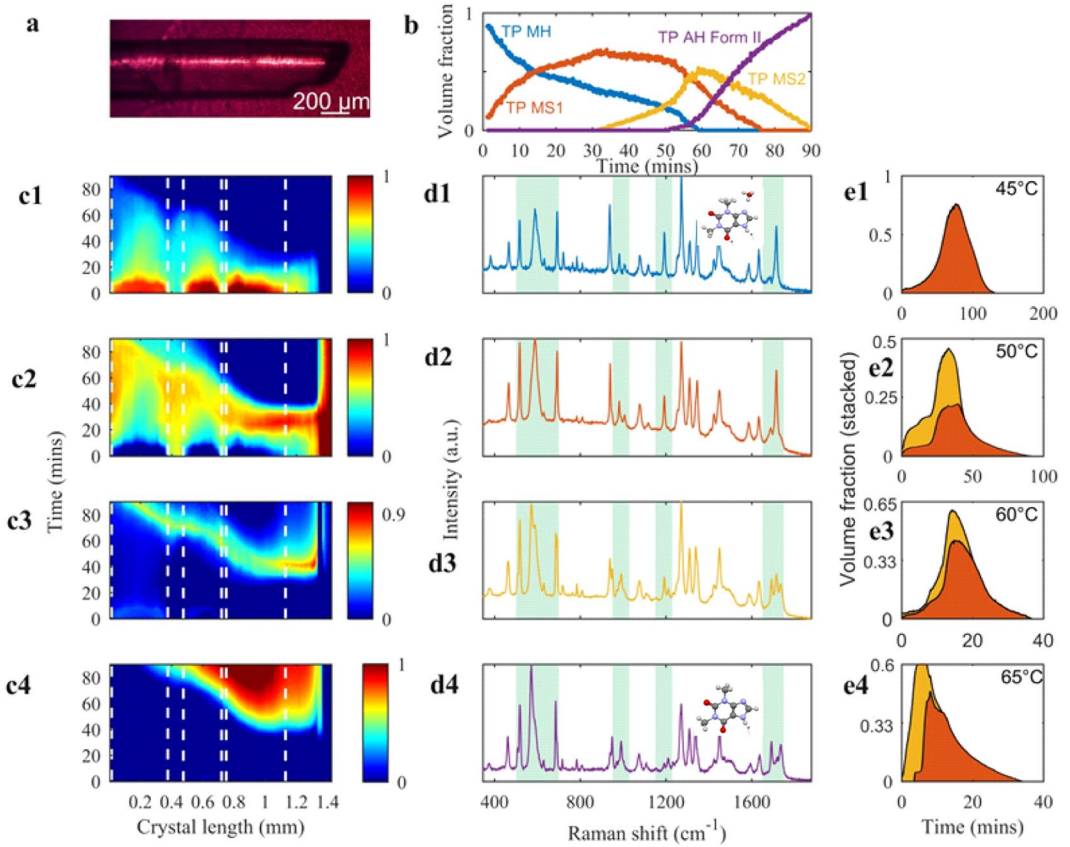

Figure 2. MCR and NNLS decomposed results of hydrate and anhydrous solid-state forms of theophylline. (**a**) Optical image of TP MH at 25 °C with laser line illumination (white line) from the Raman microscope (**b**) concentration profile of solid-state forms during isothermal dehydration at 50 °C for 90 minutes starting from TP MH to TP AH form II, via TP MS1 and TP MS2 **(c1–4)** chemical concentration maps (cut out artefacts from 1.8 mm laser line) of TP MH **(c1)**, TP MS1 **(c2)**, TP MS2 **(c3)**, TP AH form II **(c4)** in the particle during dehydration where the laser line is illuminated, (**d1–4**) Raman spectra for TP MH, TP MS1, TP MS2 and TP AH form II respectively, (**e1–e4**) area plots showing only the dehydration profiles of TP metastable intermediates at four isothermal conditions (45, 50, 60 and 65 °C) where the colour under the area plots matches the TP metastable intermediates as shown in the concentration profiles. The stable forms of TP were taken into consideration for the area plots.

Since our Raman based method was able to reveal a new metastable form of TP, a more complex model compound (NF) was studied where a limited amount of work has been done on its dehydration pathway. The crystal structures of the four solid-state forms of NF have been published[26] and formed the foundation for our proposed dehydration pathway for NF MH II to NF AH β. The crystal structures presented in Fig. 3a were taken from the Cambridge Structural Database (CSD) in order to show the differences in the arrangement of the water molecules in each form of NF and how this translates into a complex dehydration pathway due to the presence of two metastable intermediates (NF MH I and NF AH α). Hydrogen bonds play an important role in the stability of hydrates. It has been reported[27] that the C=O, N–H and C–H groups are strongly affected by hydrate formation and it is thought that the dehydration of a hydrate also strongly affects these vibrational modes via intermolecular bonding. Figure 3b shows the proposed dehydration pathway based on the hydrogen bonding arrangement from NF MH II to NF AH β. NF MH II consists of a complex hydrogen bonding herringbone arrangement (zig-zag) whereas NF MH I has a chair like the arrangement of the hydrogen bonds indicating a partial loss of water. The anhydrous forms possess a planar conformation with dimers forming a head-to-head bond between NF molecules with NF AH α having two N-H···O bonding patterns whereas β has one.

Based on the crystal structure understanding of the NF forms, isothermal dehydration of a single particle of NF MH II was conducted in the same manner as for TP MH, but at isothermal conditions from 90–130 °C each for 90 minutes using the in-house Raman line-focus setup and a hot-stage (Fig. 4a, Supplementary video 1). MCR and NNLS analysis described in the methods section was applied to the hyperspectral Raman data to reveal the concentration and spectral profiles of NF forms during the isothermal experiments. Figure 4b shows that at 120 °C from 5 minutes, both hydrates of NF were overlapping, but NF MH II is decreasing in concentration and NF MH I increasing, confirming a solid-state transformation of one monohydrate into another structurally different monohydrate. NF AH α also appeared at the 10-minute mark with both monohydrates. These two

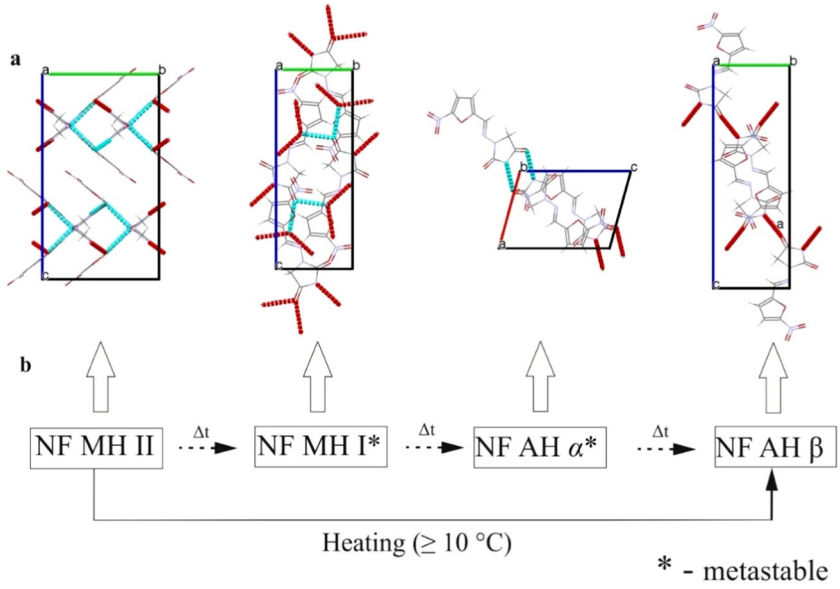

Figure 3. Solid-state forms of NF (**a**) 3-D representation of NF MH II, NF MH I, NF AH α and NF AH β respectively (light blue lines indicate hydrogen bonding) taken from the CSD (**b**) proposed complex dehydration pathway of NF MH II to NF AH β, where Δt is the change in time at a given temperature.

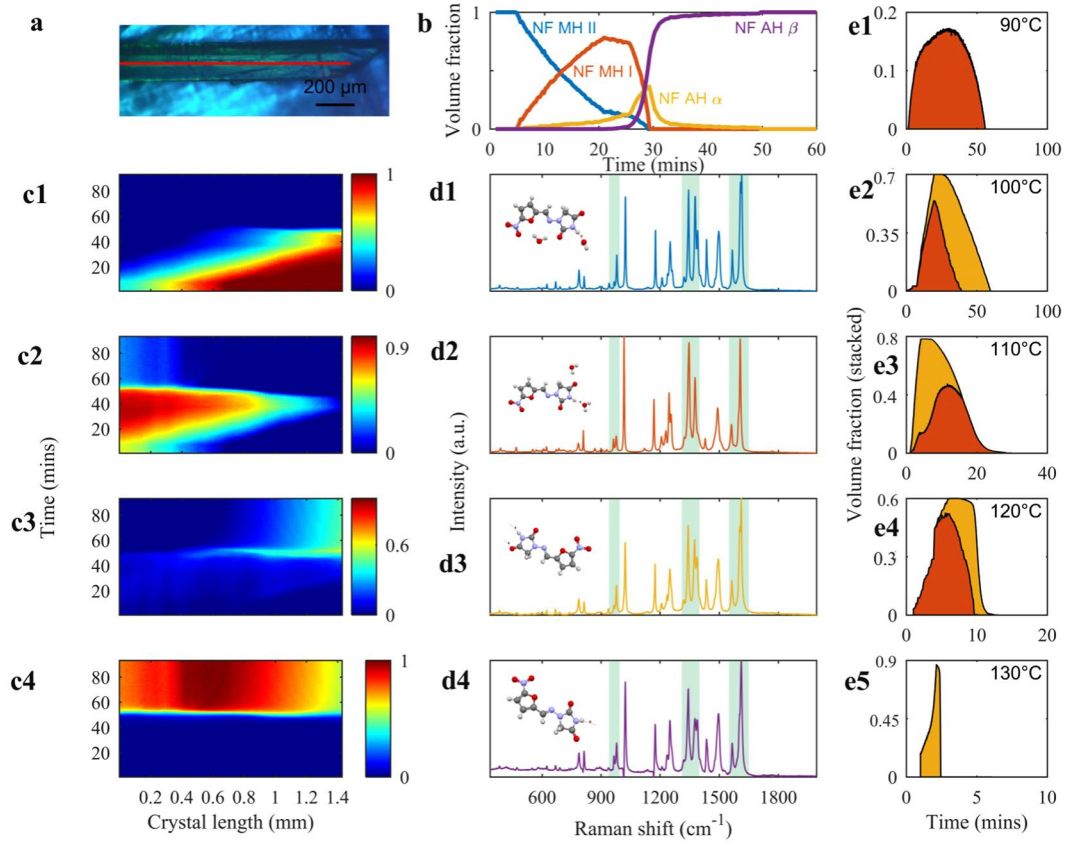

Figure 4. MCR and NNLS decomposed results of nitrofurantoin solid-state forms. (**a**) Optical image of NF MH II at 25 °C from the Raman microscope. (**b**) concentration profiles of solid-state forms during isothermal dehydration at 120 °C for 90 minutes from NF MH II to NF AH β via, NF MH I and NF AH α (**c1–4**) chemical concentration maps (cut out artefacts from 1.8 mm laser line) of NF MH II **(c1)** NF AH β **(c2)** NF MH I **(c3)** NF AH α **(c4)** in the particle during dehydration where the laser line is illuminated (**d1–4**) Raman spectra of NF MH II, NF MH I, NF AH α, NF AH β. (**e1–4**) area plots showing only the dehydration of NF MH I and NF AH α five isothermal conditions (90, 100, 110,120 and 130 °C) where the colour under the area plots matches the NF metastable intermediates as shown in the concentration profiles. The stable forms of NF were taken into consideration for the area plots.

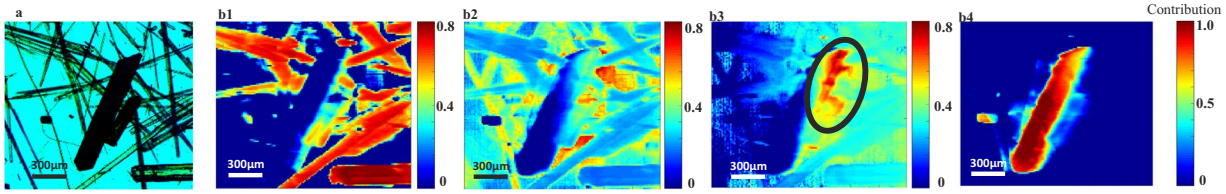

Figure 5. Multiple particles of NF solid-state forms analysis using the Raman line-focus method at room temperature. (**a**) Optical image of multiple particles of NF. (**b1**) NF MH II. (**b2**) NF MH I (**b3**) NF AH α and (**b4**) NF AH β obtained after NNLS of a depolarised Raman map.

metastable intermediates appeared simultaneously as seen with TP during isothermal dehydration. The decrease in the concentration of NF AH α at 30 minutes coincides with the formation of NF AH β at the same time point and increases until NF AH β reaches a plateau. The four chemical concentration maps of NF show that the dehydration is occurring from the centre of the particle to the boundaries heterogeneously with a gradual decrease in the concentration of NF MH II from the middle of the particle to its edge[28] (Fig. 4c1–4). In contrast to the dehydration of TP MH to that of NF MH II occurs at a higher temperature (≥90 °C), which is unusual and this could be because it is an isolated site nature of this hydrate. The results showed that NF MH I is present at higher concentrations inside the particle whereas residual amounts of NF AH α are present inside the particle at the beginning of the experiment and it protrudes to the edge of the particle where a higher concentration is present. The concentration profiles of NF metastable intermediates are different and this could be linked to their crystal structure as well as NF MH I being trapped in specific local regions in the crystal. NF AH β appears during the disappearance of the hydrated counterparts and is present from the centre to the end of the NF particle. The Raman spectra highlight the structural difference of the NF forms.

The four Raman spectra of NF solid-state forms were obtained from MCR analysis. In Fig. 4d1–4 they have pronounced differences that can be attributed to their conformational arrangement[29]. NF MH II and NF MH I differ in their C=N linkage between the nitrofuran and the hydantoin moieties (1615 cm^{-1}). The regions in the Raman spectra of NF AH α and NF AH β that have the most pronounced differences were 950–1000 cm^{-1}, 1200–1300 cm^{-1}, 1310–1400 cm^{-1}, 1550–1650 cm^{-1}.

The isothermal experiments (90, 100, 110, 120, and 130 °C for 90 minutes) demonstrated the solid-state transformation between two monohydrates (hydrate-hydrate transformation from NF MH II into NF MH I) between 90–120 °C (Fig. 4e1–5) where it should be noted, as earlier, that the Fig. 4b,e4 are from different crystals of NF MH II. The isothermal experiments of NF showed that dehydration occurred at a slower rate at below 110 °C in comparison to 120 and 130 °C. In addition, between 100 °C and 120 °C, both the NF MH I and NF AH α are present, whereas only NF AH α at 130 °C for a few minutes. The difference in the dehydration rates of both 120 °C isothermal runs is due to a difference in particle size. As with TP, the dehydration profiles of the metastable forms are different at each isothermal condition.

Visualization of the solid-state form diversity in real particles. The results presented above capture the dehydration of TP MH and NF MH II using only a single particle of both compounds. However, in order to have a more direct comparison of the Raman line-focus method with the standard thermal analytical methods such as DSC and TGA, a Raman line-focus mapping option in an area of 1170 × 2109 µm with a step size of 8 µm was performed using a real-life powder sample with different particle sizes and shapes (Supplementary Fig. 7). A batch of NF particles (Fig. 5a) that contained a mixture of its solid forms was mapped in order to simulate potential real-life temperature-driven phase transformations (Supplementary video 3–5). The maps obtained from NNLS (Fig. 5b1–4) were cut to show specific regions of interest. The maps confirmed the presence of four different solid forms of NF in the randomly orientated particles as was identified in the single particle experiment for NF. Figure 5b3 shows that even though the single particle of NF (circled) appears to be fully dehydrated based on the visual appearance of the optical image (dark particle) there are residual amounts of NF AH α present within the particle.

Previous literature has shown the particle size dependence of the dehydration process[30], which motivated us to explore the possibility to visualize multiple particles at the same time. Typically, DSC and TGA analysis will take an average thermal signal resulting from all the particles during the heating, making it challenging to reveal subtle thermal events and overlapping signals that could be taking place in these particles, such as the appearance of metastable intermediates[31]. However, the Raman line-focus method was clearly able to identify NF MH I and NF AH α in multiple single particles using NNLS of a depolarised Raman map.

Discussion

The experiments show the capability of our approach to visualize and spatially locate the different solid-state forms of TP and NF at a single particle level. DSC and TGA show the quantitative amount of water loss for hydrates, however, they are not able to spatially resolve the complex dehydration pathway at a single particle level. The concentration profiles and the chemical maps of the solid-state forms provided a deeper insight into the dehydration pathway of both model compounds, in particular, the dynamics of the metastable intermediates. Both model compounds were structurally very different resulting in different dehydration pathways. TP MH consists of a channel type crystal structure[32], where water formed directional bonding between the water (anisotropic dehydration) and TP molecules, whereas water of crystallization in NF MH II is located at isolated sites with van

der Waals forces and hydrogen bonding resulting in planar conformation with direct water-to-host bonding. The dehydration process of NF MH II can be considered 'destructive' as it contains two hydrogen bond donors and seven hydrogen bond acceptors, which could[33] play a role in the NF MH II transformation to NF MH I at high dehydration temperatures. The single particles used in these experiments contained defects and this contributed to their heterogeneous dehydration, with water disappearing at different rates in specific regions of the particle[34]. Taking into account the Rouen 96 model (largely based on observations with inorganic materials), our results show that there are crossing pathways of water release from TP MH and NF MH II. This is because these model compounds represent real-life particles, which are inherently complex[35].

Currently, there are four known forms of TP, and form IV is reported as the thermodynamically stable form at room temperature[36]. Seton *et al*. also noted the important role of the dimers between the TP and water molecules ensuring the physical stability of the monohydrate network. TP MH is known to convert to its anhydrous form II and this is the form that was found at the final stages in our experiments[37]. The reported appearance of TP MS1[38,39] show that it can transform to its stable anhydrous form during storage over a period of days or months depending on the environmental conditions[40], hence TP MS1 was present at the beginning of the isothermal measurements. To the best of our knowledge, we are the first to record experimentally the Raman spectra of TP MS1 and TP MS2 in the region 400–1800 cm^{-1}; however, computationally assisted approaches could give additional insight into these complex dehydration pathways[41,42]. As previously noted, it was surprising for TP MS1 and TP MS2 to be present in the experiment for over an hour. This could be because we have created experimental conditions in which the metastable form is stable and therefore appears for several minutes rather than seconds[43].

For NF MH II dehydration, previously reported literature using standard analytical techniques indicates that the dehydration pathway of NF MH II to NF AH β (120–145 °C) is a one-step process[44]. However, we discovered using our method that it is a complex three-step process due to the presence of two known metastable intermediates. The proposed dehydration pathway of NF MH II to NF AH β is based on the crystal structures that highlight the hydrogen bonding arrangement, which plays an important role during dehydration. Although there are pronounced differences between these forms, the metastable intermediates are still overlapping with the stable counterparts indicating that the energy difference could also be small between the four forms. This observation follows the Ostwald's rule of stages that states that matter at a high-energy state does not necessarily transform directly into its most thermodynamically stable form but can pass through several metastable intermediates[45].

Measuring multiple particles can be useful in resolving the particle-size dependence of metastable intermediates. This approach provides the possibility to resolve essential information regarding the transformation from hydrated to anhydrous forms in particulate materials, and the spatial location of metastable intermediates[46,47]. The crossing pathways of water release from particulate matter can have a detrimental impact on the physical stability of the drug and potentially its bioavailability. The limitations of our approach are that fluorescence can be a challenge with the Raman analysis. The Raman line-focus method can be used in a variety of different fields of research that require analysis of phase transformations at the particulate level and would naturally complement molecular level investigation of phase changes using a computational method such as molecular dynamics[48]. Mechanistic models and computer simulations are still challenging to implement for real-life particulate systems. Our findings are pointing towards mechanistic models based on combining information at different levels: spectroscopic imaging visualizing molecular level phenomena, such as solid-state diversity during dehydration in a single particle, combined with optical microscopy to visualize particle level phenomena, such as crack density related to this phase transformation. This can provide a basis for multiscale mechanistic models[49] and experimental validation of computer simulations. This approach would have similarities with the deep learning process in cancer diagnosis based on imaging of cellular samples[50].

Conclusion

Here we demonstrated experimentally that Raman line-focus microscopy can be used to investigate different crystalline solid-state transformations and reveal metastable intermediates that are of pharmaceutical relevance at the single particle level. The obtained concentration profiles and maps with the usage of MCR and NNLS analysis showed that the dehydration pathways of TP MH and NF MH II went through two intermediates and this approach was able to spatially locate them, which classical thermal techniques cannot do. This resulted in the discovery of TP MS2 and the dehydration pathway of NF MH II to its NF AH β. The dehydration pathway of NF MH II leads to a hydrate-hydrate transformation of one monohydrate structure into another structurally different monohydrate at dehydration temperatures. In addition, a Raman line-focus mapping option was used to analyse real-life particles, highlighting the diversity of solid-state forms present during dehydration. It is envisioned that this method can be used in providing an in-depth understanding of phase transformations, as well for explaining the practical industrial challenges related to variation in the quality of particulate materials.

Methods

Materials and general preparative methods. All particles were stored at room temperature before conducting thermal measurements with the Raman microscope. A single particle of theophylline monohydrate (Cambridge Structural Database ref code: THEOPH01)[51] and nitrofurantoin monohydrate (CSD refcode: HAXBUD)[52] was used for these experiments. Particles from the same batch were used in order to carry out the Raman measurements.

50 g of anhydrous TP (Sigma Aldrich) was dissolved in distilled water (1 L, 80 °C) and needle-like single particle (500 μm–3 mm) of TP MH appeared within 3–5 days from slow evaporation crystallization. Bulk powder of nitrofurantoin (obtained from Unikem A/S, Copenhagen, Denmark) was identified as the stable anhydrous form (β) using XRPD. NF MH II was recrystallized from one gram of bulk powder nitrofurantoin (Unikem A/S, Copenhagen, Denmark) from a hot (55 °C) acetone-water solution (3:1). The solution was cooled to room temperature and within 3 days yellow needle-like particles (500 μm–2 mm) formed. NF monohydrate (NF MH I)

was recrystallized from 75 mg of NF (Unikem A/S, Copenhagen, Denmark) dissolved in 30 cm^3 of a hot (55 °C) acetone: water mixture (2:1). The solution was then left in a sealed vessel and maintained at 40 °C allowing for slow evaporation. Plate-like particles (100 μm–2 mm) appeared within 4 days. An optical microscope (LEICA DM LM) was used to identify a single particle by observing the clarity of the particle and whether a large number of crystal defects were present.

Sample characterization. Particles of TP MH and NF MH II were characterised by polarised light microscopy, x-ray powder diffraction (XRPD), differential scanning calorimeter (DSC) and thermogravimetric analysis (TGA) and Raman microscopy.

X-ray powder diffraction (XRPD). A PANalaytical X'pert PRO X-Ray Diffractometer (purchased from PANanalytical B.V., Almelo, Netherlands) consisting of a θ/θ goniometer and a solid state PIXcel detector was used for solid-state form identification and verification. The radiation was nickel-filtered CuK_α ($\lambda = 1.5418$ Å) generated at a tube voltage of (45 kV) and current (40 mA), respectively. The samples were scanned in reflection mode between 5° and 35° with a scan speed of 0.06734° 2θ and a step size of 0.0263° 2θ. The data were analysed using the X'Pert Data Collector software (PANalytical, Almelo, Netherlands). The measurements were done in triplicate. The variable temperature-XRPD measurements were all performed using a steel sample holder (0.2 mm in depth) on an Anton Paar CHC chamber (Anton Paar GmbH, Graz, Austria). The temperature was controlled using a TCU 110 Anton Paar GmbH controller. A scan speed of 0.328 was used for NF and TP temperature measurements. For NF MH II the measurement was performed at room temperature then the temperature was ramped to 120 °C at 35 °C/min and held for 120 mins with an exposure time of 10 mins. For TP MH, the temperature was raised to 50 °C at the same heating rate and held for 90 minutes. The particle size that was used for the temperature measurements were between 50–150 μm.

Thermal analysis. A Discovery DSC (TA Instruments-Waters LLC, New Castle, USA) was used to perform the DSC measurements. The instrument is controlled by TRIOS software (TA Instruments, New Castle, DE, USA). Samples around 7 mg were placed into T-zero aluminium pans and sealed. Samples were subjected to a controlled heating rate of 10 °C/min under nitrogen purge (40 mL/min). The measurements were done in triplicate.

The water content in TP MH and NF MH II was determined using a Discovery TGA (TA Instruments, New Castle, DE, USA), which was controlled by TRIOS software (TA Instruments, New Castle, DE, USA). Samples around 7 mg were analysed in an aluminium pan and heated at 10 °C/min from 25 °C to 100 °C for TP MH and 25 °C to 200 °C for NF MH II. The measurements were done in triplicate.

Visualisation of crystal structures. The CSD was used in order to visualize and understand the intermolecular arrangement of the bonds, unit cell dimensions, and faces of the crystals of the different TP forms (CSD ref code: THEOPH01, BAPLOT01[53] and NF forms (CSD refcode HAXBUD, HAXBUD01,LABJON01[54], LABJON02) using Mercury 3.8 software that is provided by the Cambridge Crystallographic Data Centre, UK.

Raman line-focus microscope setup. An in-house built Raman microscope that is based on a line-focus method was used to track the structural changes that occurred in the single particle during dehydration. The setup consisted of three main units: laser delivery optical system, a visible light microscope and a Raman scattering optical system. A high power multimode laser (0.5 W, 785 nm) is used to generate an inhomogeneous laser line, which propagates through a number of cylindrical lenses in order to achieve a homogenous beam on the particle (s). The 1.8 mm in length laser line was focused on the particle fixed on a Linkam FTIR600 hot stage during heating at a controlled rate at 40–55% relative humidity (RH). The alignment of the particle onto the laser line was performed manually in two stages: firstly, by placing the particle within the visual field of the microscope and secondly, by obtaining a more precise alignment using the x, y and z stage controlled by the in-house Raman data acquisition software. An exposure time 8 seconds for the acquisition of 220 Raman spectra along the line length was used for all the isothermal measurements in the main body of the paper. The laser intensity at 785 nm was 100 μW/μm for all experiments. The line-focus method enables measurements that are two orders of magnitude faster than traditional point illumination Raman microscopy and requires less power per point[55]. At 100 mW power using a point measurement mode, this would generate 33.3 mW/μm^2 whereas with laser line illumination this would generate 0.15 mW/μm^2. This is a significantly less power point thereby reducing the likelihood of damage to the particle due to the laser.

Wavelength and spectrum-dependent intensity calibration of the Raman system were performed using toluene and cyclohexane. The intensity calibration included corrections on the quantum efficiency of CCD and the transparency of optical elements in the system. The wavelength calibration was done automatically during the start of the system software, and spectrum-dependent intensity calibration is done periodically every month. The Raman spectra were collected according to the international standard guides ASTM 1840, ASTM E2911.

Raman optical system. A series of images (1–4) of the different laser beam profiles were captured in order to illustrate how a homogeneous laser line was achieved with the use of cylindrical lenses (f1–f7). Image 1 consists of five different spatial modes in the vertical direction as generated from the laser source. These five spatial modes pass through f1 to f5 resulting in image 2, which shows a laser beam profile that is not yet homogenous. It is only after image 3 goes through f7 that a homogeneous laser line in the vertical direction is achieved. Image 4 is based on the field of view (FOV) of the microscope objective (10× NIR objective with a FOV of 2.2 mm). The laser beam is then reflected from the dichroic beam splitter (BS1) before it reaches the microscope objective (O1) then passes through a set of mirrors to O1. BS2 is used to combine the laser and visible light beams thereby allowing for real-time visual inspection and collection of the Raman spectra. The light projected from the light-emitting diode (LED) is cut off from the Near Infrared spectrum of the Raman shift (785–1000 nm) using an edge filter

(Ed3). The visual inspection of the crystal (s) during dehydration was very useful for the monitoring of the crystal (s) opacity, especially in "defect-rich" areas.

The microscope was designed in a manner that allowed the sample to be scanned in the X, Y and Z directions without being moved. This was important in order to ensure no misalignment of the laser and visible light beams. In order for no misalignment to take place during measurements BS2, Mirror 4 (M4) and O1 moved as one unit in the x-direction and M4 and O1 moved as one unit in the y-direction. As previously stated, image 4 is based on the projection of the laser line from the microscope objective. The Raman spectra were collected on the particle and simultaneously collected on a deep-cooling spectroscopic charged coupled detector (CCD). This setup provided the unique capabilities for simultaneous Raman mapping on an entire particle during temperature ramping or under isothermal conditions. The spectrograph is protected under a patent (DTU Patent Application No. PA201870044) and its aberration corrected imaging design provides Raman spectra from 350–2300 cm^{-1} at 785 nm.

Multivariate curve resolution (MCR) and non-negative least squares (NNLS) methodology. MCR-ALS[56,57] and NNLS were both performed in MATLAB R2017a. Raman experiments resulted in a matrix that has two dimensions [t, S(ν)], where t corresponds to the temperature or time points, while S(ν) corresponds to Raman spectra. We registered 220 spectra from the laser line at each temperature/time point, and all spectra were grouped as follows: $M_{line} = [t_1(S(\nu)_1, S(\nu)_2, \ldots S(\nu)_{220}), t_2(S(\nu)_1, S(\nu)_2, \ldots S(\nu)_{220}), \ldots t_n(S(\nu)_1, S(\nu)_2, \ldots S(\nu)_{220})]$, where n is the number of temperature/time points. In order to extract information about the concentration and spectral profiles of the studied model compounds, we used only one lateral point on the laser line that had the highest Raman spectrum signal to noise ratio (SNR).

When using MCR-ALS the following constrains were applied: non-negativity on spectral and concentration profiles, closure and unimodality constrains on concentration profiles. The "mcr_main" toolbox was downloaded from the "Multivariate Curve Resolution homepage". Before running the "mcr_main" toolbox a spectral library for the stable hydrate and anhydrous form for TP and NF dehydration experiments were created with four rows of which two-reference spectral matrix were filled containing the Raman spectra of the stable forms of the model compounds. These stable forms were used as the spectral profile constrains. The two unfilled rows in the library spectral matrix were defined as not a number (NaN). After running the "mcr_main" function on MATLAB, the rows that filled the two NaN rows contained the metastable intermediates. The best lack of fit (LoF) was reached in the case of using four Principal Components (PCs) for TP analysis (two metastable intermediates observed) and four PCs for NF analysis (two metastable intermediates observed). The averaged matrix of residuals was found to be less than 0.1% after the iteration process. As a result, we obtained four concentration and spectral profiles from our dataset from the dehydration of TP MH and NF MH II. The obtained spectral profiles of metastable intermediates of the model compounds were used as a spectral library for NNLS analysis of line-focus Raman matrixes M_{line}. NNLS results are shown in Fig. 2b–d4 and Fig. 4b–d4.

References

1. Makatun, V. N. & Shchegrov, L. N. State of Water in Inorganic Crystal Hydrates and the Characteristic Features of Their Dehydration. *Russ. Chem. Rev.* **41**, 905–918 (1972).
2. Polymorphism in the Pharmaceutical Industry Edited by R. Hilfiker. Wiley-VCH: Weinheim. 2006. 414 + xix pp. £105. ISBN 3-527-31146-7. *Org. Process Res. Dev.* **11**, 649–649 (2007).
3. Higashi, K., Ueda, K. & Moribe, K. Recent progress of structural study of polymorphic pharmaceutical drugs. *Adv. Drug Deliv. Rev.* **117**, 71–85 (2017).
4. Halasz, I. *et al.* Quantitative *in situ* and real-time monitoring of mechanochemical reactions. *Faraday Discuss.* **170**, 203–221 (2014).
5. Galwey, A. K. Structure and order in thermal dehydrations of crystalline solids. *Thermochim. Acta* **355**, 181–238 (2000).
6. Petit, S. & Coquerel, G. Mechanism of Several Solid-Solid Transformations between Dihydrated and Anhydrous Copper (II) 8-Hydroxyquinolinates. Proposition for a Unified Model for the Dehydration of Molecular Crystals. *Chem. Mater.* **8**, 2247–2258 (1996).
7. Morris, K. R. & Rodriguez-Hornedo, N. Hydrates In: *Encyclopaedia of Pharmaceutical Technology*. Swarbrick, J., Boylan, J., Eds.; Marcel Dekker: New York. 393–440 (1993).
8. Shaw, S., Henderson, C. M. B. & Komanschek, B. U. Dehydration/recrystallization mechanisms, energetics, and kinetics of hydrated calcium silicate minerals: an *in situ* TGA/DSC and synchrotron radiation SAXS/WAXS study. *Chemical Geology* **167**, 141–159 (2000).
9. Scheirs, J. *Compositional and Failure Analysis of Polymers: A Practical. John Wiley & Sons* (Wiley), https://doi.org/10.1016/S0008-8846(03)00043-7 (2000)
10. Connelly, P. R., Vuong, T. M. & Murcko, M. A. Getting physical to fix pharma. *Nat. Chem.* **3**, 692–695 (2011).
11. Bugay, D. E. Characterization of the solid-state: spectroscopic techniques. *Adv. Drug Deliv. Rev.* **48**, 43–65 (2001).
12. Jørgensen, A. C. *et al.* An insight into water of crystallization during processing using vibrational spectroscopy. *J. Pharm. Sci.* **98**, 3903–32 (2009).
13. Larsen, A. S., Rantanen, J. & Johansson, K. E. Computational Dehydration of Crystalline Hydrates Using Molecular Dynamics Simulations. *J. Pharm. Sci.* **106**, 348–355 (2017).
14. Olmos, V. *et al.* Relevant Aspects of Unmixing/Resolution Analysis for the Interpretation of Biological Vibrational Hyperspectral Images. *TrAC Trends Anal. Chem.* **94**, 130–140 (2017).
15. Ilchenko, O., Pilgun, Y., Reynt, A. & Kutsyk, A. NNLS and MCR-ALS Decomposition of Raman and FTIR Spectra of Multicomponent Liquid Solutions. *Ukr. J. Phys.* **61**(6), 519 (2019).
16. Sutor, D. J. The structures of the pyrimidines and purines. *VI. The crystal structure of theophylline. Acta Crystallogr.* **11**, 83–87 (1958).
17. Suihko, E. *et al.* Dehydration of theophylline monohydrate—a two step process. *Int. J. Pharm.* **158**, 47–55 (1997).
18. Otto, C. E. Fusion methods in chemical microscopy (McCrone, Walter C., Jr.). *J. Chem. Educ.* **34**, A410 (1957).
19. Nunes, C., Mahendrasingam, A. & Suryanarayanan, R. Investigation of the Multi-Step Dehydration Reaction of Theophylline Monohydrate Using 2-Dimensional Powder X-ray Diffractometry. *Pharm. Res.* **23**, 2393–2404 (2006).
20. Ilchenko, O. O., Nikonova, V. V., Kutsyk, A. M. & Obukhovsky, V. V. Quantitative Analysis of Complex Formation in Acetone−Chloroform and Ethyl Acetate−Cyclohexane Solutions. *Ukr. J. Phys.* **59**, 268–275 (2014).
21. Kutsyk, A., Ilchenko, O., Pilgun, Y., Obukhovsky, V. & Nikonova, V. Complex formation in liquid diethyl ether-chloroform mixtures examined by 2D correlation MID-IR spectroscopy. *J. Mol. Struct.* **1124**, 117–124 (2016).
22. Jørgensen, A. *et al.* Hydrate formation during wet granulation studied by spectroscopic methods and multivariate analysis. *Pharm. Res.* **19**, 1285–91 (2002).

23. da Silva, A. M., Steiner, T., Saenger, W., Empis, J. & Teixeira-Dias, J. J. C. Dynamics of hydration and dehydration processes of β-cyclodextrin monitored in real time by Raman spectroscopy. *Chem. Commun.* 1871–1872, https://doi.org/10.1039/CC9960001871 (1996).
24. Braun, D. E., Gelbrich, T., Wurst, K. & Griesser, U. J. Computational and Experimental Characterization of Five Crystal Forms of Thymine: Packing Polymorphism, Polytypism/Disorder, and Stoichiometric 0.8-Hydrate. *Cryst. Growth Des.* **16**, 3480–3496 (2016).
25. Beard, M. A., Ghita, O. R., McCabe, J. & Evans, K. E. Monitoring dehydration kinetics using simultaneous thermal and spectral methods. *J. Raman Spectrosc.* **41**, 1283–1288 (2010).
26. Caira, M. R., Pienaar, E. W. & Lötter, A. P. Polymorphism and Pseudopolymorphism of the Antibacterial Nitrofurantoin. *Mol. Cryst. Liq. Cryst. Sci. Technol. Sect. A. Mol. Cryst. Liq. Cryst.* **279**, 241–264 (1996).
27. Sardo, M., Amado, A. M. & Ribeiro-Claro, P. J. A. Hydrogen bonding in nitrofurantoin polymorphs: a computation-assisted spectroscopic study. *J. Raman Spectrosc.* **40**, 1956–1965 (2009).
28. Sheng, J., Venkatesh, G. M., Duddu, S. P. & Grant, D. J. W. Dehydration behavior of eprosartan mesylate dihydrate. *J. Pharm. Sci.* **88**, 1021–1029 (1999).
29. Tian, F., Qu, H., Louhi-Kultanen, M. & Rantanen, J. T. Mechanistic insight into the evaporative crystallization of two polymorphs of nitrofurantoin monohydrate. *J. Cryst. Growth* **311**, 2580–2589 (2009).
30. Taylor, L. S. & York, P. Effect of particle size and temperature on the dehydration kinetics of trehalose dihydrate. *Int. J. Pharm.* **167**, 215–221 (1998).
31. Giron, D. Thermal analysis and calorimetric methods in the characterisation of polymorphs and solvates. *Thermochim. Acta* **248**, 1–59 (1995).
32. Byrn, S. R. & Lin, C.-T. The effect of crystal packing and defects on desolvation of hydrate crystals of caffeine and L-(−)-1,4-cyclohexadiene-1-alanine. *J. Am. Chem. Soc.* **98**, 4004–4005 (1976).
33. Braun, D. E. & Griesser, U. J. Supramolecular Organization of Nonstoichiometric Drug Hydrates: Dapsone. *Front. Chem.* **6** (2018).
34. Agbada, C. O. & York, P. Dehydration of theophylline monohydrate powder — effects of particle size and sample weight. *Int. J. Pharm.* **106**, 33–40 (1994).
35. Chowdhury, A. U. *et al.* Kinetic Trapping of Metastable Amino Acid Polymorphs. *J. Am. Chem. Soc.* **136**, 2404–2412 (2014).
36. Seton, L., Khamar, D., Bradshaw, I. J. & Hutcheon, G. A. Solid State Forms of Theophylline: Presenting a New Anhydrous Polymorph. *Cryst. Growth Des.* **10**, 3879–3886 (2010).
37. Suzuki, E., Shimomura, K. & Sekiguchi, K. Thermochemical study of theophylline and its hydrate. *Chem. Pharm. Bull. (Tokyo).* **37**, 493–497 (1989).
38. Fokkens, J. G., van Amelsfoort, J. G. M., de Blaey, C. J., de Kruif, C. G. & Wilting, J. A thermodynamic study of the solubility of theophylline and its hydrate. *Int. J. Pharm.* **14**, 79–93 (1983).
39. Phadnis, N. V. & Suryanarayanan, R. Polymorphism in Anhydrous Theophylline—Implications on the Dissolution Rate of Theophylline Tablets. *J. Pharm. Sci.* **86**, 1256–1263 (1997).
40. Airaksinen, S., Karjalainen, M., Räsänen, E., Rantanen, J. & Yliruusi, J. Comparison of the effects of two drying methods on polymorphism of theophylline. *Int. J. Pharm.* **276**, 129–141 (2004).
41. Nolasco, M. M., Amado, A. M. & Ribeiro-Claro, P. J. A. Computationally-Assisted Approach to the Vibrational Spectra of Molecular Crystals: Study of Hydrogen-Bonding and Pseudo-Polymorphism. *ChemPhysChem* **7**, 2150–2161 (2006).
42. Amado, A. M., Nolasco, M. M. & Ribeiro-Claro, P. J. A. Probing Pseudopolymorphic Transitions in Pharmaceutical Solids using Raman Spectroscopy: Hydration and Dehydration of Theophylline. *J. Pharm. Sci.* **96**, 1366–1379 (2007).
43. Braun, D. E., Koztecki, L. H., McMahon, J. A., Price, S. L. & Reutzel-Edens, S. M. Navigating the Waters of Unconventional Crystalline Hydrates. *Mol. Pharm.* **12**, 3069–3088 (2015).
44. Koradia, V., de Diego, H. L., Elema, M. R. & Rantanen, J. Integrated Approach to Study the Dehydration Kinetics of Nitrofurantoin Monohydrate. *J. Pharm. Sci.* **99**, 3966–3976 (2010).
45. Chung, S.-Y., Kim, Y.-M., Kim, J.-G. & Kim, Y.-J. Multiphase transformation and Ostwald's rule of stages during crystallization of a metal phosphate. *Nat. Phys.* **5**, 68–73 (2009).
46. Byrn, S., Pfeiffer, R., Ganey, M., Hoiberg, C. & Poochikian, G. Pharmaceutical solids: a strategic approach to regulatory considerations. *Pharm. Res.* **12**, 945–54 (1995).
47. Blagden, N. Crystal engineering of polymorph appearance: the case of sulphathiazole. *Powder Technol.* **121**, 46–52 (2001).
48. Larsen, A. S., Ruggiero, M. T., Johansson, K. E., Zeitler, J. A. & Rantanen, J. Tracking Dehydration Mechanisms in Crystalline Hydrates with Molecular Dynamics Simulations. *Cryst. Growth Des.* **17**, 5017–5022 (2017).
49. Anwar, J. & Zahn, D. Polymorphic phase transitions: Macroscopic theory and molecular simulation. *Adv. Drug Deliv. Rev.* **117**, 47–70 (2017).
50. Wang, P. *et al.* Development and validation of a deep-learning algorithm for the detection of polyps during colonoscopy. *Nat. Biomed. Eng.* **2**, 741–748 (2018).
51. Sun, C., Zhou, D., Grant, D. J. W. & Young, V. G. Theophylline monohydrate. *Acta Crystallogr. Sect. E Struct. Reports Online* **58**, o368–o370 (2002).
52. Pienaar, E. W., Caira, M. R. & Letter, A. P. Polymorphs of nitrofurantoin. I. Preparation and X-ray crystal structures of two monohydrated forms of nitrofurantoin. *J. Crystallogr. Spectrosc. Res.* **23**, 739–744 (1993).
53. Ebisuzaki, Y., Boyle, P. D., Smith, J. A. & Methylxanthines., I. *Anhydrous Theophylline. Acta Crystallogr. Sect. C* **53**, 777–779 (1997).
54. Pienaar, E. W., Caira, M. R. & Letter, A. P. Polymorphs of nitrofurantoin. 2. Preparation and X-ray crystal structures of two anhydrous forms of nitrofurantoin. *J. Crystallogr. Spectrosc. Res.* **23**, 785–790 (1993).
55. Ilchenko, O. *et al.* High-speed line-focus Raman microscopy with spectral decomposition of mouse skin. *Vib. Spectrosc.* **83**, 180–190 (2016).
56. Kallepitis, C. *et al.* Quantitative volumetric Raman imaging of three dimensional cell cultures. *Nat. Commun.* **8**, 14843 (2017).
57. Motegi, H. *et al.* Identification of Reliable Components in Multivariate Curve Resolution-Alternating Least Squares (MCR-ALS): a Data-Driven Approach across Metabolic Processes. *Sci. Rep.* **5**, 15710 (2015).

Acknowledgements

The late Prof. Jan Larsen is acknowledged for discussions related to the analysis of complex data. We would like to acknowledge the Center for Intelligent Drug Delivery and Sensing Using Microcontainers and Nanomechanics (IDUN) funded by the Danish National Research Foundation (grant no. DNRF122) and the Velux Foundations (grant no. 9301) for funding of this project. We would also like to acknowledge Dr. Tomas Rindzevicius for lively discussions and guidance during the planning stages of this work.

Author Contributions

P.O.O. performed the experiments, analysed data and wrote the paper; O.I. built the Raman microscope, analysed the data and performed the experiments. R.S. wrote the software for the Raman microscope and supported in the experiments. P.E.L. revised the manuscript. A.B., T.R., J.R., supervised the project, gave conceptual advice and revised the manuscript.

Additional Information

Supplementary information accompanies this paper at https://doi.org/10.1038/s41598-019-43959-0.

Competing Interests: The authors declare no competing interests.

Publisher's note: Springer Nature remains neutral with regard to jurisdictional claims in published maps and institutional affiliations.

Supplementary Information

Imaging of dehydration in particulate matter using Raman line-focus microscopy

Peter Ouma Okeyo[1,2,3], Oleksii IIchenko[2,3], Roman Slipets[2,3], Peter Emil Larsen[2,3], Anja Boisen[2,3], Thomas Rades[1], Jukka Rantanen[1]

[1]Department of pharmacy, University of Copenhagen, Universitetsparken, 2, 2100, Copenhagen, Denmark

[2]The Danish National Research Foundation and Villum Foundation's Center for Intelligent Drug Delivery and Sensing Using Microcontainers and Nanomechanics (IDUN), Department of Health Technology, Ørsted Plads, 2800 Kgs, Lyngby, Technical University of Denmark

[3] Department of Health Technology, Technical University of Denmark, Ørsted Plads, 2800, Kgs. Lyngby, Denmark

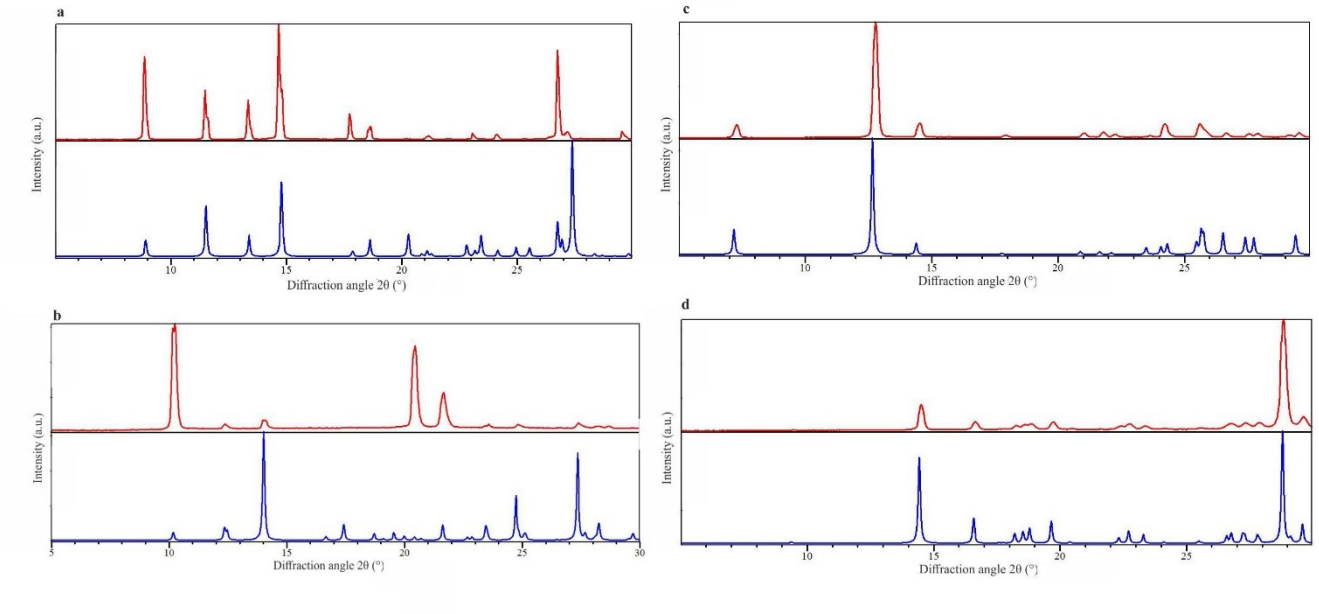

Supplementary figure 1. Experimental (in red) simulated (in blue) XRPD diffractograms. a) The diffractograms of TP MH, THEOPH01 **b)** TP AH form II, BAPLOT and **c)** NF MH II, HAXBUD **d)** NF AH β, LABJON02.

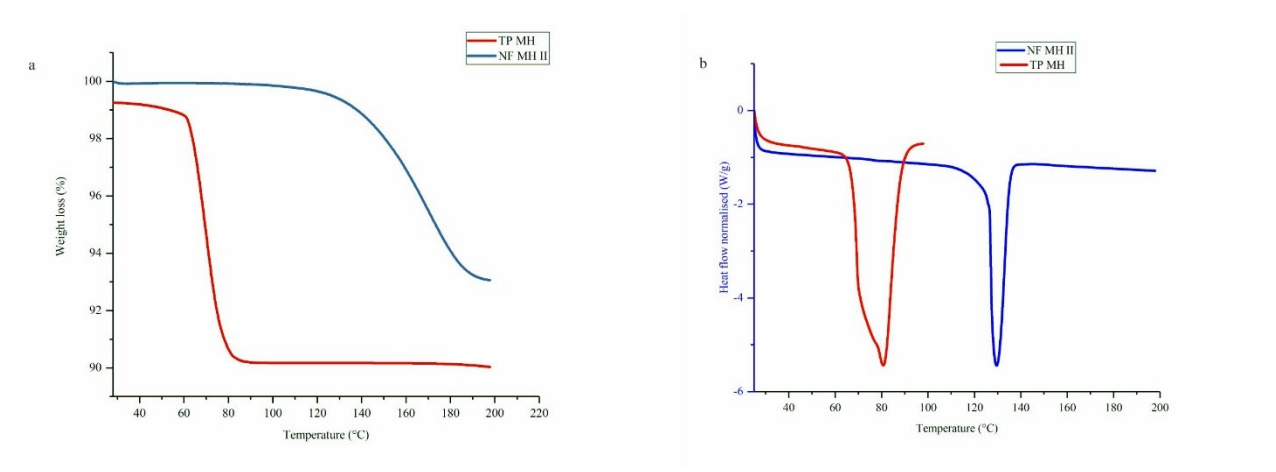

Supplementary figure 2. a) TGA thermograms, and b) the DSC thermogram of NF MH II (blue) and TP MH (red) at a heating rate of 10 °C/min. NF MH II showed a sharp endotherm between 110-140 °C and TP MH thermogram showed a broad, two-step endotherm between 63- 95 °C.

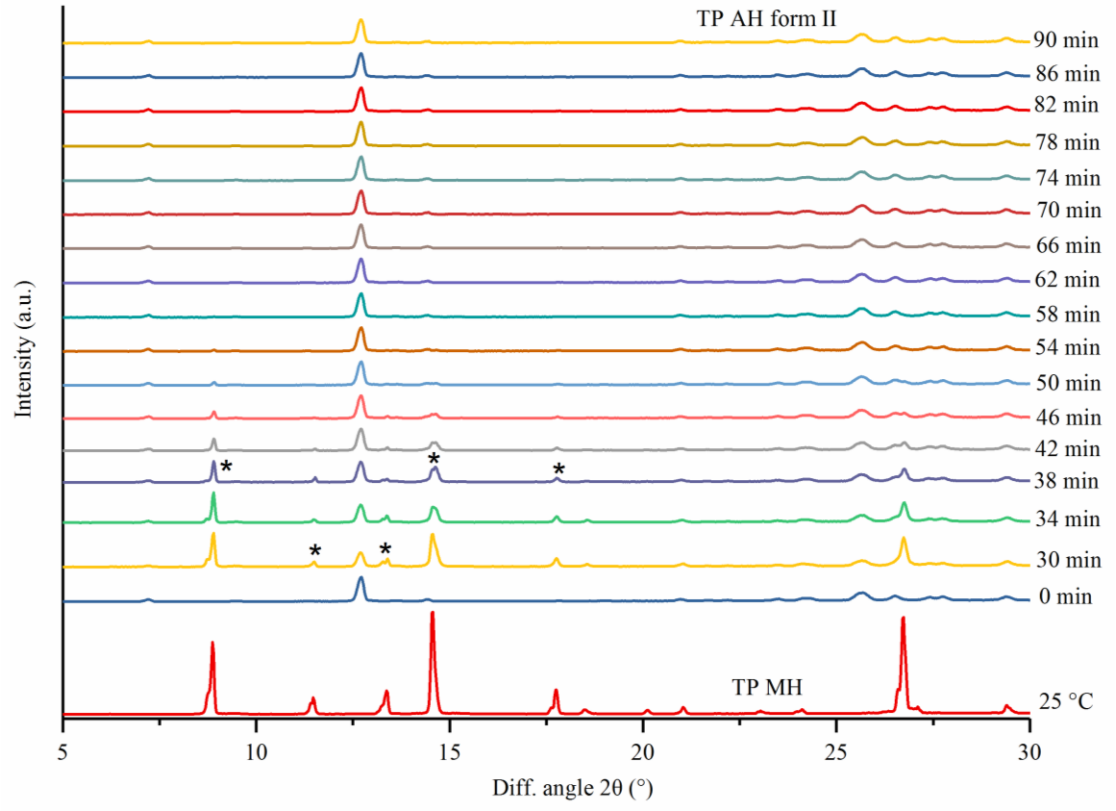

Supplementary figure 3. Variable temperature XRPD (VT-XRPD) of TP MH at 50 °C for 90 minutes. The diffractograms of TP MH is at 25 °C and TP AH form II at 90 minutes. The metastable intermediates appear to be present at 30 and 38 minutes into the experiment with the differences in peaks being marked by the asterix in comparison to their stable forms.

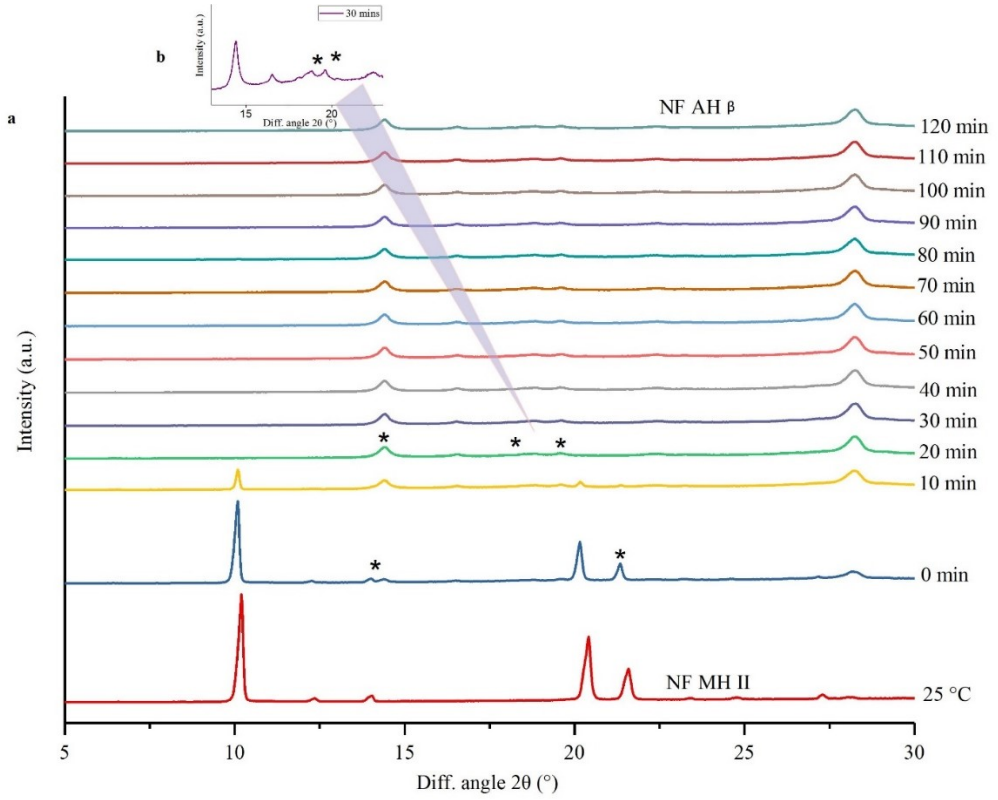

Supplementary figure 4. Variable temperature XRPD (VT-XRPD) of NF MH II at 120 °C for 120 minutes. The diffractogram of NF MH II is at 25 °C and NF AH β at 120 minutes. The metastable intermediates appear to be present at 0 and 30 minutes into the experiment with the differences in peaks being marked by the asterix in comparison to their stable forms. The zoom in of the peak features of potentially another intermediate are also shown at b.

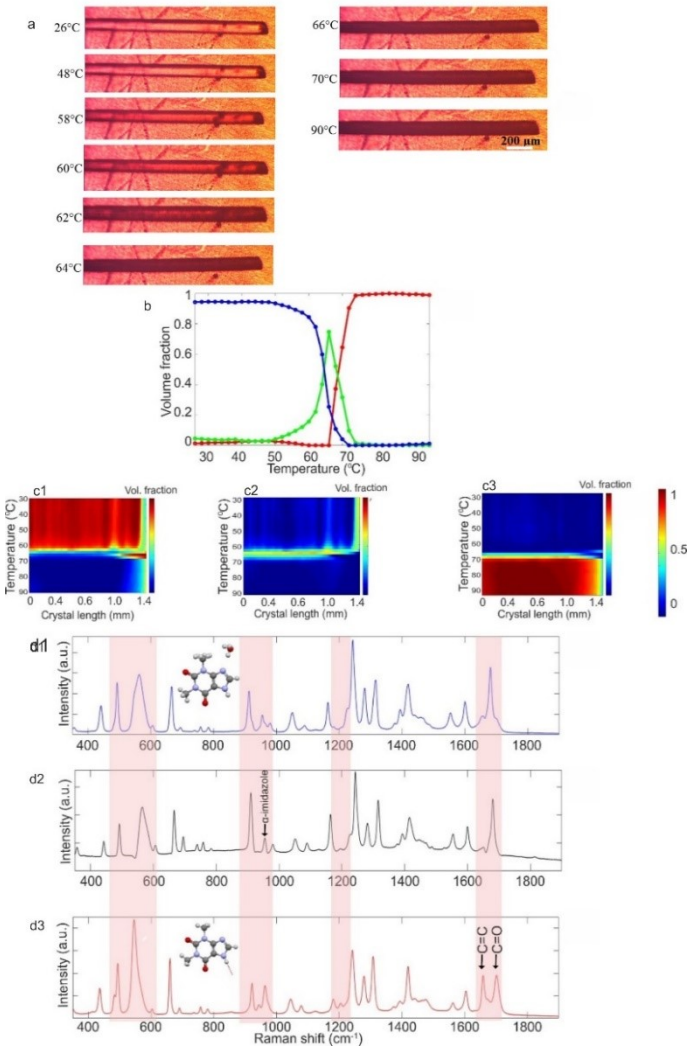

Supplementary figure 5: MCR and NNLS decomposed results of hydrated and dehydrated species of theophylline. a) Optical images showing the dehydration of TP MH to TP AH form II b) concentration profile of TP MH to TP AH form II **c1-c3)** chemical temperature dependent maps of TP MH (left map, red colour), TP MS (middle map, green colour) and TP AH form II (right map, blue colour) **d1-3)** Raman spectra for TP MH, TP MS and TP AH form II respectively.

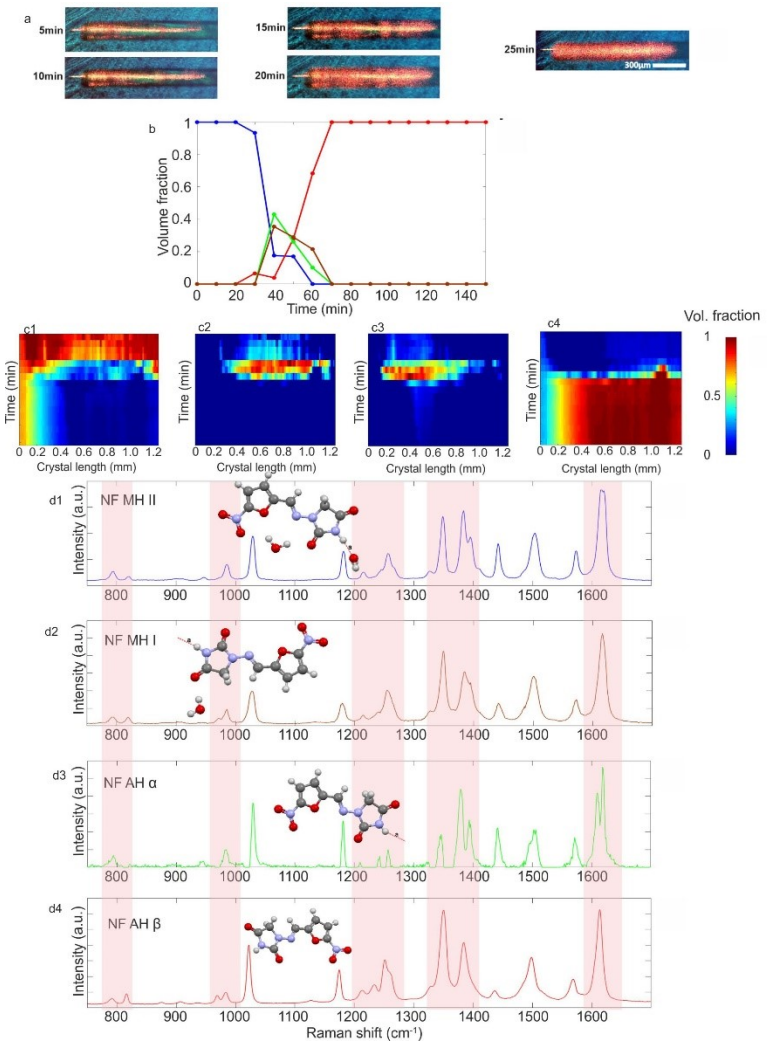

Supplementary figure 6: MCR and NNLS decomposed results of nitrofurantoin solid-state forms. a) Optical images showing dehydration of NF MH II to NF AH β. **b)** concentration profile of NF MH II dehydration mechanism to NF AH (β) **c1-c4)** chemical concentration maps and **d1-d4)** Raman spectra of NF MH II, NF MH I, NF AH α, NF AH β.

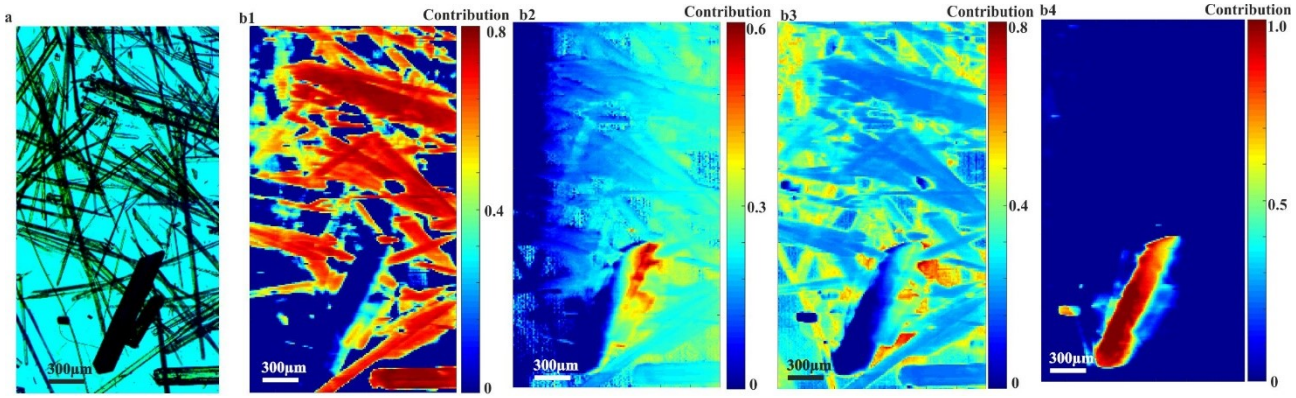

Supplementary figure 7. Multiple particles of NF solid-state forms analysis using the Raman line-focus method at room temperature (uncut) a) Optical images NF forms. **b1)** NF MH II **b2)** NF MH I **b3)** NF AH α and **b4)** NF AH β obtained after NNLS of a depolarised Raman map.

Paper IV

Fast and Quantitative 2D and 3D Orientation Mapping Using Raman Microscopy

O. Ilchenko, Y. Pilgun, A. Kutsyk, F. Bachmann, R. Slipets, M. Todeschini, P.O. Okeyo,

H.F. Poulsen, and A. Boisen

Nature Communications 10 (1). 2019

nature COMMUNICATIONS

ARTICLE

https://doi.org/10.1038/s41467-019-13504-8 OPEN

Fast and quantitative 2D and 3D orientation mapping using Raman microscopy

Oleksii Ilchenko [1*], Yuriy Pilgun [2], Andrii Kutsyk[2], Florian Bachmann[3], Roman Slipets [1], Matteo Todeschini[4], Peter Ouma Okeyo[1,5], Henning Friis Poulsen [6] & Anja Boisen [1]

Non-destructive orientation mapping is an important characterization tool in materials science and geoscience for understanding and/or improving material properties based on their grain structure. Confocal Raman microscopy is a powerful non-destructive technique for chemical mapping of organic and inorganic materials. Here we demonstrate orientation mapping by means of Polarized Raman Microscopy (PRM). While the concept that PRM is sensitive to orientation changes is known, to our knowledge, an actual quantitative orientation mapping has never been presented before. Using a concept of ambiguity-free orientation determination analysis, we present fast and quantitative single-acquisition Raman-based orientation mapping by simultaneous registration of multiple Raman scattering spectra obtained at different polarizations. We demonstrate applications of this approach for two- and three-dimensional orientation mapping of a multigrain semiconductor, a pharmaceutical tablet formulation and a polycrystalline sapphire sample. This technique can potentially move traditional X-ray and electron diffraction type experiments into conventional optical laboratories.

[1] Department of Health Technology, Technical University of Denmark, Kgs. Lyngby, Denmark. [2] Faculty of Radio Physics, Electronics and Computer Systems, Taras Shevchenko National University of Kyiv, Kyiv, Ukraine. [3] Xnovo Technology ApS, Koge, Denmark. [4] Technical University of Denmark, National Center for Micro- and Nanofabrication, Kgs. Lyngby, Denmark. [5] Department of Pharmacy, University of Copenhagen, Copenhagen, Denmark. [6] Department of Physics, Technical University of Denmark, Kgs. Lyngby, Denmark. *email: olil@dtu.dk

Many materials are polycrystalline, meaning that they are composed of a large number of grains (crystallites) of different crystallographic orientations. A full three-dimensional (3D) orientation mapping of the grains (with information about the position, size, morphology, and orientation of each grain, as well as the topological connectivity between the grains) is crucial to relate structure to properties.

Electron backscattering diffraction (EBSD) is a widespread technique for such orientation mapping[1,2], but as a surface-based method, it can only be extended to 3D by serial sectioning. Moreover, it has challenges in the analysis of semiconductors and dielectric materials[1]. Transmission electron microscopy can provide 3D orientation maps with 1 nm resolution, but only in thin foils[3]. On the other hand, imaging based on X-ray diffraction using synchrotrons can provide 3D maps of thousands of grains in mm-sized samples with a resolution of 2 μm[4,5]—in scanning[6] or microscopy mode[7] even down to 100 nm—but this is an expensive and infrastructure-demanding technique. Recently developed mapping of grain orientations in 3D by laboratory X-rays (LabDCT) is a good alternative to the synchrotron measurements; however, its spatial resolution is limited to 10–15 μm[8].

Polarized Raman microscopy (PRM) has the potential to be developed into a relatively cheap orientation mapping technique[9], with a diffraction-limited spatial resolution of around 200 nm[10]. In PRM, if the symmetry of the crystal is known, Raman tensors $\Re_j$ for crystal modes j can be obtained[11] and Raman intensities $I(\theta)$ versus sample rotation angle θ can be simulated[9]. Correlation between theoretical and experimental angular intensity dependencies $I_{\mathrm{theor}}(\theta)$ and $I_{\mathrm{exp}}(\theta)$ can, therefore, be used for the determination of the local crystallographic orientation[9] (see Supplementary Note 1). The first studies regarding polarized Raman spectroscopy began in 1964 when Loudon presented a Raman tensor analysis theory under the form of Raman scattering tensors for each of the 32 crystal classes[12]. Later, this theory was applied for crystallographic orientation analysis of inorganic[13–16] and organic single crystals[17,18], as well as inorganic crystals present in biological systems like calcite crystals in tergite exocuticles[19]. Raman tensor analysis theory was also developed and applied for the study of complex biomolecular crystals, including nucleobases in the nucleic acid of DNA[20,21], nucleosides[22,23], antihuman immunodeficiency virus agents[24], amino acids and peptides[17,25–27]. PRM has also been used for partially orientated biological systems like bone osseous tissues[28] and collagen fibrils in human osteonal lamellae[29]. During the last few years, the method has been applied to the study of crystallographic orientations, defects, doping effects, and Van der Waals interactions in 2D materials like graphene[30,31], $MoTe_2$[32], SnSe[33], ReS_2[34], MoS_2[35], GeAs[36,37], metal dehalogenases[35], and black phosphorous[35,38]. PRM has additionally been used for the investigation of GaP nanowires[39] and carbon multiwall nanotubes[40].

Most of the listed papers were focused on the determination of sample crystallographic orientations at the microscale, with the Raman microscope working in backscattering mode[9,41]. There has been a growing interest in confocal PRM studies of polycrystalline ceramics during the last years[42,43] including piezoelectric ceramics[44–46]. More recently an orientation type contrast was exploited in PRM studies of uranium oxide ceramics[47] and cancerous breast tissue[48]. In these papers, the PRM setup was used for improving the contrast in crystal features differentiation. The 3D domain orientation in $BaTiO_3$ crystals has been revealed after the sample has been mapped in a polarized Raman microscope with an a-plane crystal orientation[49]. Orientation distribution mapping of polycrystalline $CuInSe_2$ has also been demonstrated[10] by a combination of Raman contrast and EBSD mapping.

However, so far no one has presented a stand-alone orientation map based on Raman scattering, due to several experimental and theoretical problems. In particular, polarized Raman experiments have so far been carried out by rotating the sample or rotating a set of wave plates in the incident laser or on scattered beams in the Raman setup[9]. Such optical layouts require multiple Raman spectra measurements using numerous combinations of the orientation of the polarization state of the incident laser and orientation of the analyzer[41]. Due to this, Raman orientation mapping would need sequential polarization measurements at each raster-scanning point, which would make such hypothetical mapping procedures very complex and extremely slow and thus practically impossible. In addition, existing experimental PRM setups introduce ambiguities in measurements, implying that the approach fails completely for some orientations. As an example, in a scheme with normal sample illumination and on-axis collection of scattered light, it is impossible to determine a rotation of a (111) Si wafer around the [111] axis (Fig. 1a, Supplementary Fig. 1, Supplementary Note 1). Such problem can be partially avoided by tilting the sample or by realization of polarized off-axis Raman scattering registration[50] (Fig. 1b). However, as we show below, polarized Raman spectroscopy with off-axis registration also provides ambiguities in the determination of Euler angles, thus some combination of on-axis and off-axis channels must be used. To our knowledge, a theoretical investigation of the optimal number of on-axis/off-axis polarized Raman scattering channels in PRM has not been performed. Therefore, a measurement strategy for how to perform quantitative orientation mapping with an angular accuracy comparable with EBSD needs to be developed.

Here, using a concept of ambiguity-free orientation determination data analysis and simultaneous registration of multiple Raman scattering spectra obtained at different polarizations, our approach allows for 2D and 3D quantitative orientation mapping of multigrain materials. First results for silicon, a pharmaceutical tablet and for sapphire reveal favorable specifications: sub-micrometer resolution, fast data acquisition, and a high orientation resolution. The method applies to all Raman active materials independent of crystal symmetry and requires no sample preparation.

Results

Theoretical investigation of orientation ambiguity and error. To assess the orientation determination ambiguity and error we have performed simulations on Si. Si has cubic symmetry (O_h crystal class) and is well investigated by PRM[9,11] (Supplementary Note 2). We simulated a test dataset of Raman intensity variation versus wafer rotation angle ψ for three types of Si wafers with surface oriented along (100) (Supplementary Fig. 2), (110) (Supplementary Fig. 3), and (111) (Supplementary Fig. 4) planes. The orientation determination results were obtained by fitting Euler angles to simulated data and were represented in a crystallographic color code using MTEX toolbox for Matlab[51,52], see Supplementary Fig. 5. The color corresponds to orientation of the wafer normal direction relative to crystallographic axes of Si. Misorientation angle, which corresponds to undetermined rotation of the sample, is depicted in Supplementary Fig. 5 as vertical bars on the right side of each subplot.

Orientation fitting was done using varying numbers of polarized channels (2–12 channels), see Supplementary Note 3, Supplementary Fig. 5. An analysis of the simulation results reveals, that basic orientation determination becomes possible for four or more channels. However, for some specific orientations, intensity data remains ambiguous and rotation angle ψ is not recovered. This is clearly seen for the (111) wafer in misorientation plots in Supplementary Fig. 5, where the misorientation angle varies from zero to the largest possible for cubic symmetry

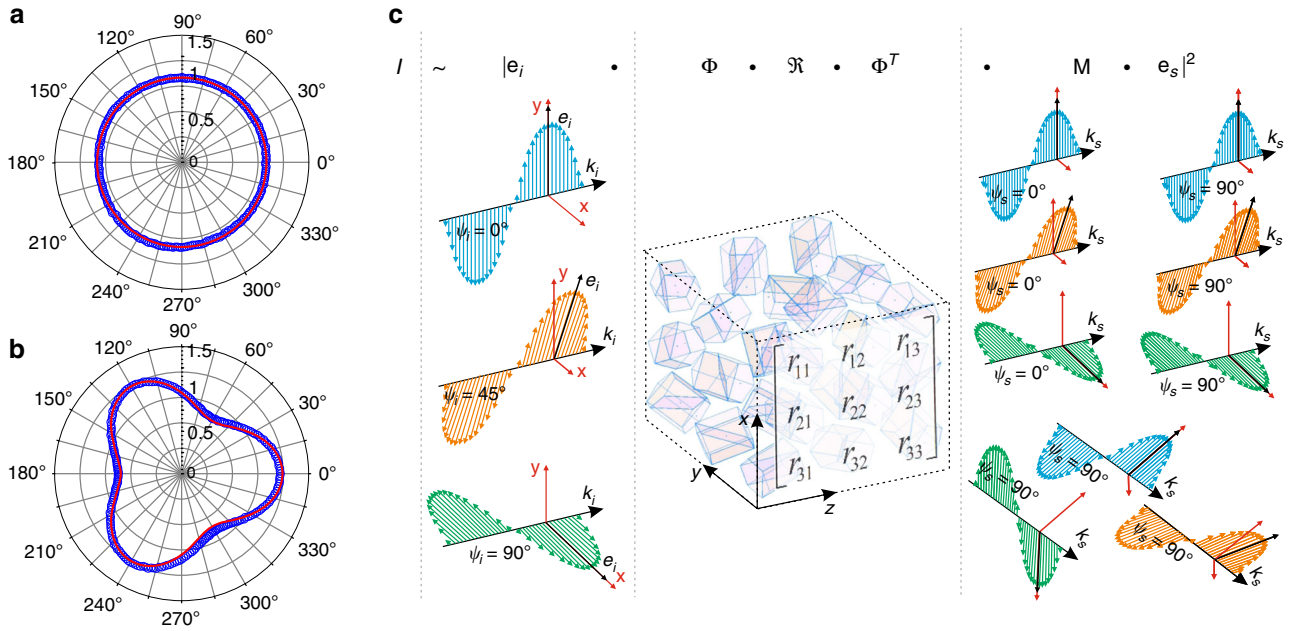

Fig. 1 Optimization of the polarized Raman signal collection geometry. Comparison between theoretical (red line) and experimental (blue circles) responses of the sum of Si modes versus wafer rotation angle ψ plotted in polar coordinates for Si wafer with surface plane (111) for on-axis (**a**) and off-axis (**b**) polarized Raman scattering channels (**c**), illustration of the incident/scattering polarization and signal collection geometries for a solution with nine polarized channels.

Table 1 Optimization of the orientation mapping configuration. Optimization results for different numbers of channels and channel polarization combinations. Orientation error percentage represents geometric area on the sample, where reliable fit was achieved. Misorientation angle column represents ambiguity of the fit; the chosen number of channels was nine (highlighted in the red box).

	On-axis channels								Off-axis channels				Number of channels	Orientation error, %	Misorientation, °
ψ_i	0°	45°	90°	135°	0°	45°	90°	135°	0°	45°	90°	135°			
ψ_s	0°				90°				90°						
	●	●	●	●	■	■	■	■	▲	▲	▲	▲	12	0.0	<1
	●	●	●	●	■	■	■	■	▲	▲	▲		11	0.6	<1
	●	●	●		■	■	■		▲	▲	▲	▲	10	0.8	<1
	●	●	●		■	■	■		▲	▲	▲		9	1.2	<1
	●	●	●		■	■	■		▲		▲		8	4.7	<1
	●	●	●	●	■	■	■	■					8	48.1	62.8
	●	●	●	●	■	■	■						7	48.1	62.8
	●	●	●		■	■	■						6	48.0	62.8
	●	●	●		■		■						5	55.7	62.8
	●	●			■	■							4	63.5	62.8
	●	●	●										3	75.2	62.8
	●		●										2	88.2	62.8

62.8°. Nevertheless, even for such ambiguous data, some orientation data is still recovered, and it is possible to clearly distinguish wafers (100), (110), (111) even for four measurement channels. Full wafer orientation determination is only possible for nine or more channels.

Simulation results shown in Supplementary Note 4 and Supplementary Fig. 5 revealed that some orientations, like those appearing in the surface plane (111) of Si, are prone to introduce ambiguity in measurement data. Although simulation helped to define minimal number of polarization channels required to determine orientation, it still has limited scope, because only (100), (110), and (111) cases were considered.

To assess the quality of the orientation determination in the general case, additional analysis using exhaustive search of indistinguishable solutions over a range of all possible Euler angles was performed (described in details in Supplementary Note 4). That search revealed, that all measurement schemes with only on-axis channels applied to samples with cubic symmetry exhibit an ambiguity where two different orientations produce exactly the same intensity measurements. These two orientations have Euler angle ψ which differs by 180°. Adding off-axis measurement channels removes this $\psi + 180°$ ambiguity.

Ambiguity simulation results for a multi-grain sample with different numbers of measurement channels are summarized in Table 1. The column "Orientation error" shows the percentage of the area where the local orientation is correctly determined. The maximum orientation error registered in the successfully fitted zones is shown in the column "Misorientation" in Table 1. The

same quantities versus total number of channels are plotted in Supplementary Fig. 6.

According to these simulations, the ambiguity can be successfully resolved when off-axis channels are added to the measurement setup. Still, adding only two off-axis channels is not sufficient to resolve ambiguity completely. Full resolution becomes possible when adding three off-axis channels to six on-axis channels, resulting in total nine measurement channels. Further addition of up to in total 12 channels does not noticeably increase the accuracy of the fit. Thus, in our experimental setup we decided to use nine channels.

The chosen geometry with nine polarized channels is illustrated in Fig. 1c. Three polarized laser beams $\mathbf{e}_i$ with orientations of polarization state 0°, 45°, and 90° interact with a multigrain material with scattering properties dependent on local crystallographic orientation and described by the Raman tensor with rotation matrices $\boldsymbol{\Phi}$ and $\boldsymbol{\Phi}^{\mathbf{T}}$. The scattered Raman signal $\boldsymbol{e}_s$ (with corresponding rotation matrix $\mathbf{M}$) from the three incident lasers is divided into nine backscattering channels (six on-axis and three off-axis) after propagation through three analyzers with orientations 0° and 90° for on-axis Raman scattering detection and 90° for off-axis Raman scattering detection. The information obtained from the nine Raman channels is used for determining the crystallographic orientation of a selected local volume. 2D or 3D orientation mapping is obtained by scanning the sample in x, y, z with respect to the incident beams.

Experimental setup. Based on theoretical investigation of quantitative orientation mapping by Raman microscopy, we have developed and demonstrated a method, Single-Acquisition Raman Orientation Mapping (SAROM), for the study of crystalline samples. Our self-made Raman setup provides two orders of magnitude faster Raman polarization measurements compared with existing techniques and the ambiguity issue is overcome. The SAROM system is capable of simultaneously illuminating the sample with multiple laser beams at different orientations of the laser polarization state and detecting Raman scattering beams at multiple on-axis/off-axis scattering directions without using any moving parts (Fig. 2a, Supplementary Fig. 7). As shown in Table 1, chosen configuration with nine channels provides theoretically estimated accuracy of the orientation measurements by SAROM of <1°.

SAROM consists of a Laser Beam Delivery System (LBDS), which directs three laser beams with different orientations of polarization state on the sample focal plane (Fig. 2a), and an aberration-corrected Raman Beam Delivery System (RBDS) (Supplementary Figs. 8–12) with Wollaston Analyzer Unit (WAU), capable of splitting the Raman beam into on-axis and off-axis scattering geometries collected with different analyzer orientations (Fig. 2b–e, Supplementary Fig. 13). In a 2D mapping configuration, the sample is illuminated with a single laser source. Three laser beams with different orientations of polarization state are spatially separated on the sample and on the spectroscopic

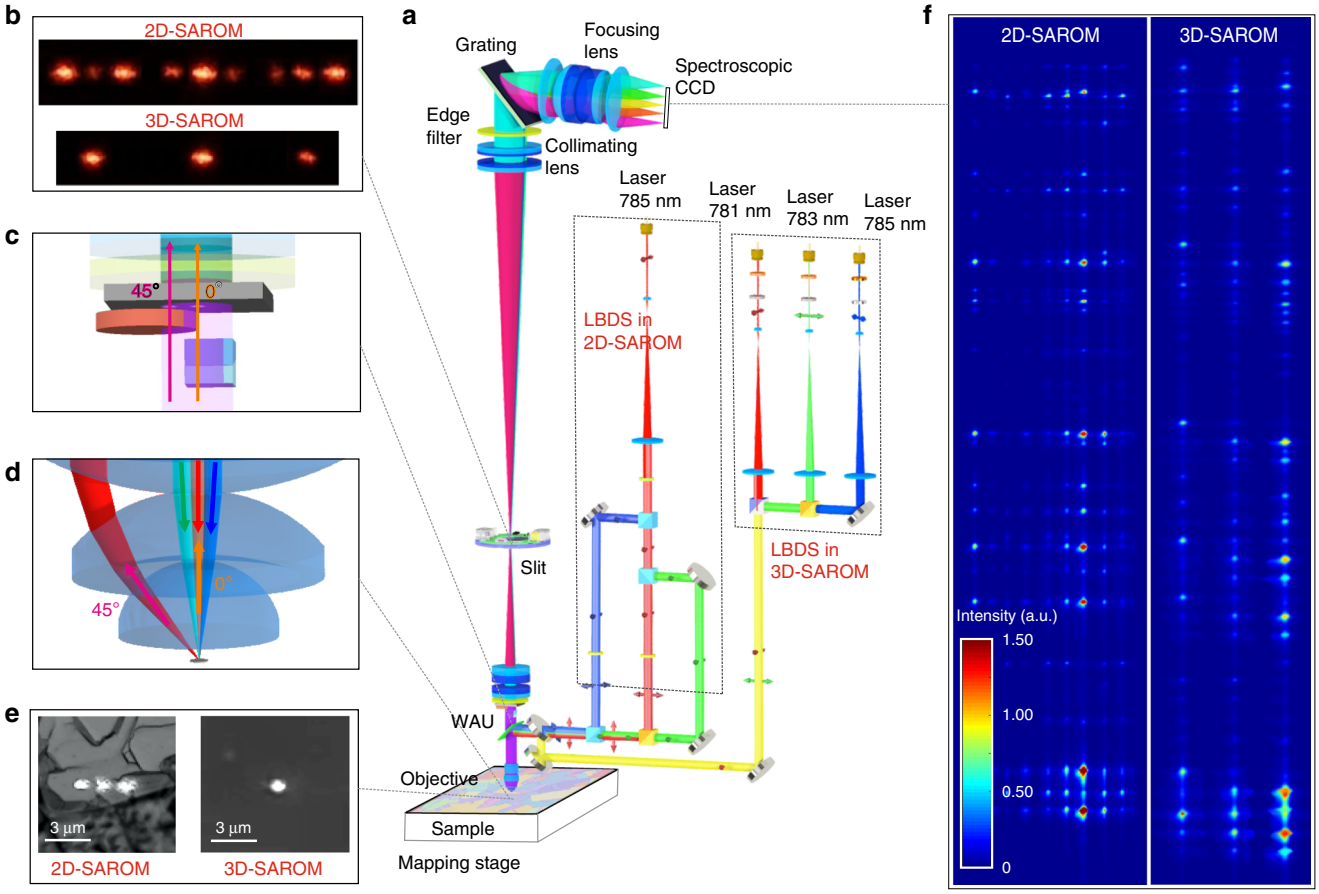

Fig. 2 SAROM system design. a Optical setup of SAROM in 2D and 3D mapping configurations designed in Zemax Optics Studio 17, **b** images of polarized beams on the spectroscopic slit focal plan, **c** on-axis and off-axis Raman scattering beam path through Wollaston Analyzer Unit (WAU), **d** sample illumination by laser beams and Raman signal collection geometry in on-axis (0°) and off-axis (45°) scattering pathways, **e** microscopy images of the laser spots on the sample in 2D- and 3D-SAROM configurations, **f** images of resulting Raman signals from carbamazepine drug obtained on a spectroscopic CCD in the 2D and 3D-SAROM configurations.

CCD focal planes (Fig. 2b-e). In a 3D mapping configuration, the sample is illuminated with three laser sources. Three laser beams with different orientations of polarization state overlap on the sample, however, they become separated on spectroscopic CCD focal plane (Fig. 1f) due to slightly different excitation wavelengths (see "Methods" section for details).

Artifact correction in polarized Raman measurements is a challenge. In order to reach an assessable error in SAROM, corrections are needed for: wavelength dependent intensity attenuation[53], Raman intensity scaling and normalization[43], Linear Phase (LP) and Linear Amplitude (LA) anisotropy of each optical element[54], and depth-dependent birefringence[13]. Since each channel has its own correction parameters, an experimentally based calibration becomes practically impossible. Therefore, we build a model, which predicts the values of the listed parameters (Supplementary Note 5, Supplementary Fig. 14).

Previously, the correction related to the Numerical Aperture (NA) of the microscope objective in PRM, has been realized by taking into account the full aperture of the microscope objective[11]. Here, we performed correction taking into account the NA values for on-axis and off-axis Raman scattering registration channels (see Supplementary Note 6, Supplementary Fig. 15).

Application examples. In the following, we demonstrate the method with a few examples. As an application in 2D, we present work on a polycrystalline Si (poly-Si) solar cell. The SAROM scanning procedure used for the poly-Si sample is shown in Supplementary Movie 1. We generated an orientation map of the poly-Si surface as shown in Fig. 3a by performing a least square fit to the Euler angles based on data from all nine polarized channels (Supplementary Note 7, Supplementary Figs. 16–18). In order to estimate the quality of the analysis technique, we compared this result with an orientation map of the same sample area using EBSD (Fig. 3b). A map of the local orientation difference: the misorientation angle (Fig. 3c) exhibited an average orientation difference of ~2.1° (Supplementary Figs. 19, 20). We argue that this error is dominated by a geometrical distortion of grains in the EBSD data (Supplementary Fig. 21). In order to minimize this effect we corrected the EBDS map for distortions and removed grain boundaries. Nevertheless, several artifact are still present on the map (Fig. 3c). Other sources of discrepancies may be connected with orientation dependent ambiguity of SAROM (Fig. 1, Supplementary Fig. 5) and an orientation determination error of EBSD.

Similar to EBSD[55], SAROM can be used for the study of extended defects like dislocations and grain boundaries, which e.g., directly correlate with the efficiency of solar cells.

Raman microscopy is often used for chemical mapping of pharmaceutical and biological materials[56]. It has been shown that PRM can be used to visualize particles on the surface of tablet formulations[57], however so far no quantitative information on the orientation of single particles has been provided. Here, we performed a content uniformity Raman measurement on a tablet containing carbamazepine dihydrate (CBZD) and polyvinylpyrrolidone (PVP). Using MCR, these components were decomposed including the fluorescence background as shown in Fig. 4a (Supplementary Fig. 22). Applying SAROM to the same area on the surface of the tablet, we obtained an orientation map of CBZD (monoclinic symmetry, C_{2h} crystal class) (Fig. 4b, Supplementary Note 8, Supplementary Figs. 23–27, Supplementary Movie 2). These findings show the potential for SAROM to provide insight on crystal face functionality in pharmaceutical research and potentially in materials science[58].

Following the SAROM workflow (Supplementary Fig. 7a), we extended the method to 3D mapping of a semitransparent polycrystalline sapphire sample having grain sizes between 5 and 40 μm (Supplementary Note 9, Supplementary Fig. 28). 3D plots of the Raman spectra versus ψ for different polarization configurations and correlations between theoretical and experimental responses of the $E_g(5)$ mode are shown in Supplementary Figs. 29–31, and in Supplementary Movie 3.

Nine maps of the intensity of $E_g(5)$ Raman mode, corresponding to the nine differently polarized Raman channels, are shown in Supplementary Fig. 35. Applying Supplementary Eq. 12 adapted to the trigonal symmetry of sapphire D^{6}_{3d}, we fitted the Euler angles at each measured point to these data (see Supplementary Note 10). The resulting 3D-SAROM volumetric orientation map is shown in Fig. 5 and in Supplementary Movie 4. 3D grain mapping is very important in ceramics technology, as properties such as fracture strength is strongly influenced by the statistical distribution of grain orientation and the grain boundary topology[59].

Discussion

SAROM has some limitations. The theoretically determined orientation resolution varies with the orientation of the grain. Typically, the theoretical variation is well below 1° (Supplementary Fig. 6). Instrumental implementation implies that the error may increase up to 2°, which however still is sufficient for most applications. SAROM cannot be used on materials with high fluorescence background at the excitation wavelength of the laser source. However, the polycrystalline sapphire sample presented fluorescence at the grain boundaries, which we used as a perfect mark for grain visualization and exploited for further segmentation (Supplementary Figs. 32–34).

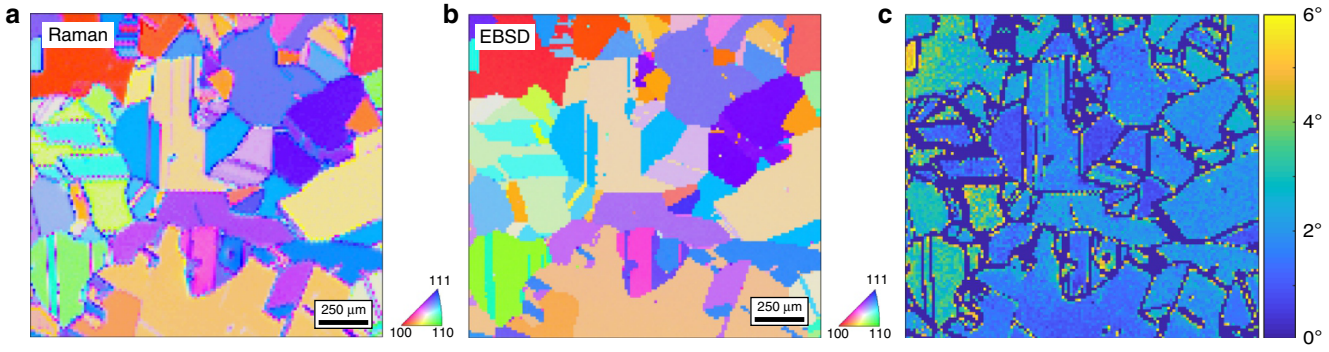

Fig. 3 2D-SAROM results for Si. a 2D-SAROM and **b** EBSD orientation maps of the surface of a polycrystalline Si sample. The colors refer to the orientations shown by the inverse pole figures (inserted). Both, SAROM and EBSD orientation maps have a step size of 13.51 μm, a map dimension of 131 × 120 pixels or 1770 × 1620 μm and an exposure time per step of 60 ms. **c** misorientation map between SAROM and EBSD data.

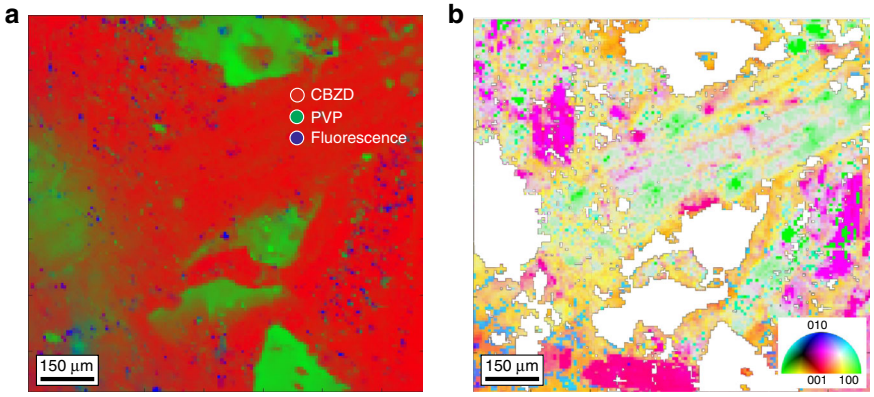

Fig. 4 2D-SAROM for a compacted tablet. a Chemical map obtained from the surface of a compacted tablet containing CBZD and PVP (2:1), **b** 2D-SAROM map showing the random orientation of CBZD particles on the surface of the tablet. The colors refer to the orientations as defined by the inverse pole figure (bottom right). SAROM was performed at a step size of 8 µm, map dimension 134 × 134 pixels or 1072 × 1072 µm, exposure time per step was 150 ms.

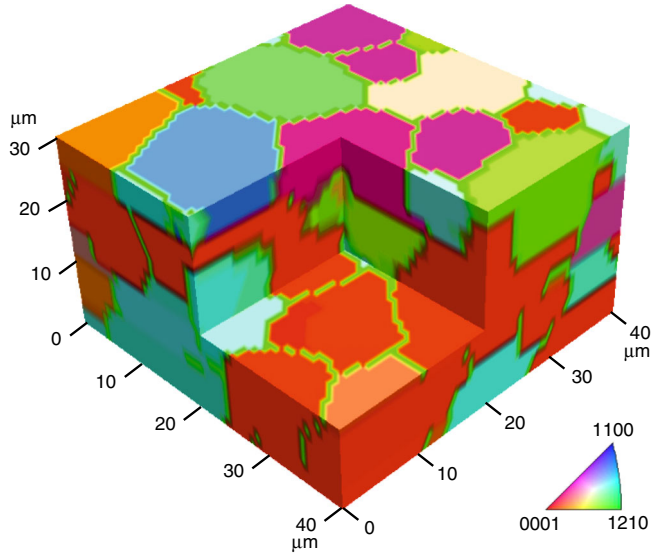

Fig. 5 3D-SAROM on a polycrystalline sapphire sample. The colors refer to orientations as shown by the inverse pole figure (inserted). The green boundaries between grains were generated as part of the segmentation procedure (Supplementary Figs. 32–34, Table S1). SAROM was performed at a lateral step size of 0.7 µm, axial step size of 1.7 µm. Map dimension is 57 × 56 × 18 pixels or 40 × 39.2 × 30.6 µm with an average exposure time per step of 180 ms.

The 3D-SAROM analysis has several limitations. The depth of scanning is limited by the material transparency and Raman scattering cross-section[45] of the sample at laser/Raman scattering wavelengths: for the polycrystalline sapphire study the maximum depth is ~0.1 mm at 785 nm laser wavelength. In-depth SAROM mapping is also limited by off-axis laser refraction effects leading to Raman signal attenuation and decreased axial resolution[60–63]. In order to minimize these effects we used oil immersion microscope objective for 3D measurements of polycrystalline sapphire (Supplementary Fig. 36). These limitations of in-depth scanning can be partly overcome by increasing the spectra acquisition time.

Further development of SAROM may include the use of visible range lasers. In comparison with near infrared lasers, used in the present study, visible lasers will increase the Raman cross-section and the SAROM spatial resolution. However, the choice of excitation sources should also take into consideration the transparency of material at the excitation wavelength and possible resonance Raman effects which may change the Raman tensor coefficients leading to errors in orientation determination or modifications in Raman tensor analysis[64].

In summary, SAROM is a nondestructive quantitative orientation mapping method with a high diffraction-limited spatial resolution, similar to that of confocal Raman microscopy (Supplementary Fig. 37). It applies to all Raman active inorganic and organic crystalline material. Due to the simultaneous measurement of multiple polarized channels, we have demonstrated fast scanning capabilities: 16 min for the 2D orientation maps of polycrystalline Si (131 × 120 pixels), 46 min for the 2D orientation map of tablet formulation (134 × 134 pixels) and 176 min for the 3D orientation map of polycrystalline sapphire (57 × 56 × 18 pixels). Furthermore, since it is a confocal method, it does not require complex tomographic data reconstruction as in the case of 3D X-ray orientation microscopy[65]. The equipment has a relatively low price compared with 3D-EBSD and high-resolution 3D X-ray microscopy[66]. SAROM is applicable to a broad range of problems in 2D materials, polymers, drugs, and biomolecular research. It is useful in mineralogy, geology, semiconductors (solar cells, microelectronic substrates), ceramics (piezo-, magneto-, and ferroelectrics), and superhard materials (abrasives, drilling tools, superhard transparent windows). Moreover, the functionality of SAROM can be extended by combination with e.g., confocal Raman microscopy, hyperspectral imaging, or polarized light microscopy. Further development of SAROM can be expanded into instantaneous polarized Raman mapping similar to wide-field Raman microscopy[67,68].

The developed method is therefore likely to become a simple, economically accessible, and broadly used characterization tool for 2D/3D crystallographic mapping. Moreover, it expands the range of materials that can be analyzed and could bring new insight into our understanding of the structure of matter.

Methods

Materials. Silicon wafers with surface planes (100), (110), (111) were provided by National Center of Micro- and Nanofabrication in Denmark.

Polycrystalline Si solar cell was provided by the factory Pillar (Kyiv, Ukraine).

Anhydrous carbamazepine was obtained from Sigma-Aldrich (CAS No.298-46-4). Povidone (polyvinylpyrrolidone, PVP, K60) was obtained from Sigma-Aldrich (CAS No. 9003-39-8).

Sapphire monocrystalline plates at a-, c-, m-, and r-planes were purchased from Crystran Ltd.

Polycrystalline sapphire sample with dimensions 10 × 5 × 5 mm and average grain size of 20 µm was purchased from CoorsTek GmbH.

EBSD analysis of poly-Si. The surface of the polycrystalline Si was mechanically polished prior to EBSD investigation. Silica microparticles having dimensions of 6, 3, and 1 µm were sprayed on a rotating diamond grinding disc for the polishing.

Starting with the larger microparticle size, the sample was alternately polished and visually inspected using an optical microscope. The inspection was necessary to verify that the surface was without scratches along a particular direction, index of an inhomogeneous polishing. The same polishing procedure was repeated using each microparticle size.

The polished sample was mounted on an EBSD holder with a 54° tilt respect to the electron beam perpendicular. The holder was installed on a FEI Nova 600 NanoSEM stage and the sample was tilted 16°, to reach a total tilt of 70° respect to the electron beam perpendicular. The microscope was equipped with a Bruker QUANTAX EBSD detector and operated at an accelerating voltage of 15 kV, a beam current of 10 nA, a 40 μm aperture and at a working distance of 12 mm. The detector was positioned in such a way that the smallest distance between the electron-beam focusing point at the specimen surface and the camera was 16.5 mm. All measurements were performed in high vacuum mode. EBSD orientation map was collected with a pattern resolution of 320 × 240 pixels, exposure time of 155 ms, and step size of 25 μm, total measurement time 3.3 h. The raw data were processed using MTEX toolbox in Matlab.

Recrystallization of carbamazepine dihydrate, tablet preparation, and solid-state analysis. Anhydrous carbamazepine was dissolved (25 mg/mL) in a vial filled with a water–ethanol solvent composition (3:1) at 60 °C. The vial was then removed from the hot plate and allowed to cool down to room temperature. After around 4 days, needle and plate shaped particles of CBZD formed via slow evaporation crystallization and were harvested by filtration.

CBZD was identified using a PANalytical Xpert PRO X-Ray Diffractometer (PANanalytical B.V., Almelo, Netherlands) with a nickel filtered CuKα ($\lambda = 1.5418$ Å) source that was generated at a tube voltage of 45 kV and current of 40 mA. A PIXcel detector with a θ/θ goniometer was used. The measurements were performed at a reflection mode between 5° and 35° at a step size of 0.0263° 2θ and a scan speed of 0.06734° 2θ. The X'Pert Data Collector software provided by PANalytical, Almelo, Netherlands was used in order to analyze the diffractograms. For reproducibility purposes, triplicate measurements were performed.

In order to visualize the molecular structure (SF2), intermolecular interactions, and different faces (SF3) of CBZD, Mercury CSD 3.10.3 (Build 205818) was used. Mercury was provided by the Cambridge Crystallographic Data Centre, UK.

A tablet press (Gamlen Tableting Ltd, UK) with a 6 mm diameter cylindrical flat-faced compacts was used in order to prepare the tablets. This tablet press was equipped with a 500 kg load cell 8CT6–500–022). 200 mg (±10 mg) of CBZD and 100 mg (±10 mg) were compacted at a compression speed of 60 mm/min. The tableting die was lubricated with magnesium stearate suspension prepared in acetone. Tablets were prepared in triplicate.

X-ray powder diffraction (XRPD) was used in order to confirm carbamazepine (CBZ) to be carbamazepine dihydrate (CBZD). In order to achieve this, the experimentally obtained XRPD diffractogram of CBZD was compared with the calculated diffractogram (CBZD, FEFNOT02, monoclinic, P21/c)[69] from the Cambridge Structural Database (CSD).

Working principle of SAROM. In order to obtain high-quality 2D/3D Raman orientation maps, we developed and experimentally verified all required data acquisition and data analysis steps. The overview of SAROM workflow is shown in Supplementary Fig. 7. It consists of six different steps: (i) the development and construction of the Raman setup, which is capable to acquire simultaneously nine polarized Raman spectra from each scanning point on the sample; (ii) the development of preprocessing and artifacts correction algorithms applied to the polarized Raman spectra; (iii) the development and verification of the Raman tensor model; (iv) single acquisition Raman orientation mapping at multiple polarization channels; (v) fitting of Euler angles at each mapping point and (vi) the color code-based representation of the orientation map.

Simultaneous measurement of polarized Raman spectra. One of the most critical steps which needed to be solved in SAROM is achievement of high speed of polarization measurements. For this purpose, we designed and constructed a Raman setup without moving parts, capable to illuminate the sample with multiple laser beams at different laser polarizations and simultaneously detect Raman scattering beams at multiple analyzer orientations (Supplementary Fig. 8). The working principle of the simultaneous measurement with nine polarized Raman channels is schematically shown in Supplementary Fig. 7b. Before starting the optical design having such complicated structure, we performed test measurements in a 'traditional' polarized Raman microscope layout[41] in order to find the minimum number of polarization measurements required for obtaining valid crystal orientations (Table 1). The 'traditional' optical setup can acquire one polarized Raman spectrum per measurement[9]. Therefore, it requires a set of sequential measurements with different combinations of incident laser polarization angle ψ_i and analyzer angle ψ_s. In order to get more flexibility in the definition of incident laser/analyzer orientation we slightly modified the common used Porto notations[54] for the back scattering on-axis and off-axis measurement configuration to the following form: $z(\psi_I, \psi_s)\bar{z}$.

We performed test simulations and data fitting on the surface of monocrystalline Si wafers with surface planes (100), (110), and (111), respectively. It was determined that at least three differently polarized laser orientations and three analyzer orientations are required, with mandatory presence of off-axis channels. In total, we got nine combinations of polarization measurements which can be defined as $z(\psi_i^1\ \psi_s^1)\bar{z}$, $z(\psi_i^1\ \psi_s^2)\bar{z}$, $z\left(\psi_i^1\psi_s^{\mathrm{off-axis}}\right)\bar{z}$, $z(\psi_i^2\ \psi_s^1)\bar{z}$, $z(\psi_i^2\ \psi_s^2)\bar{z}$, $z\left(\psi_i^2\psi_s^{\mathrm{off-axis}}\right)\bar{z}$, $z(\psi_i^3\ \psi_s^1)\bar{z}$, $z(\psi_i^3\ \psi_s^2)\bar{z}$, $z\left(\psi_i^3\psi_s^{\mathrm{off-axis}}\right)\bar{z}$. The angles ψ_i, ψ_s generally can have different values, however in the case of Si analysis with O_h symmetry we used the following angles: $\psi_i^1 = 0°$, $\varphi_i^2 = 45°$, $\psi_i^3 = 90°$, $\psi_s^1 = 0°$, $\psi_s^2 = 90°$, $\varphi_s^{\mathrm{off-axis}} = 90°$. We chose these values as a result of optimization (see Supplementary Note 4, Table 1). Simultaneously obtained experimental data in SAROM setup are shown in Supplementary Figs. 2–4. In general, our system can work at any ψ_i, ψ_s which can be beneficial for a specific crystal symmetry. If required, SAROM is capable to work with more than nine simultaneously acquired polarized channels. The actual number of channels is limited only by the optical design of the system and spectroscopic sensor dimensions.

Laser beam delivery system (LBDS). The technical realization of the three differently polarized laser spots on the sample focal plane can be performed with two different laser beam delivery optical layouts: 2D- and 3D-SAROM configurations. LBDS in 3D-SAROM consists of three thermally stabilized diode lasers L_1, L_2, L_3 operated at slightly different wavelengths 781 nm, 783.5 nm and 784.8 nm, respectively. Wavelength of each laser can be finely adjusted by the change of diode temperature in order to get the best spectral distance between vibrational modes. The laser beams have polarization angles $\psi_i^1 = 0°$, $\psi_i^2 = 45°$, $\psi_i^3 = 90°$ with respect to the x axis in laboratory coordinate system (x, y, z) (Supplementary Fig. 8). The beams are collimated and centered in the optical layout and then focused at the same spatial point on the sample focal plane. Raman scattering responses from the three differently polarized laser beams are then divided on the spectroscopic CCD focal plane due to the spectral difference in the laser frequency, which is around 20 cm^{-1} (Fig. 2f). 3D-SAROM is beneficial for 3D mapping and for materials with low number of phonon modes, where Raman peaks overlap does not lead to significant data analysis problems.

In 2D-SAROM, three differently polarized laser channels were formed via splitting of the beam from one laser source with a wavelength of 785 nm. Three laser beams then focused at different coordinates on the sample focal plane (Supplementary Fig. 8). Similar concept was demonstrated in polarization-resolved Raman measurements in liquids[70].

Comparing with 3D-SAROM, spectral profiles in 2D-SAROM are not overlapped at spectroscopic CCD. Therefore, 2D-SAROM is beneficial for 2D mapping with complex Raman spectra, where peaks overlapping can lead to uncertainties in vibration mode responses.

On the other hand, 2D-SAROM needs separate rows on the spectroscopic CCD for the registration of Raman signals from differently polarized laser beams. In the case of 3D orientation measurements in 2D-SAROM configuration, the diffraction limited laser points become blurred and overlapped, due to reflection index-caused aberrations when the laser is focused in the depth of the material[49]. Therefore, for the 3D orientation mapping of polycrystalline sapphire we decided to use 3D-SAROM configuration. In such a way, the responses from differently polarized laser spots become non-overlapped on spectroscopic CCD.

Raman beam delivery system (RBDS). Another big challenge in SAROM setup is connected with the design of the Raman beam delivery optical path, including Wollaston Analyzer Unit (WAU), which provides simultaneous measurements at three different analyzer orientations: 0° and 90° in on-axis registration and 90° in off-axis registration.

The key module of RBDS is the WAU. It consists of quartz Wollaston prism, analyzer, and mask (Supplementary Fig. 13). Wollaston prism splits on-axis Raman scattering into two analyzer configurations 0° and 90°, off-axis Raman beam pass through the analyzer. Mask works as a spatial filter for improved separation between on-axis and off-axis channels.

After the WAU, Raman beams are coupled by slit focusing lens with a self-designed and patent pending imaging spectrograph (application number PCT/DK2019/050027) (Supplementary Fig. 9). It is a lens-based spectrograph with a transmission fused silica grating. This grating provides almost polarization-independent spectral efficiency at the level of 96%, which leads to the minimized artifacts in polarized Raman measurements and high sensitivity of the spectrograph[53]. Unique feature of the spectrograph design consists in combination of low NA collimation lens with high NA focusing lens. These lenses provide magnification equal to 0.2×, which leads to the compression of the Raman beam energy down to the size when an entire Raman spectrum covers only one row on the spectroscopic CCD (Supplementary Fig. 36). The spectrograph focusing lens is a self-designed achromatic double-gauss type lens, which consists of six spherical elements (Supplementary Fig. 10). It has a diffraction limited spot size through the entire focal plane, equal to the size of the spectroscopic CCD (30 mm), which provides excellent imaging conditions required for the multichannel SAROM setup. The overall photograph of the SAROM setup is shown in Supplementary Fig. 11.

Linear phase and linear amplitude effects in SAROM setup. The most critical problem in optical path is related to the polarization artifacts compensation for

each polarization channel. For this purpose, we performed numerical polarization analysis using Zemax Optics Studio and obtained estimation about LP and LA anisotropy parameters for propagation through each optical element (Supplementary Fig. 14). In order to minimize LP effects produced by the dielectric mirrors and dichroic beamsplitters during beam propagation from the laser source to the detector and from the sample focal plane to the WAU, we optimized the geometry of beam propagation as shown in Supplementary Fig. 14. In this layout, the phase shift between the S and P components of the Raman scattering vector $\mathbf{e}_s$ produced on the first reflective surface was compensated by the next reflective surface and finally delivered to the sample with minimized artifacts.

LA effects are mostly produced by the dichroic mirrors DM1, DM2 and which leads to the rotation of $\mathbf{e}_s$ in the range of 0−2.2°, depending on the original $\mathbf{e}_s$ orientation. This deviation was compensated by corresponding choice of polarizations during least square fitting of Euler angles.

Custom microscope objective. In order to provide efficient simultaneous off-axis and on-axis Raman scattering signal registration we designed and constructed custom Raman microscope objective (Supplementary Fig. 12). Zoomed area in Supplementary Fig. 12A illustrates the difference between collecting cones of light scattered in the Silicon sample at on-axis and off-axis geometries. Immersion-type objective allows performing off-axis measurements at 45° with regard to the surface normal. However, due to high reflective index of Si, real collected scattering angle from depth of the sample was around 15°. We confirmed resulting internal angle by the fit of off-axis experimental data on Si wafer with plane (111) (see Supplementary Fig. 4E).

Optical path and components description in SAROM. Here we provide a detailed description of the Raman system, where all components are listed at its appearance in the optical path from the source to the detector. The names of the component correspond to those in Supplementary Fig. 8.

As an excitation sources a single mode diode lasers from Thorlabs LD785-SE400 (785 nm, 400 mW) were used.

The laser clean-up filters Lf1-Lf4 (Semrock, cat. no. LD01–785/10–12.5) are placed on the beam path after the laser output in order to block unwanted emission background from the laser pumping, reducing its intensity of about six orders of magnitude.

In 2D-SAROM setup, the collimated beam from laser was expanded in beam expander (two NIR coated spherical lenses, f1 = 20 mm (Edmund Optics, cat. no. 45–792) and f2 = 100 mm (Edmund Optics, cat. no. 45–806)) up to the diameter of 10 mm. Expanded beam was divided into three beams by a set of beamsplitters BS1-BS3 and polarized BS1 (Edmund Optics, cat. no. 49–005, Edmund Optics, cat. no. 49–870).

In 3D-SAROM setup, we used three diode lasers stabilized at different temperatures in order to control laser wavelength. Each laser beam propagates through separate beam expanders (lenses f1, f2). Final beam diameter for three laser beams was 10 mm. All beams combined by polarized beamsplitter BS2 (Edmund Optics, cat. no. 49–870) and non-polarized beamsplitter BS4 (Edmund Optics, cat. no. 49–005).

The collimated beams from LBDS in 2D and 3D configurations reflect from mirrors M1-M6 (Thorlabs, cat. no. BB1-E03) and pass through a motorized power attenuation filter wheel (Standa, cat. no. 10MWA168) with seven optical density (OD) filters inside.

SAROM can be commutated to the 2D-SAROM or 3D-SAROM geometries by switching of the motorized flipper mirror MFM (Newport Corp., cat. no. 8893-K-M, mirror from Edmund Optics, cat. no. 63–145).

Then the laser beams reflect from dichroic mirror DM1 (Semrock, cat. no. Di02-R785–25x36) and passes through the dichroic mirror DM2 responsible for the coupling with a visible microscope. Finally, laser beams are delivered to the custom made microscope objective (NA = 1.2, focal length 4.1 mm, Supplementary Fig. 12).

The microscope is equipped with a white light LED illumination unit (Thorlabs, cat. no. MNWHL4) and imaging CCD (ToupTek, cat. no. E3CMOS02300KPB). White light from the LED collimates and passes through the edge filter (Semrock, cat. no. FF01–650/SP-25), in order to block the NIR part of the LED emission spectrum. In such a way a visible real-time image can be monitored during the registration of Raman spectra (see Supplementary Movie 1). After that, a white-light beam is reflected by 2-in. mirror M7 (Thorlabs, cat. no. BB2-E03) and focused at the back focus of the microscope objective using a focusing lens f7 (Edmund Optics, cat. no. 47–317). Commutation between illumination and light reflection from the sample is organized via beamsplitter BS5 (Thorlabs, cat. no. BSW10R). The sample illumination unit of the microscope is combined with Raman channel via short-pass dichroic beamsplitter DM2 with cut-off wavelength 749 nm (Semrock, cat. no. FF749-SDi01–25 × 36 × 3.0).

The collected Raman beam passes through microscope objective and DM1, DM2 to the slit lens f3 (Edmund Optics, cat. no. 47–271). Lens f3 is a NIR achromatic doublet pair which focuses Raman beam on the motorized spectrograph slit (Newport, cat. no. 77738).

Spectrograph consists of NIR achromatic doublet pair lenses f4 (Thorlabs, cat. no. AC508-750-B), custom designed Double-Gauss focusing lens f5, transmission fused silica polarization independent grating (Light Smith) and edge filter Ef2 (Semrock, cat. no. BLP01-785R-50). Raman spectra collected on the air cooled CCD (Andor, iDus 416).

Aberration corrected design of the spectrograph and double-gauss lens design are shown in Supplementary Figs. 9 and 10. Spectrograph design is covered by the patent of Technical University of Denmark (application number PCT/DK2019/050027). Unique protected feature of the spectrograph design consists in combination of low NA collimation lens with high NA focusing lens. Focusing lens is a double-gauss type lens which consists of six spherical elements. It is corrected on coma, astigmatism and spherical aberration in the entire focal plane equal to the size of CCD (30 mm). The quality of objective can be verified by MTF curves (Supplementary Fig. 10E, F). Point spread function adjusted to the size of CCD pixel (Supplementary Fig. 10C). Spectrograph stray light parameters were optimized using nonsequential analysis mode in Zemax Optics Studio 17. It was experimentally verified that stray light level at wavenumber shift of 30 cm^{-1} from laser line was at the level of 2.1×10^{-4} which is very good result taking into account relatively small spectrograph dimensions and focal lengths. Spectrograph inside view is shown in Supplementary Fig. 9B.

SAROM measurement conditions. In the case of SAROM microscopy of mono- and polycrystalline Si laser power on the sample in each polarized channel was 50 mW, laser spot size was 3 µm, exposure time per mapping point was 0.05 s, CCD readout mode was multitrack.

In the case of SAROM microscopy of CBZD drug laser power on the sample in each polarized channel was 10 mW, laser spot size was 3 µm, exposure time per mapping point was 0.15 s, CCD readout mode was multitrack.

In the case of SAROM microscopy of mono- and polycrystalline sapphire laser power on the sample in each polarized channel was 100 mW, laser spot size was 0.8 µm, exposure time per mapping point was varied from 50 ms to 2 s (exponentially scaled depending on the mapping depth), CCD readout mode was multitrack.

Data availability

The source data for Figs. 3–5 are provided with the paper. The data that support the other findings of this study are available from the corresponding author upon reasonable request.

Received: 19 July 2019; Accepted: 8 November 2019;
Published online: 05 December 2019

References

1. Adams, B. L. Orientation imaging microscopy: emerging and future applications. *Ultramicroscopy* **67**, 11–17 (1997).
2. Zaefferer, S., Wright, S. I. & Raabe, D. Three-dimensional orientation microscopy in a focused ion beam-scanning electron microscope: a new dimension of microstructure characterization. *Metall. Mater. Trans. A Phys. Metall. Mater. Sci.* **39**, 374–389 (2008).
3. Liu, H. H. et al. Three-dimensional orientation mapping in the transmission electron microscope. *Science* **332**, 833–834 (2011).
4. King, A., Johnson, G., Engelberg, D., Ludwig, W. & Marrow, J. Observations of intergranular stress corrosion cracking in a grain-mapped polycrystal. *Science* **321**, 382–385 (2008).
5. Poulsen, H. F. et al. Three-dimensional maps of grain boundaries and the stress state of individual grains in polycrystals and powders. *J. Appl. Crystallogr.* **34**, 751–756 (2001).
6. Larson, B. C., Yang, W., Ice, G. E., Budai, J. D. & Tischler, J. Z. Three-dimensional X-ray structural microscopy with submicrometre resolution. *Nature* **415**, 887–890 (2002).
7. Simons, H. et al. Dark-field X-ray microscopy for multiscale structural characterization. *Nat. Commun.* **6**, 6098 (2015).
8. McDonald, S. A. et al. Non-destructive mapping of grain orientations in 3D by laboratory X-ray microscopy. *Sci. Rep.* **5**, 14665 (2015).
9. Ramabadran, U. & Roughani, B. Intensity analysis of polarized Raman spectra for off axis single crystal silicon. *Mater. Sci. Eng. B Solid-State Mater. Adv. Technol.* **230**, 31–42 (2018).
10. Schmid, T., Schäfer, N., Levcenko, S., Rissom, T. & Abou-Ras, D. Orientation-distribution mapping of polycrystalline materials by Raman microspectroscopy. *Sci. Rep.* **5**, 1–7 (2015).
11. Mizoguchi, K. & Nakashima, S. I. Determination of crystallographic orientations in silicon films by Raman-microprobe polarization measurements. *J. Appl. Phys.* **65**, 2583–2590 (1989).
12. Loudon, R. The Raman effect in crystals. *Adv. Phys.* **13**, 423–482 (1964).
13. Kranert, C., Sturm, C., Schmidt-Grund, R. & Grundmann, M. Raman tensor elements of β-Ga2O3. *Sci. Rep.* **6**, 1–9 (2016).
14. Sanna, S. et al. Raman scattering efficiency in $LiTaO_3$ and $LiNbO_3$ crystals. *Phys. Rev. B - Condens. Matter Mater. Phys.* **91**, 1–9 (2015).

15. Steele, J. A., Puech, P. & Lewis, R. A. Polarized Raman backscattering selection rules for (hhl)-oriented diamond- and zincblende-type crystals. *J. Appl. Phys.* **120**, 055701 (2016).
16. Mossbrucker, J. & Grotjohn, T. A. Determination of local crystal orientation of diamond using polarized Raman spectra. *Diam. Relat. Mater.* **5**, 1333–1343 (1996).
17. Tsuboi, M. & Thomas, G. J. Raman scattering tensors in biological molecules and their assemblies. *Appl. Spectrosc. Rev.* **32**, 263–299 (1997).
18. Presser, V. et al. Raman polarization studies of highly oriented organic thin films. *J. Raman Spectrosc.* **40**, 2015–2022 (2009).
19. Seidl, B. H. M., Reisecker, C., Hild, S., Griesshaber, E. & Ziegler, A. Calcite distribution and orientation in the tergite exocuticle of the isopods Porcellio scaber and Armadillidium vulgare (Oniscidea, Crustacea). *Z. f.ür. Krist. - Cryst. Mater.* **227**, 777–792 (2012).
20. Tsuboi, M. et al. Raman scattering tensors in thymine molecule from an ab initio MO calculation. *Spectrochim. Acta Part A Mol. Biomol. Spectrosc.* **53**, 409–419 (1997).
21. Thomas, G. J. et al. Polarized Raman spectra of oriented fibers of A DNA and B DNA: anisotropic and isotropic local Raman tensors of base and backbone vibrations. *Biophys. J.* **68**, 1073–1088 (1995).
22. Ushizawa, K., Ueda, T. & Tsuboi, M. Raman scattering tensors of thymidine. *J. Mol. Struct.* **412**, 169–179 (1997).
23. Ushizawa, K., Ueda, T. & Tsuboi, M. Polarized raman spectrum of single crystal uridylyl (3′-5′) adenosine: local raman tensors of some functional groups. *Biopolymers* **45**, 135–147 (1998).
24. Kumakura, A., Tsuboi, M., Ushizawa, K. & Ueda, T. Polarized Raman spectrum of a single crystal of AZT. *Biospectroscopy* **2**, 233–242 (1996).
25. Tsuboi, M., Benevides, J. M. & Thomas, G. J. Jr Raman tensors and their application in structural studies of biological systems. *Proc. Jpn. Acad. Ser. B* **85**, 83–97 (2009).
26. Galvis, L., Dunlop, J. W. C., Duda, G., Fratzl, P. & Masic, A. Polarized Raman anisotropic response of collagen in tendon: towards 3D orientation mapping of collagen in tissues. *PLoS ONE* **8**, 1–9 (2013).
27. Carey, P. R. Raman Crystallography and other biochemical applications of Raman microscopy. *Annu. Rev. Phys. Chem.* **57**, 527–554 (2006).
28. Kazanci, M., Roschger, P., Paschalis, E. P., Klaushofer, K. & Fratzl, P. Bone osteonal tissues by Raman spectral mapping: orientation–composition. *J. Struct. Biol.* **156**, 489–496 (2006).
29. Schrof, S., Varga, P., Galvis, L., Raum, K. & Masic, A. 3D Raman mapping of the collagen fibril orientation in human osteonal lamellae. *J. Struct. Biol.* **187**, 266–275 (2014).
30. Budde, H. et al. Raman radiation patterns of graphene. *ACS Nano* **10**, 1756–1763 (2016).
31. Yoon, D. et al. Strong polarization dependence of double-resonant Raman intensities in graphene. *Nano Lett.* **8**, 4270–4274 (2008).
32. Caramazza, S. et al. First- and second-order Raman scattering from $MoTe_2$ single crystal. *Eur. Phys. J. B* **91**, 35 (2018).
33. Xu, X. et al. In-plane anisotropies of polarized Raman response and electrical conductivity in layered tin selenide. *ACS Appl. Mater. Interfaces* **9**, 12601–12607 (2017).
34. Miao, P. et al. Unraveling the Raman enhancement mechanism on 1T′-phase ReS2 nanosheets. *Small* **14**, 1–8 (2018).
35. Zhang, S. et al. Erratum: spotting the differences in two-dimensional materials-the Raman scattering perspective. *Chem. Soc. Rev.* **47**, 3380, https://doi.org/10.1039/c7cs00874k (2018).
36. Yang, S. et al. Highly in-plane optical and electrical anisotropy of 2D germanium arsenide. *Adv. Funct. Mater.* **28**, 1–10 (2018).
37. Guo, J. et al. Few-layer GeAs field-effect transistors and infrared photodetectors. *Adv. Mater.* **30**, 1–6 (2018).
38. Kim, J. et al. Anomalous polarization dependence of Raman scattering and crystallographic orientation of black phosphorus. *Nanoscale* **7**, 18708–18715 (2015).
39. Wu, J., Zhang, D., Lu, Q., Gutierrez, H. R. & Eklund, P. C. Polarized Raman scattering from single GaP nanowires. *Phys. Rev. B—Condens. Matter Mater. Phys.* **81**, 1–8 (2010).
40. Yang, X. et al. Polarized Raman study of aligned multiwalled carbon nanotubes arrays under high pressure. *J. Phys. Chem. C* **119**, 27759–27767 (2015).
41. Yoo, W. S., Harima, H. & Yoshimoto, M. Polarized Raman signals from Si wafers: dependence of in-plane incident orientation of probing light. *ECS J. Solid State Sci. Technol.* **4**, P356–P363 (2015).
42. Zhu, W. & Pezzotti, G. Tensor and spatially resolved analysis of microscopic stress fields in polycrystalline alumina by polarized Raman spectroscopy. *Phys. Status Solidi Appl. Mater. Sci.* **208**, 1141–1150 (2011).
43. Pezzotti, G. & Zhu, W. Resolving stress tensor components in space from polarized Raman spectra: polycrystalline alumina. *Phys. Chem. Chem. Phys.* **17**, 2608–2627 (2015).
44. Colomban, P. & Thi, M. P. Raman imaging of grain growth mechanism in highly textured Pb(Mg 1/3 Nb 2/3)O_3 -$PbTiO_3$ piezoelectric ceramics*. *J. Phys. IV* **126**, 73–76 (2005).
45. Gouadec, G., Makaoui, K., Perrière, L., Colomban, P. & Mazerolles, L. Ruby micro-piezospectroscopy in $GdAlO_3/Al_2O_3(/ZrO_2)$, $Er_3Al_5O_{12}/Al_2O_3(/ZrO_2)$ and $Y_3Al_5O_{12}/Al_2O_3(/ZrO_2)$ binary and ternary directionally solidified eutectics. *J. Eur. Ceram. Soc.* **32**, 2145–2151 (2012).
46. Rubio-Marcos, F., Del Campo, A. & Fernández, J. F. Resolution of the ferroelectric domains structure in (K,Na)NbO 3 -based lead-free ceramics by confocal Raman microscopy. *J. Appl. Phys.* **113**, 187215 (2013).
47. Maslova, O. A. et al. Materials characterization Raman imaging and principal component analysis-based data processing on uranium oxide ceramics. *Mater. Charact.* **129**, 260–269 (2017).
48. Abramczyk, H. & Kopec, M. Polarized Raman microscopy imaging: capabilities and challenges for cancer research. *J. Mol. Liq.* **259**, 102–111 (2018).
49. Pezzotti, G., Higashino, M., Tsuji, K. & Zhu, W. Non-destructive three-dimensional Raman analysis of domain orientation in barium titanate single-crystal. *J. Eur. Ceram. Soc.* **30**, 199–204 (2010).
50. Loechelt, G. H., Cave, N. G. & Menéndez, J. Polarized off-axis Raman spectroscopy: a technique for measuring stress tensors in semiconductors. *J. Appl. Phys.* **86**, 6164–6180 (1999).
51. Hielscher, R. & Schaeben, H. A novel pole figure inversion method: specification of the MTEX algorithm. *J. Appl. Crystallogr.* **41**, 1024–1037 (2008).
52. Mainprice, D., Bachmann, F., Hielscher, R. & Schaeben, H. Descriptive tools for the analysis of texture projects with large datasets using MTEX: strength, symmetry and components. *Geol. Soc. Lond., Spec. Publ.* **409**, 251–271 (2015).
53. Adar, F. Raman Polarization Measurements: Keeping Track of the Instrumental Components' Behavior. *Spectroscopy* **32**, 14–22 (2017).
54. Kranert, C., Sturm, C., Schmidt-Grund, R. & Grundmann, M. Raman tensor formalism for optically anisotropic crystals. *Phys. Rev. Lett.* **116**, 1–5 (2016).
55. Mehl, T., Di Sabatino, M., Adamczyk, K., Burud, I. & Olsen, E. Defects in multicrystalline si wafers studied by spectral photoluminescence imaging, combined with EBSD and dislocation mapping. *Energy Procedia* **92**, 130–137 (2016).
56. Kallepitis, C. et al. Quantitative volumetric Raman imaging of three dimensional cell cultures. (2017). https://doi.org/10.1038/ncomms14843
57. Moriyama, K., Onishi, H. & Ota, H. Visualization of primary particles in a tablet based on Raman crystal orientation mapping. *Pharm.Anal. Acta* **6**, 10–12 (2015).
58. Belenguer, A. M. & Sanders, J. K. M. Solvation and surface effects on polymorph stabilities at the nanoscale. *Chem. Sci.* **7**, 6617 (2016).
59. Ma, Q. & Clarke, D. R. Piezospectroscopic determination of residual stresses in polycrystalline alumina. *J. Am. Ceram. Soc.* **77**, 298–302 (1994).
60. Everall, N. J. Modeling and measuring the effect of refraction on the depth resolution of confocal raman microscopy. *Appl. Spectrosc.* **54**, 773–782 (2000).
61. Bruneel, J. L., Lassègues, J. C. & Sourisseau, C. In-depth analyses by confocal Raman microspectrometry: experimental features and modeling of the refraction effects. *J. Raman Spectrosc.* **33**, 815–828 (2002).
62. Sourisseau, C. & Maraval, P. Confocal Raman microspectrometry: a vectorial electromagnetic treatment of the light focused and collected through a planar interface and its application to the study of a thin coating. *Appl. Spectrosc.* **57**, 1324–1332 (2003).
63. Gouadec, G., Bellot-Gurlet, L., Baron, D. & Colomban, P. Raman mapping for the investigation of nano-phased materials. in: Raman Imaging: Techniques and Applications 85–118 (2012). https://doi.org/10.1007/978-3-642-28252-2_3
64. Sood, A. K., Menéndez, J., Cardona, M. & Ploog, K. Resonance Raman scattering by confined LO and TO phonons in GaAs-AlAs superlattices. *Phys. Rev. Lett.* **54**, 2111–2114 (1985).
65. Viganò, N. et al. Three-dimensional full-field X-ray orientation microscopy. *Sci. Rep.* **6**, 1–9 (2016).
66. Simons, H., Jakobsen, A. C., Ahl, S. R., Detlefs, C. & Poulsen, H. F. Multiscale 3D characterization with dark-field x-ray microscopy. *MRS Bull.* **41**, 454–459 (2016).
67. Schlücker, S., Schaeberle, M. D., Huffman, S. W. & Levin, I. W. Raman microspectroscopy: a comparison of point, line, and wide-field imaging methodologies. *Anal. Chem.* **75**, 4312–4318 (2003).
68. Morris, H. R., Hoyt, C. C., Miller, P. & Treado, P. J. Liquid crystal tunable filter raman chemical imaging. *Appl. Spectrosc.* **50**, 805–811 (1996).
69. Harris, R. K. et al. Structural studies of the polymorphs of carbamazepine, its dihydrate, and two solvates. *Org. Process Res. Dev.* **9**, 902–910 (2005).

70. Kiefer, J. Simultaneous acquisition of the polarized and depolarized raman signal with a single detector. *Anal. Chem.* **89**, 5725–5728 (2017).

Acknowledgements
We would like to acknowledge Chaoling Xu for help with acquiring EBSD data and Erik Lauridsen for discussions related to the analysis of 3D Raman data and color code based visualization of the orientation maps. We would like to acknowledge Yury Gogotsy and Asia Sarycheva for conceptual advices regarding manuscript structure. Center for Intelligent Drug Delivery and Sensing Using Microcontainers and Nanomechanics (IDUN) funded by the Danish National Research Foundation (grant no. DNRF122) and the Velux Foundations (grant no. 9301), Proof of Concept grant (33009) of the Technical University of Denmark.

Author contributions
O.I. invented SAROM principles, designed and built the SAROM microscope, analyzed the data, performed the experiments and wrote the paper, Y.P. analyzed and resolved ambiguities in SAROM, developed algorithms for Raman tensor analysis and color code data visualization, A.K. developed algorithms for Raman tensor analysis and color code data visualization, F.B. identified SAROM ambiguities and supported misorientation analysis, R.S. wrote the software for the Raman microscope and supported in the experiments, M.T. performed EBSD measurements of poly Si, P.O.O. supported pharmaceutical tablet related experiments, H.F.P. and A.B. gave conceptual advice and revised the manuscript

Competing interests
The authors declare no competing interests.

Additional information
Supplementary information is available for this paper at https://doi.org/10.1038/s41467-019-13504-8.

Correspondence and requests for materials should be addressed to O.I.

Peer review information *Nature Communications* thanks the anonymous reviewer/s for their contribution to the peer review of this work. Peer reviewer reports are available.

Reprints and permission information is available at http://www.nature.com/reprints

Publisher's note Springer Nature remains neutral with regard to jurisdictional claims in published maps and institutional affiliations.

Supplementary Information

Fast and quantitative 2D and 3D orientation mapping using Raman microscopy

O. Ilchenko et al.

Supplementary Note 1: Raman tensor analysis

Raman scattering in crystalline media is described by second-rank symmetric tensor $\Re$ [1]. Intensity of Raman scattered light is dependent on polarization of incident and scattered photons, and also on orientation of a crystal in space. It means that sample crystallographic orientations can be determined by the investigation of Raman scattering anisotropy. In turn, anisotropic parameters can be determined by the measuring of Raman intensity passed through the analyzer in the Raman scattering beam.

Raman scattering intensity I of the phonon mode in the case of back scattering Raman setup is given by the following equation[1]:

$$I \sim \left| e_i^T \, \Re \, e'_s \right|^2, \tag{1}$$

$$\mathbf{e}_i = \begin{pmatrix} \cos\psi_i \\ \sin\psi_i \\ 0 \end{pmatrix}, \qquad \mathbf{e}'_s = \mathbf{M}\,\mathbf{e}_s = \mathbf{M} \begin{pmatrix} \cos\psi_s \\ \sin\psi_s \\ 0 \end{pmatrix}. \tag{2}$$

where $\mathbf{e}_i$ and $\mathbf{e}_s$ are the unit vectors of the polarization of the electric field for incident and scattered irradiation, respectively. In order to describe Raman intensities in off-axis registration geometry, vector $\mathbf{e}_s$ is multiplied by rotation matrix $\mathbf{M}$ which result in $\mathbf{e}'_s$ (in the case of on-axis registration $\mathbf{e}'_s = \mathbf{e}_s$.) Matrix $\mathbf{M}$ depends on off-axis tilt angle β defining rotation of scattered light collection optics around laboratory *x* axis

$$\mathbf{M} = \begin{pmatrix} 1 & 0 & 0 \\ 0 & \cos\beta & -\sin\beta \\ 0 & \sin\beta & \cos\beta \end{pmatrix}. \tag{2a}$$

Elements of Raman scattering tensor are usually defined in crystal coordinate system, and should be transformed with the change of reference coordinate system. In order to move from crystal related coordinate system (X,Y,Z) to the laboratory coordinate system (x,y,z) we need to apply a rotation matrix $\mathbf{\Phi}(\theta,\phi,\psi)$:

$$\Re_j(x,y,z) = \mathbf{\Phi}(\theta,\phi,\psi)\Re_j(X,Y,Z)\mathbf{\Phi}^{-1}(\theta,\phi,\psi). \tag{3}$$

Here $\mathbf{\Phi}^{-1}(\theta,\phi,\psi)$ is an inverse matrix; (θ,ϕ,ψ) are the Euler angles, j is an index of phonon mode under consideration. Euler angles vary in the following ranges: $0 \le \theta \le \pi,\ 0 \le \phi \le 2\pi,\ 0 \le \psi \le \pi$.

For Euler angles defined as in reference[2] rotation matrix has the form:

$$\mathbf{\Phi}(\theta,\phi,\psi) = \begin{pmatrix} \cos\theta\cos\phi\cos\psi - \sin\phi\sin\psi & -\sin\phi\cos\psi - \cos\theta\cos\phi\sin\psi & \sin\theta\cos\phi \\ \cos\theta\sin\phi\cos\psi + \cos\phi\sin\psi & \cos\phi\cos\psi - \cos\phi\sin\phi\sin\psi & \sin\theta\sin\phi \\ -\sin\theta\cos\psi & \sin\theta\sin\psi & \cos\theta \end{pmatrix} \tag{4}$$

Owing to orthogonality of rotation matrix $\mathbf{\Phi}$ its inverse can be found by simple transposition:

$$\boldsymbol{\Phi}^T(\theta,\phi,\psi)=\begin{pmatrix}\cos\theta\cos\phi\cos\psi-\sin\phi\sin\psi & \cos\theta\sin\phi\cos\psi+\cos\phi\sin\psi & -\sin\theta\cos\psi\\ -\sin\theta\cos\psi-\cos\theta\cos\phi\sin\psi & \cos\phi\cos\psi-\cos\theta\sin\phi\sin\psi & \sin\theta\sin\psi\\ \sin\theta\cos\phi & \sin\theta\sin\phi & \cos\theta\end{pmatrix} \quad (5)$$

Finally, Raman intensity in Supplementary Equation 1 can be written as:

$$I(\theta,\phi,\psi;\psi_i,\psi_s)\sim\sum_j\left|\boldsymbol{e}'^T_s\boldsymbol{\Phi}^T(\theta,\phi,\psi)\Re_j(X,Y,Z)\boldsymbol{\Phi}(\theta,\phi,\psi)\boldsymbol{e}_i\right|^2, \quad (6)$$

where summation occurs over the all degenerate phonon modes j and order of matrix multiplication is reversed.

Supplementary Note 2: Si Raman tensor model development

In order to develop a Raman orientation mapping model for Si analysis we need to apply Supplementary Equation 3 to the Si case. Silicon belongs to O_h crystal class, and its sole Raman active phonon mode is F_{2g}. Since it is triply degenerated, Raman intensity is determined by summation over three modes represented by the Raman tensors[7]

$$\Re_x=\begin{pmatrix}0&0&0\\0&0&d\\0&d&0\end{pmatrix},\quad \Re_y=\begin{pmatrix}0&0&d\\0&0&0\\d&0&0\end{pmatrix},\quad \Re_z=\begin{pmatrix}0&d&0\\d&0&0\\0&0&0\end{pmatrix}. \quad (19)$$

Here d is a material constant. Tensor $\Re_x$ corresponding for the longitude crystal mode LO, tensors $\Re_y$, $\Re_z$ corresponding for the transversal crystal modes, TO1 and TO2, respectively.

$$\begin{aligned}
&I_{TO1}(\theta,\phi,\psi;\psi_i,\psi_s)=\sin^2\theta(2\cos\theta\sin\phi\cos(\psi+\psi_i)\cos(\psi+\psi_s)+\cos\phi\sin(2\psi+\psi_i+\psi_s))^2\\
&I_{TO2}(\theta,\phi,\psi;\psi_i,\psi_s)=\sin^2\theta(\sin\phi\sin(2\psi+\psi_i+\psi_s)-2\cos\theta\cos\phi\cos(\psi+\psi_i)\cos(\psi+\psi_s))^2\\
&I_{LO}(\theta,\phi,\psi;\psi_i,\psi_s)=(\cos^2\theta\sin(2\phi)\cos(\psi+\psi_i)\cos(\psi+\psi_s)\\
&+\cos\theta\sin(2\phi)\sin(2\psi+\psi_i+\psi_s)-\sin(2\phi)\sin(\psi+\psi_i)\sin(\psi+\psi_s))^2
\end{aligned} \quad (20)$$

Supplementary Note 3: Orientation determination error

In order to get a quantitative answer with regard to the orientation determination error, we simulated a testing dataset of Raman intensity variation versus ψ . The dataset consists of intensity values calculated for three classes corresponding to silicon wafer cuts (100), (110) and (111). Each orientation class has 1440 positions of wafer rotation angle ψ in the interval $0°$ - $360°$ taken with step 0.25°.

The orientation determination results were obtained by fitting of Euler angles to simulated data and were represented in a crystallographic color code using MTEX toolbox for Matlab[8,9], see Supplementary Figure 5. The color corresponds to orientation of the wafer normal direction (ND) relative to crystallographic axes of silicon. Misorientation angle, which corresponds to

undetermined rotation of the sample, is depicted in Supplementary Figure 5 as vertical bars on the right side of each subplot.
Orientation fitting was done using varying number of polarized channels from 2 to 12 channels, see subplots in Supplementary Figure 5. Analysis of simulation results reveals, that basic orientation determination become possible for four or more channels. However, for some specific orientations, intensity data remains ambiguous and rotation angle ψ is not recovered. This is clearly seen for (111) wafer in misorientation plots in Supplementary Figure 5, where misorientation angle varies from zero to maximal possible for cubic symmetry angle 62.8°. Nevertheless, even for such ambiguous data, some orientation data is still recovered, and it is possible to clearly distinguish wafers (100), (110), (111) even for four measurement channels.
According to simulation, the ambiguity can be successfully resolved when off-axis channels are added to the measurement setup. Still, adding only two off-axis channel is not enough to resolve ambiguity completely. Full resolution become possible when adding three off-axis channels to six on-axis channels, resulting in total nine measurement channels. Combination of polarizations used in this simulation for different number of channels is in correspondence to Fig. 1c. Further addition to number of channels up to 12 does not noticeably increase accuracy of fit, so we decided to use nine channels in our experimental setup as reasonable minimum ensuring unambiguous measurements.

Supplementary Note 4: Analysis of ambiguities in Raman orientation mapping

Simulation performed in Section 4 revealed that some orientations, like those appearing in surface plane (111) of silicon, prone to introduce ambiguity in measurement data. Although simulation helped to define minimal number of polarization channels required to determine orientation, it still has limited scope, because only (100), (110) and (111) cases were considered. To confirm possibility of orientation determination in general case additional analysis was performed.
Ambiguity analysis was done by exhaustive search of indistinguishable solutions over range of all possible Euler angles. Each Euler angle was incremented in 0.5° step and calculated Raman intensities for corresponding orientation were stored in a list. At next step, for each orientation defined by three Euler angles, other orientations having nearest Raman intensities were searched in the list using Euclidian norm as a distance function. Only matches with resulting distance less than predefined threshold 5% of maximal level were selected. Number of matching orientations was recorded as metric of ambiguity. For absolutely unambiguous case, recorded metric should equal to one for all tested orientations. However, such ideal case is never realized it practice, because presence of symmetry elements in tested crystal class make some orientations inherently indistinguishable. Thus in present analysis we are mainly interested in minimal realizable ambiguity metric.
Ambiguity analysis of many polarization combinations containing only on-axis channels quickly revealed, that all of them have ambiguity metric not less than 2. That directly indicates, that each tested orientation have at least one competitive orientation with indistinguishable Raman intensities, but different Euler angles. Quick check showed that this competitive orientation have Euler angle ψ which differs to 180° from true orientation.

Applying off-axis measurement scheme, that means rotating scattered light collecting channels away from direction of irradiation channels, removed $\psi + 180°$ ambiguity. Most of the orientation space in this case have ambiguity metric equal to one, except zones associated with symmetry elements, and some new zones, which appeared due to specific selection of off-axis angle and polarization directions. Using combined scheme, where both on-axis and off-axis channels are present, allowed to minimize volume of orientation space where ambiguity persist.

To verify ambiguity analysis further, test fit was performed. Synthetic 2D map containing grains with different crystal orientations was prepared, and corresponding Raman intensities were calculated. Using simulated intensity data, orientation fit was carried out with different combination of polarization channels (see Table 1). For each channel combination geometric area were fit was erroneous was determined, and presented as percentage of total map area (column "Orientation error" of Table 1). Maximal misorientation angle registered in successfully fitted zones is recorded in column "Misorientation" of the table. The same quantities versus total number of channels are plotted in Supplementary Figure 6.

For number of channels less or equal than 5 orientation of larger part of the map fitted incorrectly. For number of channels from 6 to 8 part of successfully fitted data point approach 50%, that means fit is successful in half of the cases. It is explained by $\psi + 180°$ ambiguity and is the result of mere luck – fitting algorithm correctly guessed orientation only in half of points. Misorientation is still 62.8° (maximal possible in cubic symmetry), because we can not be sure which orientation ψ or $\psi + 180°$ is actually correct. For number of channels greater or equal to 9, which must include off-axis channel, part of incorrectly fitted points is around 1% or less, with minimal misorientation.

Supplementary Note 5: Intensity corrections in SAROM channels

Experimental realization of off-axis scheme (Supplementary Figure 11a) revealed, that obtained measurements are highly sensitive to variations of the sample surface profile when large off-axis angles are used. Defocusing caused by varying surface height results in change of intensity of scattered light. These changes of channels intensities should be compensated before orientation fitting. One possible solution is to use level of fluorescence background for Raman intensity normalization, as being insensitive to crystal orientation.

Another solution, which proved to be also effective, is to rely on relative intensity between channels but not on absolute intensity. To make this possible, fitting procedure should be modified to use normalized values instead of absolute ones. We implemented such normalization as division of intensity in each off-axis channel by Euclidian norm of vector composed of all off-axis intensities. It is done in assumption that all off-axis polarization channels experience the same or similar variation of intensity due to changes in the sample surface profile. The same normalization can also be applied to on-axis channels if they experience uncompensated intensity variation. Our experiments show, that such procedure generally is not required for on-axis channels, but for off-axis channels it allows to efficiently compensate even large intensity variations and obtain reliable orientation fit. Normalization applied to channels which are already well calibrated results in slightly decreased accuracy of the fit, because it actually reduce the effective number of independent channels in group of channels. For the best results, number of channels which are normalized in one group should be at least three or more. Proposed normalization can be applied on different groups of channels independently based on actual quality of registered data.

Supplementary Note 6: Artifacts correction

Geometries and optical coatings in SAROM setup were optimized for the minimum effect of LA and LP anisotropy using Zemax Optics Studio (Supplementary Figure 14). In order to determine the Jones matrix coefficients, we performed numerical polarization analysis and obtained values of phase shift and attenuation between S and P components of the EM field in LBDS and RBDS.

LA and LP anisotropy compensation. During signal propagation through the reflective and transmitting optical elements LA and LP anisotropy usually take place[3]. These effects can be described by the usage of Jones matrix formalism[4], where each optical element is represented by matrix $\mathbf{J}$ with dimensions 3×3.

When the signal is propagating through the multiple optical elements of LBDS described by matrices $\mathbf{J}_1, \mathbf{J}_2, ..., \mathbf{J}_N$, effective matrix can be expressed as:

$$\mathbf{J}_i = \mathbf{J}_N \mathrm{L}\ \mathbf{J}_2 \mathbf{J}_1. \tag{7}$$

During the propagation through the RBDS the matrix will be expressed as:

$$\mathbf{J}_i = \mathbf{J}'_M \mathrm{L}\ \mathbf{J}'_2 \mathbf{J}'_1, \tag{8}$$

where $\mathbf{J}'_1, \mathbf{J}'_2, ..., \mathbf{J}'_M$ describe elements in the path of scattered light with required coordinate transformations applied to represent on-axis or off-axis channel.

Therefore, Raman intensity in Supplementary Equation 1 can be re-written as:

$$I \sim \sum_j \left| \boldsymbol{e}'^T_s \boldsymbol{J}^T_s \boldsymbol{\Phi}^T(\theta,\phi,\psi) \Re_j(X,Y,Z) \boldsymbol{\Phi}(\theta,\phi,\psi) \boldsymbol{J}_i \boldsymbol{e}_i \right|^2, \tag{9}$$

In the case of LBDS, orthogonal laser beams propagate with angle of polarization state: $\psi_i^1 = 0°$, $\psi_i^2 = 45°$, $\psi_i^3 = 90°$. LP anisotropy do not appear at $\psi_i^1 = 0°$ and $\psi_i^3 = 90°$ [5] and present laser intensity attenuation can be experimentally measured and corrected. However, $\mathbf{J}_i$ will acquire more complex view at $\psi_i^2 = 45°$ where LP and LA anisotropy must be taken into account.

Objective NA compensation. Before, we assumed that the laser beam has normal incidence to the sample surface (Supplementary Figure 12). However, we use apertures for on-axis and off-axis Raman scattering collection that have certain NA value. This effect becomes especially critical for high NA objectives[6] relevant for confocal 3D-SAROM measurements. Taking into consideration this angular distribution Raman intensity can be described in the following way:

$$I_\Omega \sim \sum_j \int_{\Omega_i} \int_{\Omega_s} \left| \boldsymbol{e}'^T_s \boldsymbol{J}^T_s \boldsymbol{\Phi}^T(\theta,\phi,\psi) \Re_j(X,Y,Z) \boldsymbol{\Phi}(\theta,\phi,\psi) \boldsymbol{J}_i \boldsymbol{e}_i \right|^2 d\Omega_i d\,\Omega_s, \tag{10}$$

where Ω_i, Ω_s – solid angles of incident and scattering irradiation, respectively. Integration is done within the range of cones formed by optical setup for incident and scattered path.

Raman microscopy require high-power illumination to obtain suitable signal-to-noise ratio, thus the sample is irradiated with coherent laser source. Most of Raman response comes from focus spot, where laser beam have parallel or near-to-parallel wave fronts, which means that actual polarization of irradiating wave does not change much over the registration volume. Thus we can safely drop integration over Ω_i in Supplementary Equation 10 assuming we have irradiation conditions similar to plane-wave case.

Effect of registration of scattered light coming from different angles due to integration over a collecting aperture can be estimated analytically. For uniform intensity response of the collecting lenses, registered intensity is proportional to an integral

$$I_{\Omega_S} \sim \sum_j \int_0^{2\pi} \int_0^{\theta_S} \left| \boldsymbol{e'}_S^T(\theta,\varphi) \mathfrak{R}'_j \boldsymbol{e'}_i \right|^2 \sin\theta \, d\theta \, d\varphi, \tag{11}$$

where θ_S is half-angle of collection aperture. It is convenient to calculate this integral in local spherical coordinate system (Supplementary Figure 15), where *z* axis is oriented along optical axis of collection lens and polarization $\mathbf{e}'_S$ lays in the XOZ plane.

Scattered polarization $\mathbf{e}'_S$ is perpendicular to wave vector $\mathbf{k}_S$ and explicitly depends on integration angles θ and φ. Components of vector $\mathbf{e}'_S$ can be found via rotation matrices

$$\mathbf{e}'_s = \begin{pmatrix} \cos\varphi & -\sin\varphi & 0 \\ \sin\varphi & \cos\varphi & 0 \\ 0 & 0 & 1 \end{pmatrix} \begin{pmatrix} \cos\theta & 0 & \sin\theta \\ 0 & 1 & 0 \\ -\sin\theta & 0 & \cos\theta \end{pmatrix} \begin{pmatrix} \cos\varphi & \sin\varphi & 0 \\ -\sin\varphi & \cos\varphi & 0 \\ 0 & 0 & 1 \end{pmatrix} \begin{pmatrix} 1 \\ 0 \\ 0 \end{pmatrix}. \tag{12}$$

Raman tensor $\mathfrak{R}'$ rotated to local coordinate system and incident polarization vector $\mathbf{e}'_i$ remain constant during integration. Result of their tensor multiplication we define as a vector

$$\mathbf{p}_j = \begin{pmatrix} p_x \\ p_y \\ p_z \end{pmatrix} = \mathfrak{R}'_j \mathbf{e}'_i. \tag{13}$$

To make comparison easier we normalize aperture-integrated intensity on solid angle

$$\Omega_S = \int_0^{2\pi} \int_0^{\theta_S} \sin\theta \, d\theta \, d\varphi = 2\pi(1-\cos\theta_S) \tag{14}$$

Normalized intensity integral (S11) transforms to

$$I_S \sim \frac{1}{2\pi(1-\cos\theta_S)} \sum_j \int_0^{2\pi} \int_0^{\theta_S} \left| \boldsymbol{e'}_S^T \boldsymbol{p}_j \right|^2 \sin\theta \, d\theta \, d\varphi \tag{15}$$

This integral can be computed analytically. For specific angle θ_S total intensity is

$$I_S \sim \sum_j \left(\frac{1}{48}(33+12\cos\theta_S+3\cos 2\theta_S)p_x^2 + \frac{1}{48}(3-4\cos\theta_S+\cos 2\theta_S)p_y^2 + \frac{1}{48}(12-8\cos\theta_S-4\cos 2\theta_S)p_z^2 \right) \quad (16)$$

For small θ_S most intensity comes from term p_x^2, which is in accordance to used selection of local coordinate system. For increasing θ_S coefficient near p_x^2 decreases, and contribution from p_z^2 correspondingly increases. Effect of p_y^2 is much smaller and can be neglected even for as large θ_S angles as 30°.

For transparent samples collection angle value should be corrected for refractive index of a material when signal collection is done from internal sample volume. All samples in this work were collected at aperture with half-angle of 24°. Silicon has quite large index of refraction *n*=3.8 at 785 nm, so internal collection angle decrease significantly comparing to external collection angle and is limited to $\theta_S = 6°$. Corresponding contributions from different components of vector $\mathbf{p}_j$ are

$$I_S \sim \sum_j (0.9971p_x^2 + 1.37\times 10^{-6}p_y^2 + 0.0029p_z^2) \quad (17)$$

Resulting intensity change due to component intermixing will be smaller than 0.3%, so this effect can be safely ignored in Silicon samples. For CBZD and poly-sapphire samples intensity change caused by component intermixing will be around 1.5% due to lower refractive index. For larger collection apertures or samples with lower refractive index collection aperture effect can be fully taken into account by introduction of three multiplicative correction factors applied to the squares of $\mathbf{p}_j$ vector components according to Supplementary Figure 15.

Sample birefringence. Sample birefringence can also leads to the artifacts in the Raman spectra[6]. Depth dependent birefringence correction becomes especially important for 3D-SAROM measurements. Therefore Supplementary Equation 6 will take form:

$$I_\Omega \sim \sum_j \int_{\Omega_i} \int_{\Omega_S} \left| \boldsymbol{e}_s'^T \boldsymbol{J}_s^T \boldsymbol{\Phi}^T(\theta,\phi,\psi) \boldsymbol{X}_s \Re_j(X,Y,Z) \boldsymbol{X}_i \boldsymbol{\Phi}(\theta,\phi,\psi) \boldsymbol{J}_i \boldsymbol{e}_i \right|^2 d\Omega_i d\,\Omega_s, \quad (18)$$

where $\mathbf{X}_{i,s}$ are the birefringence correction matrixes.

Background correction and denoising. Before applying artifact correction procedures described above all Raman spectra in nine polarized channels were background corrected and Savitzky–Golay noise reduction algorithm was applied.

Supplementary Note 7: Poly-Si mapping

The surface of poly- Si is shown on the visible image of Supplementary Figure 16a. We performed mechanical polishing of the sample, in order to reach a surface flatness comparable with that of single-crystal Si wafers. This was a methodologically important step, which helped us to obtain a Raman intensity and reflectivity comparable to those of the single crystal Si. We used a fluorescence intensity map of the surface of the polycrystalline Si plotted at the maximum of Si fluorescence band for Raman intensity calibration (Supplementary Figure 16b). To compensate intensity variations during scanning the sample, we applied intensity normalization procedure described in Section S6 for off-axis group of channels. On-axis channels were initially calibrated using single-crystal samples and weren't re-normalized during processing of Poly-Si data. The polarized Raman maps collected simultaneously from the nine channels are presented in Supplementary Figure 17. The polycrystalline structure of the Si sample can't be seen on the visible microscopy image (Supplementary Figure 16a) due to the polishing, however it can be clearly recognized in the polarized Raman maps (Supplementary Figure 17). Giving a closer look at the data, it is possible to reveal that each single crystal in the polycrystalline sample has different Raman intensity for each polarized channel. The crystals which are not discernible in one polarized channel can be clearly separated in another one.
Due to the high throughput of the SAROM system from the sample to the detector (9.8% of energy for each polarized channel, 88% in all nine channels) and a spectral binning up to 16cm^{-1}, we obtained a high signal-to-noise ratio (SNR) of 1500:1 for each channel in the acquired maps, which is comparable to the SNR ratio of the single-crystal Si (Supplementary Figure 2-4).

Supplementary Note 8: CBZD Raman tensor model development

Monocrystalline CBZD has point group symmetry C_{2h} [10,11]. Therefore, it has two Raman active modes A_g and B_g [1], with the following Raman tensors:

$$\Re_{A_{1g}} = \begin{pmatrix} a & 0 & d \\ 0 & b & 0 \\ d & 0 & c \end{pmatrix}, \quad \Re_{B_g} = \begin{pmatrix} 0 & e & 0 \\ e & 0 & f \\ 0 & f & 0 \end{pmatrix}. \tag{21}$$

a, b, c, d, e, f – material parameters.
According to Supplementary Equation 3 intensity of Raman modes can be expressed as:

$$I_{A_g}(\theta,\phi,\psi,a,b,c,d,\psi_i,\psi_s)=\frac{1}{4}(\cos^2(\theta)\cos(\psi+\psi i)\cos(\psi+\psi s)((a-b)\cos(2\phi)+a+b)-$$
$$2d\sin(2\theta)\cos(\phi)\cos(\psi+\psi_i)\cos(\psi+\psi_s)+2b\sin^2(\psi)\cos(\psi_i)\cos(\psi_s)\cos^2(\phi)+$$
$$2a\sin^2(\psi)\cos(\psi_i)\cos(\psi_s)\sin^2(\phi)+2d\sin(\theta)\sin(2\psi)\cos(\psi_i)\cos(\psi_s)\sin(\phi)-$$
$$2d\sin(\theta)\sin^2(\psi)\sin(\psi_i)\cos(\psi_s)\sin(\phi)+a\sin(2\psi)\sin(\psi_i)\cos(\psi_s)\sin^2(\phi)-$$
$$2d\sin(\theta)\sin^2(\psi)\cos(\psi_i)\sin(\psi_s)\sin(\phi)+a\sin(2\psi)\cos(\psi_i)\sin(\psi_s)\sin^2(\phi)+$$
$$2c\sin^2(\theta)\sin^2(\psi)\sin(\psi_i)\sin(\psi_s)-2\sin(\theta)\sin(\psi)\cos(\psi)(\sin(\psi_s)(c\sin(\theta)\cos(\psi_i)+$$
$$2d\sin(\psi_i)\sin(\phi))+c\sin(\theta)\sin(\psi_i)\cos(\psi_s))+2\cos^2(\psi)(\sin(\psi_i)(a\sin(\psi_s)\sin^2(\phi)+$$
$$b\sin(\psi_s)\cos^2(\phi)+d\sin(\theta)\cos(\psi_s)\sin(\phi))+\sin(\theta)\cos(\psi_i)(c\sin(\theta)\cos(\psi_s)+$$
$$d\sin(\psi_s)\sin(\phi)))-(a-b)\cos(\theta)\sin(2\phi)\sin(2\psi+\psi_i+\psi_s)+b\sin(2\psi)\cos^2(\phi)\sin(\psi_i+\psi_s))^2$$

(22)

$$I_{B_g}(\theta,\phi,\psi,e,f,\psi_i,\psi_s)=\frac{1}{16}(-2\cos(\phi)(4e\sin(\phi)\sin(\psi+\psi_i)\sin(\psi+\psi_s)+f\cos(\theta-2\psi-\psi_i-\psi_s)-$$
$$f\cos(\theta+2\psi+\psi_i+\psi_s))+\cos(\theta)(4e\cos(\theta)\sin(2\phi)\cos(\psi+\psi_i)\cos(\psi+\psi_s)-$$
$$2e\sin(-2\psi-\psi_i-\psi_s+2\phi)+2e\sin(2\psi+\psi_i+\psi_s+2\phi)-f\cos(\theta-2\psi-\psi_i-\psi_s-\phi)+$$
$$f\cos(\theta-2\psi-\psi_i-\psi_s+\phi)-f\cos(\theta+2\psi+\psi_i+\psi_s-\phi)+f\cos(\theta+2\psi+\psi_i+\psi_s+\phi)-$$
$$f\cos(\theta+\psi_i-\psi_s-\phi)+f\cos(\theta+\psi_i-\psi_s+\phi)-f\cos(\theta-\psi_i+\psi_s-\phi)+f\cos(\theta-\psi_i+\psi_s+\phi)))^2$$

(23)

For surface plane (001) Raman intensity has the following view:

$$I_{A_g}(0,0,\psi,a,b,c,d,\psi_i,\psi_s)=\frac{1}{4}\left((a-b)\cos(2\psi+\psi_i+\psi_s)+(a+b)\cos(\psi_i-\psi_s)\right)^2 \quad (24)$$

$$I_{B_g}(0,0,\psi,a,b,c,d,\psi_i,\psi_s)=e^2\sin(2\psi+\psi_i+\psi_s)^2 \quad (25)$$

For surface plane (010) Raman intensity has the following view:

$$I_{A_g}(\frac{\pi}{2},0,\psi,a,b,c,d,\psi_i,\psi_s)=\frac{1}{4}\left((c-b)\cos(2\psi+\psi_i+\psi_s)+(b+c)\cos(\psi_i-\psi_s)\right)^2 \quad (26)$$

$$I_{B_g}(\frac{\pi}{2},0,\psi,a,b,c,d,\psi_i,\psi_s)=f^2\sin(2\psi+\psi_i+\psi_s)^2 \quad (27)$$

For surface plane (100) Raman intensity has the following view:

$$I_{A_g}(\frac{\pi}{2},\frac{\pi}{2},\psi,a,b,c,d,\psi_i,\psi_s)=\frac{1}{4}\left((c-a)\cos(2\psi+\psi_i+\psi_s)+2d\sin(2\psi+\psi_i+\psi_s)+(a+c)\cos(\psi_i-\psi_s)\right)^2$$

(28)

$$I_{B_g}(\frac{\pi}{2},\frac{\pi}{2},\psi,a,b,c,d,\psi_i,\psi_s)=0 \quad (29)$$

By the fitting of experimental angular Raman intensity dependencies of the several CBZD vibrational modes we verified that peak at 1636cm^{-1} (νCC vibration) belongs to the A_g mode. We made this conclusion because fitting the same peak to Raman tensor which corresponds to B_g mode was not possible and produced inconsistent results. After the fitting procedure based on A_g mode Raman tensor (Supplementary Figure 27) we obtained the following values of the material parameters: a=0.43, b=0.06, c=0.45, d=−0.81.

Supplementary Note 9: Sapphire Raman tensor model development

Crystallographic structure of monocrystalline sapphire belongs to point group D_{3d} and space group D_{3d}^6. As a result we have the following irreducible representation for optical modes[12]:

$$\Gamma_{opt} = 2A_{1g} + 2A_{1u} + 3A_{2g} + 2A_{2u} + 5E_g + 4E_u, \tag{30}$$

And the following representation for the phonon modes:

$$\Gamma_{phonon} = A_{2u} + A_u. \tag{31}$$

Due to the fact that elementary cell has the center of inversion, the Raman active vibrations are not present in the IR spectra, and vice versa. As a result, we have seven modes, which are active in Raman spectra: two A_{1g} and five E_g modes (Supplementary Figure 30). Raman scattering tensors in the crystal coordinate frame have the following form[2]:

$$\Re_{A_{1g}} = \begin{pmatrix} a & 0 & 0 \\ 0 & a & 0 \\ 0 & 0 & a \end{pmatrix}, \quad \Re_{E_{g(x)}} = \begin{pmatrix} c & 0 & 0 \\ 0 & -c & d \\ 0 & d & 0 \end{pmatrix}, \quad \Re_{E_{g(y)}} = \begin{pmatrix} 0 & -c & -d \\ -c & 0 & 0 \\ -d & 0 & 0 \end{pmatrix}. \tag{32}$$

Here a, b, c, d – material parameters.

By the use of Supplementary Equation 3, Raman intensity of A_{1g} and E_g modes can be written as:

$$I_{A_{1g}}(\theta,\phi,\psi,\psi_i,\psi_s) = \frac{1}{64}((a-b)\cos(2\theta-2\psi-\psi_i-\psi_s)+(a-b)(\cos(2\theta+2\psi+\psi_i+\psi_s)+ \\ +\cos(2\theta+\psi_i-\psi_s)+\cos(2\theta-\psi_i+\psi_s)-2\cos(2\psi+\psi_i+\psi_s))+2(3a+b)\cos(\psi_i-\psi_s))^2 \tag{33}$$

$$I_{E_{g(x)}}(\theta,\phi,\psi,\psi_i,\psi_s) = \Big(\sin(\psi_i)\Big(\sin(\phi)\Big(\sin(\psi)\cos(\psi)\cos(\psi_s)\Big(c\Big(\cos^2(\theta)+1\Big)\sin(\phi)+d\sin(2\theta)\Big)- \\ -\cos(\theta)\sin^2(\psi)\sin(\psi_s)(c\cos(\theta)\sin(\phi)+2d\sin(\theta))+c\cos^2(\psi)\sin(\psi_s)\sin(\phi)\Big)- \\ -\cos(\phi)\cos(2\psi+\psi_s)(2c\cos(\theta)\sin(\phi)+d\sin(\theta))-\frac{1}{4}c\cos^2(\phi)\Big(-4\cos^2(\theta)\sin^2(\psi)\sin(\psi_s)+ \\ +(\cos(2\theta)+3)\sin(2\psi)\cos(\psi_s)+4\cos^2(\psi)\sin(\psi_s)\Big)\Big)+ \\ +\cos(\psi_i)\Big(\cos(\psi_s)\Big(\sin(\psi)\Big(c\sin(\psi)\sin^2(\phi)-c\sin(\psi)\cos^2(\phi)-2d\sin(\theta)\cos(\psi)\cos(\phi)\Big)- \\ -2\cos(\theta)\cos(\psi)\sin(\phi)(2c\sin(\psi)\cos(\phi)+d\sin(\theta)\cos(\psi))+c\cos^2(\theta)\cos^2(\psi)\cos(2\phi)\Big)+ \\ +\sin(\psi_s)\Big(\sin(\psi)\cos(\psi)\sin(\phi)\Big(c\Big(\cos^2(\theta)+1\Big)\sin(\phi)+ \\ +d\sin(2\theta)\Big)-\cos(2\psi)\cos(\phi)(2c\cos(\theta)\sin(\phi)+d\sin(\theta))-\frac{1}{4}c(\cos(2\theta)+3)\sin(2\psi)\cos^2(\phi)\Big)\Big)\Big)^2 \tag{34}$$

$$I_{E_{g(y)}}(\theta,\phi,\psi,\psi_i,\psi_s)=\Big(\sin(\psi_i)\Big(\cos(\psi_s)\Big(\cos(\theta)\Big(-c\cos(2\psi)\cos^2(\phi)+c\cos(2\psi)\sin^2(\phi)-$$
$$-2d\sin(\theta)\sin(\psi)\cos(\psi)\cos(\phi)\Big)+\sin(\phi)\Big(c\sin(2\psi)\cos(\phi)+d\sin(\theta)\sin^2(\psi)-d\sin(\theta)\cos^2(\psi)\Big)+$$
$$+2c\cos^2(\theta)\sin(\psi)\cos(\psi)\sin(\phi)\cos(\phi)\Big)+2\sin(\psi_s)(\cos(\theta)\sin(\psi)\cos(\phi)+\cos(\psi)\sin(\phi))(\sin(\psi)(d\sin(\theta)-$$
$$-c\cos(\theta)\sin(\phi))+c\cos(\psi)\cos(\phi)))+\cos(\psi_i)\Big(\cos(\theta)\Big(c\sin^2(\phi)\sin(2\psi+\psi_s)-c\cos^2(\phi)\sin(2\psi+\psi_s)+$$
$$+2d\sin(\theta)\cos(\psi)\cos(\phi)\cos(\psi+\psi_s)\Big)+\sin(\phi)\Big(2c\sin^2(\psi)\cos(\psi_s)\cos(\phi)+c\sin(2\psi)\sin(\psi_s)\cos(\phi)+$$
$$+d\sin(\theta)\sin^2(\psi)\sin(\psi_s)-d\sin(\theta)\cos^2(\psi)\sin(\psi_s)-2d\sin(\theta)\sin(\psi)\cos(\psi)\cos(\psi_s)\Big)-$$
$$-c\cos^2(\theta)\cos(\psi)\sin(2\phi)\cos(\psi+\psi_s)\Big)\Big)^2 \tag{35}$$

The general-form Raman intensity for E_g mode:

$$I_{E_g}(\theta,\phi,\psi,\psi_i,\psi_s)=\frac{1}{2}I_{E_{g(x)}}(\theta,\phi,\psi,\psi_i,\psi_s)+\frac{1}{2}I_{E_{g(y)}}(\theta,\phi,\psi,\psi_i,\psi_s) \tag{36}$$

Using Supplementary Equation 32-36 it possible to obtain Raman intensity for different cuts of monocrystalline sapphire as a function of ψ , ψ_i , ψ_s .

<u>c-plane/a-axis</u> ($\theta=0$, $\phi=0$)

$$I_{A_{1g}}(0,0,\psi,\psi_i,\psi_s)=c^2\cos^2(\psi_i-\psi_s) \tag{37}$$

$$I_{E_g}(0,0,\psi,\psi_i,\psi_s)=\frac{c^2}{2} \tag{38}$$

<u>a-plane/c-axis</u> ($\theta=\frac{\pi}{2}$, $\phi=0$)

$$I_{A_{1g}}(\frac{\pi}{2},0,\psi,\psi_i,\psi_s)=\frac{1}{4}((d-c)\cos(\psi_i+2\psi+\psi_s)+(c+d)\cos(\psi_i-\psi_s))^2 \tag{39}$$

$$I_{E_g}(\frac{\pi}{2},0,\psi,\psi_i,\psi_s)=\frac{1}{8}(-c\cos(\psi_i+2\psi+\psi_s)+c\cos(\psi_i-\psi_s)+2d\sin(\psi_i+2\psi+\psi_s))^2 \tag{40}$$

<u>m-plane/c-axis</u> ($\theta=\frac{\pi}{2}$, $\phi=\frac{\pi}{2}$)

$$I_{A_{1g}}(\frac{\pi}{2},\frac{\pi}{2},\psi,\psi_i,\psi_s)=\frac{1}{4}((d-c)\cos(\psi_i+2\psi+\psi_s)+(c+d)\cos(\psi_i-\psi_s))^2 \tag{41}$$

$$I_{E_g}(\frac{\pi}{2},\frac{\pi}{2},\psi,\psi_i,\psi_s)=\frac{1}{16}(-2c^2\cos(2(\psi_i+\psi))+c^2\cos(2(\psi_i+2\psi+\psi_s))+c^2\cos(2\psi_i-2\psi_s)-$$
$$-2c^2\cos(2(\psi+\psi_s))+2c^2-4d^2\cos(2(\psi_i+2\psi+\psi_s))+4d^2) \tag{42}$$

<u>r-plane/a-axis</u> ($\theta=\frac{58\pi}{180}$, $\phi=\frac{\pi}{2}$)

$$I_{A_{1g}}(\frac{58\pi}{180},\frac{\pi}{2},\psi,\psi_i,\psi_s)=((0.36d-0.36c)\cos(\psi_i+2\psi+\psi_s)+(0.64c+0.36d)\cos(\psi_i-\psi_s))^2 \tag{43}$$

$$I_{E_g}(\frac{58\pi}{180},\frac{\pi}{2},\psi,\psi_i,\psi_s)=0.5\Big(((-0.64c-0.45d)\cos(\psi_i+2\psi+\psi_s)+(0.36c-0.45d)\cos(\psi_i-\psi_s))^2+$$
$$+(\cos(\psi_i)((0.53c-0.85d)\cos(2\psi)\sin(\psi_s)+(1.06c-1.7d)\sin(\psi)\cos(\psi)\cos(\psi_s))+$$
$$+(0.85d-0.53c)\sin(\psi_i)(2\sin(\psi)\cos(\psi)\sin(\psi_s)-\cos(2.\psi)\cos(\psi_s)))^2\Big)$$
(44)

Raman intensity of A_{1g} mode for $a-$ and $m-$planes are identical. As a result, it is better to use Raman intensity of E_g mode for the orientation determination.

Supplementary Note 10: Poly-sapphire 3D mapping

As an example of raw polarized Raman spectrum of monocrystalline sapphire we show spectrum acquired at r-plane in on-axis configuration $z(0\ 90)\bar{x}$ (Supplementary Figure 30). For the sapphire model development experiments we performed measurements in 2D-SAROM configuration (Supplementary Figure 8). System in 2D-SAROM configuration gave us an opportunity to collect non-overlapped polarized spectra of a-, c-, m- and r-planes at multiple polarization combinations and fit intensity versus rotation dependencies using Supplementary Equation 3.

By the analysis of obtained data in 2D-SAROM configuration, we verified that polarized Raman spectra of sapphire are rather similar for a- and r- planes. Among two A_{1g} modes (417 and 645cm^{-1}) and five E_g modes (378, 430, 451, 578 and 750cm^{-1}) of sapphire[2] we chose fifth E_g mode (750cm^{-1}) for the further analysis because it provides more variation in polarized Raman spectra than other modes where a- and r-planes were successfully distinguished (Supplementary Figure 29). Raman tensor element values obtained by fitting are c=0.045, d=−0.49 which are rather close to the values presented in reference[2].

An example of 3D plots of the Raman spectra of sapphire for polarization configuration $z(0\ 90)\bar{x}$ versus sample rotation angle ψ for a-, c-, m- and r-planes is shown in Supplementary Figure 29. Comparison between theoretical (red line) and experimental (blue circles) responses of the $E_g(5)$ mode versus sapphire sample rotation angle ψ plotted in polar coordinates for polarization configuration $z(0\ 90)\bar{x}$ is shown in Supplementary Figure 31.

In order to keep comparable signal to noise ratio of Raman spectra captured at different depth during 3D mapping of the sample, we implemented depth-dependent acquisition algorithm which exponentially increases exposure time for each mapping Z stack. Therefore, polarized 3D measurements of polycrystalline sapphire were performed with exposure time per point varied from 50ms to 2s resulting in total mapping time 176min. Due to the aberration corrected SAROM system design, we were able to reach a diffraction limited axial resolution without a pinhole which is used in classical confocal microscopy schemes. The confocal mode was organized in a cross slit geometry, where the vertical slit orientation is implemented at the entrance of the spectrometer and the horizontal slit orientation is performed by the readout of the selected rows on the spectroscopic CCD focal plane (Supplementary Figure 37).

We performed a simulation of lateral (Supplementary Figure 36f, 36g) and axial (Supplementary Figure 36d, 36e, 36h, 36i) resolution for typically used high resolution dry metallurgic objective in confocal Raman microscopy (Supplementary Figure 36a) and self-designed oil immersion objective for 3D measurements in Raman microscopy (Supplementary Figure 36b). For the correct

comparison, as a dry objective, we have chosen an infinity-corrected, semi-apochromatic microscope objective having an N.A. of 0.85 at laser beam diameter 6.5mm which provides a magnification of 50 times when used with a telescope objective having an effective focal length of 183 mm (Olympus patent US04417787) (Supplementary Figure 36a). Our self-designed objective has similar parameters: NA=0.85 at laser beam diameter of 8.8mm, magnification 45x at telescope objective having an effective focal length of 183 mm (Supplementary Figure 36b).
Therefore, both objectives provided equal lateral resolution on the sample surface (black lines in Supplementary Figure 36f, 36g). However, Huygens point spread function (PSF) simulation has shown that axial resolution becomes significantly worth in the case of dry objective in the depth of sapphire (-50μm) (Supplementary Figure 36h) rather than for oil immersion objective (Supplementary Figure 36i). Taking into account the values on the scale bar in Supplementary Figure 36d-36i, it is possible to conclude that aberration driven signal attenuation in the depth of 50μm is around 55% for dry metallurgic objective and 11% for oil immersion objective.
During 3D mapping of sapphire using oil immersion objective (Supplementary Figure 36b) we observed much more signal attenuation than 11% due to signal absorbance and reflections on grains in polycrystalline sapphire.
Polycrystalline sapphire manifested fluorescence at the grain boundaries, a perfect mark for grain visualization. In this particular sample we decided to realize grain segmentation based on the combined response from fluorescence and Raman channels. Fluorescence-based signal helped us to avoid ambiguities in the determination of grain boundaries which could be present when Raman signal is used (for example, when neighboring domains have identical or close orientation). However, the usage of only Raman maps obtained at different polarization configurations for segmentation is also a good decision in the general case. A comparison of segmentation results obtained on fluorescence and Raman responses is shown in Supplementary Figure 32. The illustration of segmentation procedure applied to the nine acquired polarized Raman maps at first 2D layer in 3D map presented in Supplementary Figure 33, where grain boundary distribution map based on the fluorescence peak intensity at 1418 cm^{-1} shown on top, segmented domains based on combined fluorescence and Raman responses are shown under it. Described segmentation was applied to each layer in 3D (Supplementary Figure 34).
3D orientation map of polycrystalline sapphire was visualized in Paraview software.

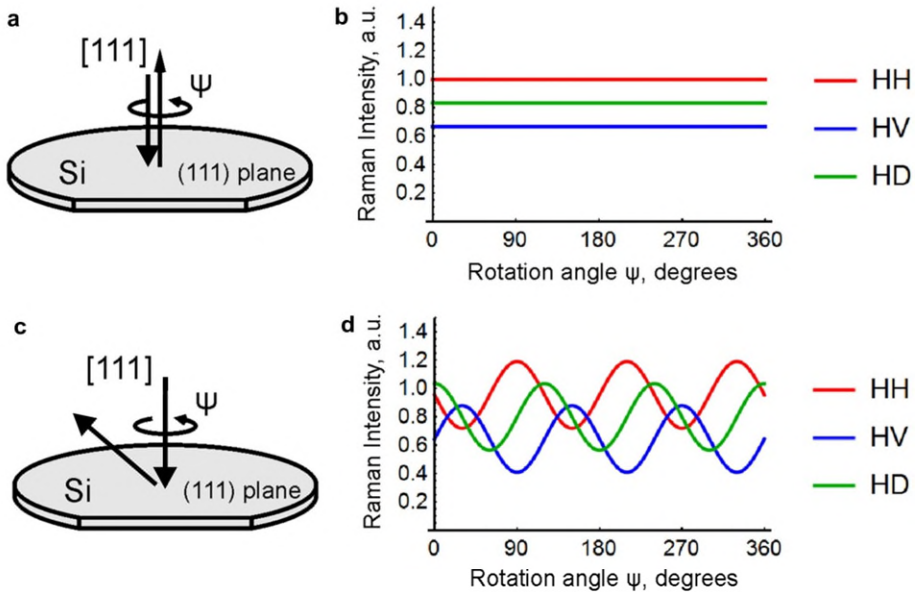

Supplementary Figure 1. On axis and off-axis registration differences. a, On-axis scheme with normal sample illumination and on-axis collection of scattered light and **b,** corresponding Raman intensity dependence on wafer rotation angle ψ, **c,** off-axis illumination scheme and **d,** Raman intensity dependence on wafer rotation angle ψ. HH – horizontal/horizontal polarizer/analyzer configuration, HV – horizontal/vertical polarizer/analyzer configuration, HD - horizontal/tilted at 45 degrees polarizer/analyzer configuration.

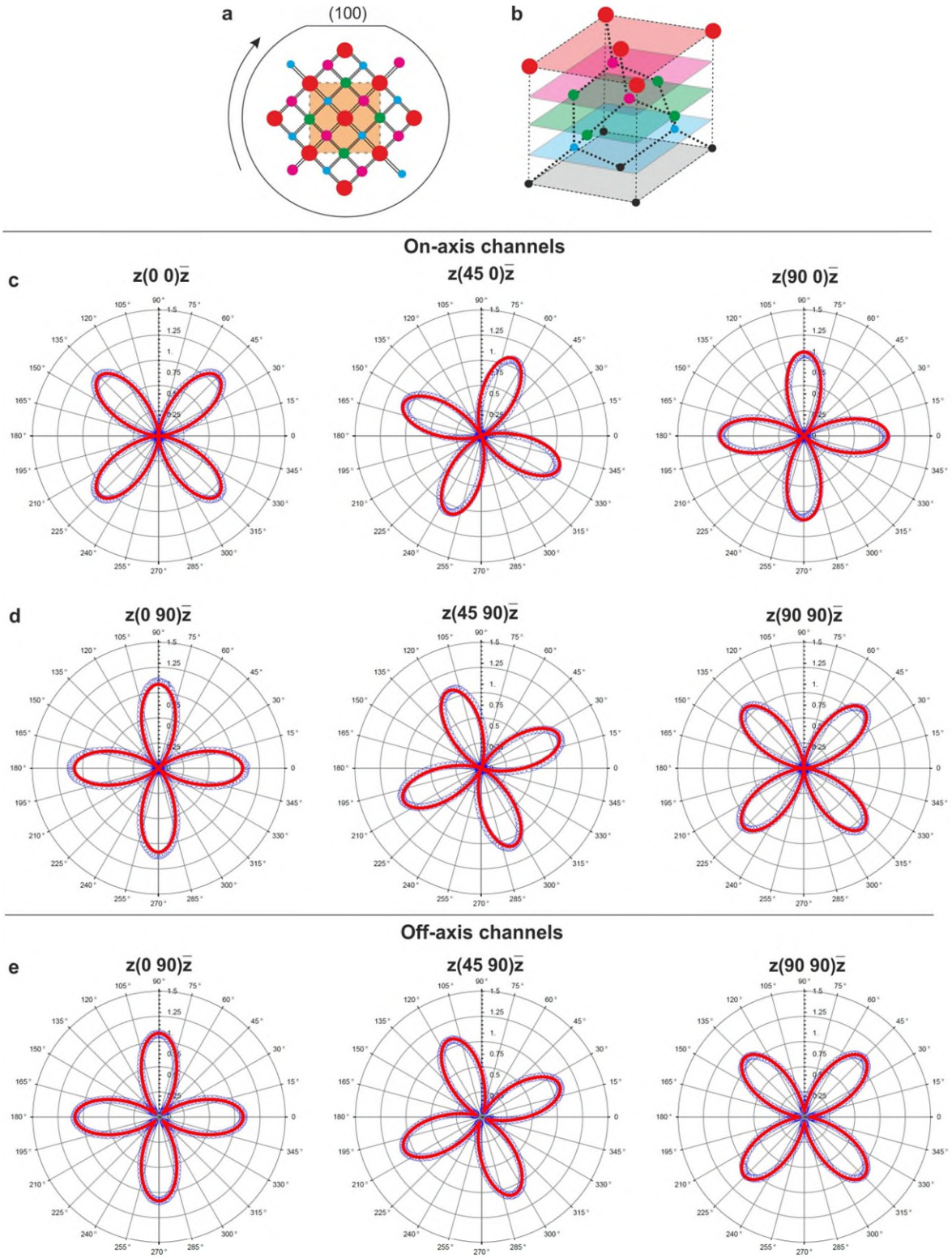

Supplementary Figure 2. Wafer rotation experiment on Si (100). a,b, Top and 3D view of Si unit cell. Comparison between theoretical (red line) and experimental (blue circles) responses of the sum of Si modes versus wafer rotation angle ψ plotted in polar coordinates for Si wafer with surface plane (100) for on-axis (**c,d)** and off-axis (**e)** polarization channels of SAROM system.

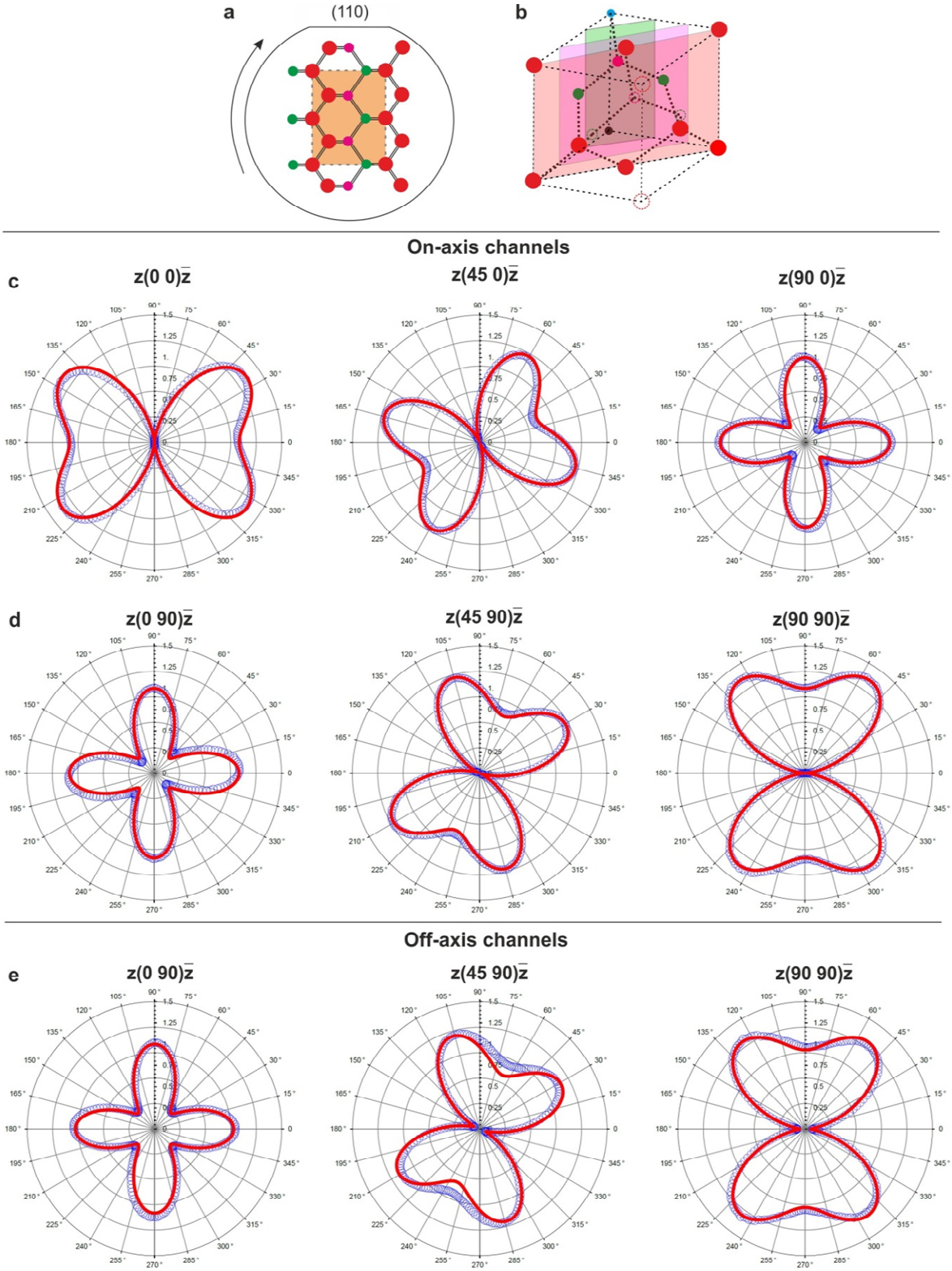

Supplementary Figure 3. Wafer rotation experiment on Si (110). a,b, Top and 3D view of Si unit cell. Comparison between theoretical (red line) and experimental (blue circles) responses of the sum of Si modes versus wafer rotation angle ψ plotted in polar coordinates for Si wafer with surface plane (110) for on-axis (**c,d)** and off-axis (**e)** polarization channels of SAROM system.

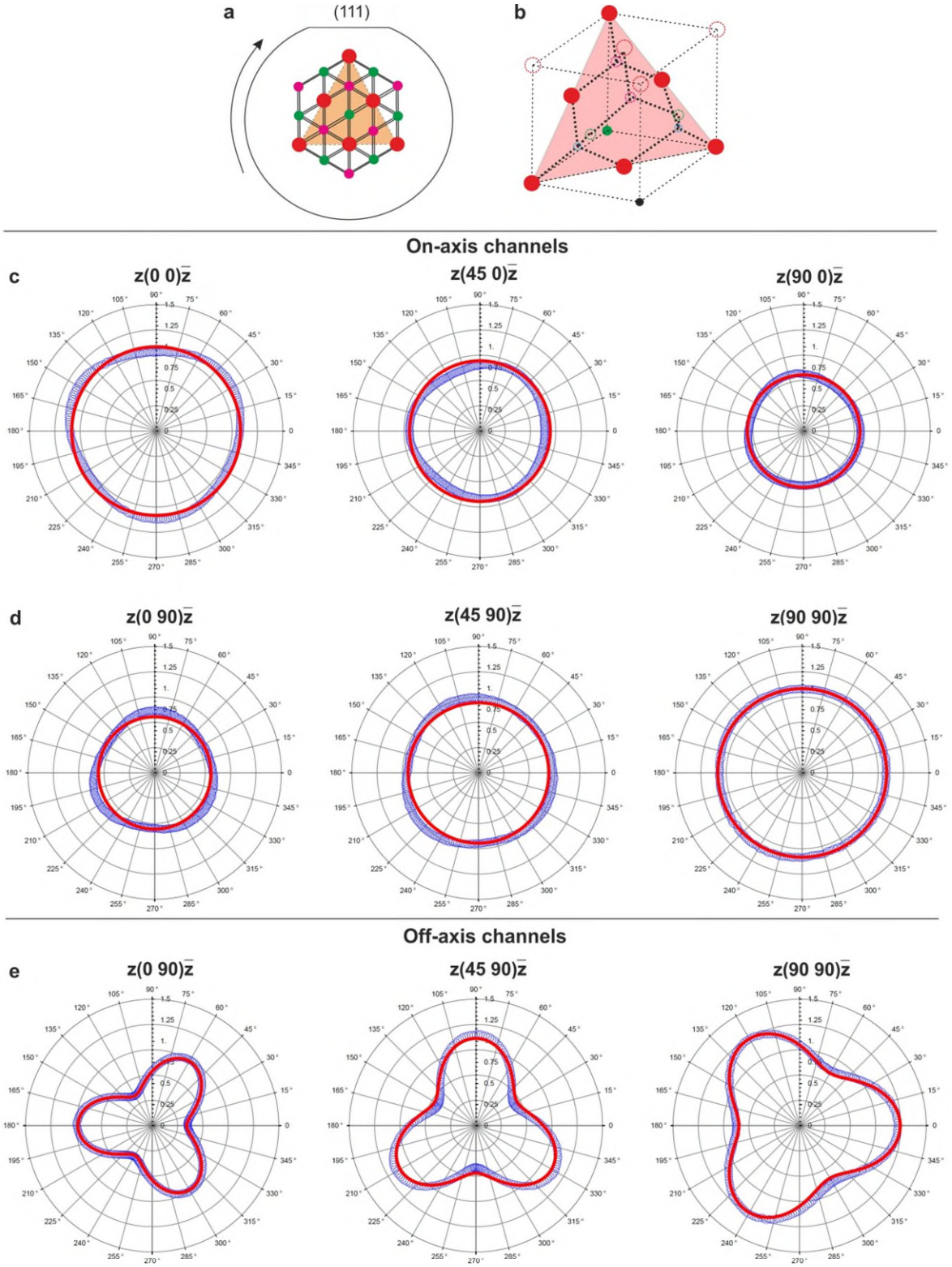

Supplementary Figure 4. Wafer rotation experiment on Si (111). a,b, Top and 3D view of Si unit cell. Comparison between theoretical (red line) and experimental (blue circles) responses of the sum of Si modes versus wafer rotation angle ψ plotted in polar coordinates for Si wafer with surface plane (111) for on-axis (**c,d)** and off-axis (**e)** polarization channels of SAROM system.

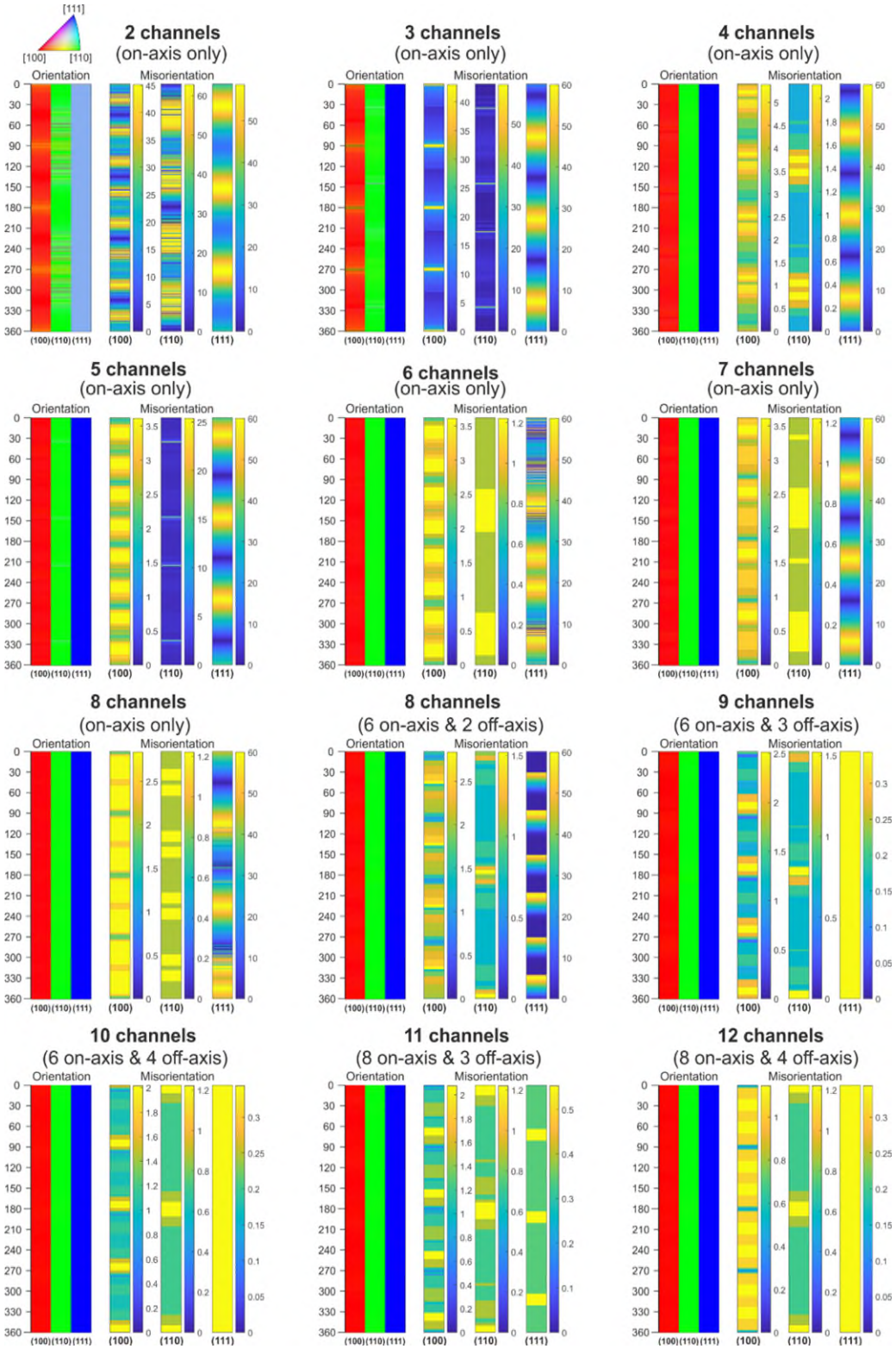

Supplementary Figure 5. Simulation based orientation determination error versus a number of polarized channels. The colors refer to the orientations shown by the inverse pole figure (inserted). Misorientation data presented separately on each set. Refer to colored scale bars for misorientation angle range.

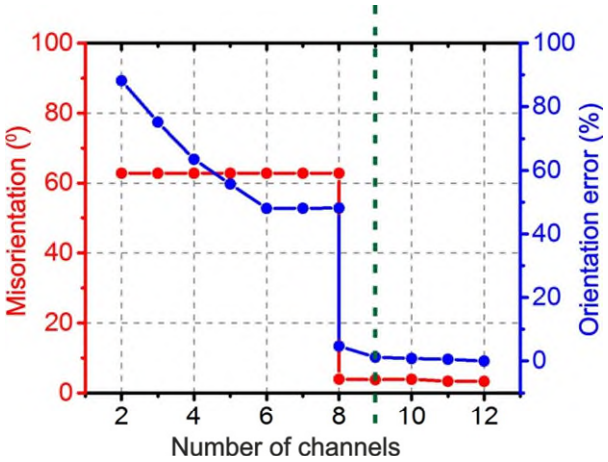

Supplementary Figure 6. Simulation based orientation determination error and misorientation versus the number of polarized channels.

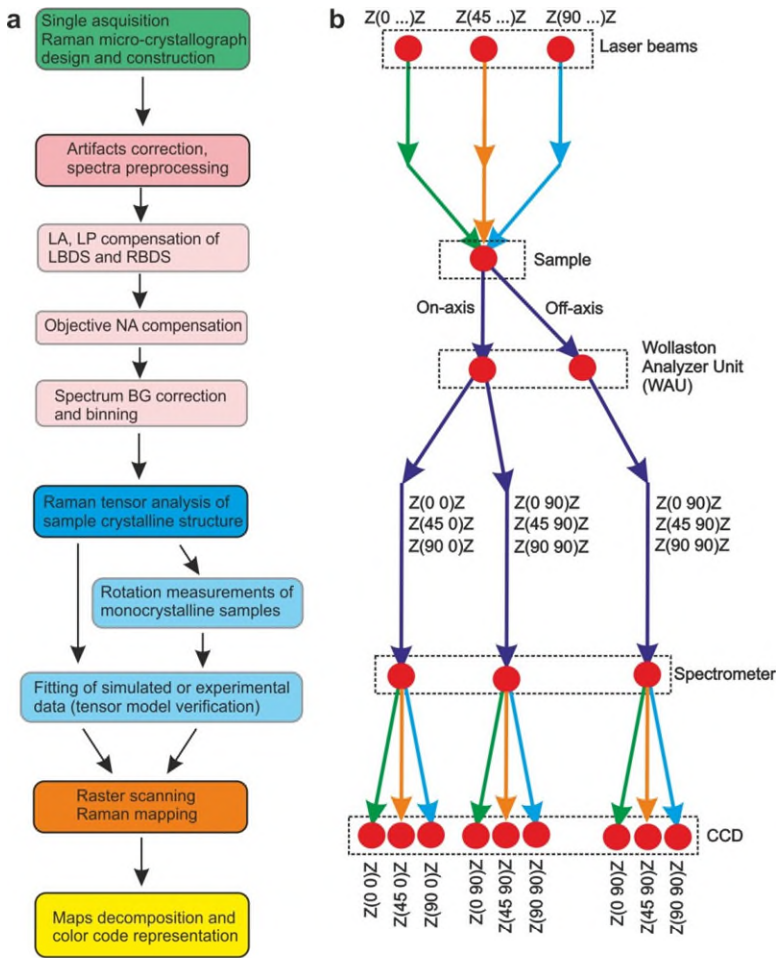

Supplementary Figure 7. SAROM principle. Illustration of a SAROM workflow (**a)** and schematic representation of simultaneous measurements with nine polarized Raman channels **(b)**.

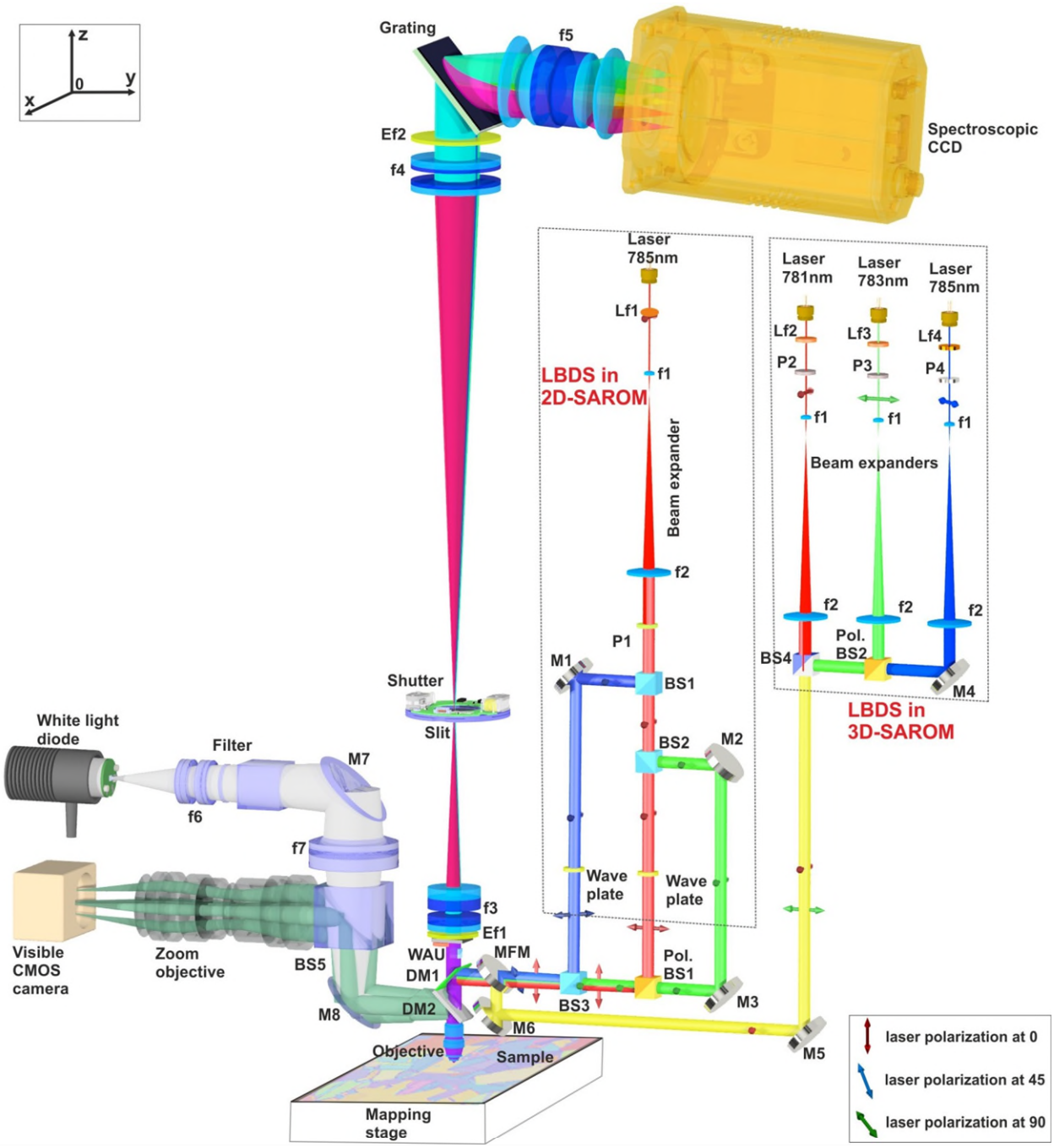

Supplementary Figure 8. Detailed illustration of SAROM optical design. Abbreviations: LBDS – Laser Beam Delivery System, Lf – laser filter, P – polarizer, f – lens, BS – beam splitter, Pol.BS – polarized beam splitter, M – mirror, MFM – motorized flip mirror, DM – dichroic mirror, WAU – Wollaston Analyzer Unit, Ef – edge filter.
Unique properties of spectrograph design covered by pending patent of Technical University of Denmark (application number 18183474.8).

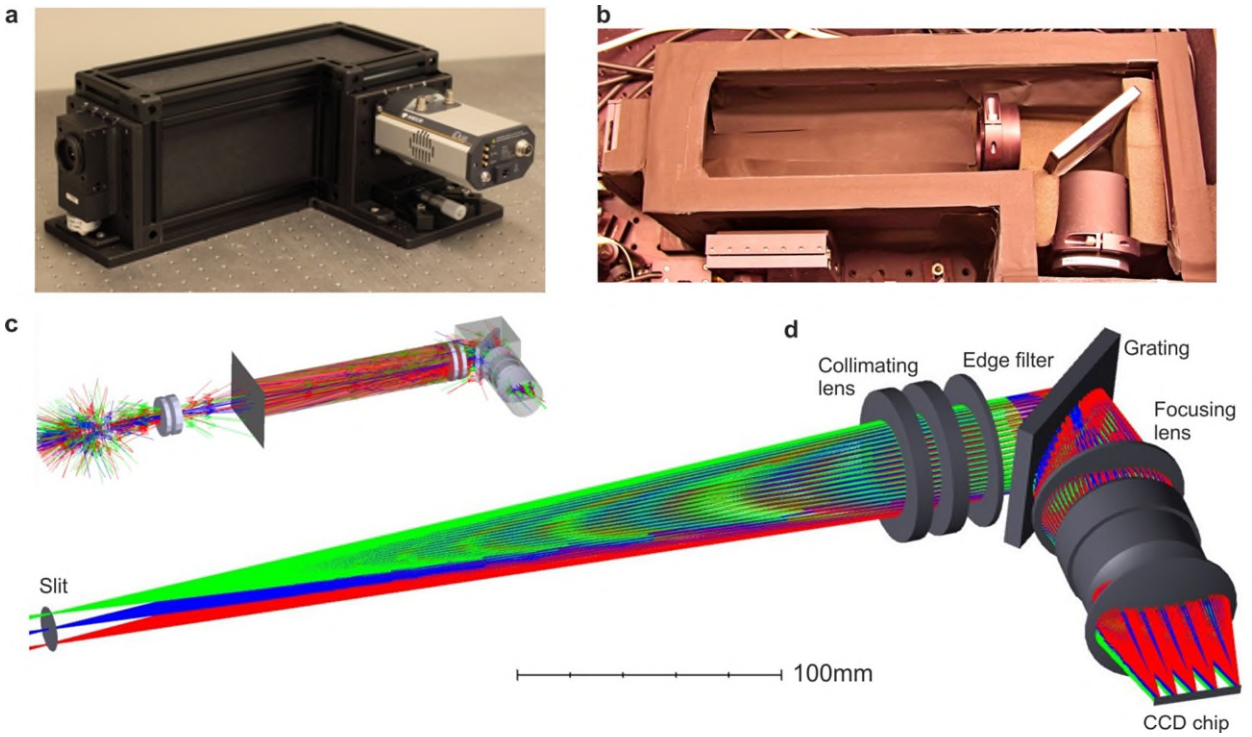

Supplementary Figure 9. SAROM spectrograph. a, Photograph of the spectrograph coupled with spectroscopic CCD, **b,** photograph of the spectrograph optical components, **c,** stray light analysis, **d,** optical design of the spectrograph. Unique features of spectrograph design are covered by pending patent of Technical University of Denmark (application number PCT/DK2019/050027).

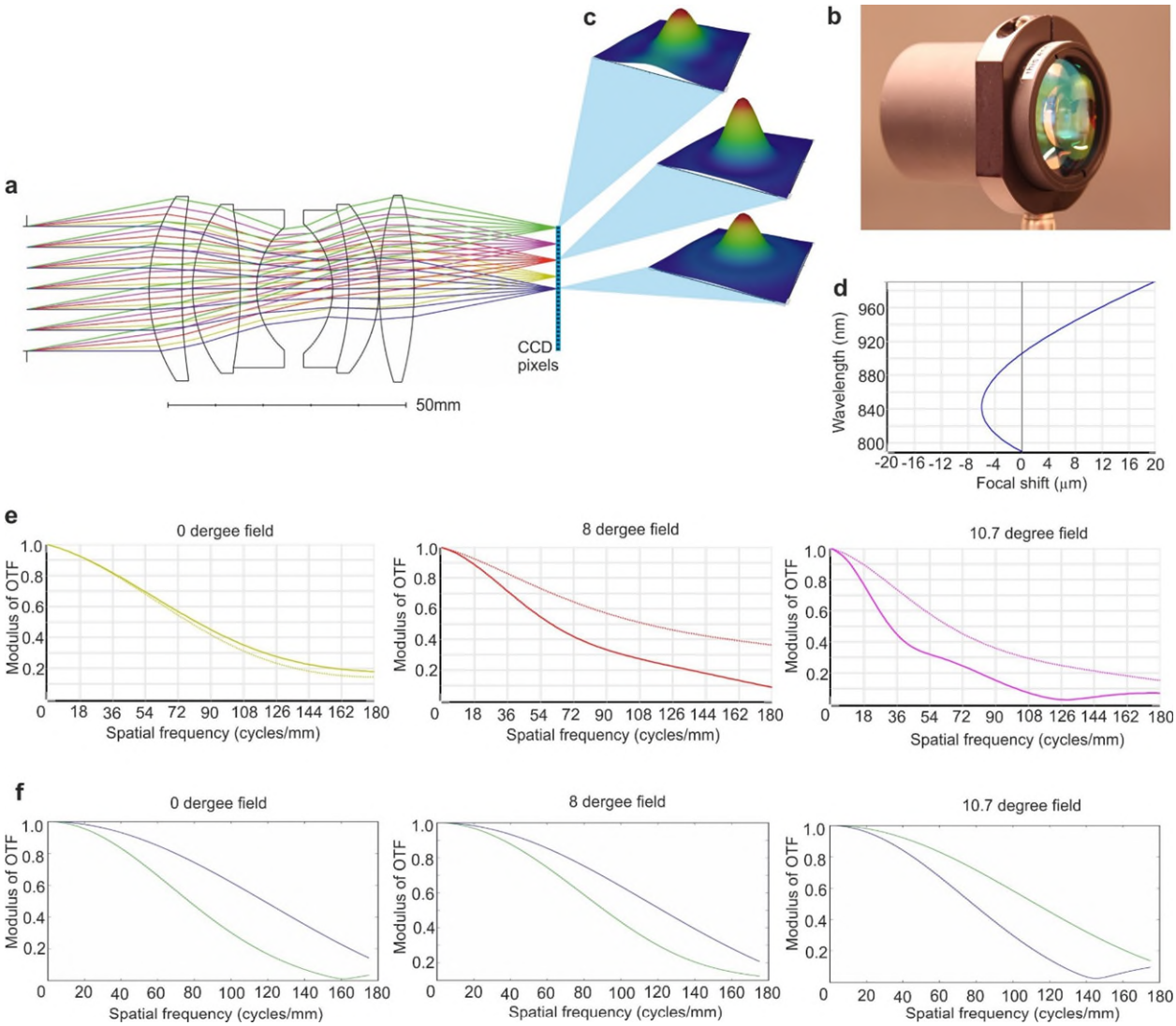

Supplementary Figure 10. Spectrograph focusing objective. a, optical design, **b,** photograph, **c,** point spread functions at different fields (0, 8 and 10.7 degrees), **d,** achromatic focal shift, experimental (**e)** and designed (**d)** modulus of OTF versus spatial frequency for different fields (0, 8 and 10.7 degrees).

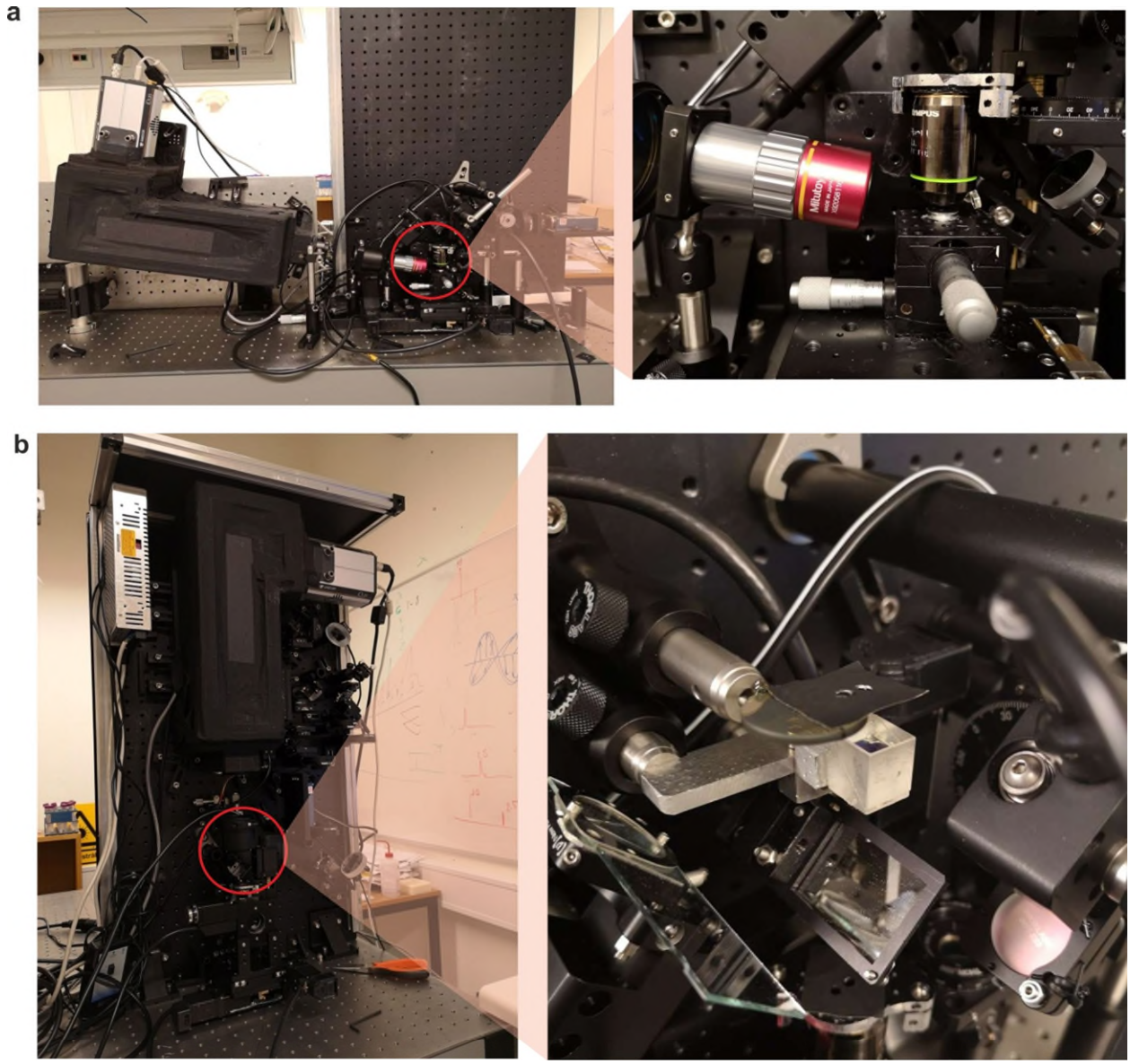

Supplementary Figure 11. Experimental setup development process. a, Photograph of setup for off-axis polarization experiments only, **b,** photograph of final SAROM setup with simultaneous on-axis and off-axis polarization measurements

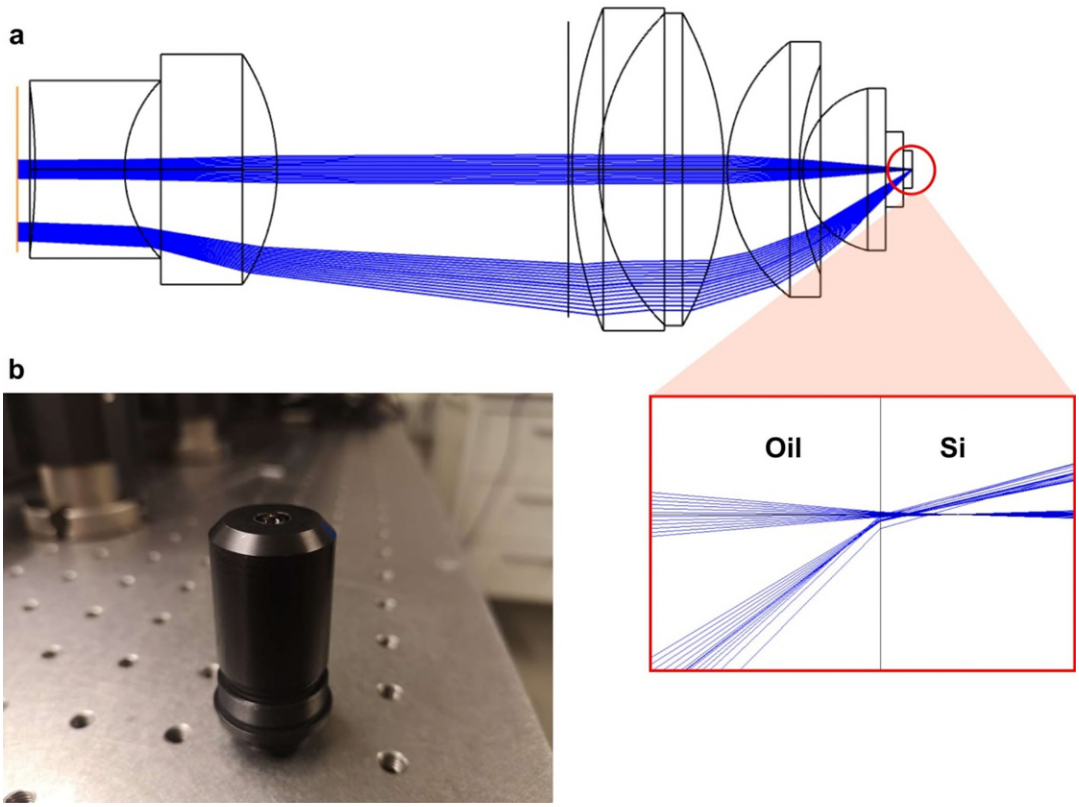

Supplementary Figure 12. Custom designed microscope objective. a, optical design of the objective (zoomed area illustrates the difference between collecting cones of light scattered in the Silicon sample at on-axis and off-axis geometries), **b,** objective photograph.

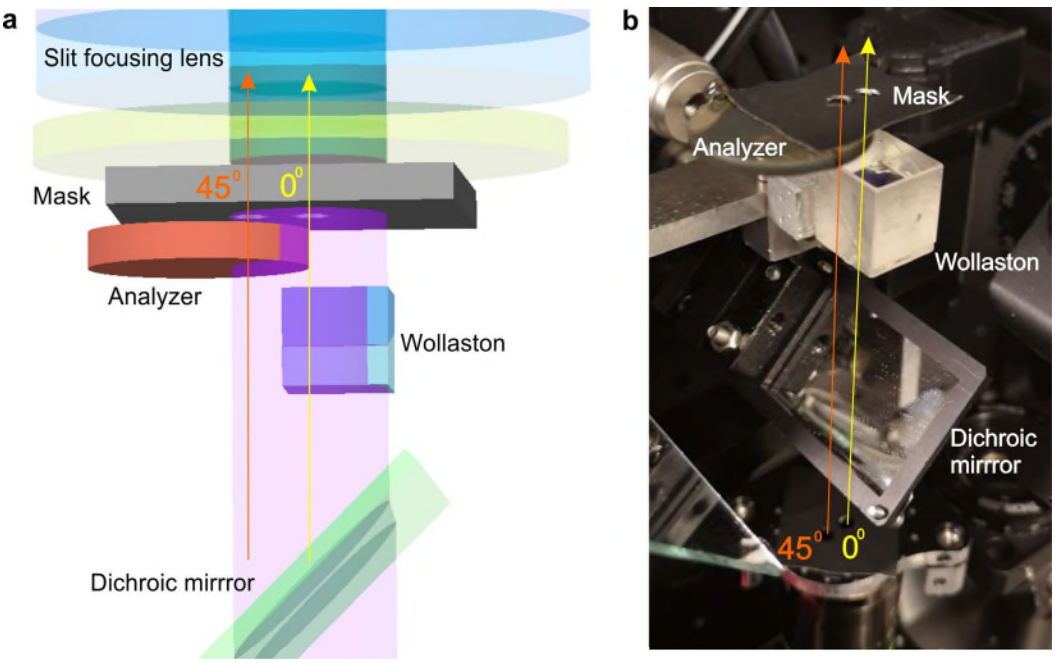

Supplementary Figure 13. Wollaston Analyzer Unit (WAU). a, Illustration of the Raman scattering beam path through WAU, **b,** photograph of WAU inserted into experimental setup.

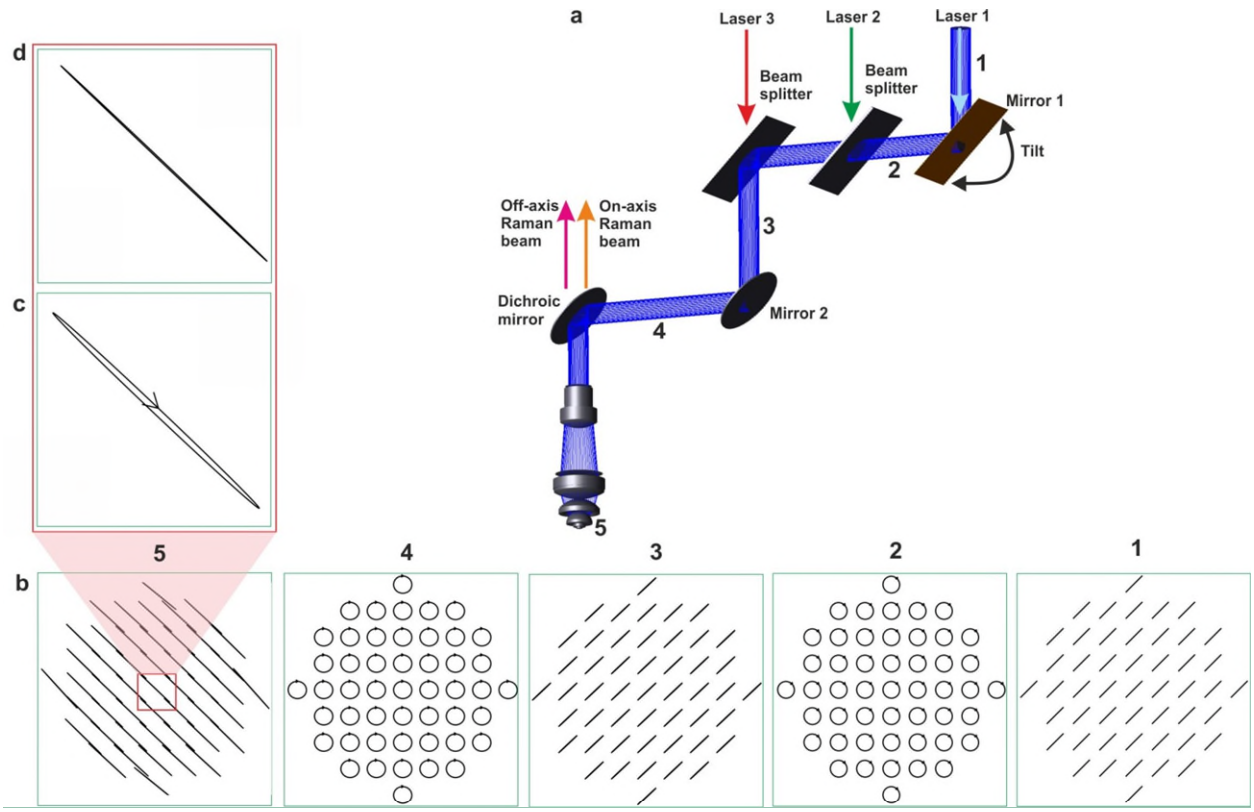

Supplementary Figure 14. Laser polarization propagation. a, Optical schema of Laser Beam Delivery System (LBDS), **b,** LBDS analyzed on laser polarization propagation with input angle of polarization state of 45°. The polarization state of laser beam focused onto diffraction limited spot on a sample focal plane before (**c)** and after (**d),** compensation of phase shift between S and P components of electromagnetic wave. Compensation was realized by the tilt of mirror M1 on 0.8°.

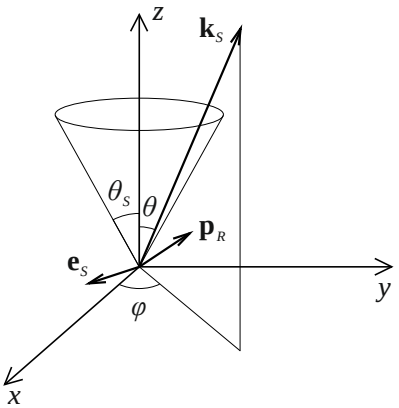

Supplementary Figure 15. Local spherical coordinate system associated with collection aperture.

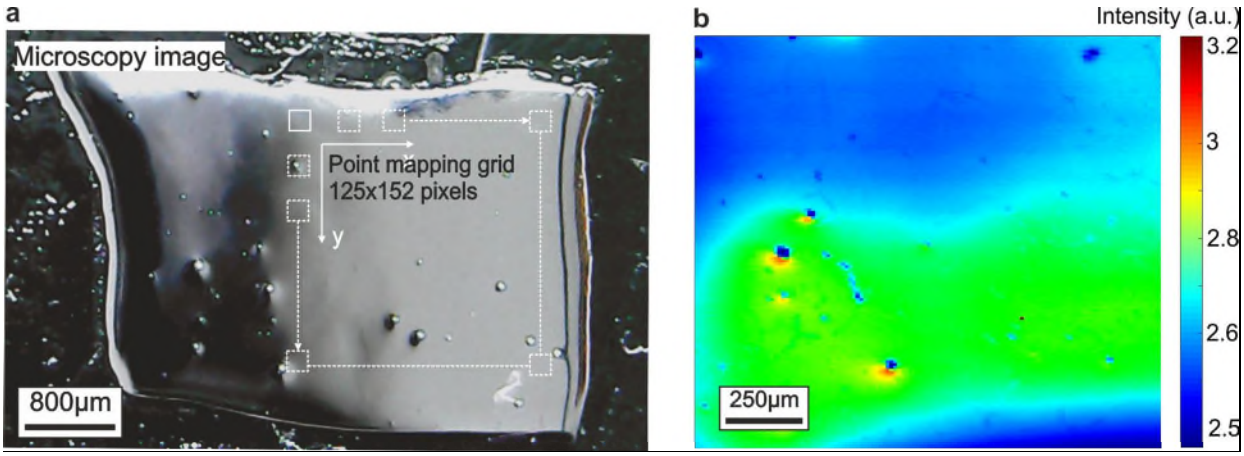

Supplementary Figure 16. Visible light and fluorescence microscopy of polycrystalline Si. a, Light microscopy image of the sample of polycrystalline Si, **b,** map of the surface of the polycrystalline Si plotted at the maximum of fluorescence intensity band.

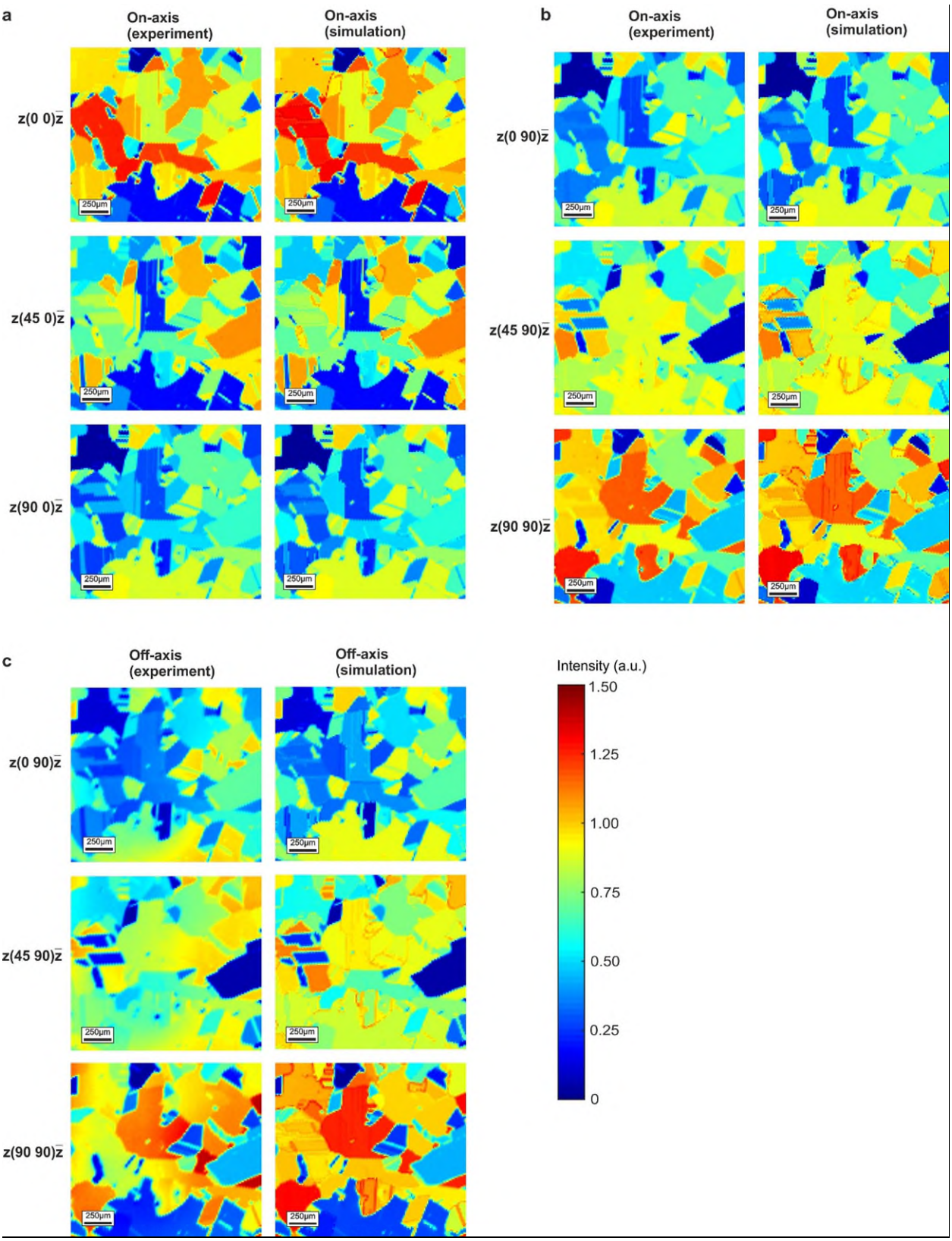

Supplementary Figure 17. Raman intensity map of polycrystalline Si. a, On-axis simulated and experimental Raman intensity maps at polarization channels $z(0\ 0)\bar{z}$, $z(45\ 0)\bar{z}$, $z(90\ 0)\bar{z}$, **b,**

on-axis simulated and experimental Raman intensity maps at polarization channels $z(0\ 90)\bar{z}$, $z(45\ 90)\bar{z}$, $z(090)\bar{z}$, **c,** off-axis simulated and experimental Raman intensity maps at polarization channels $z(0\ 90)\bar{z}$, $z(45\ 90)\bar{z}$, $z(090)\bar{z}$.

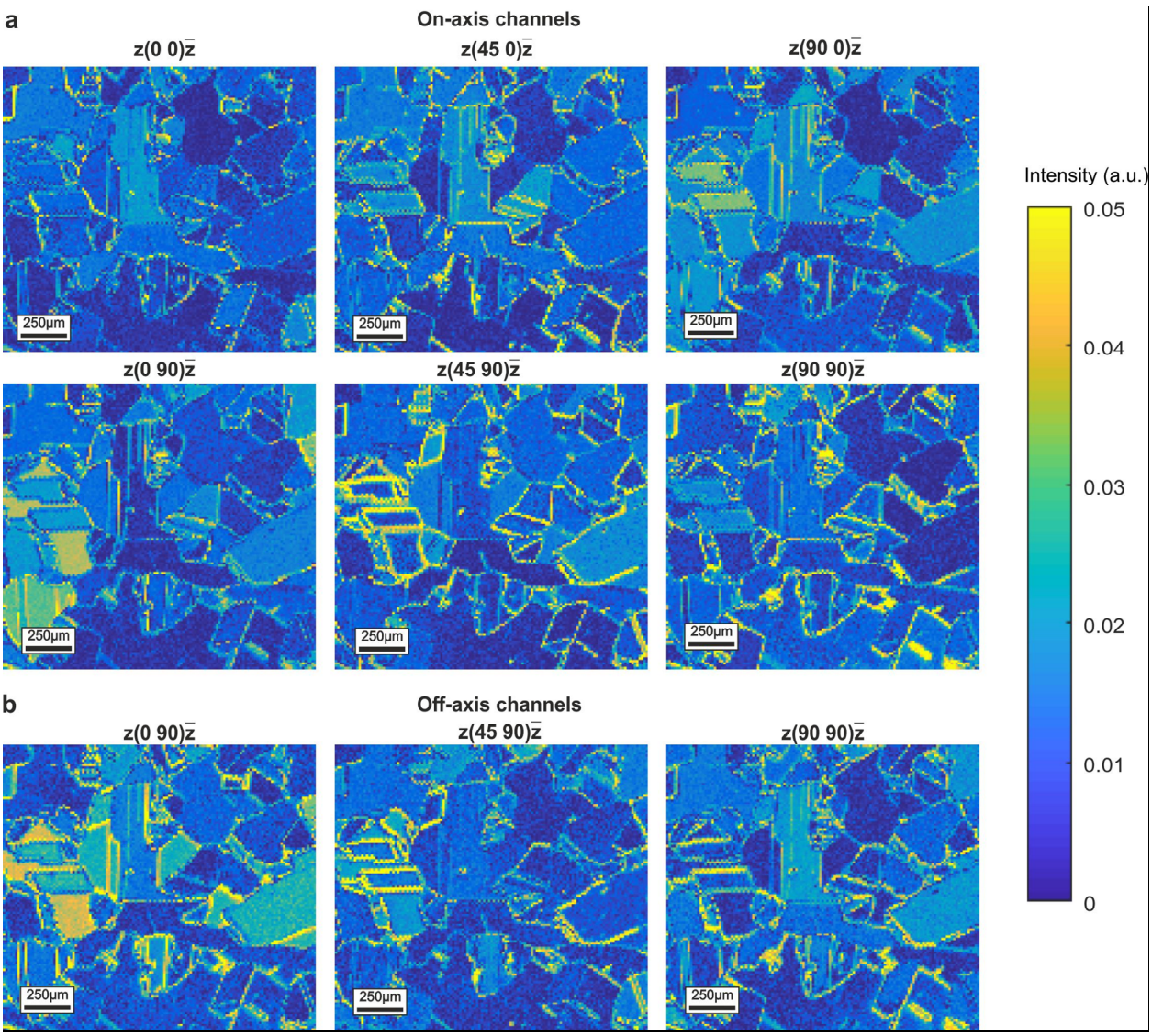

Supplementary Figure 18. Residual Raman intensity maps. **a,** On-axis residual Raman intensity maps at polarization channels $z(0\ 0)\bar{z}$, $z(45\ 0)\bar{z}$, $z(90\ 0)\bar{z}$, $z(0\ 90)\bar{z}$, $z(45\ 90)\bar{z}$ and $z(090)\bar{z}$, **b,** off-axis residual Raman intensity maps at polarization channels $z(0\ 90)\bar{z}$, $z(45\ 90)\bar{z}$, $z(090)\bar{z}$. Residual Raman intensity maps were obtained as a result of subtraction between simulated and experimental polarization data from each of the nine polarized channels.

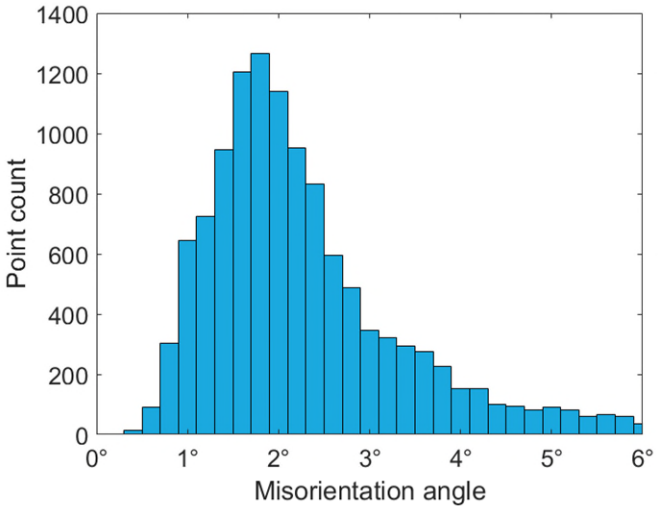

Supplementary Figure 19. Histogram of the misorientation map from the sample of polycrystalline Si.

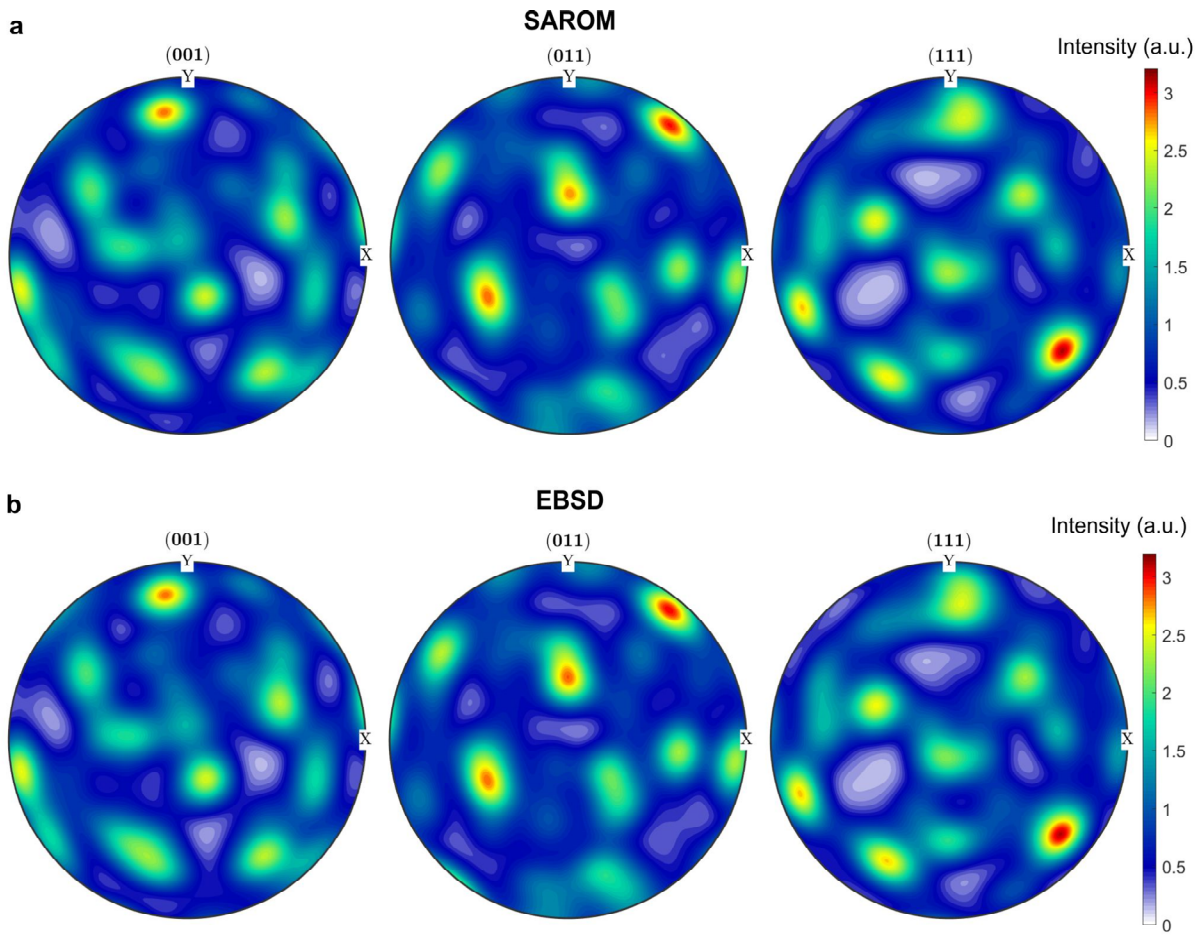

Supplementary Figure 20. Inverse Pole Figures of polycrystalline Si. Comparison between Inverse Pole Figures (IPF) plotted on SAROM (**a)** and EBSD (**b)** orientation maps of polycrystalline Si.

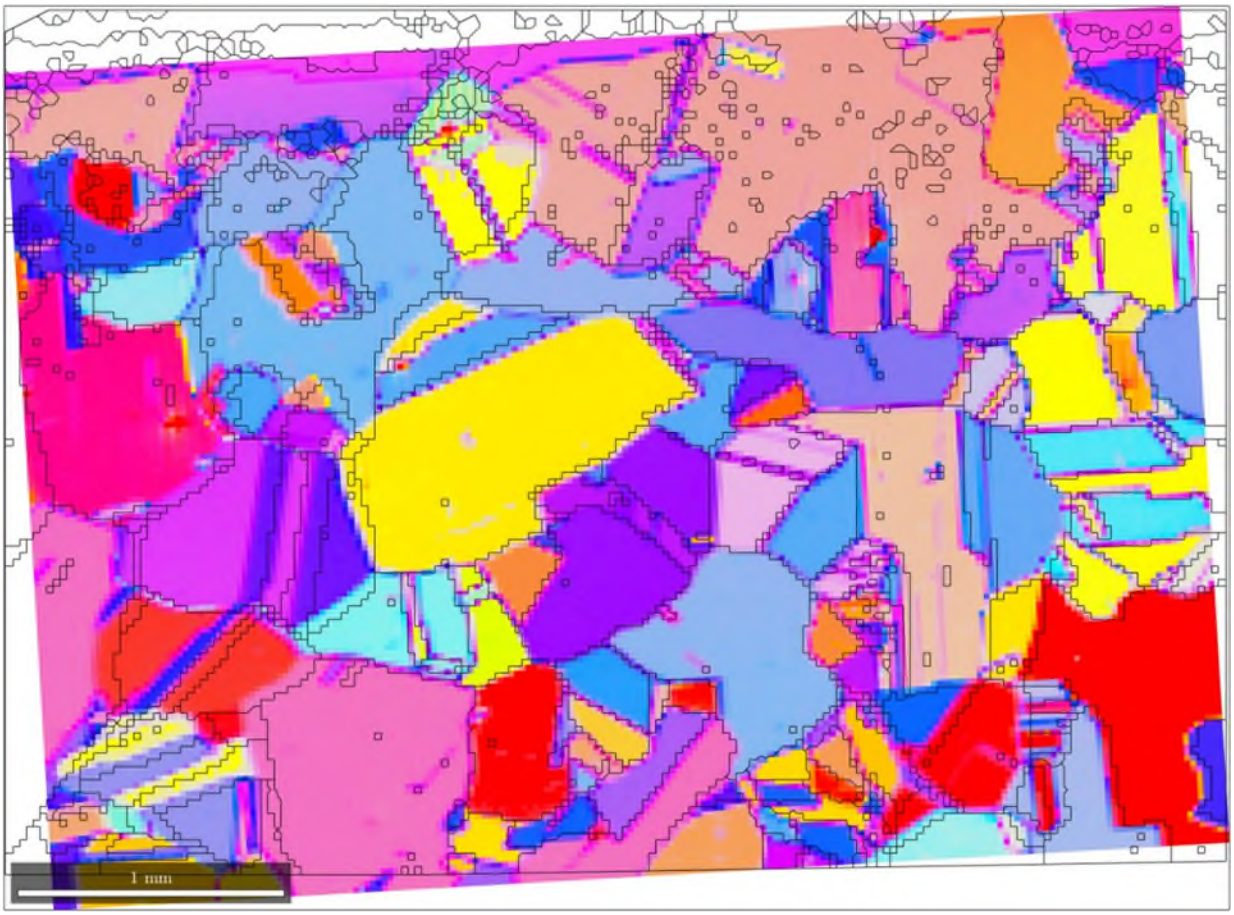

Supplementary Figure 21. Geometrical distortions. Illustration of the geometrical distortions of the EBSD map demonstrated on overlapping SAROM and EBSD images.

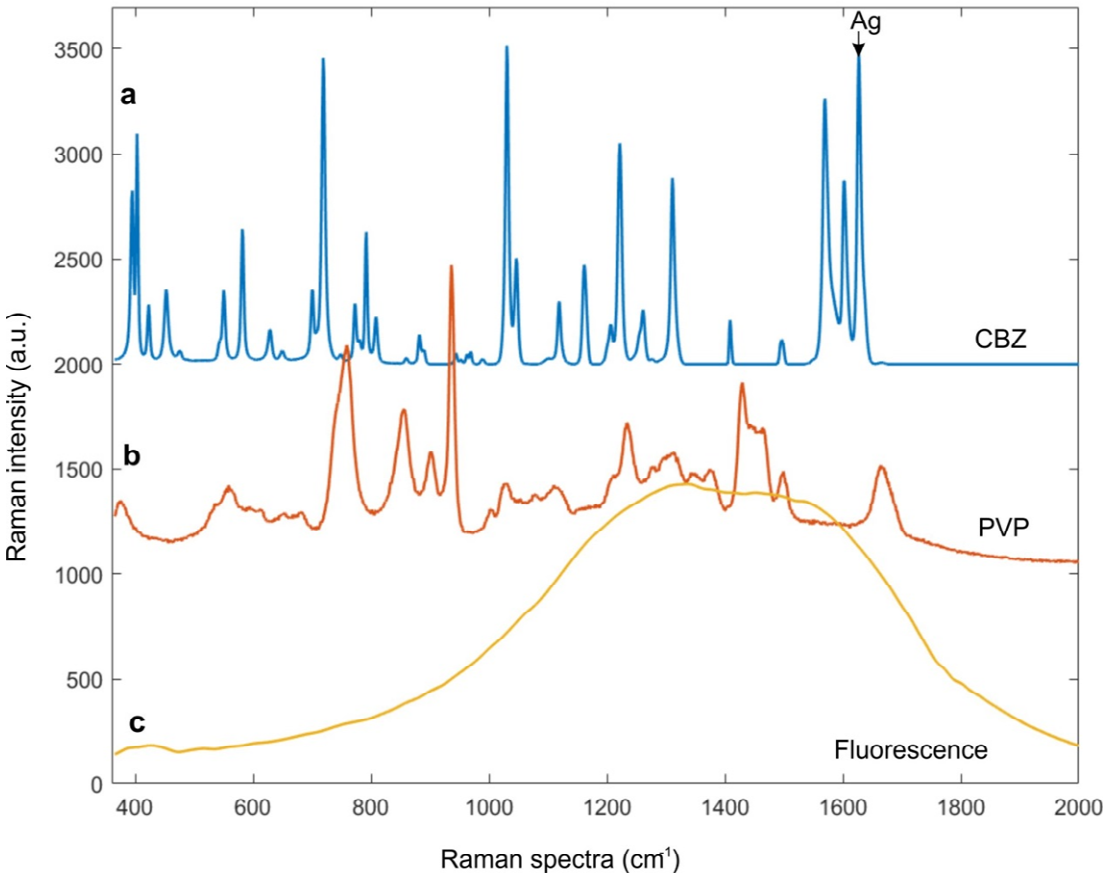

Supplementary Figure 22. Raman spectra of a pharmaceutical tablet. a, Raman spectrum of CBZD, **b,** Raman spectrum of PVP, **c,** fluorescence spectrum potentially due to magnesium stearate (tablet die) and impurities on the surface of the tablet.

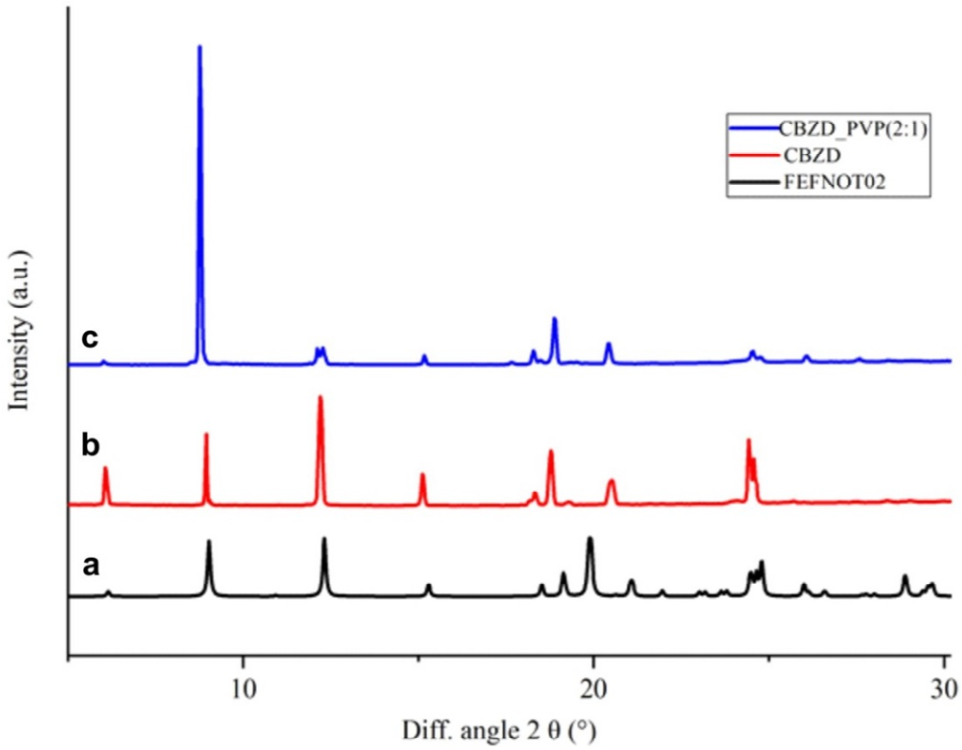

Supplementary Figure 23. XRPD diffractograms of CBZ. a, Calculated XRPD diffractogram of CBZD, **b,** experimentally obtained XRPD diffractorgam of CBZD and (**c)** CBZ and PVP (2:1).

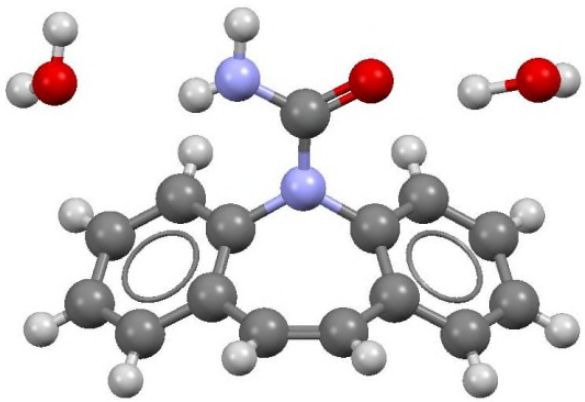

Supplementary Figure 24. Carbamazepine dihydrate molecular structure

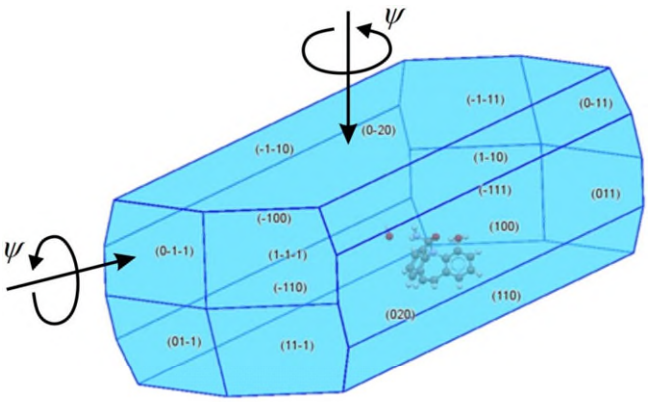

Supplementary Figure 25. The illustration of SAROM rotation experiments (see movie S4) applied to the CBZD. The predicted CBZD crystal morphology (CSD refcode FEFNOT02, monoclinic crystal system).

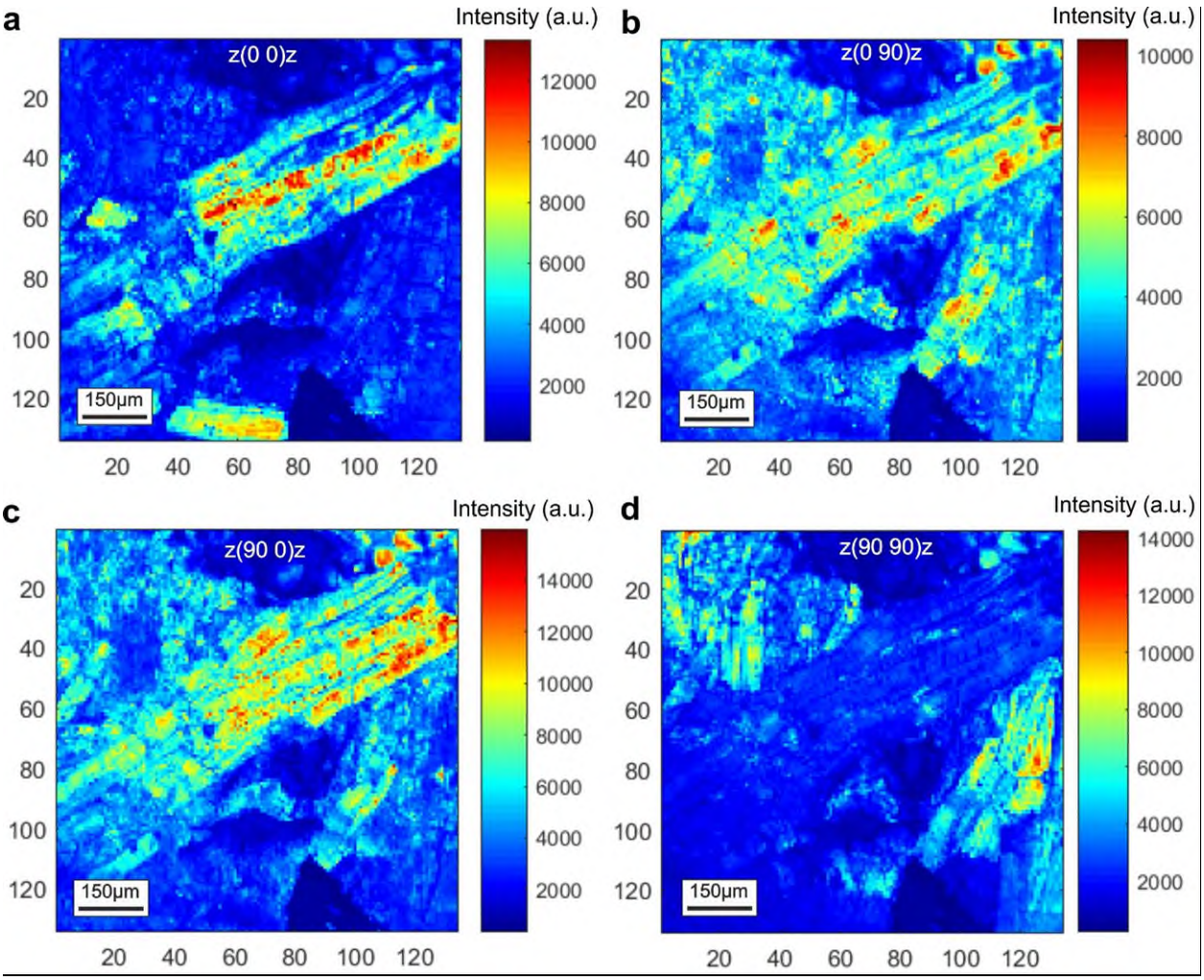

Supplementary Figure 26. Polarized Raman maps. Polarized Raman intensity maps of the surface of CBZD tablet obtained at polarization configurations $z(0\ 0)\bar{z}$ (**a**), $z(0\ 90)\bar{z}$ (**b**), $z(90\ 0)\bar{z}$ (**c**) and $z(90\ 90)\bar{z}$ (**d**).

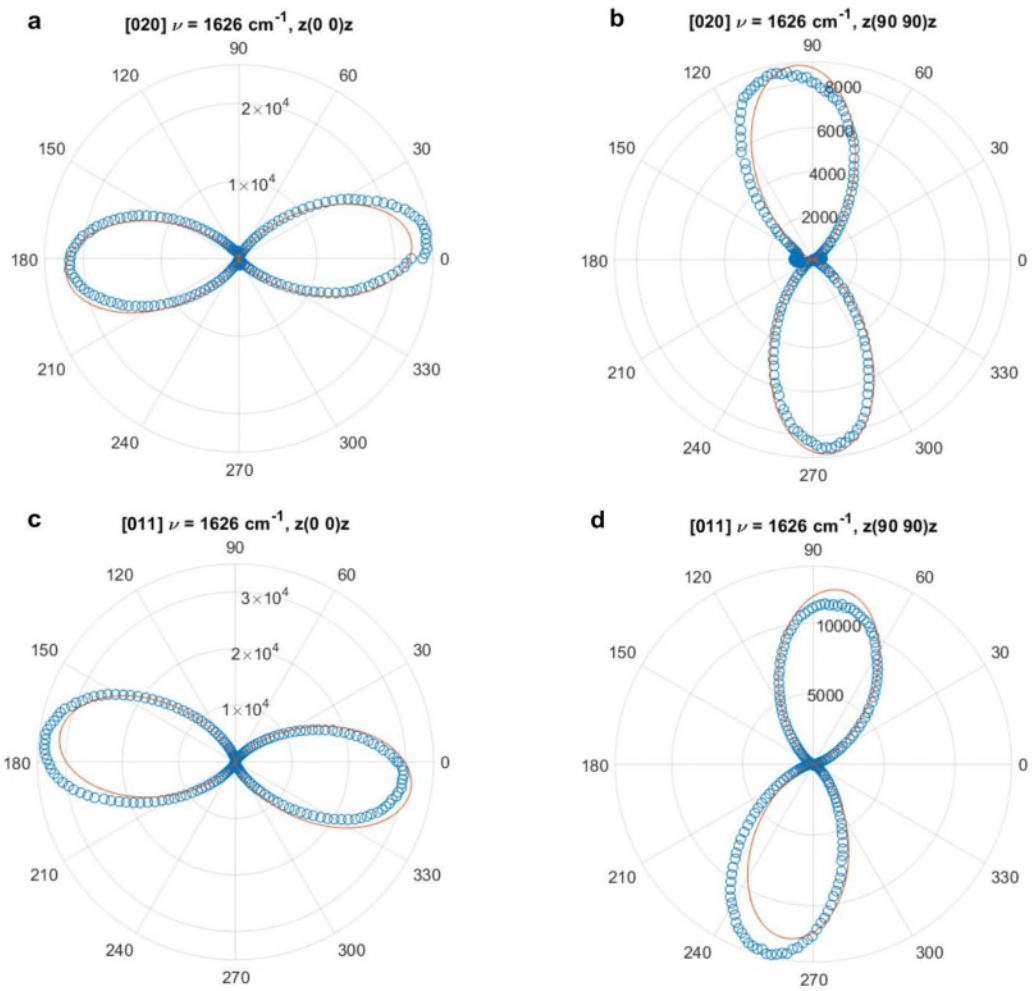

Supplementary Figure 27. Polarized Raman responses of CBZD. Comparison between theoretical (red line) and experimental (blue circles) responses of A_g mode of CBZD versus wafer rotation angle ψ plotted in polar coordinates for the monocrystal of CBZD around axis [020] (**a,b)** and [011] (**c,d)** at polarizer/analyzer orientations $z(0\ 0)\bar{z}$ (**a,c**), $z(90\ 90)\bar{z}$ (**b,d**).

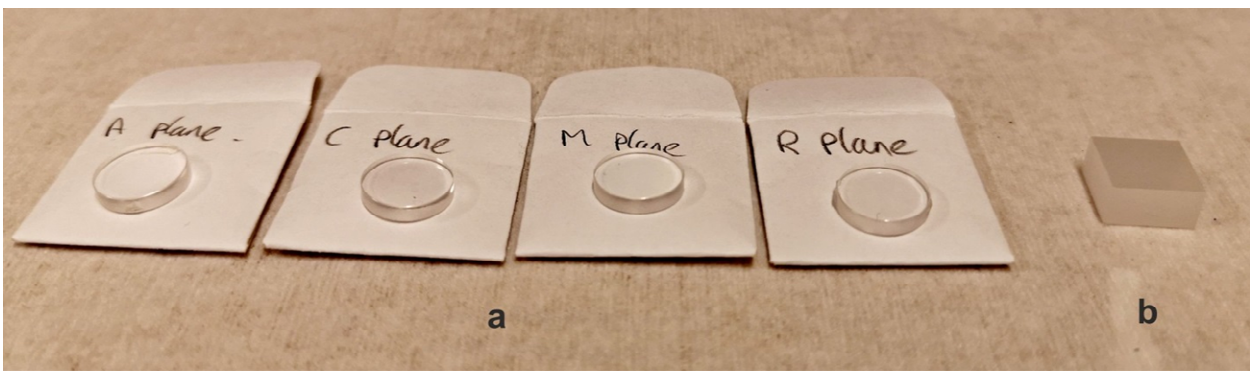

Supplementary Figure 28. Sapphire photographs. a, Photographs of the monocrystalline sapphire plates with cut at different surface planes, **b,** photograph of the polycrystalline sapphire sample.

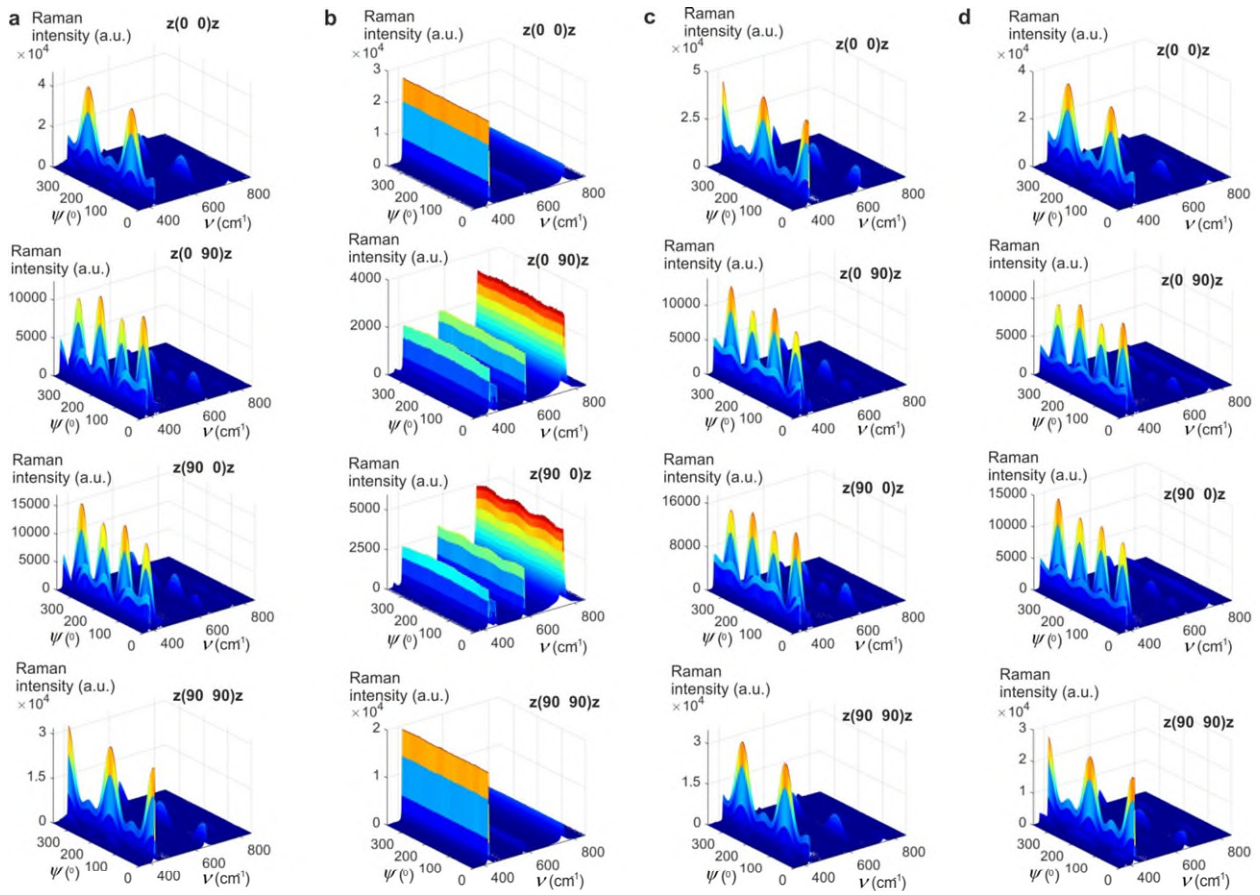

Supplementary Figure 29. Polarized Raman spectra of sapphire. 3D plots of the Raman spectra of sapphire for different on-axis polarization configurations versus sample rotation angle ψ for a- (**a**), c- (**b**), m- (**c**) and r- (**d**) planes.

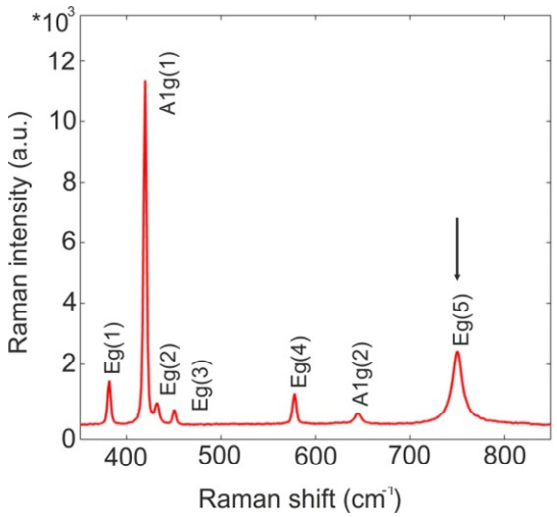

Supplementary Figure 30. Polarized Raman spectrum of sapphire with illustration of E_g and A_g modes.

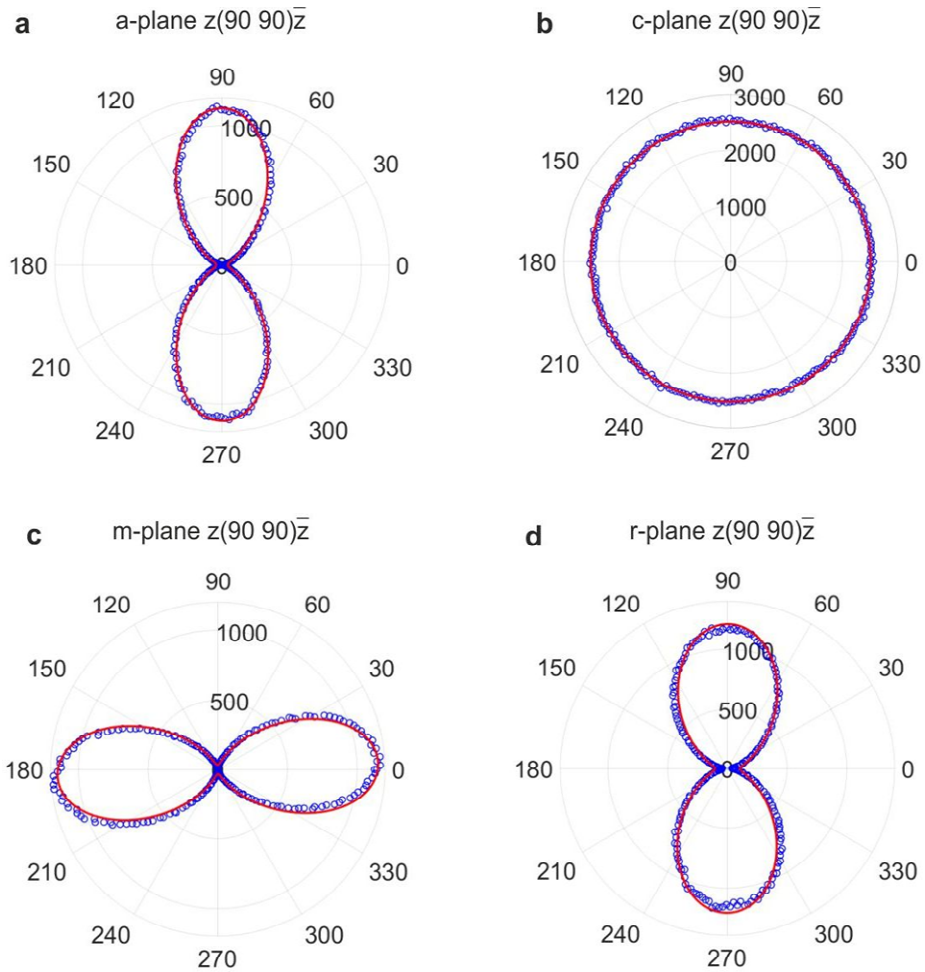

Supplementary Figure 31. Polarized Raman responses of sapphire. Comparison between theoretical (red line) and experimental (blue circles) responses of the $E_g(5)$ mode versus sapphire sample rotation angle ψ plotted in polar coordinates for polarization configuration $z(90\ 90)\bar{z}$ at a- (**a**), c- (**b**), m- (**c**) and r- (**d**) sapphire planes.

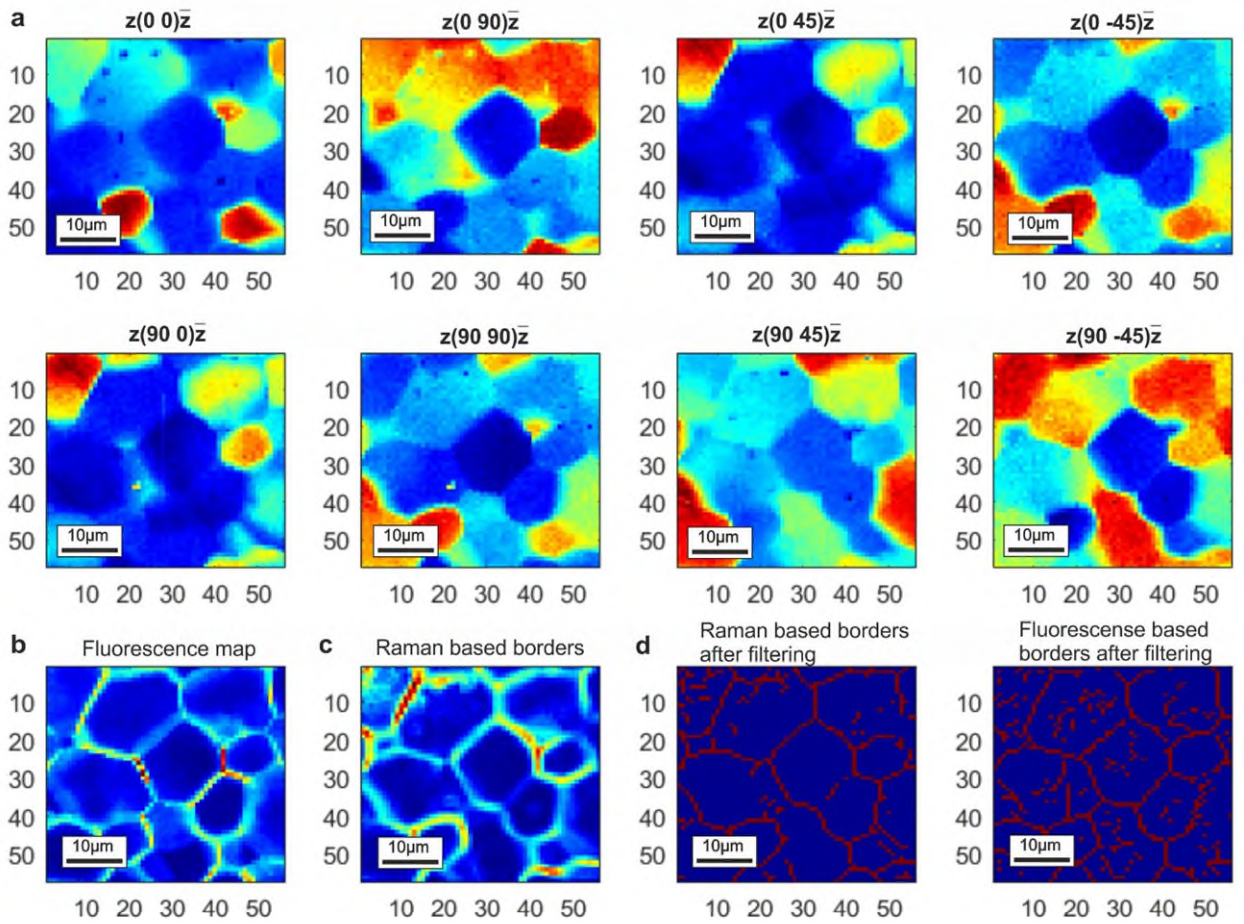

Supplementary Figure 32. SAROM mapping of polycrystalline sapphire. a, Polarized Raman maps of $E_g(5)$ mode at different polarization configurations, **b,** grained boundaries plotted based on fluorescence band, **c,** grained boundaries plotted based on Raman maps, **d,** comparison of segmentation results obtained on fluorescence and Raman responses.

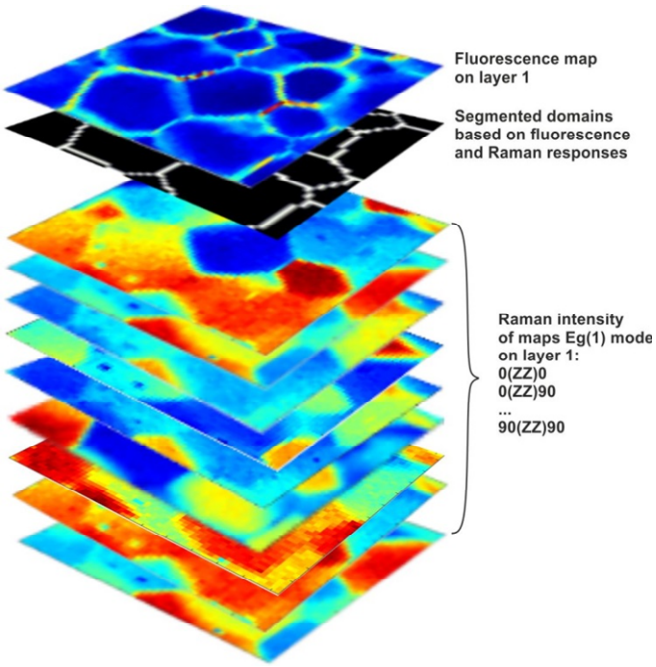

Supplementary Figure 33. Grain boundaries in polycrystalline sapphire. On top is grain boundary map based on the fluorescence, under it there is segmented domains based on combined fluorescence and Raman responses are shown, below are nine polarized Raman intensity maps for Eg(5) vibrational mode.

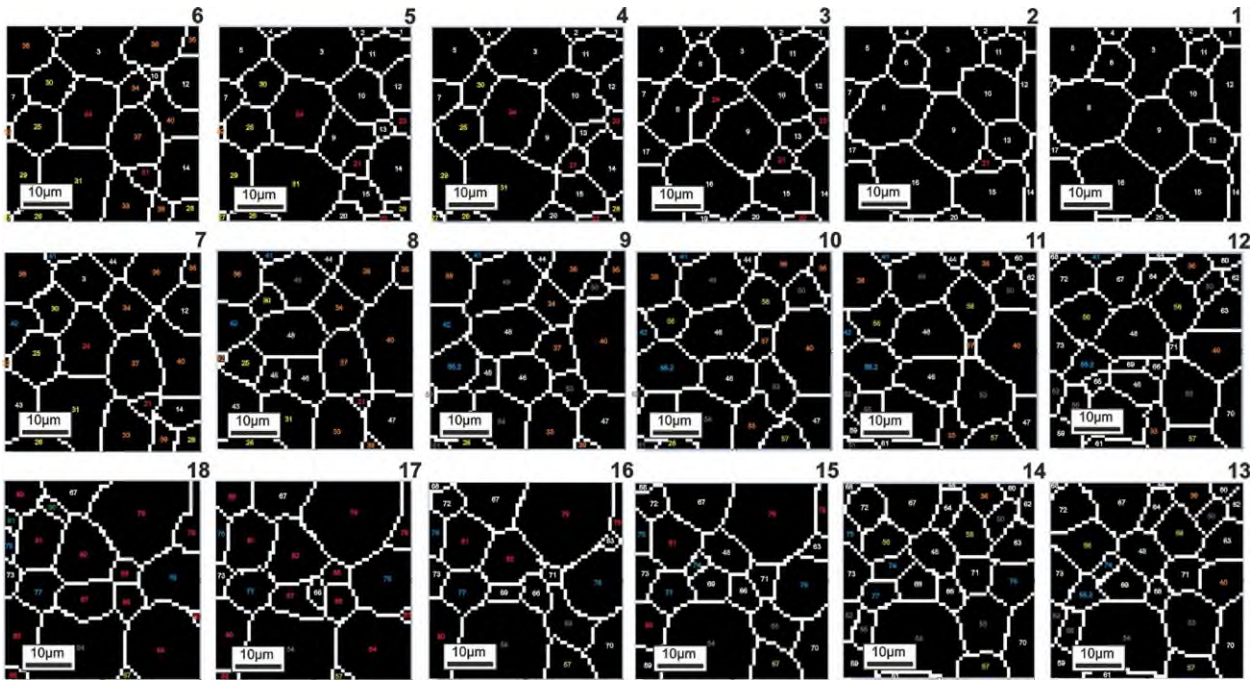

Supplementary Figure 34. Segmentation. Illustration of segmentation procedure applied to the nine acquired polarized Raman maps for 18 depth layers in 3D map, where segmented domains were plotted based on combined fluorescence and Raman responses.

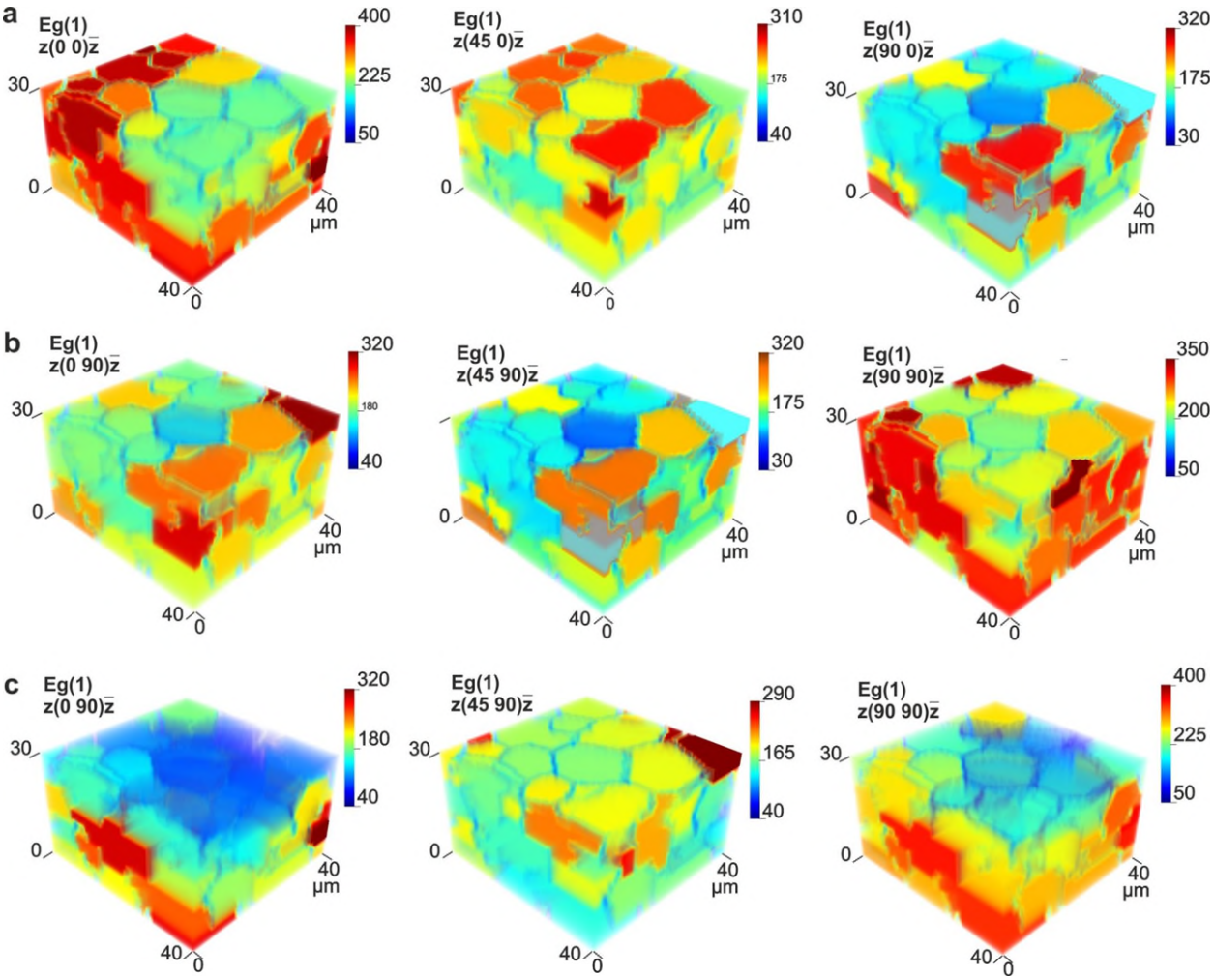

Supplementary Figure 35. Volumetric polarized Raman maps of polycrystalline sapphire for the nine polarization channels based on the Eg(5) mode. a, on-axis channels with analyzer orientation 0°, **b,** on-axis channels with analyzer orientation 90°, **c,** off-axis channels with analyzer orientation 90°. Intensity scale is in arbitrary units.

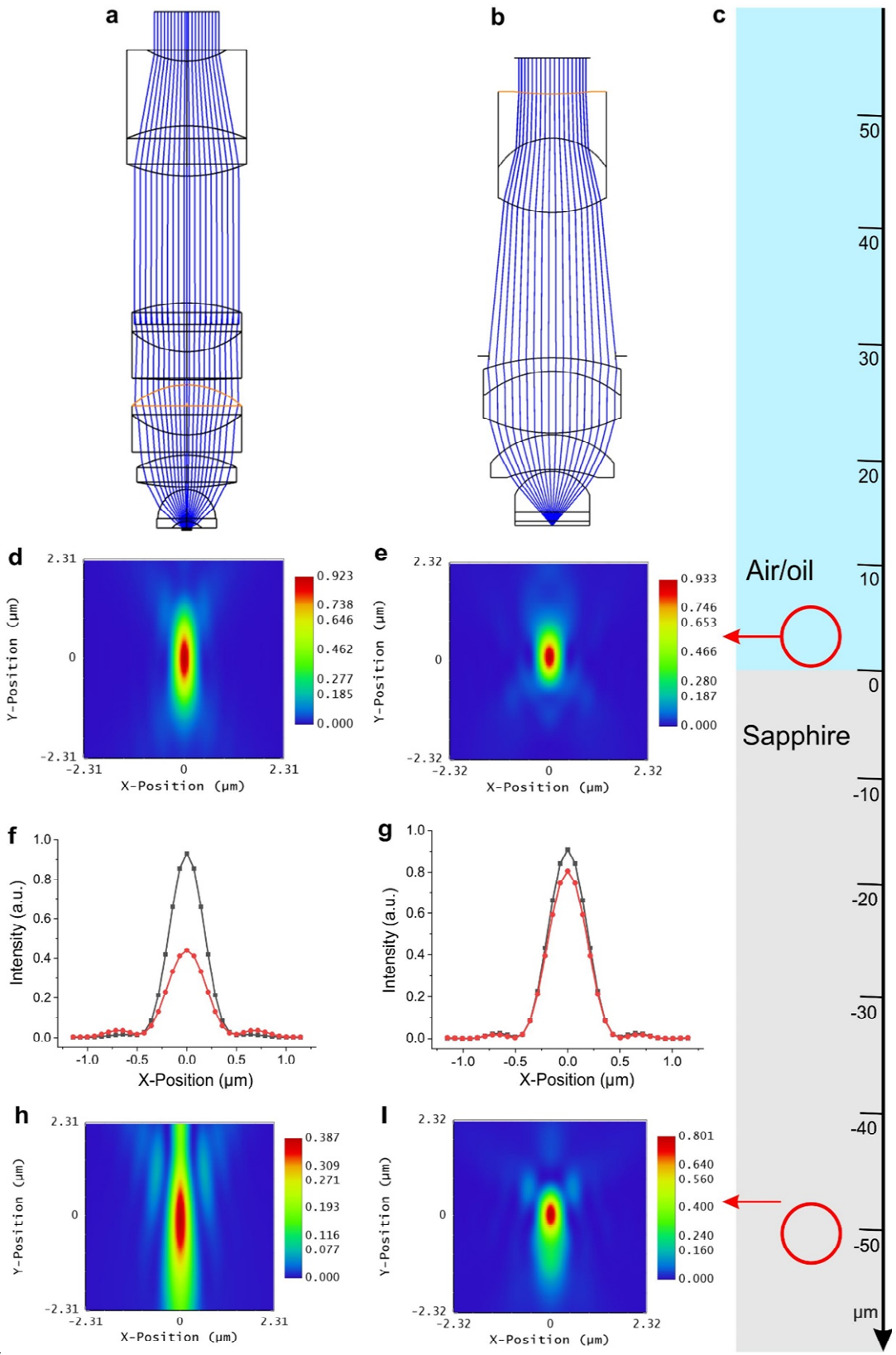

Supplementary Figure 36. Point spread function (PSF) of microscope objectives. a, an infinity-corrected, semi-apochromatic dry microscope objective (N.A.=0.85 at laser beam

diameter 6.5mm, magnification 50x, **b,** self-designed oil immersion objective for 3D measurements in Raman microscopy (NA=0.85 at laser beam diameter 8.8mm, magnification 45x), **c,** illustration of air-sapphire interface with regions of simulated PSF, **d,** axial PSF of dry objective in air, **e,** axial PSF of oil immersion objective in oil, **f,** cross sections of lateral PSF of dry objective in air (black line) and in the depth of sapphire at -50µm (red line), **g,** cross sections of lateral PSF of oil immersion objective in oil (black line) and in the depth of sapphire at -50µm (red line), **h,** axial PSF of dry objective in the depth of sapphire at -50µm, **i,** axial PSF of oil immersion objective in the depth of sapphire at -50µm.

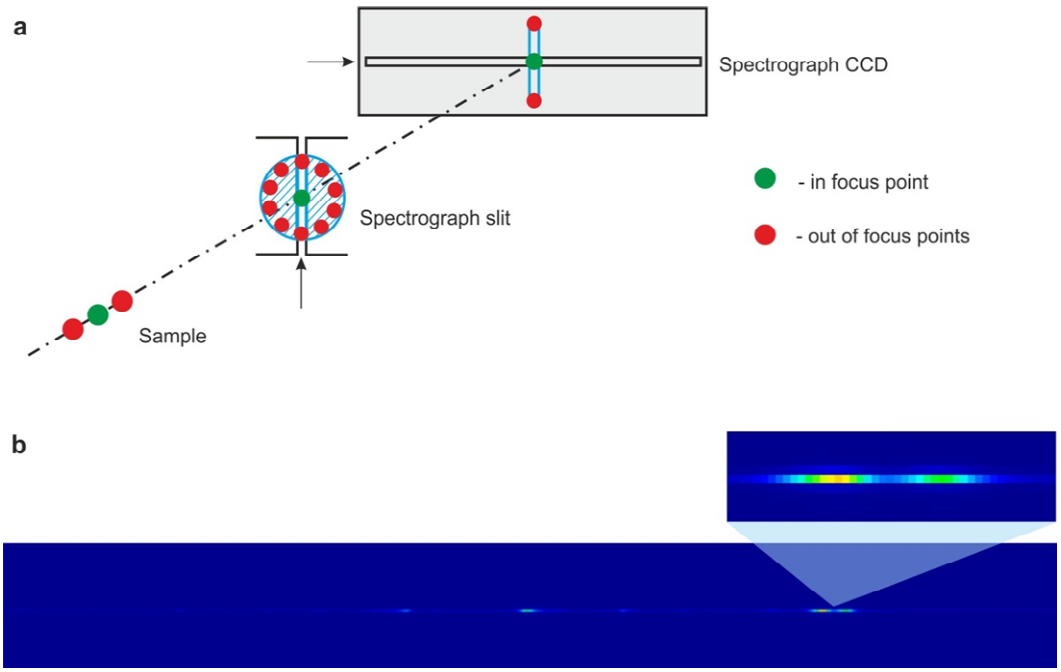

Supplementary Figure 37. Slit based confocal Raman setup. a, Slit based confocality principle used in aberration corrected Raman microscopy setup, **b,** the typical image from spectroscopic CCD Raman signal; zoomed region shows that spectrum compressed into one row on CCD sensor.

	Layers																	
Segments	1	2	3	4	5	6	7	8	9	10	11	12	13	14	15	16	17	18
1																		
2																		
3																		
4																		
5																		
6																		
7																		
8																		
9																		

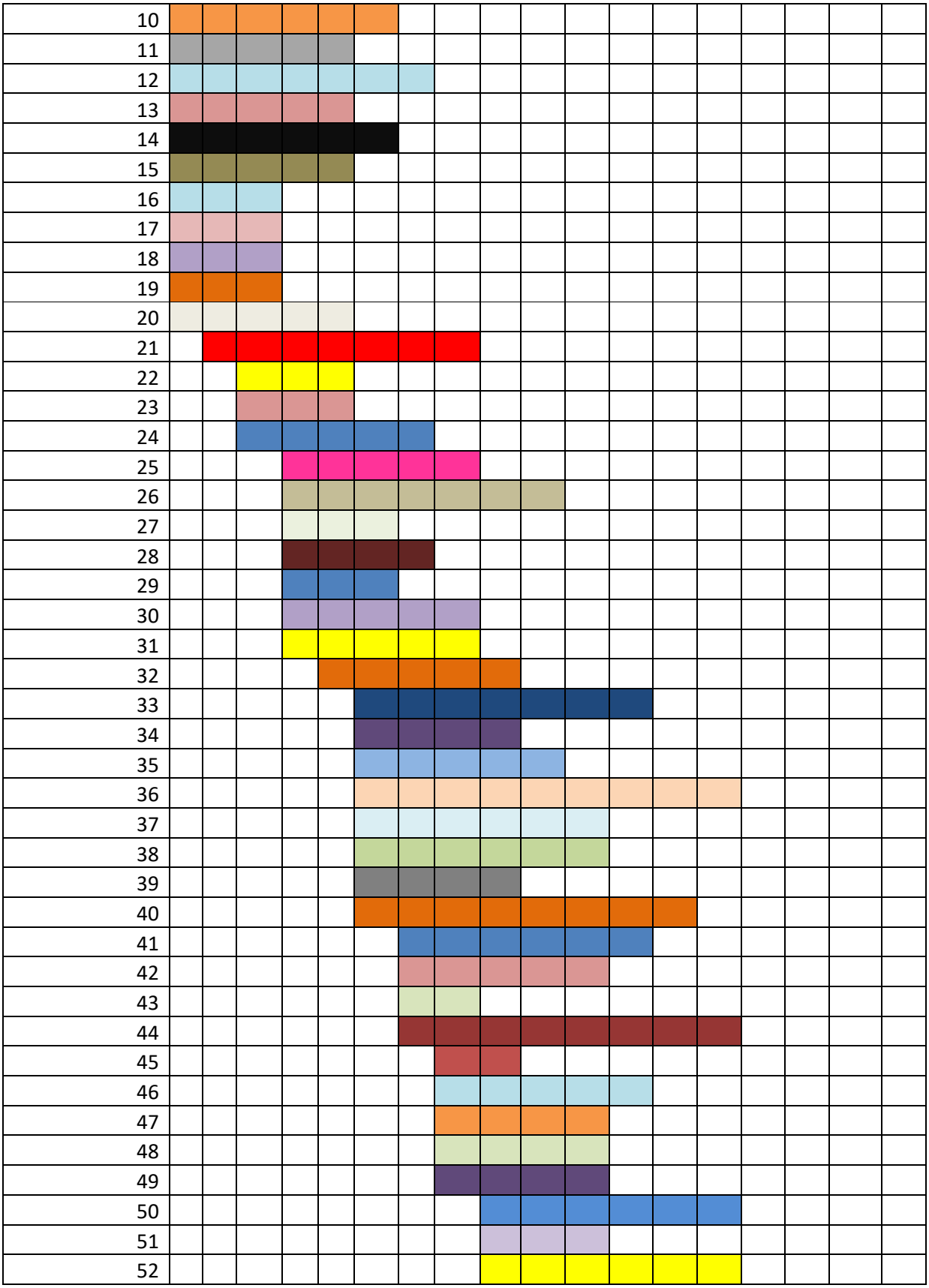
10
11
12
13
14
15
16
17
18
19
20
21
22
23
24
25
26
27
28
29
30
31
32
33
34
35
36
37
38
39
40
41
42
43
44
45
46
47
48
49
50
51
52

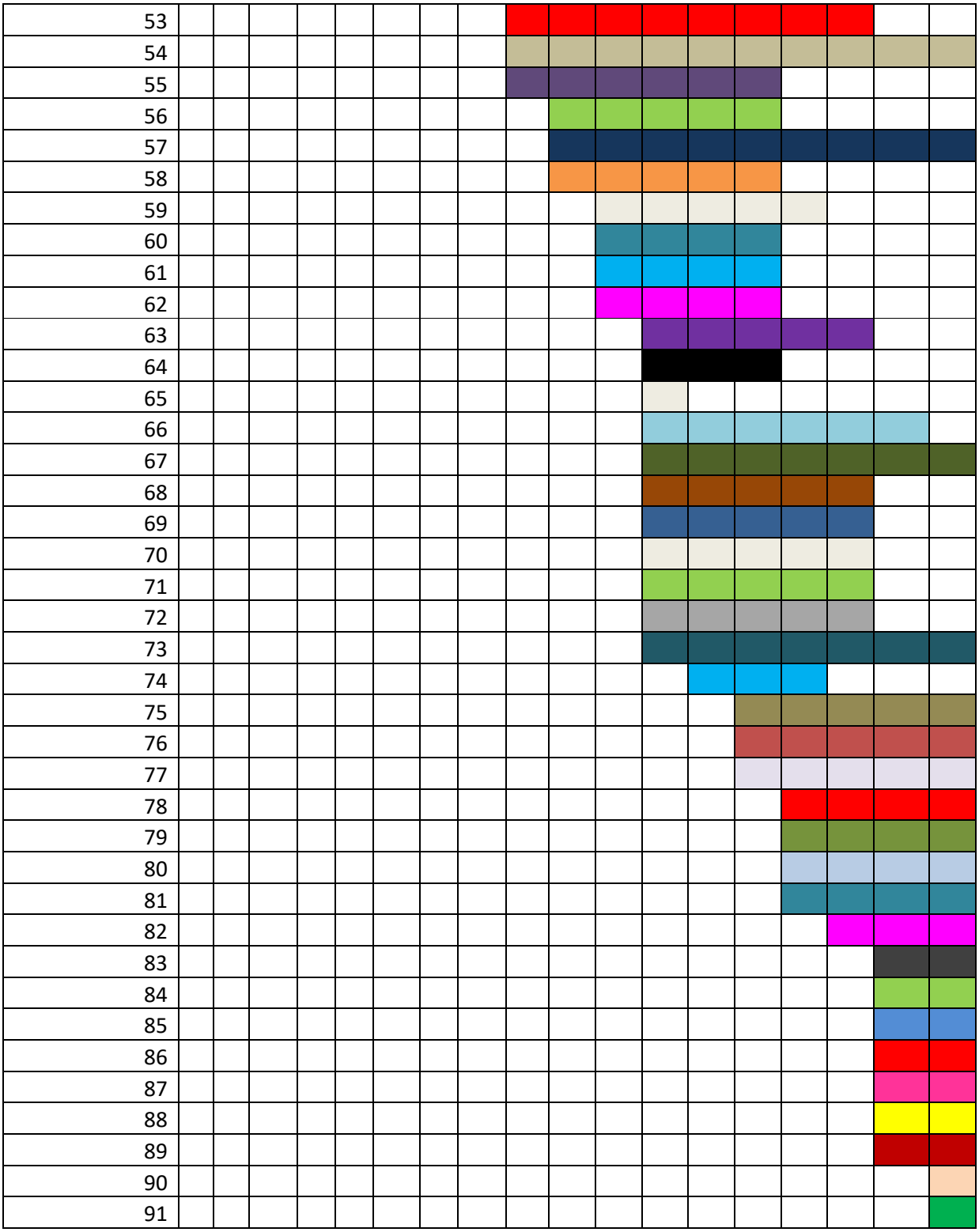

Supplementary Table 1. Sapphire segmentation results showing the propagation of domains from layer to layer in 3D map.

Supplementary References

1. Loudon, R. The Raman effect in crystals. *Adv. Phys.* **13**, 423–482 (1964).
2. Pezzotti, G. & Zhu, W. Resolving stress tensor components in space from polarized Raman spectra: Polycrystalline alumina. *Phys. Chem. Chem. Phys.* **17**, 2608–2627 (2015).
3. Kranert, C., Sturm, C., Schmidt-Grund, R. & Grundmann, M. Raman Tensor Formalism for Optically Anisotropic Crystals. *Phys. Rev. Lett.* **116**, 1–5 (2016).
4. Kranert, C., Sturm, C., Schmidt-Grund, R. & Grundmann, M. Raman tensor elements of β-Ga2O3. *Sci. Rep.* **6**, 1–9 (2016).
5. Is, W. & Analysis, P. Raman Polarization Measurements : Keeping Track of the Instrumental Components ' Behavior Raman Polarization Measurements : Keeping Track of the Instrumental Components ' Behavior Raman Polarization Measurements : Keeping Track of the Instrumental Compone. 1–9 (2018).
6. Mizoguchi, K. & Nakashima, S. I. Determination of crystallographic orientations in silicon films by Raman-microprobe polarization measurements. *J. Appl. Phys.* **65**, 2583–2590 (1989).
7. Becker, M., Scheel, H., Christiansen, S. & Strunk, H. P. Grain orientation, texture, and internal stress optically evaluated by micro-Raman spectroscopy. *J. Appl. Phys.* **101**, (2007).
8. Hielscher, R. & Schaeben, H. A novel pole figure inversion method: specification of the MTEX algorithm. *J. Appl. Crystallogr.* **41**, 1024–1037 (2008).
9. Mainprice, D., Bachmann, F., Hielscher, R. & Schaeben, H. Descriptive tools for the analysis of texture projects with large datasets using MTEX : strength, symmetry and components. *Geol. Soc. London, Spec. Publ.* **409**, 251–271 (2015).
10. Harris, R. K. *et al.* Structural Studies of the Polymorphs of Carbamazepine, Its Dihydrate, and Two Solvates. *Org. Process Res. Dev.* **9**, 902–910 (2005).
11. Strachan, C. J., Howell, S. L., Rades, T. & Gordon, K. C. A theoretical and spectroscopic study of carbamazepine polymorphs. *J. Raman Spectrosc.* **35**, 401–408 (2004).
12. Munisso, M. C., Zhu, W. & Pezzotti, G. Raman tensor analysis of sapphire single crystal and its application to define crystallographic orientation in polycrystalline alumina. *Phys. status solidi* **246**, 1893–1900 (2009).

Paper V

Where Is the Drug? Quantitative 3D Distribution Analyses of Confined Drug-Loaded Polymer Matrices

C. Mazzoni, F. Tentor, A. Antalaki, R.D. Jacobsen, J. Mortensen, R. Slipets, O. Ilchenko, S.S. Keller,

L.H. Nielsen, and A. Boisen

ACS Biomaterials Science and Engineering 5 (6). 2019

ACS Biomaterials SCIENCE & ENGINEERING
Cite This: ACS Biomater. Sci. Eng. 2019, 5, 2935−2941
Article
pubs.acs.org/journal/abseba

Where Is the Drug? Quantitative 3D Distribution Analyses of Confined Drug-Loaded Polymer Matrices

Chiara Mazzoni,*[,†] Fabio Tentor,[†] Anastasia Antalaki,[†] Rasmus D. Jacobsen,[†] Jacob Mortensen,[†] Roman Slipets,[†] Oleksii Ilchenko,[†] Stephan S. Keller,[‡] L. Hagner Nielsen,[†] and Anja Boisen*[,†]

[†]The Danish National Research Foundation and Villum Foundation's Center for Intelligent Drug Delivery and Sensing Using Microcontainers and Nanomechanics (IDUN), Department of Health Technology, Technical University of Denmark, Ørsteds Plads Building 345C, Kgs. Lyngby 2800, Denmark

[‡]The Danish National Research Foundation and Villum Foundation's Center for Intelligent Drug Delivery and Sensing Using Microcontainers and Nanomechanics (IDUN), National Centre for Nano Fabrication and Characterization, Technical University of Denmark, Ørsteds Plads Building 345B, Kgs. Lyngby 2800, Denmark

Supporting Information

ABSTRACT: To enhance oral bioavailability of poorly soluble drugs, microfabricated devices can be utilized. One example of such devices is microcontainers. These are cylindrical in shape with an inner cavity for drug loading and with only the top side open for release. Supercritical CO_2 ($scCO_2$) impregnation is an interesting technique for loading drugs into polymeric matrices in, for example, microcontainers since it avoids the use of organic solvents and is cheap. One of the main drawbacks of this technique is the unknown three-dimensional drug distribution in the polymer matrix. The aim of this study was to investigate the loading of two poorly soluble drugs, naproxen and ketoprofen, by $scCO_2$ impregnation into confined polymer matrices of different sizes. Three different sizes of microcontainers (small, medium, and large) and, thereby, different surface areas accessible for impregnation were compared. From *in vitro* studies, the amount of naproxen and ketoprofen loaded into the different microcontainers and their corresponding release profiles were seen to be similar. A custom-made Raman microscope facilitated volumetric Raman maps of an entire microcontainer filled with polyvinylpyrrolidone (PVP) and $scCO_2$ impregnated with either naproxen or ketoprofen. In all microcontainer sizes, the drugs were only detected in the top layer of the polymer matrix, explaining the observed similar release profiles. Using X-ray powder diffraction and Raman spectroscopy, the solid state form of the drugs was evaluated, showing that ketoprofen was amorphous in all microcontainer sizes. Naproxen was found not to be crystalline nor amorphous but in a less ordered configuration than the crystalline state. In conclusion, volumetric Raman mapping is a powerful technology for imaging drug distribution and drug crystallinity in polymers and allowed us to conclude that (i) $scCO_2$ impregnation depth does not depend on surface area and (ii) impregnated drugs are noncrystalline.

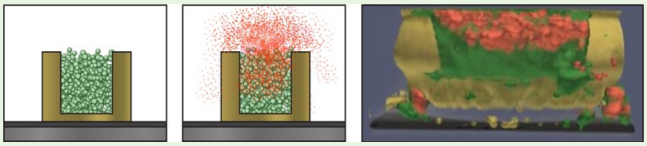

KEYWORDS: *microdevices, polymer matrix, drug distribution, poorly soluble drug, supercritical CO_2 impregnation, Raman spectroscopy*

1. INTRODUCTION

Among the different administration routes for drugs, oral delivery is preferred by patients since the drug can be self-administered leading to high compliance.[1] However, oral drug delivery is often challenging due to, for example, harsh conditions in the stomach and poor permeability over the intestinal wall.[1] Many drugs are classified as poorly water-soluble in the biopharmaceutics classification system (BCS, class II and IV).[2,3] For oral delivery of poorly soluble drugs, solubility and dissolution rate need to be improved to obtain an acceptable bioavailability. One approach for achieving this, is to convert the drug to its amorphous form.[4] Here, the long-range order in the crystal lattice is lacking and the disordered structure results in improved solubility and dissolution rate.[4,5] The disadvantage of the amorphous form is its physical and chemical instability. It can convert back to its metastable or stable counterpart during storage or dissolution.[6] There are various techniques to improve the physical stability of the amorphous form, for example, coamorphization of two drugs[7] or use of polymers as excipients.[8] Another approach for protecting the amorphous drugs is the use of microcontainers.[5,9] Microcontainers are cylindrical, polymeric microdevices with an inner cavity for drug loading and with only the top side open. Previously, confinement of the amorphous poorly soluble drug indomethacin reduced the recrystallization rate by 1.8-fold compared to unconfined bulk samples.[5] In particular, for microcontainers with cavity diameters of 174 μm, 29.0% ± 2.6% of the amorphous indomethacin crystallized

Received: April 10, 2019
Accepted: May 10, 2019
Published: May 10, 2019

DOI: 10.1021/acsbiomaterials.9b00495
ACS Biomater. Sci. Eng. 2019, 5, 2935−2941

over a period of 30 days compared to 38.3% ± 1.5% in microcontainers with diameters of 223 μm. This indicates that microcontainers with smaller diameters enhance the stability of the amorphous drug loaded inside.[5] Unconfined indomethacin crystallized within a few days. In addition to the stabilization properties, microcontainers have been used for improving oral drug delivery by protecting the drug from the harsh gastric environment and providing a release in the small intestine.[10−12] Furthermore, it has been demonstrated that microcontainers adhere to the intestinal mucus layer leading to higher relative oral bioavailability in rats of model drugs such as ketoprofen and furosemide compared to controls.[13,14]

In spite of the advantages of utilizing microdevices for oral drug delivery, loading drugs into the small cavities can be challenging since all of the well-known techniques for preparing oral formulations, such as tableting, cannot be used. Supercritical CO_2 ($scCO_2$) impregnation is one of the techniques that can be used for loading drugs into polymer-filled microcontainers. The critical point of CO_2 is 31.1 °C and 73.8 bar, and due to those mild conditions, this technique is suitable for drug loading. In addition, it can be used in combination with various polymers.[15,16] It has previously been demonstrated that the hydrophilic polymer polyvinylpyrrolidone (PVP) can be loaded into microcontainers as a polymer matrix and impregnated using $scCO_2$ with the drug ketoprofen.[17,18] It was found that ketoprofen was in its amorphous form after impregnation in the PVP matrix inside the microcontainers.[14] However, the influence of the size of the confined polymer volumes loaded by supercritical impregnation has never been investigated. One of the main challenges for systematic studies of drug loading with this technique has been the unknown three-dimensional (3D) drug distribution in the polymer matrix after CO_2 impregnation. Therefore, it has not been possible to understand the influence of the parameters on the release profiles and the drug−polymer interactions.[16,17,19]

In the literature, the distribution of impregnated or encapsulated material has been studied with various techniques. Polymeric membranes have been examined with energy dispersive X-ray analyses, obtaining a two-dimensional map,[19] and this technique has also been successfully used for 3D mapping of nanoparticles.[20] Dispersive X-ray absorption spectroscopy (μED-XAS) tomography has been utilized and was able to resolve both 2D and 3D spatial distribution of chemical species from different iron mineral standards.[21] Alternatively, Raman spectroscopy has been used to evaluate the distribution of a drug inside a 3D printed tablet.[22] Previously, a 2D map of a cross section of tablets using Raman spectroscopy has been obtained, revealing the distribution of three different components in an area of 4 mm × 4 mm.[23] Raman spectroscopy has successfully been used as a quantification technique in the case of inkjet-printed pharmaceuticals requiring, however, the sectioning of the sample prior to analyses in order to measure a cross section.[24] Cross sectional mapping with Raman spectroscopy is a destructive method, and in case of a confined polymer matrix (i.e., for microcontainers), this application is not possible. Furthermore, for investigations with Raman spectroscopy, the polymer and drug normally have a relatively low transparency under laser excitation. For reaching an acceptable Raman signal at the bottom of samples as deep as, for example, a microcontainer reservoir, a highly sensitive method for confocal Raman microscopy has been developed.

The aim of this study was to investigate the loading of two BCS class II drugs, naproxen and ketoprofen, using $scCO_2$ impregnation into confined polymer matrices of different sizes. For this purpose, three different sizes of microcontainers (small, medium, and large), and thereby different surface areas accessible for impregnation, were compared. Furthermore, the quantity and solid state form of ketoprofen and naproxen loaded into the microcontainers were evaluated. Finally, the 3D distribution of the drugs in 225 μm deep polymer matrices was analyzed by confocal Raman microscopy.

2. EXPERIMENTAL SECTION

2.1. Materials. Silicon (Si) wafers (4-in, b100N n-type) were provided by Okmetic (Vantaa, Finland). SU-8 2075 and SU-8 developer were purchased from Microresist Technology GmbH (Berlin, Germany). Polyvinylpyrrolidone (PVP) (Molecular weight of 10 000 Da), ketoprofen powder (≥98%, racemate) and phosphate buffered saline (PBS) were obtained from Sigma-Aldrich (St. Louis, MO, USA). Naproxen was purchased from Fagron (Newcastle upon Tyne, England). Deionized water (18.2 mΩ) was acquired from Merck KGaA (Darmstadt, Germany).

2.2. Methods. *2.2.1. Fabrication of Microcontainers.* Squared chips of microcontainers with dimensions of 12.8 × 12.8 mm^2 were fabricated on Si wafers in the epoxy-based photoresist SU-8 using a similar procedure as described previously.[5] Three different sizes of microcontainers were produced having three different cavity diameters (small, medium, and large) and the same cavity height. The number of microcontainers per chip for the three different sizes was chosen to keep the total polymer surface exposed to the $scCO_2$ per chip constant and thereby also the total polymer volume constant. The dimensions of the microcontainers were measured using an Alpha-Step IQ Stylus Profilometer (KLA-Tencor Corporation, Milpitas, USA) and an optical microscope.

2.2.2. Loading of Naproxen and Ketoprofen into Microcontainers Using Supercritical CO_2 Impregnation. The microcontainers on Si chips were manually filled with PVP powder. Excess powder between the microcontainers was blown away using an air gun in a similar setup as described previously.[14] One chip of each size (small, medium, and large) was placed within a supercritical CO_2 chamber, together with 4.8 ± 0.1 mg (n = 3) of ketoprofen powder or 6.0 ± 0.03 mg (n = 3) of naproxen. The impregnation with ketoprofen was conducted by bringing CO_2 to its supercritical state at 120 bar and 45 °C keeping it under stirring for 1 h. The impregnation with naproxen was performed by bringing CO_2 to 100 bar and 40 °C. These parameters were chosen to have a solubility in the supercritical CO_2 of 0.06 g/L for both drugs.[25,26] The pressurization and depressurization rates were 3.9 and 2.5 bar/min, respectively, for both drugs. The chips with microcontainers were weighed before and after filling with PVP to determine the amount of polymer loaded into the microcontainers. A tabletop scanning electron microscope (SEM) TM3030Plus (Hitachi High-Technologies, Tokyo, Japan) was used to visualize the microcontainers after filling with PVP and after the impregnation process.

2.2.3. In Vitro Release of Ketoprofen or Naproxen from Microcontainers. For determining the release of ketoprofen or naproxen over time, a μ-Diss profiler (pION Inc., Woburn, MA), equipped with *in situ* UV probes with a path length of 10 mm for ketoprofen and 5 mm for naproxen was used. The release studies were performed in PBS at pH 6.5 for 120 min. Standard curves of either ketoprofen or naproxen were obtained before each release experiment. In order to prepare the standard curves, aliquots of a stock solution of ketoprofen (5 mg/mL in ethanol) or naproxen (3 mg/mL in ethanol) were added to known volumes of PBS, and the absorbance was assessed in a wavelength range of 250−260 nm for ketoprofen and at a wavelength of 230 nm for naproxen.

For release experiments, the chips with drug-loaded microcontainers were attached to cylindrical magnets and placed inside glass vials. Ten milliliters of PBS buffer was added to the vials immediately before starting an experiment. All the release studies

DOI: 10.1021/acsbiomaterials.9b00495
ACS Biomater. Sci. Eng. 2019, 5, 2935−2941

were run at 37 °C stirring the chips at 100 rpm. The experiments were performed in triplicate for each drug and for each size of microcontainers, the data are presented as mean (normalized by the quantity of PVP filled) ± SD.

2.2.4. Three-Dimensional Distribution of Drugs in Microcontainers. Volumetric Raman microscopy was used to evaluate the distribution of ketoprofen or naproxen in the microcontainers. The microscope collected Raman spectra in the range of 350−2400 cm^{-1} with a spectral resolution of 2.5 cm^{-1} under the excitation of a 785 nm laser. The laser power was 35 mW, and the diffraction limited spot size was equal to 1.7 μm with the use of a 100x/0.75 HD DIC Zeiss microscope objective. The chip of microcontainers was placed on the surface of a custom-made Peltier stage and kept at 8 °C during Raman measurements. These Raman spectra were studied performing a non-negative least-squares analysis to obtain quantitative chemical response, visualized as voxel based 3D images.[27,28]

2.2.5. Solid State Analyses of the Drugs Loaded into Microcontainers. X-ray powder diffraction (XRPD) was used to determine the solid state form of ketoprofen or naproxen in the microcontainers. An X'Pert PRO X-ray diffractometer (PANalytical, Almelo, The Netherlands, MPD PW3040/60 XRD; Cu KR anode, λ = 1.541 Å, 45 kV, 40 mA) was utilized. A starting angle of 5° 2θ and an end angle of 28° 2θ were employed for the scans with a scan speed of 0.67335° 2θ/min and a step size of 0.0262606° 2θ. Data were collected using X'Pert Data Collector software (PANalytical B.V.). The diffractograms of naproxen or ketoprofen loaded in the microcontainers were compared to the pure crystalline drugs. In addition, Raman microscopy was used to investigate the solid state form of the drugs. The spectra measured from the naproxen or ketoprofen loaded into the microcontainers were collected as described in section 2.2.4. For the spectra of crystalline and amorphous ketoprofen, naproxen, and PVP, the laser power was 35 mW and the exposure time was 2 s. The amorphous ketoprofen was prepared by melting the crystalline ketoprofen powder at 98 °C on a heating plate followed by immediate measurements of the sample.

2.2.6. Statistics. All data are expressed as mean ± standard deviation (SD). Statistical analyses were carried out, where relevant, using Student t tests (GraphPad Prism, La Jolla, CA, USA, version 7.04). P values below 5% ($p < 0.05$) were considered statistically significant.

3. RESULTS AND DISCUSSION

3.1. Fabrication of Microcontainers. Cylindrical microcontainers with three different sizes were successfully fabricated (Table 1 and Figure 1). The cavity depth of the microcontainers with the different sizes was kept constant at 225 μm. The number of microcontainers per chip was chosen to keep the total polymer volume and the total surface area exposed to the supercritical CO_2 similar for the different sizes (Table 1). Due to this, it was possible to compare the influence of the microcontainer size on quantity and distribution of the poorly soluble model drugs loaded using supercritical CO_2 impregnation.

Table 1. Numbers Showing the Dimensions of the SU-8 Microcontainers, Amount of Microcontainers per Chip, and Total Polymer Surface Area per Chip[a]

sample	internal microcontainer diameter [μm]	number of microcontainers per chip	total polymer surface area exposed to $scCO_2$ per chip [mm^2]
small	97 ± 6	1024	31 ± 4
medium	191 ± 9	256	30 ± 3
large	413 ± 5	64	34 ± 1

[a]The data represents mean ± SD in 8 replicates.

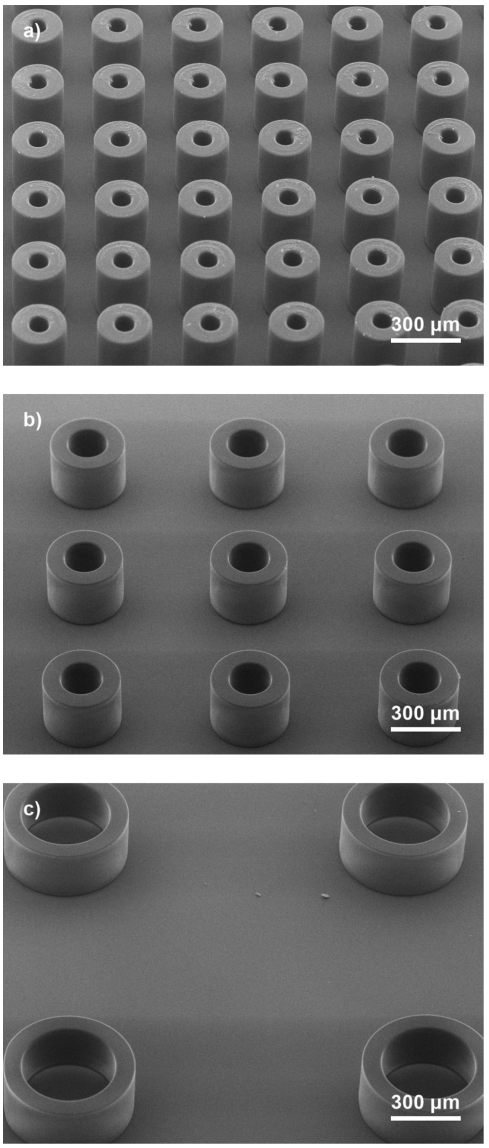

Figure 1. SEM images of SU-8 microcontainers in the size of (a) small, (b) medium, and (c) large having an internal diameter of 97 ± 6, 191 ± 9, and 413 ± 5 μm, respectively.

3.2. Loading of Ketoprofen or Naproxen into Microcontainers Using Supercritical CO_2 Impregnation. Every chip was manually filled with approximately 0.9 mg of PVP powder (Figure 2a), the amount varied slightly for the different sizes (Table 2). Following filling with PVP, one chip per size was then simultaneously loaded with ketoprofen or naproxen. An SEM image of the medium size microcontainers after $scCO_2$ impregnation with ketoprofen can be seen in Figure 2b. In a previous study, the amount of PVP filled per chip was higher.[14] This is because even if the medium size microcontainers have similar dimensions to thos used in the previously reported study, the number of microcontainers is here reduced from 625 to 256.

3.3. *In Vitro* Release of Ketoprofen or Naproxen from Microcontainers. The quantity of ketoprofen or naproxen loaded into the microcontainers with different sizes was evaluated in order to assess if there was an influence of the dimension of the surface exposed to $scCO_2$. The quantity of the loaded ketoprofen or naproxen in small, medium, or large

DOI: 10.1021/acsbiomaterials.9b00495
ACS Biomater. Sci. Eng. 2019, 5, 2935−2941

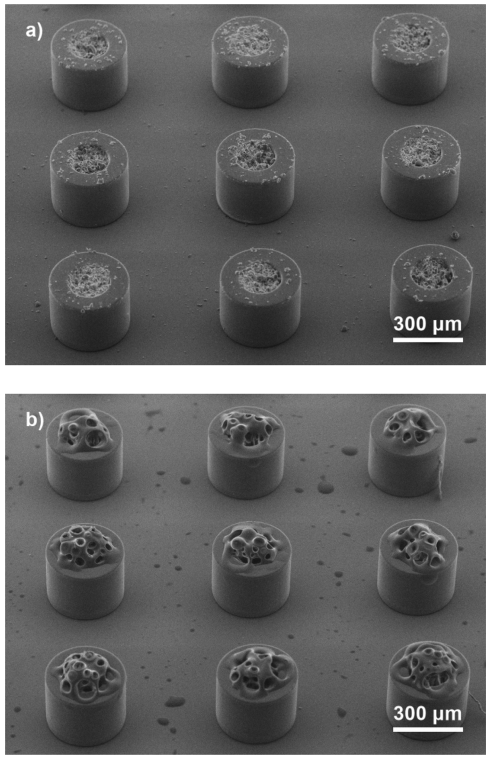

Figure 2. SEM images of medium sized microcontainers (a) filled with PVP and (b) loaded with ketoprofen using $scCO_2$ impregnation. These images are representative examples of the PVP filling and the drug loading with the supercritical impregnation method.

Table 2. Amount of Ketoprofen or Naproxen Loaded in the Three Different Sizes of Microcontainers[a]

	amount of PVP filled per chip [mg]	total amount of ketoprofen loaded per chip [μg]	total amount of naproxen loaded per chip [μg]
small	0.94 ± 0.36	128.3 ± 65.9	89.7 ± 40.95
medium	0.82 ± 0.1	91.3 ± 20.1	160.54 ± 42.8
large	1.03 ± 0.17	86.1 ± 28.7	128.23 ± 26.50

[a]The data represents mean ± SD in triplicates.

microcontainers was obtained from the release studies (Table 2 and Figure 3). The release profiles of the small, medium, and large microcontainers loaded with ketoprofen showed similar release profiles without any significant differences (Figure 3a). The same behavior was observed in the case of naproxen (Figure 3b).

The total amount of ketoprofen loaded in the small size microcontainers compared to the medium and large microcontainers was not significantly different (p-value 0.4049 and 0.3667, respectively). No significant difference was observed between the loaded quantity of ketoprofen in the medium and in the large microcontainers (p-value 0.8098). The similarities observed for ketoprofen were found for the total amount of loaded naproxen. In fact, the amount of naproxen in the small size microcontainer was not statistically different from the amount of drug in the medium or large microcontainers (p-value 0.1071 and 0.2431, respectively). Comparing the medium with the large size microcontainers, the total amount of loaded naproxen also did not result in statistically different drug loadings (p-value = 0.3286).

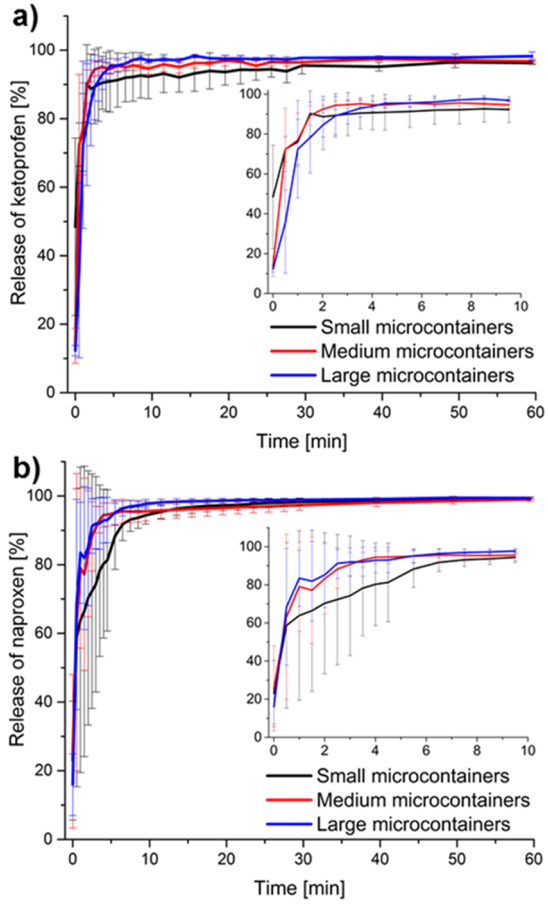

Figure 3. Release profiles of (a) ketoprofen and b) naproxen from small, medium, and large microcontainers performed on a μ-Diss profiler in PBS at pH 6.5. The inserts represent the same profiles zoomed in on the first 10 min. The graphs represent mean ± SD in triplicate.

Since the solubility of the two drugs in the $scCO_2$ was set to be the same, the release experiments allowed for comparison of loading the two poorly water-soluble drugs into the microcontainers with three different sizes. Within the first 10 min, 90% of ketoprofen or naproxen was released (Figure 3) from all sizes of microcontainers even though the release from small microcontainers loaded with naproxen showed a larger variability. No statistical difference in the loaded amount of ketoprofen or naproxen was discernible, independent of the size of the microcontainers. Comparing the loaded amount of ketoprofen and naproxen in small microcontainer sizes, the p-value was equal to 0.4374. For medium and large microcontainer sizes, the p-values corresponded to 0.0642 and 0.1351, respectively.

Consequently, there was no difference in loading a BCS class II drug such as ketoprofen or naproxen in a polymer matrix (PVP) having smaller or larger surfaces exposed to the $scCO_2$. This suggests that the size of the microcontainer opening has no influence on the quantity of drug loaded into the microcontainers. Furthermore, both BCS class II drugs were released with similar kinetics from the different sizes of microcontainers.

3.4. Three-Dimensional Distribution of Drugs in Microcontainers. It was possible to obtain 3D maps of polymer and drug-loaded microcontainers down to a depth of 225 μm (the entire height of the microcontainer) using our

DOI: 10.1021/acsbiomaterials.9b00495
ACS Biomater. Sci. Eng. 2019, 5, 2935−2941

custom-made Raman microscopy technique. To avoid heating of the sample, due to relatively high absorption of the laser, the temperature was kept constant at 8 °C. To distinguish the various materials (PVP, ketoprofen/naproxen, SU-8, or Si) in the samples, a chemical decomposition was performed on the spectra (Figure 4). In Figure 4, the same microcontainer 3D map reconstruction is shown in three different perspectives: an overview, a cross section view and a top view.

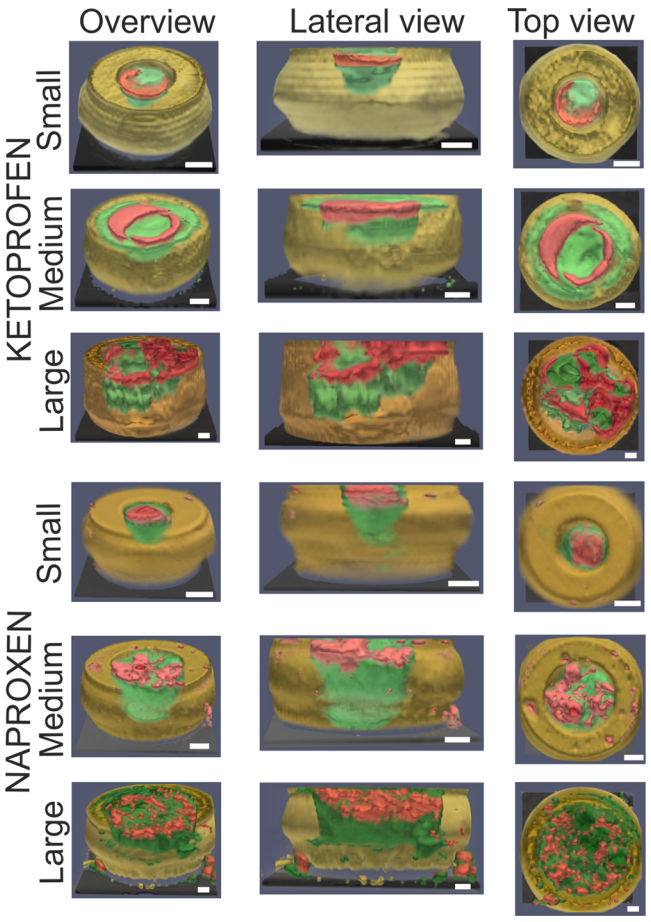

Figure 4. Volumetric Raman maps of ketoprofen or naproxen loaded into the microcontainers. The overview, the lateral view, and the top view can be seen from left to right for each of the different sizes of microcontainers: small, medium, and large from top to bottom. Ketoprofen or naproxen are represented in red, PVP in green, SU-8 in yellow, and Si in black. The scale bars correspond to 50 μm.

For all sizes of microcontainers loaded with either ketoprofen or naproxen, the drug was mainly impregnated in the top layers of the polymer matrix confined within the microcontainer walls. The results obtained in the *in vitro* release studies showed that both drugs reached 90% release within 10 min. The fast release could be explained by the fact that the drugs were mostly in the top part of the polymer matrix and not deep inside the microcontainer cavity. It is important to notice that the drug was distributed with the same morphology as PVP. It can therefore be speculated that, in a more porous polymer matrix, the drug could have penetrated deeper during the supercritical impregnation. In the top view of the microcontainers, it is possible to notice that both drugs were homogeneously distributed on the PVP. Furthermore, ketoprofen and naproxen were absent at the edge of the microcontainers meaning that both drugs were preferentially deposited in the PVP matrix and not in microcontainer material, SU-8. This technique can be useful to analyze polymer matrices for drug delivery in tissue engineering since the drug depth in the polymer matrix affects the release kinetics of the drug.[29] A pharmaceutical application, in which this technique can also be successfully used, is the characterization of tablet coatings as the presence of holes or different thicknesses can change the solubility kinetics of the tablet.[30]

3.5. Solid State Analyses of the Drugs Loaded into Microcontainers. It has previously been shown that loading ketoprofen in a PVP matrix led to its conversion into its amorphous form.[14,18] In Figure 5a, the diffractograms from

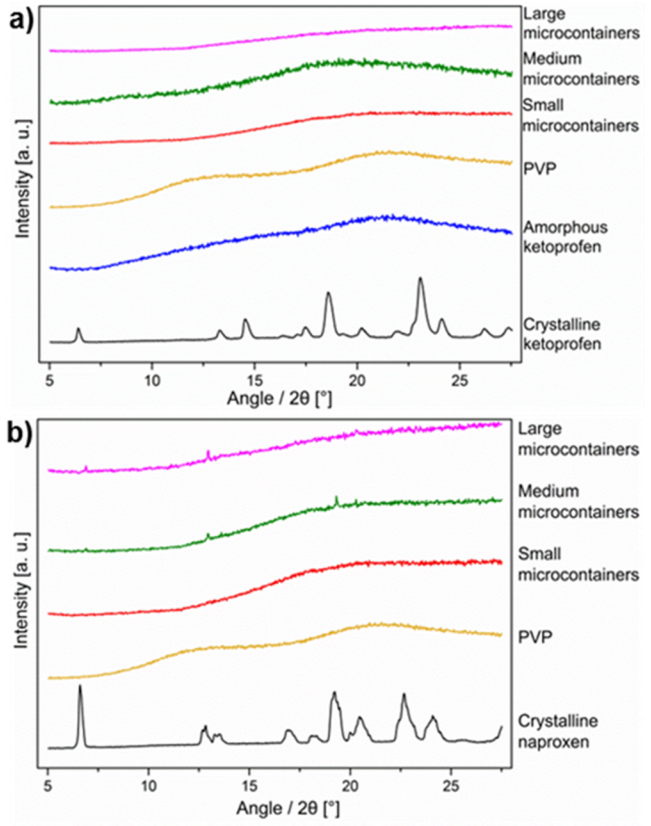

Figure 5. (a) XRPD diffractograms of crystalline and amorphous ketoprofen and PVP small, medium, and large microcontainers filled with PVP followed by impregnation with ketoprofen. (b) XRPD diffractograms of crystalline naproxen and PVP small, medium, and large microcontainers filled with PVP followed by impregnation with naproxen.

XRPD of the small, medium, and large size microcontainers loaded with ketoprofen showed a halo, indicative of an amorphous form. This indicated that the loaded ketoprofen was amorphous. In the case of naproxen loaded into the PVP matrix in the different sizes of microcontainer, the diffractograms also showed a halo for the small microcontainers (Figure 5b). For the medium and large microcontainers, the halo still appeared but with a few peaks comparable to those of the crystalline diffractogram of naproxen. Probably, a low crystallization of the drug occurred in the medium and large microcontainers. In the literature, studies have showed that when naproxen has been combined with excipients or other

DOI: 10.1021/acsbiomaterials.9b00495
ACS Biomater. Sci. Eng. 2019, 5, 2935−2941

drugs, a stable amorphous form could be obtained[6,31] despite the high tendency of naproxen to recrystallize.[32] In particular, Liu et al. showed that naproxen was amorphous even after 4 months when it was thermally treated and combined with PVP.[6] A connection between the microcontainer size and the stability of the amorphous form of naproxen may therefore exist. This confirms what has previously been shown: smaller sizes of microcontainers prolong the stability of the amorphous form of indomethacin (a BCS class II drug).[5]

The results obtained by means of XRPD were confirmed by Raman spectroscopy for both drugs (Figure 6). The spectra from the microcontainers loaded with ketoprofen were similar to an amorphous ketoprofen spectrum, confirming that ketoprofen is amorphous when loaded in PVP matrices by $scCO_2$ impregnation (Figure 6a).[14] Due to the instability of naproxen, it was not possible to obtain a Raman spectrum of its amorphous form. Therefore, the peak shifts were analyzed (Figure 6b). In particular, the peaks at 1626, 1390, and 740 cm^{-1} in the crystalline naproxen spectrum are shifted to 1630–1632, 1387–1389, and 742 cm^{-1} in the spectra corresponding to microcontainers loaded with naproxen meaning that naproxen loaded in the microcontainers is not in its crystalline form. The Raman signal from large microcontainers loaded with naproxen, at the wavenumber of 740 cm^{-1}, showed a larger peak shift compared to the other sizes of microcontainers (Figure 6b, zoom-in). This might be because the Raman spectra were acquired from a random spot within a microcontainer in which also the contribution from other materials might be measured. Previously, the same peak shifts have been considered, together with other techniques, to show the amorphous state of naproxen when comilled with cimetidine.[33]

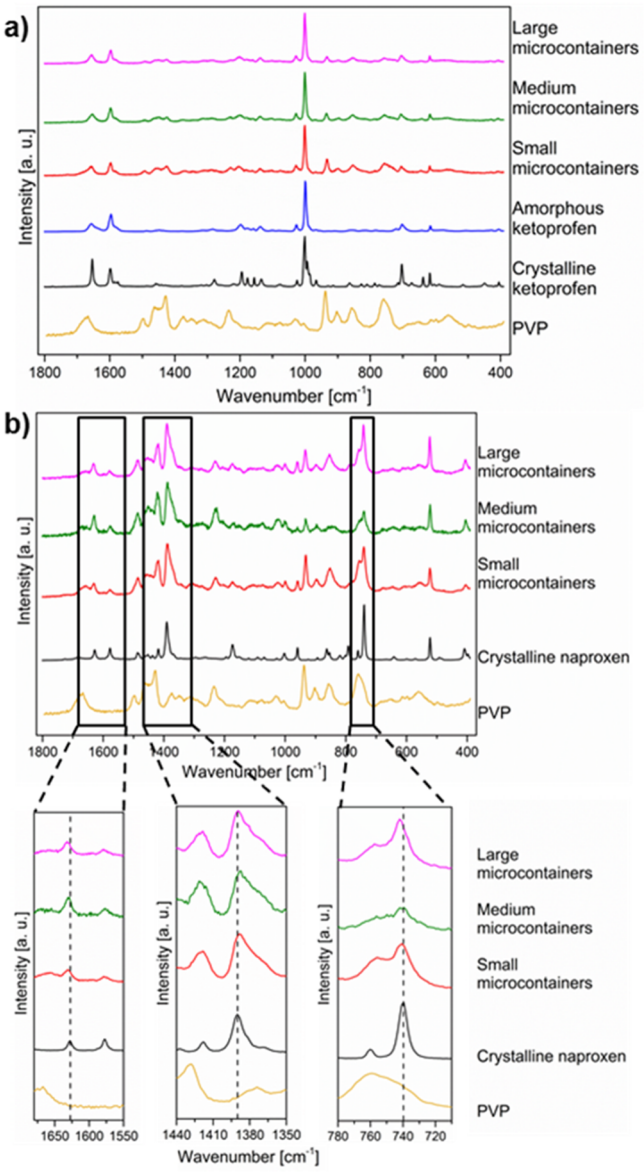

Figure 6. (a) Raman spectra of PVP and crystalline and amorphous ketoprofen small, medium, and large microcontainers filled with PVP followed by impregnation with ketoprofen. (b) Raman spectra of PVP and crystalline naproxen small, medium, and large microcontainers filled with PVP followed by impregnation with naproxen. The zoom-in areas show the peak shifts in naproxen loaded in microcontainers compared to its crystalline form.

4. CONCLUSIONS

In this study, the influence of the surface exposed to $scCO_2$ was evaluated for two poorly water-soluble drugs loaded in a PVP polymer matrix confined in microcontainers. The release studies showed that the amount of loaded naproxen or ketoprofen was the same, when the total surface area was kept constant, and the release profiles were similar, 90% of the drug being released within 10 min. For microcontainers of different sizes, the loaded amount of drug nicely correlated with the surface area of the PVP matrix exposed to supercritical CO_2 during impregnation. To evaluate the 3D distribution of the drug in the polymer matrix in the microcontainers, a custom-made Raman microscope allowed obtaining volumetric Raman maps of the complete microcontainer volume. In the small, medium, and large microcontainers, ketoprofen or naproxen was impregnated in the top of the polymer matrix, explaining the fast release observed in the release studies. Moreover, the solid state form of the drugs was evaluated, showing that ketoprofen was amorphous in all microcontainer sizes and naproxen, despite its instability, was found only to be partly crystalline.

■ ASSOCIATED CONTENT

Supporting Information

The Supporting Information is available free of charge on the ACS Publications website at DOI: 10.1021/acsbiomaterials.9b00495.

SEM images of small and large microcontainers filled with PVP and SEM images of the different sizes of microcontainers loaded by $scCO_2$ impregnation with either ketoprofen or naproxen (PDF)

■ AUTHOR INFORMATION

Corresponding Authors

*E-mail: chimaz@dtu.dk.

*E-mail: anja.boisen@dtu.dk.

ORCID

Chiara Mazzoni: 0000-0002-0988-3108

Fabio Tentor: 0000-0002-5207-0508

Notes

The authors declare no competing financial interest.

DOI: 10.1021/acsbiomaterials.9b00495
ACS Biomater. Sci. Eng. 2019, 5, 2935–2941

■ ACKNOWLEDGMENTS

The authors would like to acknowledge the Danish National Research Foundation (DNRF122) and Villum Fonden (Grant No. 9301) for Intelligent Drug Delivery and Sensing Using Microcontainers and Nanomechanics (IDUN). Nanna Bild, DTU Nanotech, is acknowledged for the drawings of the graphical abstract.

■ REFERENCES

(1) Tibbitt, M. W.; Dahlman, J. E.; Langer, R. Emerging Frontiers in Drug Delivery. *J. Am. Chem. Soc.* **2016**, *138* (3), 704−717.
(2) Amidon, G. L.; Lennernäs, H.; Shah, V. P.; Crison, J. R. A Theoretical Basis for a Biopharmaceutic Drug Classification: The Correlation of in Vitro Drug Product Dissolution and in Vivo Bioavailability. *Pharm. Res.* **1995**, *12* (3), 413−420.
(3) Davis, M.; Walker, G. Recent Strategies in Spray Drying for the Enhanced Bioavailability of Poorly Water-Soluble Drugs. *J. Controlled Release* **2018**, *269*, 110−127.
(4) Grohganz, H.; Priemel, P. A.; Löbmann, K.; Nielsen, L. H.; Laitinen, R.; Müllertz, A.; Van den Mooter, G.; Rades, T. Refining Stability and Dissolution Rate of Amorphous Drug Formulations. *Expert Opin. Drug Delivery* **2014**, *11* (6), 977−989.
(5) Nielsen, L. H.; Keller, S. S.; Gordon, K. C.; Boisen, A.; Rades, T.; Müllertz, A. Spatial Confinement Can Lead to Increased Stability of Amorphous Indomethacin. *Eur. J. Pharm. Biopharm.* **2012**, *81* (2), 418−425.
(6) Liu, X.; Zhou, L.; Zhang, F. Reactive Melt Extrusion To Improve the Dissolution Performance and Physical Stability of Naproxen Amorphous Solid Dispersions. *Mol. Pharmaceutics* **2017**, *14* (3), 658−673.
(7) Petry, I.; Löbmann, K.; Grohganz, H.; Rades, T.; Leopold, C. S. Undesired Co-Amorphisation of Indomethacin and Arginine during Combined Storage at High Humidity Conditions. *Int. J. Pharm.* **2018**, *544* (1), 172−180.
(8) Ting, J. M.; Porter, W. W.; Mecca, J. M.; Bates, F. S.; Reineke, T. M. Advances in Polymer Design for Enhancing Oral Drug Solubility and Delivery. *Bioconjugate Chem.* **2018**, *29* (4), 939−952.
(9) Nielsen, L. H.; Keller, S. S.; Boisen, A.; Müllertz, A.; Rades, T. A Slow Cooling Rate of Indomethacin Melt Spatially Confined in Microcontainers Increases the Physical Stability of the Amorphous Drug without Influencing Its Biorelevant Dissolution Behaviour. *Drug Delivery Transl. Res.* **2014**, *4* (3), 268−274.
(10) Fox, C. B.; Cao, Y.; Nemeth, C. L.; Chirra, H. D.; Chevalier, R. W.; Xu, A. M.; Melosh, N. A.; Desai, T. A. Fabrication of Sealed Nanostraw Microdevices for Oral Drug Delivery. *ACS Nano* **2016**, *10* (6), 5873−5881.
(11) Fox, C. B.; Nemeth, C. L.; Chevalier, R. W.; Cantlon, J.; Bogdanoff, D. B.; Hsiao, J. C.; Desai, T. A. Picoliter-Volume Inkjet Printing into Planar Microdevice Reservoirs for Low-Waste, High-Capacity Drug Loading. *Bioeng. Transl. Med.* **2017**, *2* (1), 9−16.
(12) Nielsen, L. H.; Nagstrup, J.; Gordon, S.; Keller, S. S.; Østergaard, J.; Rades, T.; Müllertz, A.; Boisen, A. PH-Triggered Drug Release from Biodegradable Microwells for Oral Drug Delivery. *Biomed. Microdevices* **2015**, *17* (3), 55.
(13) Nielsen, L. H.; Melero, A.; Keller, S. S.; Jacobsen, J.; Garrigues, T.; Rades, T.; Müllertz, A.; Boisen, A. Polymeric Microcontainers Improve Oral Bioavailability of Furosemide. *Int. J. Pharm.* **2016**, *504* (1−2), 98−109.
(14) Mazzoni, C.; Tentor, F.; Strindberg, S. A.; Nielsen, L. H.; Keller, S. S.; Alstrøm, T. S.; Gundlach, C.; Müllertz, A.; Marizza, P.; Boisen, A. From Concept to in Vivo Testing: Microcontainers for Oral Drug Delivery. *J. Controlled Release* **2017**, *268*, 343−351.
(15) Kikic, I.; Vecchione, F. Supercritical Impregnation of Polymers. *Curr. Opin. Solid State Mater. Sci.* **2003**, *7* (4−5), 399−405.
(16) Champeau, M.; Thomassin, J.-M.; Tassaing, T.; Jérôme, C. Drug Loading of Polymer Implants by Supercritical CO2 Assisted Impregnation: A Review. *J. Controlled Release* **2015**, *209*, 248−259.
(17) Marizza, P.; Pontoni, L.; Rindzevicius, T.; Alopaeus, J. F.; Su, K.; Zeitler, J. A.; Keller, S. S.; Kikic, I.; Moneghini, M.; De Zordi, N.; et al. Supercritical Impregnation of Polymer Matrices Spatially Confined in Microcontainers for Oral Drug Delivery: Effect of Temperature, Pressure and Time. *J. Supercrit. Fluids* **2016**, *107*, 145−152.
(18) Marizza, P.; Keller, S. S.; Müllertz, A.; Boisen, A. Polymer-Filled Microcontainers for Oral Delivery Loaded Using Supercritical Impregnation. *J. Controlled Release* **2014**, *173*, 1−9.
(19) Cardea, S.; Scognamiglio, M.; Reverchon, E. Supercritical Fluid Assisted Process for the Generation of Cellulose Acetate Loaded Structures, Potentially Useful for Tissue Engineering Applications. *Mater. Sci. Eng., C* **2016**, *59*, 480−487.
(20) Slater, T. J.; Lewis, E. A.; Haigh, S. J. Energy Dispersive X-Ray Tomography for 3D Elemental Mapping of Individual Nanoparticles. *J. Visualized Exp.* **2016**, *113*, 52815.
(21) Sanchez, D. F.; Simionovici, A. S.; Lemelle, L.; Cuartero, V.; Mathon, O.; Pascarelli, S.; Bonnin, A.; Shapiro, R.; Konhauser, K.; Grolimund, D.; et al. 2D/3D Microanalysis by Energy Dispersive X-Ray Absorption Spectroscopy Tomography. *Sci. Rep.* **2017**, *7* (1), 16453.
(22) Trenfield, S. J.; Goyanes, A.; Telford, R.; Wilsdon, D.; Rowland, M.; Gaisford, S.; Basit, A. W. 3D Printed Drug Products: Non-Destructive Dose Verification Using a Rapid Point-and-Shoot Approach. *Int. J. Pharm.* **2018**, *549* (1−2), 283−292.
(23) Cerea, M.; Maroni, A.; Palugan, L.; Bellini, M.; Foppoli, A.; Melocchi, A.; Zema, L.; Gazzaniga, A. Novel Hydrophilic Matrix System with Non-Uniform Drug Distribution for Zero-Order Release Kinetics. *J. Controlled Release* **2018**, *287*, 247−256.
(24) Edinger, M.; Bar-Shalom, D.; Rantanen, J.; Genina, N. Visualization and Non-Destructive Quantification of Inkjet-Printed Pharmaceuticals on Different Substrates Using Raman Spectroscopy and Raman Chemical Imaging. *Pharm. Res.* **2017**, *34* (5), 1023−1036.
(25) Ting, S. S. T.; Macnaughton, S. J.; Tomasko, D. L.; Foster, N. R. Solubility of Naproxen in Supercritical Carbon-Dioxide with and without Cosolvents. *Ind. Eng. Chem. Res.* **1993**, *32* (7), 1471−1481.
(26) Garmroodi, A.; Hassan, J.; Yamini, Y. Solubilities of the Drugs Benzocaine, Metronidazole Benzoate, and Naproxen in Supercritical Carbon Dioxide. *J. Chem. Eng. Data* **2004**, *49* (3), 709−712.
(27) Ilchenko, O.; Pilgun, Y.; Makhnii, T.; Slipets, R.; Reynt, A.; Kutsyk, A.; Slobodianiuk, D.; Koliada, A.; Krasnenkov, D.; Kukharskyy, V. High-Speed Line-Focus Raman Microscopy with Spectral Decomposition of Mouse Skin. *Vib. Spectrosc.* **2016**, *83*, 180−190.
(28) Ilchenko, O. O.; Pilgun, Y. V.; Reynt, A. S.; Kutsyk, A. M. NNLS and MCR-ALS Decomposition of Raman and FTIR Spectra of Multicomponent Liquid Solutions. *Ukr. J. Phys.* **2016**, *61* (6), 519−522.
(29) Gaikwad, V. V.; Patil, A. B.; Gaikwad, M. V. Scaffolds for Drug Delivery in Tissue Engineering. *Int. J. Pharm. Sci. Nanotechnol.* **2008**, *1* (2), 113−122.
(30) El Hagrasy, A. S.; Chang, S.-Y.; Desai, D.; Kiang, S. Raman Spectroscopy for the Determination of Coating Uniformity of Tablets: Assessment of Product Quality and Coating Pan Mixing Efficiency during Scale-Up. *J. Pharm. Innov.* **2006**, *1* (1), 37−42.
(31) Beyer, A.; Grohganz, H.; Löbmann, K.; Rades, T.; Leopold, C. S. Influence of the Cooling Rate and the Blend Ratio on the Physical Stability of Co-Amorphous Naproxen/Indomethacin. *Eur. J. Pharm. Biopharm.* **2016**, *109*, 140−148.
(32) Sibik, J.; Löbmann, K.; Rades, T.; Zeitler, J. A. Predicting Crystallization of Amorphous Drugs with Terahertz Spectroscopy. *Mol. Pharmaceutics* **2015**, *12* (8), 3062−3068.
(33) Allesø, M.; Chieng, N.; Rehder, S.; Rantanen, J.; Rades, T.; Aaltonen, J. Enhanced Dissolution Rate and Synchronized Release of Drugs in Binary Systems through Formulation: Amorphous Naproxen−cimetidine Mixtures Prepared by Mechanical Activation. *J. Controlled Release* **2009**, *136* (1), 45−53.

DOI: 10.1021/acsbiomaterials.9b00495
ACS Biomater. Sci. Eng. 2019, 5, 2935−2941

Where is the drug? - Quantitative 3D distribution analyses of confined drug-loaded polymer matrices

Chiara Mazzoni, Fabio Tentor, Anastasia Antalaki, Rasmus D. Jacobsen, Jacob Mortensen, Roman Slipets, Oleksii Ilchenko, Stephan S. Keller, L. Hagner Nielsen, Anja Boisen**

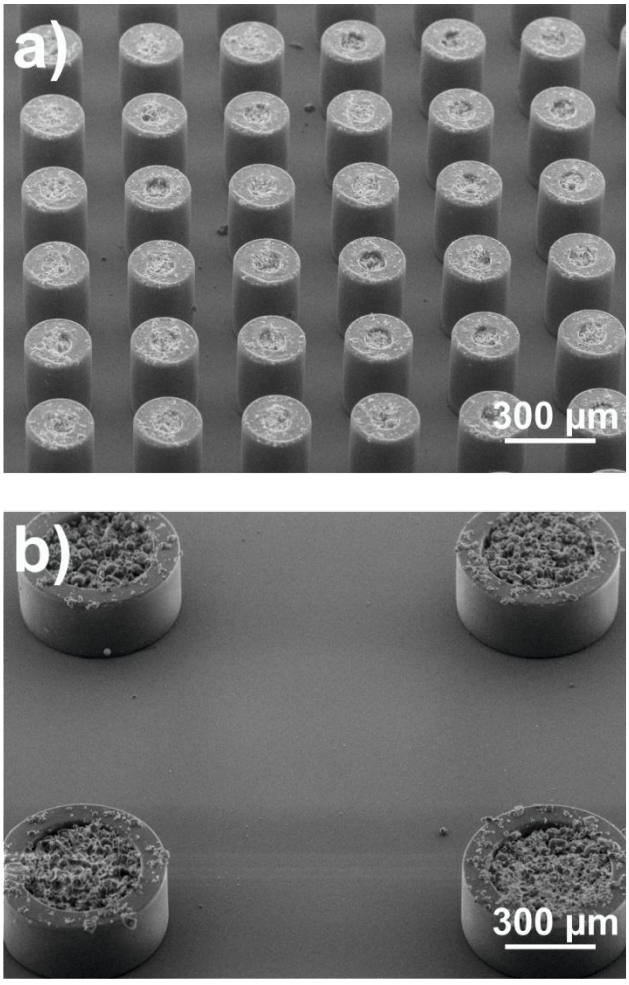

Figure S1. SEM images of microcontainers filled with PVP in the size of a) small and b) large.

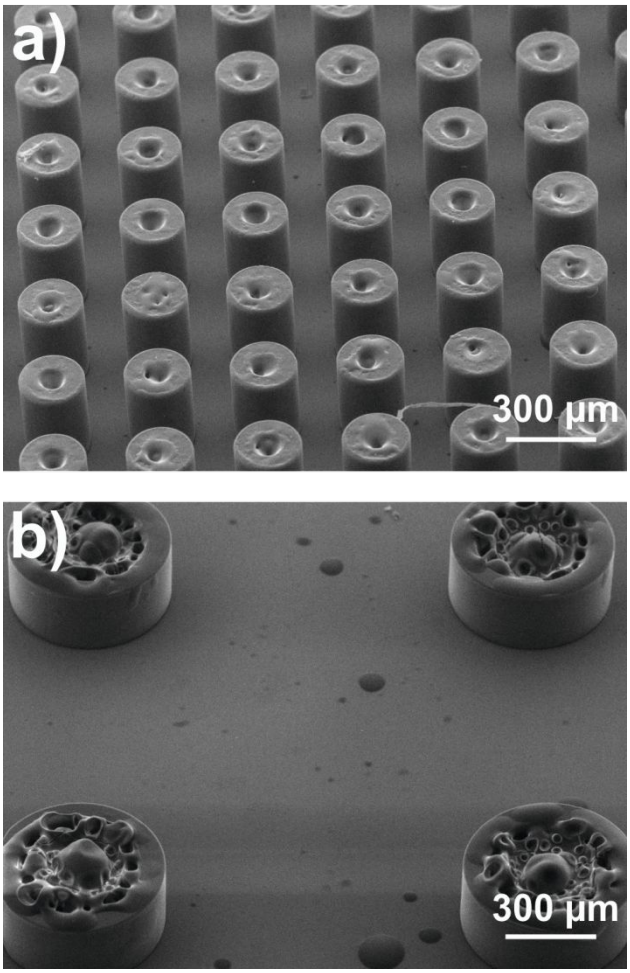

Figure S2. SEM images of microcontainers filled with PVP and loaded with ketoprofen using $scCO_2$ impregnation in the size of a) small and b) large.

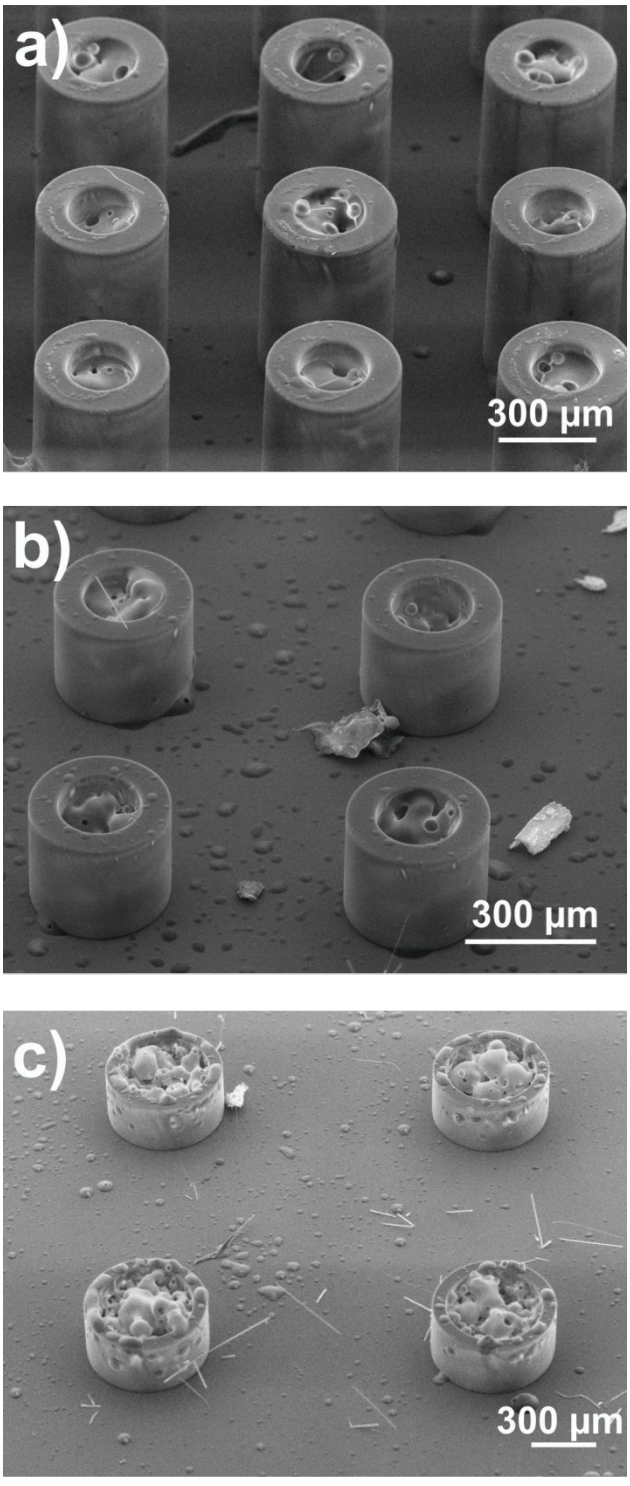

Figure S3. SEM images of microcontainers filled with PVP and loaded with naproxen using $scCO_2$ impregnation in the size of a) small, b) medium and c) large.